ELEVATED TEMPERATURE- AND TEMPERATURE-DEPENDENCE OF THE QUASI-STATIC, UNIAXIAL TENSILE BEHAVIOUR OF ADDITIVELY MANUFACTURED TI6AL4V(ELI)

TUMELO DANIEL MOLOI

Dissertation submitted in fulfilment of the requirements for the degree

MASTER OF ENGINEERING

in

MECHANICAL ENGINEERING

in the

Department of Mechanical and Mechatronics Engineering
Faculty of Engineering, Built Environment, and Information Technology
at
Central University of Technology, Free State

Supervisor: Dr T.C. Dzogbewu

Co-supervisors: Prof M. Maringa

Dr A. Muiruri

BLOEMFONTEIN

Date

Declaration of independent work

DECLARATION WITH REGARD TO

INDEPENDENT WORK

I, TUMELO DANIEL MOLOI, identity number ############## and student number #########, do hereby declare that this research project submitted to Central University of Technology, Free State for the degree MASTER OF ENGINEERING: ENGINEERING: MECHANICAL, is my own independent work; and complies with the Code of Academic Integrity, as well as other relevant policies, procedures, rules and regulations of Central University of Technology, Free State; and has not been submitted before to any institution by myself of any other person in fulfilment (or partial fulfilment) of the requirements for the attainment of any qualification.

_____ _____

SIGNATURE OF STUDENT **DATE**

ABSTRACT

The use of additive manufacturing (AM) techniques has increased in the past years. These technologies have a significant potential to replace traditional manufacturing methods such as casting, forging, moulding, machining, and joining. Laser powder bed fusion (LPBF) technologies are widely used in AM to produce complicated structures consisting of interconnected parts with minimal waste of material. Additively manufactured metallic parts exhibit features such as surface roughness, porosity, and residual stress that affect the mechanical properties of the parts and determine the sites where fatigue failure is likely to initiate. Post-heat treatment processes such as stress relief and high-temperature annealing are employed to improve the microstructure and, therefore, mechanical properties of additively manufactured metallic parts.

The Ti6Al4V alloy is the most popular titanium alloy due to its appealing combination of characteristics such as high strength and lightweight. The alloy can be used in a wide range of applications in the aerospace, automotive, and biomedical sectors at both room temperature and high temperatures. The Ti6Al4V alloy is used in aircraft for various parts, including window frames, compressor blades, and fan disks. In the biomedical industry, the alloy is used for bone implants and dental prostheses. It finds application in the automotive industry in the manufacture of parts such as outlet valves, suspension springs, and wheels. Additively manufactured Ti6Al4V occurs in various microstructures, including martensite, lamellar, equiaxed, bimodal, and the Widmanstätten microstructures.

It has been almost two centuries since fatigue was first recognised in metals subjected to repetitive or fluctuating stress due to applied load. Until today, fatigue has remained a big problem in the engineering world, occurring with little to no warning. Failure due to fatigue in engineering structures has been thoroughly studied, and engineers have developed techniques to mitigate it, but its prevention is never assured. However, some measures have been developed to study and manage fatigue. Metals and their alloys can display different types of fracture surfaces depending on the prevailing temperature, microstructure, stress state, and methods of manufacture. Consequently, further research on the fatigue behaviour of metallics is still required.

Testing at high temperatures can affect the fatigue properties of metallics. Hence, metallics that are used at high temperatures need a combination of microstructural stability and mechanical strength. As temperature rises, microstructural changes take place in metals, which affect their mechanical properties. These include strength, ductility, and stiffness. The fatigue behaviour of metallics is dependent on the microstructure and its mechanical properties. Metallics undergo a decrease in fatigue strength and fatigue resistance with increased temperature, which leads to a reduction in their fatigue life. Therefore, studies on the effect of temperature on the fatigue behaviour of the alloy are necessary to guide their use in industry.

In this study, uniaxial tensile test and fatigue test specimens were manufactured using a DMLS EOSINT M290. The specimens printed were exposed to stress relief and high-temperature annealing heat treatment. Uniaxial tensile tests and fatigue tension-tension tests were performed at various temperatures. After both uniaxial tensile testing and fatigue testing, scanning electron microscopy (SEM) was used to study the characteristics of failure on the fracture surfaces and investigate the causes of failure. An optical microscope was used to establish the changes from the edge of the fracture surface away along the gauge length. Vickers microhardness tests were performed to measure the hardness of the alloy.

The Ti6Al4V alloys used in the aircraft industry undergo temperature variations while in operation, which might have an impact on their quasi-static behaviour. Therefore, this study aimed to investigate the effect of elevated temperatures on the quasi-static behaviour of additively manufactured titanium Ti6Al4V(ELI) alloy. Considerations of this effect on the fatigue behaviour of the alloy led to the extension of the material in the literature review to fatigue. Moreover, preliminary fatigue testing at room temperature and two elevated temperatures was conducted, and the results were analysed to lay the groundwork for future fatigue testing at elevated temperatures. The results showed that a test temperature of 475 °C significantly influenced the mechanical properties, and a temperature below 325 °C had little effect on the fatigue behaviour of the alloy. Temperature changes showed little influence on the fracture characteristics and the microstructures of the alloy.

ACKNOWLEDGEMENT

First and foremost, I would like to express my gratitude and praise to Ntate Modimo, kere “Ntate o moholo, o lokelwa ke dithoko tsohle, boholo ba hae ha bona ho lekanngwa” *Psalm 145:3*.

My deepest gratitude to Dr Thywill Cephas Dzogbewu and Prof Maina Maringa for their guidance, encouragement, and patience. I am truly indebted to them. I would also like to thank Dr Amos Muiruri for his support and advice. I thank every individual at CUT who made this study a success. I also extend my gratitude to my family, friends, and brethren for their love, support, and prayers.

I would like to thank the following organizations for their support through the experimental work. The Centre for Rapid Prototyping Manufacture (CRPM) for the production of test specimens; the Product Development Technology Station (PDTS) for machining of test specimens; Mintek for tensile testing; the University of South Africa (UNISA) for fatigue and tensile testing of test specimens; and the University of the Free State (UFS) for allowing us to use their scanning electron microscope.

I want to acknowledge the financial support from the Department of Science and Innovation (DSI) through the Collaborative Program in Additive Manufacturing (CPAM) (Contract no CSIR-NLC-CPAM-21-MOA-CUT-03) and Central University of Technology, Free State through Research Grants and Scholarship Committee.

LIST OF PUBLICATIONS EMANATING FROM THIS STUDY

PEER-REVIEWED JOURNAL ARTICLES

1. Moloi T., Dzogbewu T.C., Maringa M., and Muiruri A., '*Quasi-static tensile properties of DMLS TI6AL4V(ELI) specimens exposed to two different heat treatment processes and tested at different elevated temperatures*', Results in Engineering, vol. 22, p. 102290, Jun. 2024, https://doi.org/10.1016/j.rineng.2024.102290
2. Moloi T.D., Dzogbewu T.C., Maringa M., and Muiruri A.M, "*The effect of temperature on the microstructures of additively manufactured Ti6Al4V(ELI)*", Iranian Journal of Materials Science and Engineering, vol. 21(3), p. 41–52, Sept. 2024, http://dx.doi.org/10.22068/ijmse.3589
3. Moloi T., Dzogbewu T.C., Maringa M., and Muiruri A., "*A Review of the Fatigue Behaviour of Laser Powder Bed Fusion Ti6Al4V*". Metallurgical and Materials Engineering, vol. 31(1), p. 288-310, 2025, https://metall-mater-eng.com/index.php/home/article/view/1245

SUBMITTED TO DHET-APPROVED PEER-REVIEWED JOURNALS FOR POSSIBLE PUBLICATION

1. Moloi T., Dzogbewu T.C., Maringa M., and Muiruri A., "*Review on the effect of heat treatment on microstructure and mechanical properties of metallics"*.

TABLE OF CONTENTS

LIST OF FIGURES

LIST OF TABLES

ACRONYMS

3D	Three Dimensional
AM	Additive Manufacturing
ASTM	American Society for Testing and Materials
BCC	Body centred Cubic
CAD	Computer Aided Design
COV	Coefficient of Variance
DED	Directed Energy Deposition
DMLS	Directed Metal Laser Sintering
EBM	Electron Beam Melting
EDM	Electrical Discharge Machine
ELI	Extra-Low Interstitial
EOS	Electro Optical Systems
EPFM	Elastic Plastic Fracture Mechanics
FDM	Fused Deposition Modelling
HCF	High-Cycle Fatigue
HCP	Hexagonal Close Packed
HIP	Hot Isostatic Pressing
HTA	High Temperature Annealing
HV	Vickers Hardness

LAM	Laser Additive Manufacturing
LCF	Low-Cycle Fatigue
LEFM	Linear Elastic Fracture Mechanics
LENS	Laser Engineered Net Shaping
LPBF	Laser Powder Bed Fusion
SEI	Scanning Electron Imaging
SEM	Scanning Electron Microscopy
SLA	Stereolithography Apparatus
SLS	Selective Laser Sintering
SLM	Selective Laser Melting
SR	Stress Relief
TBC	Thermal Barrier Coating
TEM	Transmission Electron Microscopy

SYMBOLS

σ	Stress
R	Stress ratio
σ_a	Stress amplitude
σ_m	Mean stress
σ_{max}	Maximum stress
σ_{min}	Minimum stress
$\Delta\sigma$	Change in stress
K	Stress intensity factor
ΔK	Change in stress intensity factor
K_{th}	Stress intensity threshold
K_c	Fracture toughness
K_{IC}	Plane strain fracture toughness
α	Alpha hcp phase
β	Beta bcc phase

CHAPTER 1: BACKGROUND OF THE STUDY

1.1. Summary

This chapter contains a background on fatigue in metallics, with a focus on the effect of temperature on the fatigue behaviour of Ti6Al4V alloy. A summary on additive manufacturing (AM) is also presented, followed by a problem statement, aim and objectives of the study and finally scope and outline of the dissertation.

1.2. Introduction

Fatigue was first discovered in the 19th century after several serious fatigue failures were reported. At that time, materials were failing under cyclic loading without warning [1]. Fatigue failure was observed to occur at low-amplitude stresses, below the material's ultimate tensile strength and even yield strength [2]. Extensive experimental investigations proved that the fatigue phenomenon is largely a process that occurs progressively in the following stages: crack initiation, crack growth, and fast fracture [1]. Factors such as mean stress, stress concentration, type of fluctuating loading, presence of internal and surface flaws, frequency of loading, heat treatment, microstructure, as well as build orientation in the case of AM and temperature are known today to influence the fatigue behaviour of metal alloys [3, 4, 5, 6].

For high-temperature applications, metals and metal alloys need a combination of microstructural stability, mechanical strength, and corrosion resistance [7]. An alloy is categorized as a high-temperature alloy if it remains effective at 500 °C or higher. Testing at high temperatures can affect the fatigue properties of a material. An increase in operating temperature causes a reduction in the metallic's fatigue strength because, at high temperatures, cracks grow faster, resulting in a reduction in fatigue life [8]. Tokaji [9] observed a reduction in fatigue strength with an increase in temperature when investigating the effect of elevated temperature on the fatigue life of Ti6Al4V alloy at room temperature and 623 K and 723 K [9]. Jiao *et al*. [10] compared the fatigue crack resistance of SLM Ti6Al4V tested at room temperature and a temperature of 400 ℃ and stated that at a temperature of 400 ℃, the fatigue crack growth rate is higher than at room temperature [10]. On the other hand, Arakere *et al*. [11] studied the behaviour of Ti6Al4V at room temperature, 175 ℃, 230 ℃, 290 ℃, and

345 ℃. They observed no significant change in the rates of crack growth due to these varying temperatures [11]. These converse results call for further testing to establish the dependence of fatigue on testing temperature fully. Titanium alloys are used for many applications across several industries, such as aerospace, biomedical, and automobile because they possess combinations of desirable material characteristics such as high specific strength, low density, and adequate ductility [12].

Subtractive manufacturing, which includes machining, drilling, milling, turning, and grinding, is a manufacturing process that involves removing material from a solid block or sheet to create a desired shape [13]. This leads to a significant wastage of material and is time-consuming. In contrast to subtractive manufacturing, AM is described by the ASTM standard as a process of joining materials to make objects from 3D model data, usually layer upon layer [14, 15]. It is typical to use metallic powders that are melted successively using a laser or electron beam source of energy. AM was established in 1987 [16], as a solution for faster product development and since then, the use of AM has increased rapidly [12]. Powder bed fusion (PBF) technologies are the most widely used AM techniques. They use metal powder to create three-dimensional (3D) parts, layer upon layer, from computer-aided drawings (CAD). These techniques allow for high precision with little material wastage of material in the development of complex structures made up of connecting parts [17], [18]. Parts made of Ti6Al4V(ELI) have been widely produced through laser powder bed fusion (LPBF) [19]. The LPBF is a PBF technology that uses a laser as a source of energy and is one of the most promising and flexible metal fabricating methods [17].

1.3. Problem Statement

Since the establishment of fatigue in 1830 [20] till today, fatigue remains an issue in many industries such as automobile, aircraft, biomedical, marine, power, and energy sectors. In these industries, engineering structures are subjected to cyclic loading. Failure in these structural components, though undesirable, is inevitable. Extensive reports on fatigue have revealed that fatigue occurs progressively in the progressive stages of crack initiation, crack growth, and final fracture with little to no warning. Today, though the causes of fatigue and its impacts are well known, its prevention cannot be guaranteed. Even though a lot of investigations on fatigue have been conducted, fatigue remains a problem. Therefore, there is still a need to carry out extensive studies on the fatigue behaviour of metallics.

The Ti6Al4V alloy is applied in the aerospace industries for components in jet engines, airframes, and panes. In this industry, the alloy's components experience changes in temperature while in service, which can affect their fatigue life. Studies have reported the effect of temperature on fatigue behaviour to be significant. Studies [21, 22, 23, 24], have shown that as the temperature is increased above room temperature, there are changes in the microstructure of the alloy, particularly when such exposure occurs over extended periods. The fatigue behaviour of Ti6Al4V, just as that of other metallics, is dependent on the microstructure of the alloy. The prevailing microstructure of the alloy is dependent on the initial cooling rate of the alloy, and subsequent temperatures at which the alloy is soaked and the periods over which such temperatures are maintained. Therefore, studies on the effect of temperature on the fatigue behaviour of the alloy are necessary to guide their use in industry. It was reported [11], that fatigue testing at temperatures below 350 °C has little to no effect on the fatigue behaviour of Ti6Al4V alloy. As to why this is so, needs to be investigated.

The fatigue life of Ti6Al4V is dependent on its mechanical properties, which are known to depend on the microstructure. An increase in temperature has been reported [10, 25, 26], to cause a reduction in tensile strength and a rise in ductility. A reduction in tensile strength results in a decrease in fatigue strength and an increase in ductility improves fatigue performance. The relationship between the tensile strength and ductility as the temperature changes is very important, as an increase in one property occurs at the expense of a reduction of the other property. There is a need to investigate this dichotomy further.

1.4. Aim and Objectives

This study aimed to determine the effect of changes of temperature above room temperature and the effect of elevated temperatures on the quasi-static behaviour of the additively manufactured Ti6Al4V(ELI) alloy, as a prelude to high temperature fatigue testing of the material.

The objectives of this research include:

- Develop a test matrix for the research study.
- Additively manufacture fatigue and tensile test specimens, apply post-heat treatment processes on them and machine them to comply with relevant ASTM International standards.

- Carry out uniaxial tensile testing of the specimens at room temperature and at elevated temperatures to investigate the effects of changes in temperature and effects of elevated test temperature on the strength and ductility of the alloy.
- Carry out tension-tension fatigue testing at room temperature and two elevated temperatures to lay the groundwork for future fatigue testing at elevated temperatures.
- Undertake fractography of the tested specimens and investigate the effects of changes in temperature and the effects of elevated temperatures on the characteristics of the fracture surfaces of the alloy separately under uniaxial tensile loading and under tension-tension fatigue loading.
- Carry out analysis of microstructural changes in the tested specimens due to changes in temperature and elevated temperatures.
- Undertake Vickers microhardness testing to evaluate the effects of changes in temperature and effects of elevated temperatures on the hardness of the alloy.

1.5. Scope and Outline of the Dissertation

Figure 1.1 below shows the structure of the dissertation.

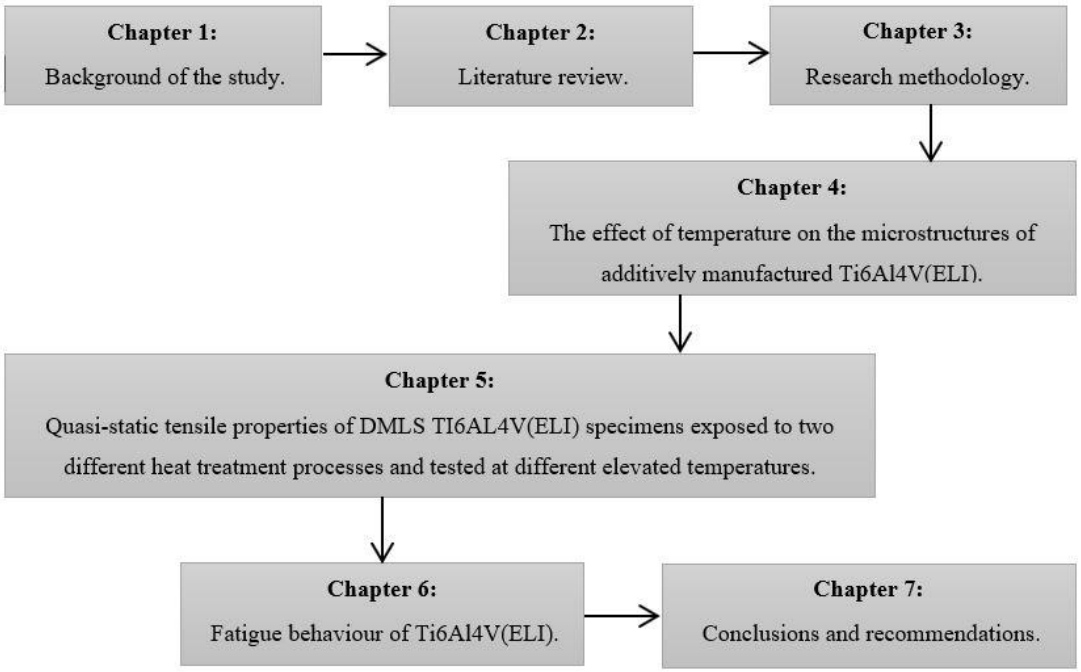

Figure 1.1: Flow diagram of the research study.

CHAPTER 2: LITERATURE REVIEW

Some of the material contained in this chapter was published in a peer-reviewed journal, as detailed below:

Moloi T., Dzogbewu T.C., Maringa M., and Muiruri A., "*A Review of the Fatigue Behaviour of Laser Powder Bed Fusion Ti6Al4V*". Metallurgical and Materials Engineering, vol. 31(1), p. 288-310, 2025, https://metall-mater-eng.com/index.php/home/article/view/1245

2.1. Introduction

This chapter contains a literature review on AM, its history, technologies, advantages, and disadvantages, focusing on the production of Ti6Al4V(ELI) by LPBF; titanium and its alloys, focussing on Ti6Al4V, its crystal structures, and microstructures as well as its mechanical properties. The review of literature is extended to fatigue, the history of fatigue, types of fatigue loading, and factors that affect fatigue, with a focus on the effect of temperature. An overview of post-heat treatment processes and their effect on the microstructure and mechanical properties of the alloy is also provided.

2.2 Additive Manufacturing

2.2.1. History of additive manufacturing

The first application of AM was in 1980. The company 3D Systems, formed by Chuck Hull in 1986, produced the first stereolithography (SL) system, which used a UV laser to solidify thin layers of liquid polymer, one layer at a time [16, 27, 28]. Stereo-Lithography-Apparatus-1 (SLA-1) is recognised as the forerunner of the well-known SLA 250 machine and was the first commercially available AM system in the world. The Viper SLA followed shortly after. Ciba-Geigy created and introduced the first-generation acrylate resins in SL materials in 1988. Asahi Denka Kogyo introduced the first epoxy resin for the CMET SL machine in the same year [16], [29]. The first stereolithography system was sold by the German company Electro-Optical Systems (EOS) in 1990 [16, 28]. Three AM technologies were brought to the market in 1991 [28, 29]: solid-ground curing (SGC) from Cubital, laminated object manufacturing (LOM) from Helisys, and fused deposition modelling (FDM) from Stratasys. The solid form

stereolithography system and selective laser sintering (SLS), which use laser heat to fuse powder materials, were made available in 1992 [16].

The first 3D printer, the Actua 2100, was sold by 3D Systems in 1996, following eight years of selling stereolithography systems. This printer uses an inkjet printing mechanism to deposit wax material layer by layer [16]. A high-power laser and powdered titanium alloys were used in the development of AeroMet's 1997 [29] laser additive manufacturing (LAM) method. The business provided services and produced parts for the aircraft industry [16]. Optomec used Sandia National Laboratories technology to commercialise its laser-engineered net shaping (LENS) metal powder system in 1998. In 1999, Germany's Fockele & Schwarze jointly developed a selective laser-melting system based on steel powder at the Fraunhofer Institute for Laser Technology [16]. The Direct Steel 20-V1 product, a powder made of steel with particles as small as 20 microns, was introduced by EOS in 2001. Layers of metal with a thickness of 20 microns are created using the powder. Shortly after, EOS unveiled the EOSINT 380, a laser-sintering device that provided increased laser scanning speed. The first two EOSINT laser-sintering machines were sold in North America, according to an announcement made by EOS in 2003. The company first presented the EOSINT M 270 direct metal laser sintering machine at EuroMold 2003. Unlike the CO_2 laser used in the EOSINT M 250 extended machine, the system for the EOSINT M270 machine make use of a Ytterbium laser fibre. The EOSINT P 385, a system for plastics that can produce thinner layers than its predecessor, the EOSINT P 380, was unveiled by the EOS at EuroMold 2004. For the EOSINT M 270 systems, EOS introduced its cobalt-chrome powder material in 2006. The company also offered 17-4 stainless steel powder for use with its EOSINT M 270 apparatus [16, 28].

In the early 2000s, AM was used to manufacture prostheses and dental implants. Apart from medical devices, AM is currently utilized in the production of biological chips, circulatory networks, bones, tissues, and organs [30]. Given its ability to shorten development cycles and lower manufacturing and product costs, AM technologies have been widely adopted by the automotive industry for the design and manufacturing of components, including drive shafts, gearbox components, braking systems, and engine exhausts [31]. Advanced materials, such as titanium alloys, nickel super-alloys, and special steels, which are difficult, expensive, and time-consuming to produce using conventional methods, are used to create the intricate structures that make up aerospace components. Applications for AM technology in aerospace are very promising. AM can be used to create parts with weight-saving features like internal cavities

and lattice structures without sacrificing their mechanical functionality. [31]. The AM technology is widely accepted in the above-mentioned industries and many other industries and metal is used as the material of choice [30].

2.2.2. Additive manufacturing technologies

AM is a manufacturing technique commonly known as 3D printing. The AM technique has seven categories, namely, binder jetting, directed energy deposition, material extrusion, material jetting, sheet lamination, vat polymerization, and powder bed fusion [14, 32, 33, 34, 35, 36].

Binder jetting is an AM technique in which an inkjet is placed on top of a powder bed and uses liquid droplets to bind the powder material [14, 32]. Parts made with this technology frequently need to be post-processed to densify the constituent powder and remove the binder. Using thermal energy, directed energy deposition (DED), as illustrated in Figure 2.1, melts feed powder that is then deposited onto a surface, where it solidifies into a 3D part [14, 32, 37]. LENS is a specific DED process, also referred to as direct metal deposition (DMD) [38]. It utilizes multiple nozzles to spray powder into a melt pool that is created by a focused laser beam [12, 35]. Numerous metal-based materials, including nickel, copper, Inconel, titanium alloys, stainless steel, aluminium alloys, and tungsten, are compatible with DED. This process creates parts with a high-density [30]. Based on the number of fabricators in use today, material extrusion is the most popular AM technology. In this process, the feedstock is forced through a nozzle that determines the voxel size [14, 32]. The Fused Deposition Modelling (FDM) technology is an example of material extrusion. Material jetting involves depositing photosensitive thermoset polymer material droplets onto a build platform that subsequently cures. Another AM technology is sheet lamination, in which the feedstock takes the shape of a sheet and forms a layer within the build. The earliest commercial AM process still in use today is called vat polymerisation, and it involves photolithographically cross-linking liquid thermoset polymer resins to create a solid [14, 32].

To facilitate the fusion of powder, powder bed fusion (PBF) is an AM process in which a laser or electron beam is used as the heat source directed onto the surface of a powder bed [14]. Different atmospheres are needed for different energy sources. For laser systems, nitrogen or argon gas is usually needed, and when using an electron beam, a vacuum is preferred [39]. To fill in the design that the CAD data provides, the powder is scanned using a high-energy power

source to selectively melt or sinter the powder. Once the first layer has taken the desired shape, the next layer of powder is spread, and the process is repeated. Every new layer is fused to the one before it because the process parameters of the system are set to ensure the laser/electron beam has a deeper penetration than a single layer. The leftover powder at the end of the process can be combined with fresh powder for the manufacture of other components [30]. Electron beam melting (EBM), laser-engineered net shaping (LENS), and selective laser melting (SLM) are the main AM techniques utilized to fabricate metallic parts. Selective laser sintering (SLS) and SLM or DMLS are categorized as LPBF techniques [12]. DMLS is sometimes referred to as SLM. The two technologies use the same process, but they differ in terms of trademarks; the DMLS technology is a product of EOS GmbH, while SLM is a product of Nikon SLM Solutions AG.

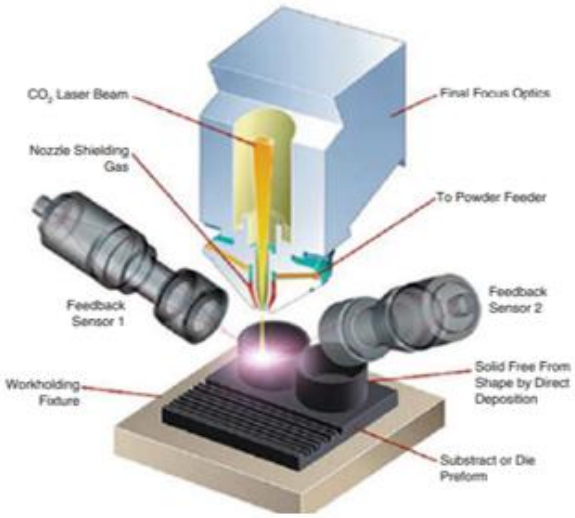

Figure 2.1: Representative schematic of DED [40]

Electron beam melting operates at a temperature of 700 °C and has high scanning speeds, which allow preheating of each layer through melting. The technology utilizes two scanning runs: a pre-melting scan and a melting scan. For the pre-melting scan, high scanning speeds and lower beam currents are typically used to ensure that the powder bed warms up in preparation for the melting scan. The desired microstructure and mechanical characteristics of the final component are taken into consideration when adjusting the current and scanning speed of the beam following the pre-melting scan [30]. Heat treatment reduces the residual stresses caused by the process by lowering temperature gradients and local cooling rates. High vacuum conditions are necessary to prevent electron collisions with gas particles, which would scatter the electron beam, reducing its focus and energy, thus ensuring the precision and quality of the machining

process by minimising contamination and allowing the electron beam to travel directly to the workpiece without disruption [41].

2.2.3. Laser powder bed fusion

LPBF is a promising method for the fabrication of metallic components [55]. The schematic displayed in Figure 2.2 serves as a representation of LPBF technology.

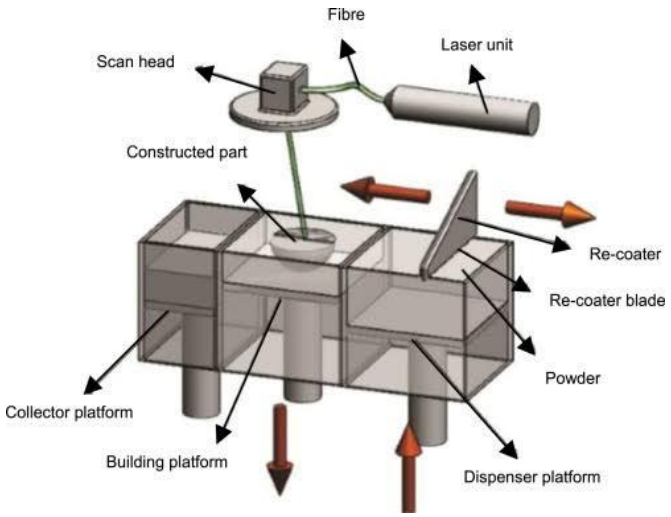

Figure 2.2: A schematic of laser powder bed fusion [42]

The technology has a high tolerance (± 0.15 mm to ± 0.25 mm [43]) and can create complex structures made of interconnected parts with minimal wastage of material. This method works well with a wide range of elemental metals and alloys and produces thin-walled parts with good accuracy [17, 35]. However, the process has a weakness that prevents its widespread acceptance and use as a standard manufacturing process. This is its tendency to build an unbalanced stress profile into the parts between the layers during processing [35]. Post-heat treatment processes, such as stress relief, are applied to metallic parts to reduce undesired residual stresses, and this is done without necessarily changing the parts' mechanical characteristics [44]. Though this method addresses the problem, it comes with an increase in cost and duration of production. For Ti6Al4V, the LPBF process is preferred over other alternative PBF technologies [45, 46]. Because of its low ductility with an elastic strain of less than 10%, the α' martensitic Ti6Al4V microstructure found in LPBF as-built parts is undesirable in the biomedical industry that requires parts with a minimum elastic strain of 10%, per ASTM F13-12a [45].

During the LPBF process, the laser beam energy is chosen so that the metallic layer of powder is completely liquefied by heat throughout its thickness at the laser beam point of application. Each track built by the laser beam is set to partially overlap the previous one to ensure good intertrack bonding. The laser beam's power and scanning speed are set to ensure penetration of the mean through the top layer of powder and beyond to ensure good bonding between layers. Following the complete printing of a layer, the build table is lowered by one layer thickness, a fresh layer of powder is applied to the build platform, levelled out using a re-coater, and the printing process is restarted. This cycle is repeated until the 3D part is completely built. The heat from the building platform facilitates the quick solidification of the molten portion. This is done by directing heat away from the built parts, which increases the rate of solidification of the parts. A protective gas environment is charged into the working chamber to shield the built parts from oxidation. One layer of powder is normally between 20 and 100 µm thick [47]. As-built parts may contain some structural defects due to the process' propensity to produce a lack of fusion, gas porosity, keyhole collapse, surface-connected porosity, solid-state cracking, and solidification cracking [48]. EBM-built parts are less vulnerable to residual stresses than LPBF parts because the building environment is at temperatures between 600 and 700 °C. Titanium alloy components exposed to prolonged periods of high temperatures during fabrication may require stress relief [48, 49].

Residual stresses are self-equilibrium stresses of deformed material that remain within the structure after the deforming load is removed. Residual stresses arise from the printed layers constraining the contraction of the current layer. They can initiate cracks and delamination, as well as shorten the fatigue lives of parts [47]. Residual stresses can be decreased by using optimum process parameters or post-heat treatment techniques like stress relief. To lessen residual stress, further mechanical processes like surface rolling and shot peening are employed [49]. Gas pores and lack-of-fusion holes are frequent flaws in AM [50]. Gas can become trapped in the molten metal during rapid solidification [51]. Non-optimum process parameters, including scanning speed, layer thickness, laser power [52], powder quality, a wide particle size distribution, and powder contamination, as well as unstable chamber pressure and temperature gradients, are conditions that result in the formation of gas pores [51, 52]. Fotovvati *et al*. [53] reported that high laser power or low scanning speed led to the production of parts with porosity. Another reason for the formation of gas pores is that a contaminated or constricted gas hose can interfere with the gas supply. In a comparison of lack-of-fusion defects, it was found that samples that fail because of gas pores have a longer fatigue life [54,

55]. This is because gas pores are often rounded and smaller, less likely to concentrate stress, while lack-of-fusion pores are sharp and irregular in shape and show areas of molten material that have failed to fuse fully. These points act as initiation sites for cracks, leading to reduced fatigue life and increasing the likeliness of failure under cyclic loading. Defects related to lack of fusion are typically found at the interface between layers and are orientated perpendicular to the build direction [50, 51]. In LPBF samples, porosity, especially in the form of near-surface internal defects, reduces fatigue life. A micro-CT scanner is typically utilized to assess porosity. Some holes may be overlooked due to differences in contrast between the scans, as well as the kind of metal and size of the pores in relation to the scan resolution [55]. New technologies with high quality have been developed to address this matter. These new technologies come with improved features such as adjustable X-ray energy to maximise contrast, the use of appropriate filters to reduce scatter radiation and improve quality, the use of 3D visualisation tools, and the tomographic microscopy, which offers higher image resolution. The problem of porosity and large microstructure defects can degrade tensile properties and can be solved by optimising the LPBF process parameters [56]. To have the best mechanical properties, maximum density should be achieved. The scanning speed, layer thickness, scanning strategy, and other process parameters must be optimal to produce non-porous LPBF parts [52]. Nonetheless, the impact of residual stress and porosity on the material's fatigue properties is not as great as that of the microstructure [54].

2.2.4. The advantages and disadvantages of AM over traditional methods of manufacturing

The advantages of AM over traditional methods of manufacturing include:

- Printing a complex item with intricate geometry is less expensive than printing a straightforward cube of the same size [35].
- All it takes to change a component is to make changes to the original CAD file like adding supports and slice the part [36]; once this is done, the modified product may be produced right away.
- Often no assembly required, as parts can be printed in metal, which reduces the number of parts required significantly [35].
- The process takes little lead time, and prototypes can be made immediately with a 3D printer once the stereolithography (STL) file for the part is completed [17, 35].

- Because only the necessary material is used—very little if any—is wasted, there is less waste overall [17, 36].

The disadvantages of AM over traditional methods of manufacturing include:

- Slow build rates [36]: a lot of AM techniques deposit material at a rate of between (0.06 to 0.3 m^3/s), or one to five cubic inches per hour.
- Its production costs are high [57] additional time spent on the process may result in higher costs as AM is not always the fastest way to make items.
- Post-processing is required because the surface finish and dimensional precision may be worse than with alternative manufacturing methods [35, 36].
- The production process is erratic and not suitable for mass production [57].
- It features a tiny build volume and restricted component size [36, 57]. Polymer items often have a volume of one cubic metre, but metal parts might only have 0.03 m^3. Larger machines are available, but they are not cheap.

2.3. Titanium and its Alloys

2.3.1. History of titanium

In 1791, Pastor William Gregor, a mineralogist, found a new element and named it 'Gregorite' [30, 58]. Four years later, Martin Heinrich Klaproth, who is regarded as the founder of modern analytical chemistry, discovered many new elements. Klaproth identified the element that Gregor found and called it titanium, meaning 'earth' in Latin [58, 59]. Before pure metallic titanium was first extracted in 1910 by heating titanium tetrachloride with sodium in a steel bomb, the process of extracting titanium from its ore had been unsuccessful for more than a century [59]. It was Wilhelm Justin Kroll in 1932, who came up with a process to reduce titanium from titanium tetrachloride ore using calcium, which brought titanium outside of the laboratory and into the commercial market; the process is now known as Kroll's Process [59]. Additional adjustments were made to the procedure to increase its commercial efficiency, such as substituting calcium with magnesium as the reducing agent [30].

Titanium is recognised as an element with the symbol Ti, atomic number 22, atomic weight 47.9, and a density of 4.51 g/cm^3 [30, 60]. Titanium is the fourth most common structural metal in the crust of the Earth, after aluminium, iron, and magnesium [59]. It is a non-ferrous metal,

is not found in its pure form, and its extraction process is costly. Titanium has a low coefficient of thermal expansion, nearly half that of aluminium and lower than that of steel. It is a non-magnetic element with a low heat transfer coefficient compared to steel and aluminium. It is not suitable for use at temperatures above 400 ˚C [30].

2.3.2. Titanium crystal structures

Similar to other metals, titanium may crystallise in a variety of crystal forms within a broad temperature range. Allotropic transformation refers to the change from one crystal structure to another, and transition temperature is the temperature at which that transformation occurs. Figure 2.3 shows crystal structures that are found in titanium and its alloys.

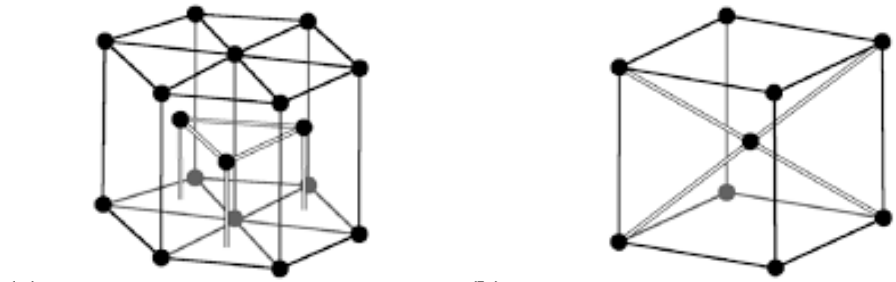

(a) **(b)**

Figure 2.3: Titanium crystal structures, (a) hexagonal-close-packed and (b) body-centred-cubic [61]

At low temperatures, most titanium alloys and pure titanium crystallise in an idealised hexagonal-close-packed (hcp) structure, known as α-titanium, which is depicted in Figure 2.3(a). At elevated temperatures, the bcc (body-centred-cubic) structure, depicted in Figure 2.3(b), known as β-titanium prevails. Pure titanium has a β-transition temperature of 882±2 ℃, also known as beta transus [58]. The microstructures of titanium alloys are susceptible to changes in temperature [62].

2.3.3. Classification of titanium alloys

Titanium alloys are categorized based on the amount of α and β present in their room-temperature structures. A number of categories exist for titanium alloys, including α-alloys, near-α-alloys, α+β alloys, near-β-alloys, and β-alloys [58]. The α-alloys all have an α-phase microstructure, have no β-stabilizers and consequently no β-phase. About 1–2% of the near-α

alloys contain β-stabilizers, while 5–10% contain the β-phase [30]. The $\alpha+\beta$ alloys are composed of both β- and α-stabilizers. The β-stabilizers are present in greater quantities in the near-β and β-alloy, which make up the majority of the β-phase alloys. The alloys of titanium are employed in place of pure titanium in industries to make up for its shortcomings [30, 58, 59].

a) The α-titanium alloys

At room temperature, α-titanium alloys have a hcp crystal structure with a high α-stabilizer content. The properties of α-titanium alloys include oxidation resistance, good notch toughness, low to medium strength, and reasonable ductility. Compared to other titanium alloys, they demonstrate superior resistance against creep at elevated temperatures [30, 60]. Both interstitial and substitutional alloying elements are present in the α-stabilizers. The elements aluminium, gallium, germanium, tin, and zirconium are substitutional α-stabilizers [58], while oxygen, nitrogen, and carbon are interstitial α-stabilizers [59]. Aluminium is the most widely employed substitutional alloying element because of its high solubility in both the α- and β-phases and its ability to lower the alloy's density. The creation of alpha alloys with substitutional α-stabilizing components is ideal for cryogenic and high-temperature uses. Alpha titanium alloys do not respond to heat treatment [30, 58, 60].

b) Near-α titanium alloys

These titanium alloys exhibit 5–10% of the β-phase into the microstructure at ambient temperature [30, 58, 63]. Because of the increase in β-stabilizers, compared to the α-alloys, these alloys are suited for high operating temperatures of approximately 500–550 °C for their application in compressor blades, discs, and casings. The alloy's strength and resistance to oxidation and temperature creep, compared to alpha alloys, can be attributed to its increase in content of the β-phase. Near-α titanium alloys react to heat treatment because the application of heat treatment causes a change in their microstructure [30, 58].

c) The $\alpha+\beta$ titanium alloys

The α- and β-phases are present in these titanium alloys. The relative amount of each phase can vary significantly depending on the specific alloy composition and heat treatment process. These alloys combine strength and ductility better than any other classes of titanium alloys [30,

60, 63]. Since the decrease in the α-phase from the previous two classes, this class is accompanied by an increase in the β-phase; α+β titanium alloys are more weldable and have lower creep strength than near-α and α-alloys [30]. They are used in the aircraft sector in the compressor blade structural parts of gas turbine engines. Heat treatment of these titanium alloys can provide a variety of microstructures. The majority of titanium alloys produced are $\alpha+\beta$ alloys, with Ti6Al4V accounting for over half of the market share [30, 58].

d) The β and near-β titanium alloys

At an approximate temperature of 885 ℃ [64] these titanium alloys, with a greater β-stabilizer concentration, exhibit a bcc crystal structure. The β-isomorphous and β-eutectoid are the two classes into which they are divided. Tantalum and tungsten are rarely utilized because of their density, although vanadium, niobium, and molybdenum are β-isomorphous [30, 60, 63]. Copper, nickel, manganese, and tungsten are known to have extremely limited usage, whereas silicon, chromium, and iron are the β-eutectoid stabilizers that are most frequently employed for alloying with titanium [58]. These alloys have strength levels exceeding 1300 MPa [30]. Because of these alloys' desirable qualities of high strength-to-weight ratio, exceptional combinations of corrosion resistance, toughness, crack growth resistance, and creep resistance at intermediate temperatures (~400 ℃), they are crucial in the aerospace and automotive industries [30, 64].

Table 2.1 shows the classification of titanium alloys and alloys failing in each class.

Table 2.1: Titanium alloys [30, 58, 64, 65]

α-alloys	**Near-α alloys**	**$\alpha+\beta$ alloys**	**Near-β alloys**	**β-alloys**
Ti	Ti-5Al-6Sn-2Zr-1Mo-0.2Si	Ti-4Al-4Mo-2.5Sn	Ti-10V-2Fe-3Al	Ti-3Al-8V-6Cr-4Mo-4Zr
Ti-5Al-2.5Sn	Ti–6Al–5Zr–0.5Mo–0.25Si	Ti-5Al-2Sn-2Zr-4Mo-4Cr	Ti-5Al-5Mo-5V-1Cr-1Fe	Ti-13V-11Cr-3Al
	Ti-8Al-1Mo-1V	Ti-3Al-2,5V		Ti-8Mo-8V-2Fe-3Al
	Ti-6Al-2Sn-4Zr-2Mo	**Ti-6Al-4V**		Ti-11.5Mo-6Zr-4.5Sn
	Ti-6Al-2Nb-1Ta-0.8Mo	Ti-6Al-6V-2Sn		Ti-11V-11Cr-3Al
		Ti-6Al-2Sn-4Zr-6Mo		
		Ti-3Al-2,5V		
		Ti-7Al-4Mo		

2.3.4. Mechanical properties of titanium alloys

Table 2.2 presents the mechanical properties of alpha, some of the alpha/beta, and beta titanium alloys.

Table 2.2: Mechanical properties of titanium alloys [66]

Titanium and its Alloys	**Alloy type**	**Modulus of elasticity *(GPa)***	**Ultimate tensile strength *(MPa)***	**Yield strength (0.2%) *(MPa)***	**Percentage elongation *(%)***	**Percentage reduction area *(%)***
Alpha	Ti	105	240-617	165-520	12-27	-
Alpha/ beta	**Ti6Al4V**	**88-116**	**990-1184**	**789-1013**	**2-30**	**2-41**
	Ti-5Al-2.5Fe	110	943-1050	818-892	13-16	33-42
	Ti-6Al-7Nb	108	900-1100	910-970	11-14	
Beta	Ti-13Nb-13Zr	79	550-1035	345-932	8-15	15-30
	Ti-11.5Mo-6zr-2Fe	74-85	1060-1100	910-970	18-22	46-73
	Ti-15Mo-5Zr-3Al	15-113	882-1312	870-1284	11-20	43-83

Table 2.5 shows that the alpha titanium has the lowest ultimate tensile and yield strength. Ahmed *et al*. [58] stated that industries use titanium alloys rather than pure titanium to make up for such disadvantages. The alpha/beta alloys have well-balanced properties, high strength, and good ductility. The beta alloys have lower moduli of elasticity and, therefore, deform more easily than the other classes of titanium alloys.

2.4. The Ti6Al4V(ELI)

The most researched titanium alloy is Ti6Al4V, an $\alpha+\beta$ alloy in which vanadium, the β-stabilizing element, constitutes 4 by weight percent, and aluminium, the α-stabilizing element nearly 6 by weight percent. The alloy is characterised by high strength, low density, and high fracture toughness, as well as good corrosion resistance and biocompatibility. The alloy was initially developed in the 1950s for structural applications in aircraft. The alloy's good strength and light weight make it ideal for use in jet engines, gas turbines, and airframe parts [67].

Several other industries such as marine, automobile, energy, and biomedical use titanium alloys due to their good strength-to-density ratio [41]. Today, the alloy is used in the biomedical, automotive, and aerospace for components such as bone implants, as well as connecting rods, compressor blades and discs in the front stages of gas turbine, respectively [23].

Despite the strong demand for the alloy, Ti6Al4V products have poor thermal conductivity, thus making traditional machining difficult [68]. Temperatures between 250 ℃ and 400 ℃ are considered medium to high for Ti6Al4V. Temperatures exceeding 400 °C do have an impact on the microstructure, and therefore, mechanical properties of the alloy [68].

2.4.1. Microstructures of Ti6Al4V(ELI)

As an α+β alloy, Ti6Al4V has both β-phase BCC and α-phase HCP grains, both of which then determine the microstructure and, therefore, mechanical and service properties of the alloy [30, 67]. The alloy's cooling rate from the β-phase region determines the size and arrangement of the α- and β-phases in the microstructure. Different heating conditions and cooling rates can give rise to different microstructures of the alloy, namely martensite, lamellar, equiaxed, bimodal, and Widmanstätten [30]. Figure 2.4 shows the Ti6Al4V alloy's phase diagram and phase transformation as a function of cooling rates. The alloy undergoes the following phase transformation during complete melting and solidification: α+$\beta \rightarrow \beta \rightarrow$ liquid $\rightarrow \beta \rightarrow \alpha$+$\beta \rightarrow \alpha$'.

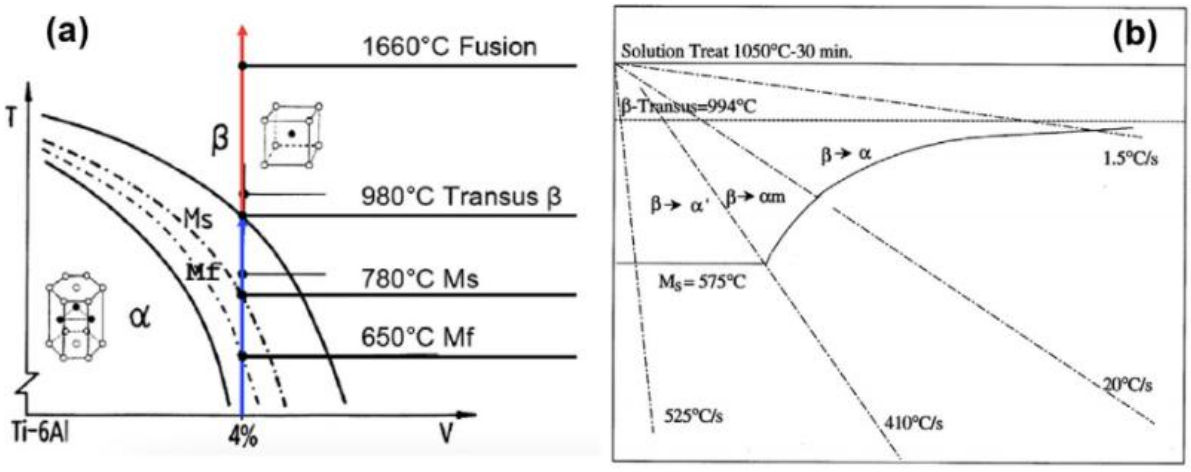

Figure 2.4: The (a) phase transformation diagram of Ti6Al4V and (b) phase transformation as a function of cooling rates [67]

a) Martensitic microstructure

The temperature range for martensite start (M_s) is 575 ℃ to 800 ℃. The M_s temperature can change because of the initial microstructure, alloying elements, and composition, where in some cases, a cooling rate less than 410 ℃/s can lead to the formation of acicular α' martensite

[69, 70]. Any cooling rate below 20 ℃/s will not result in the formation of acicular α' martensite [67]. Due to rapid changes in temperature during quenching from the alloy's β-phase region, the original bcc beta crystals are entirely transformed into hcp alpha crystals, with no β-phase remaining. This results in a material with high strength, stiffness and hardness but low ductility [30, 71, 72]. A typical SEI micrograph of Ti-6Al-4V produced by SLM is shown in Figure 2.5. The micrography shows the needle-like structures called acicular α' martensite microstructure.

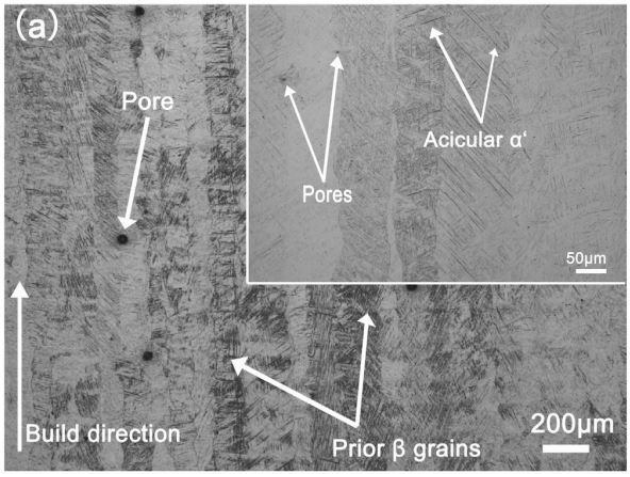

Figure 2.5: A typical optical micrograph of SLM Ti-6Al-4V [73]

b) Fully lamellar microstructure

The lamellar microstructure is made up of plate-like shapes of the α-phase. The flow diagram in Figure 2.6 provides a better understanding of the processes involved in achieving this type of microstructure

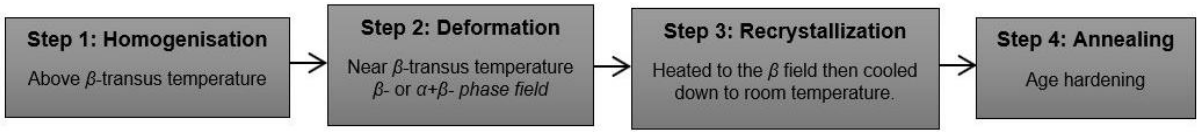

Figure 2.6: Processing route resulting in a fully lamellar microstructure [30]

The process starts when the alloy is heated above the β-transus temperature, leading to homogenisation—a term used to describe the formation of a homogenous β-phase. The β-transus temperature for the Ti6Al4V(ELI) is at around 995 °C [74]. The grains are then deformed by rolling or forging the alloy at temperatures close to but below the β-transus temperature. Thereafter, the alloy is heated back to raise its temperature above the β-transus.

Recrystallization occurs at temperature just above the beta transus temperature following onto which the alloy is cooled down to room temperature at a controlled cooling rate. It is this rate of cooling that dictates the development of distinctive microstructural characteristics. An increase in cooling rate leads to decreases in the width of α lamellae, size of α colonies, and width of the α layer at β-grain boundaries. Recrystallization at 30–50 °C above the β-transus temperature ensures the formation of small crystals of the β-phase, which then transform to $\alpha+\beta$ phases below the beta transus temperature [30]. The microstructure of a Ti6Al4V alloy produced this way is characterised by low strength and ductility as well as better resistance to fatigue crack growth than equiaxed microstructure [71, 72].

c) Bimodal microstructure

Four steps are taken to achieve the bimodal microstructure. Heating the alloy well above the β-transus temperature is the first step taken to achieve homogenisation of the formed β-phase. In the second stage, as the alloy is cooled from the β-transus temperature, plastic deformation of α-lamellae takes place in the $\alpha+\beta$ phase field. Recrystallization is done in the third stage, the alloy is cooled gradually from the β-transus temperature, to allow the β-phase to transform into equiaxed grains instead of forming lamellae grains. Both equiaxed and lamellae α-grains are obtained in the last stage [30]. The duplex bimodal microstructure has better fatigue properties arising from a combination of the good resistance to the initiation of fatigue cracks of equiaxed microstructures with the high resistance to fatigue crack propagation of lamellae microstructure. The microstructure also has the highest ductility among the microstructures of Ti6Al4V alloy [37, 75]. Figure 2.7 shows typical micrographs of bimodal microstructures obtained at different cooling rates.

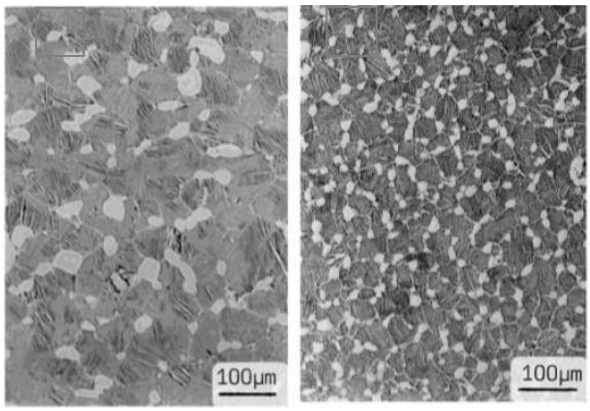

Figure 2.7: The bimodal microstructure at (a) slow and (b) fast cooling rates [30]

d) Fully equiaxed microstructure

With a few minor adjustments, the equiaxed microstructure is created using the same procedure as the bimodal microstructure. To establish the entire α-phase microstructure, the lamellae α-grains that remain after the homogenisation process are transformed into equiaxed grains. There are two ways to accomplish this. Initially, low-temperature recrystallization guarantees the presence of the α-phase in a sufficient equilibrium volume fraction to develop the equiaxed microstructure at the cost of the lamellar microstructure [30]. As a result of the high temperature, the atoms' thermal energy rises, causing them to move around and overcome the grain boundaries' surface energy. Grain growth and grain boundary movement are the outcomes of this. Consequently, applying higher temperatures to Ti6Al4V causes the grains to move more freely, which coarsens the α-laths [21, 26, 76, 77]. A sufficiently low cooling rate recrystallization annealing temperature is imposed in the method. This leads to a fully equiaxed microstructure by allowing only equiaxed α-grains and not α-lamellae to grow during the cooling process [30]. This microstructure has good resistance to the initiation of fatigue cracks but poor resistance to fatigue crack propagation [71, 72].

e) Widmanstätten microstructure

Widmanstätten microstructure is achieved when the alloy is gradually cooled by air from the β-phase region. As the alloy's temperature begins to decrease below the β-transus temperature, nucleation and growth of hcp α-phase plates occur from the β-grain boundaries. The α-phase shows more affinity towards crystals of a similar orientation, and hence, plane parallel growth is more compared to plane perpendicular growth, which results in plate-like regions of α-grains. The growth persists until it encounters another plane of β crystals, which prevents the α-grains from growing in a planar manner. The β-grains may contain non-parallel growth plane sites, which lead to the formation of non-parallel α-grain sets. Figure 2.8 shows the formation of Widmanstätten microstructure [30].

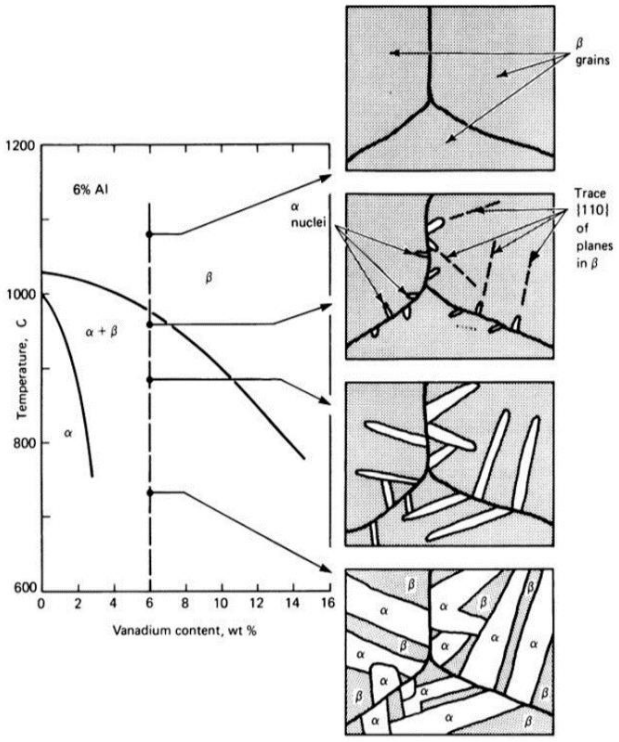

Figure 2.8: The formation of the Widmanstätten microstructure [30]

2.4.2. The chemical composition of Ti6Al4V(ELI)

Ti6Al4V(ELI) is a 6% wt. aluminium α-stabilizing element and 4% wt. vanadium β-stabilizing element, with extra-low interstitial elements like oxygen, nitrogen, and carbon to improve ductility and fracture toughness with some reduction in strength. Table 2.3 shows the composition of Ti6Al4V(ELI) and details the percentage content of all the elements that make up the alloy, according to ASTM F3001-14.

Table 2.3: The chemical composition of Ti6Al4V(ELI) [15]

Element	C	Fe	N_2	O_2	H_2	Al	V	Y	Others	Ti
Content %	<0.08	<0.25	<0.05	<0.13	<0.012	5.5-6.5	3.5-4.5	<0.005	<0.1	Balance

From Table 2.3, it is clear that aluminium has the highest content after titanium, while hydrogen has the lowest content. An increase in aluminium content reduces the density of the alloy, which suits the requirements of the aerospace industry. When the carbon content is less than 0.05%, an increase in carbon content increases strength and hardness, and a decrease in carbon content improves ductility and reduces surface hardness, thus resulting in an increase in the number of cycles to failure during fatigue testing. The reduction of the content of oxygen below

0.13% improves ductility and fracture toughness, with some reduction in strength. However, with an increase in the content of oxygen above this percentage, tensile strength increases, and ductility is reduced significantly, speeding up the rate of propagation of fatigue cracks and leading to shorter fatigue lives.

2.4.3. Physical properties of Ti6Al4V(ELI)

The physical properties are properties that can be observed or measured without alteration of the composition of the material. Table 2.4 shows the physical properties of Ti6Al4V compared to those of steel and aluminium.

Table 2.4: Physical properties of Ti6Al4V compared to those of steel and aluminium [78, 79, 80]

Property	Ti6Al4V	Steel	Aluminium
Density (*g/cm$^{3)}$*	4.43	7.8-8	2.69
Melting point (*°C*)	1604-1660	1510	660
Boiling point (*°C*)	3285	2900	2467
Specific heat (*J/kg.°C*)	560	470	215
Volume electrical resistivity (*ohm.m*)	1.7	9.9	2.655
Thermal conductivity (*W/m. K*)	7.1	44-52	205
Mean co-efficient of thermal expansion 0-100 (*°C/°C*)	8.6X10^{-6}	12.2X10^{-6}	22.4X10^{-6}

The data in this table shows that the density of Ti6Al4V is higher than that of aluminium but lower than that of steel. This is one of the reasons why the alloy is suited for aircraft components, as it is lightweight yet tougher than steel. The Ti6Al4V alloy has a higher melting point and boiling point than steel and aluminium; this means that the alloy can withstand higher temperatures than the other two materials. The traditional machining of Ti6Al4V products is often challenging due to its poor thermal conductivity [68]. It is evident from the data in Table 2.4 that the thermal conductivity of Ti6Al4V is lower than that of aluminium and steel. The lower thermal conductivity of Ti6Al4V can be an advantage in applications where heat needs to be minimised, such as in aircraft and automobile components, and a disadvantage in applications where heat needs to be dissolved, such as in heat sinks. The Ti6Al4V alloy has a higher specific heat capacity than steel and aluminium. This implies that less energy compared to the other two materials will be required to raise its temperature by one unit.

2.4.4. The mechanical properties of Ti6Al4V(ELI)

A uniaxial quasi-static tensile test is frequently used to ascertain the mechanical properties of metallics to provide additional details regarding their strength and ductility. In this test, a specimen of a prescribed material is subjected to a continually increasing uniaxial tensile load [6] till failure and complete separation. For additively manufactured specimens, parameters such as the building orientation, scanning strategies, the powder layer's thickness, laser power, hatch distance, volumetric energy density, and the protective atmosphere play a vital role in the mechanical properties of the material [55]. Table 2.5 compares the mechanical properties of Ti6Al4V(ELI) alloy to that of steel and aluminium.

Table 2.5: The mechanical properties of Ti6Al4V(ELI) compared to that of steel and aluminium [15, 78, 79, 80, 81]

Property	**Ti6Al4V**	**Steel**	**Aluminium**
Tensile strength (*MPa*)	1170-1330	420	100
Specific tensile strength (*kNm/kg*)	211	140	18
Elastic modulus (*GPa*)	120	200	68.3
Yield strength (*MPa*)	1190	350	55
Specific yield strength (*kNm/kg*)	200	132	10
Percentage elongation (*%*)	10	15	12
Reduction area (*%*)	25	40-70	35-39
Specific stiffness (*MNm/kg*)	24	28	28
Knoop hardness (*MPa*)	363	140	100-140
Specific Knoop hardness (*kNm/kg*)	81	18	42

Table 2.5 clearly shows that Ti6Al4V(ELI) is the strongest of the three materials in the table. The percentage elongation of Ti6Al4V(ELI) alloy is lower than that of steel and aluminium, which means that the alloy is the least ductile. The Ti6Al4V(ELI) alloy forms the bcc and hcp structures, while steels form the bcc and face-centred cubic (fcc) [82]. The number of slip systems for bcc is 48 and in fcc it is 12. The fcc metallics are more ductile than bcc because of close-packed planes which allow easier slip and plastic deformation, while bcc metallics require higher energy to activate slip on the less densely packed planes [6, 82, 83]. The stiffness of Ti6Al4V(ELI) alloy is lower than that of steel and aluminium, which implies that the ability of the alloy to resist a force causing deformation is low. It also has the highest Knoop hardness among the three types of alloys. The high hardness makes alloy applications like engine components, bearings, and cutting tools resistant to wear, leading to improved durability and

longer service life. The aerospace industry requires materials with high tensile strength. The Ti6Al4V(ELI), being the toughest of the three materials, is suited for its application there. Steel is applied the most in building and infrastructure industries because it is durable. Ti6Al4V is not suited there because of its low stiffness. The alloy is suited for applications in the biomedical industry because of its ductility. The alloy has a good strength-weight ratio [41] 2.5 shows that Ti6Al4V(ELI) has higher specific yield strength, which makes the alloy suited for application in the biomedical industry.

2.4.5. The characteristics of tensile fracture surfaces of Ti6Al4V(ELI)

The Ti6Al4V alloy often exhibits dimple fracture, which indicates the alloy is ductile. The fracture surface of the alloy is rough and irregular, indicating that the specimen has undergone appreciable plastic deformation during the propagation of cracks on the fracture surface. As with the shear lips on the outer edges or periphery or the fracture surface, the central region of this surface is typically quite irregular, not perpendicular to the longitudinal direction of the specimen and is known as a region of the fibrous fracture [23, 55, 84]. Additively manufactured Ti6Al4V alloy, being a ductile metal, usually experiences failure following necking [84], [85]. Figure 2.9 below shows the features of a typical fracture surface of as-built Ti6Al4V samples exposed to tensile loading.

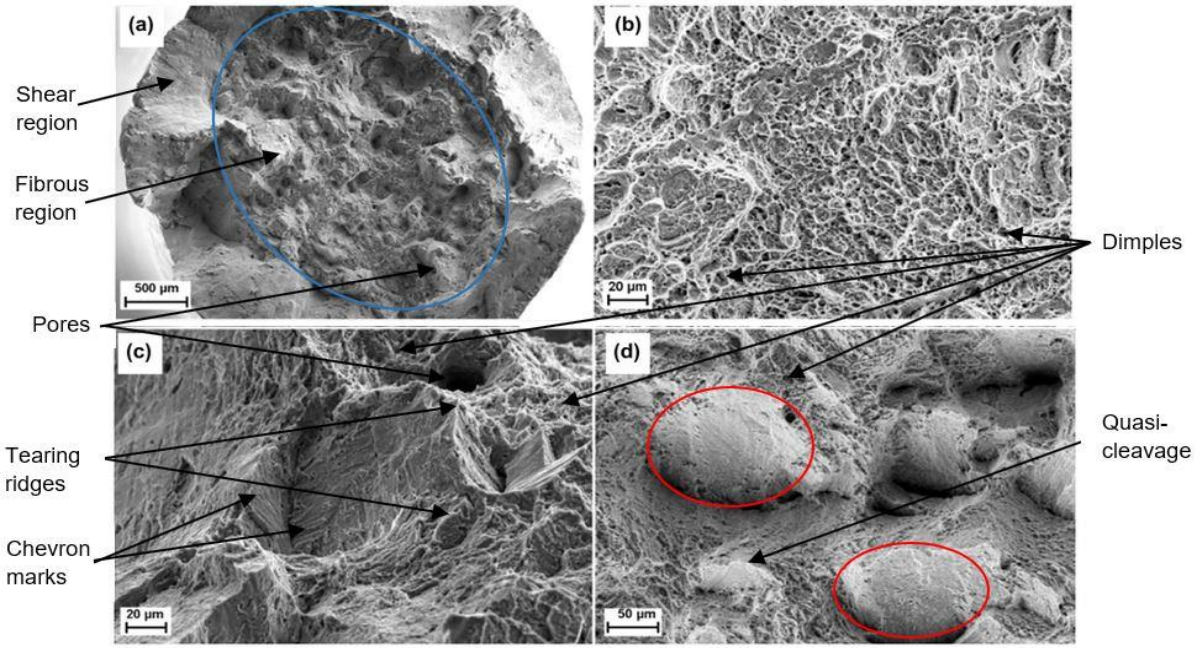

Figure 2.9: Tensile fracture surfaces of as-built SLM Ti-6Al-4V samples (a) cup-and-cone, (b) dimples, (c) and (d) quasi-cleavage [84]

Figure 2.9(a) shows a cup-and-cone fracture with rough surfaces primarily at the centre but also at the edges of the fracture surface. Ductile specimens undergo appreciable plastic deformation during the propagation of cracks. The middle portion of the fracture surface is marked by ridges. The specimen finally fails as a result of shear in the outer zone, which is smoother than the middle portion. Figure 2.9(b) shows a fracture surface with dimples. Figure 2.9(c) shows alternating lines called chevron marks that run approximately parallel to the directions of cracks. The figure also shows tearing ridges coexisting with dimples. Figure 2.8(d) shows some regions' smooth surfaces outlined with red circles as adjacent regions with dimples. Both Figures 2.9(c) and 2.9(d) show quasi-cleavage fracture [84]. The term quasi-cleavage, observed at low temperatures, is related to but not distinct from cleavage fracture [6]. Jin *et al*. [86], Bai *et al*. [87], Moletsane *et al*. [55], and Malefane *et al*. [85], investigated the fracture behaviour on Ti6Al4V samples, and observed cup-and-cone fracture features with the surfaces exhibiting dimples indicating ductile fracture.

2.5. Fatigue

2.5.1. A brief history of fatigue

Researchers, scientists, and engineers have all made contributions to our understanding of fatigue since its inception. This started in the Oberhartz mines in 1830 when Albert saw an iron chain break under cyclic load. He then used test equipment to produce the first fatigue test results for conveyor chains that had broken while in use, which were published in 1837 [20]. He evaluated the entire iron chain because there were no guidelines or standards in place at the time for doing fatigue tests on small specimens [2]. It was either the Englishman Braithwaite in 1854 or, most probably, the French Poncelet in 1839 who first named this phenomenon fatigue. The term fatigue is certainly the most appropriate to define precisely this continuous accumulation of damage in the material that weakens and eventually fails because, unfortunately, this damage is not recoverable and does not heal as in humans after they rest for a while [2].

A fatal accident in 1842 prompted scientists and researchers to investigate more, the phenomenon of fatigue [20]. In an accident involving an abnormally long train, the boiler blew up, and the engine’s axle snapped. A boiler in a train is a steam generator that generates steam for a number of uses, such as moving the train, heating potable water, and controlling the climate; and a train’s engine axle is connected to a motor that drives the wheels of the train. In

his 1850 study, German engineer Wöhler examined the axis of railway carriage axles. His research indicated that the prevailing stress determined a material's fatigue life; a higher stress level would lower the material's fatigue life. Additionally, he found that fatigue life was significantly affected by the existence of notches, and he displayed his results as a table [20]. Wöhler was the first to recognise the significance of the tensile mean stress and the impact of the stress amplitude on the fatigue resistance of materials. In 1870, his work led to the development of a fundamental law which was named after him, Wöhler's law [2].

Following this, England witnessed a great deal of accidents due to fatigue failure, and the study of fatigue became interesting. This was done to prevent catastrophic failures and optimise the design and material selection to be more safe, reliable and durable. While addressing axle failures, English engineer Rankine found that the main cause of fatigue in mechanical components was the existence of stress concentration zones [20]. German researcher Neuber used the Neuber technique, sometimes known as hyperbola, to study the impact of notches prior to World War II [2]. According to this technique, the geometric mean of the actual stress concentration factor plus the strain concentration factor equals the theoretical stress concentration factor [88]. Later, the American Peterson used the method to create a groundbreaking manual on stress concentration variables, which is now considered to be among the greatest reference books [2]. Knowledge of low-cycle fatigue, strain-controlled fatigue behaviour began to take shape in 1860 with the emergence of the Coffin-Manson link between plastic strain amplitude and fatigue life [9]. In 1864, Fairbairn made a contribution to the research of fatigue. He conducted fatigue tests on riveted wrought iron girders and discovered that failure would happen at cyclic stress levels up to one-third of the material's maximum strength [89]. He and Gerber developed design methods for different fatigue stress cycles in 1874 [9]. The first study on the stress-strain behaviour of materials under cyclic loading was published in 1886 by J. Bauschinger. Similar research was conducted in 1899 by Goodman. Gerber, Soderberg, and Goodman investigated the impact of mean stress near the end of the 19th century and presented simpler fatigue theories through systematic parametric research.

Using a microscope, English researchers Hewing and Humfrey revealed in 1903 that cyclic deformation is the cause of the slip bands and fatigue cracks that form in crystals. This was perhaps the first time that metal fatigue damage had been examined metallurgically [2]. The results of Wöhler were presented in a table by the American Basuim in 1910. He represented

the data as curves, which are now known as S-N curves, where the symbol *S* stands for the applied stress and *N* for the number of cycles till failure. The "Wöhler curve" is another name for the S-N curve [20]. In order to investigate the effect of heat treatment on fatigue resistance, In 1911, Boudouard used steel bars that were vibrated by electromagnetic fields [89]. Following several investigations on crack propagation theory, Griffith introduced fracture mechanics in 1920 [20, 90]. The first textbook on fatigue based on Wöhler's work was published in 1924 by the Englishman Gough. The study of fatigue experienced a notable upsurge between 1939 and 1960 as scientific and technological attention migrated from the railway sector to the aviation and space industries. The necessity for war drove this change, which ultimately led to competition between the economy and the military [2]. Zappa and Worden initially discovered fatigue striations as ripple patterns on fatigue fracture surfaces in 1951. Surface markings that, even after some material was removed near the surface, kept resurfacing at the same areas throughout further cycling were referred to as "persistent slip bands" by Thompson, Wadsworth, and Louat (1957). These tired metals' slip bands were the areas where deformation was concentrated. Forsyth and Ryder made a substantial contribution to the study of fatigue and failure in engineered structures in 1960 by evaluating the rate of fatigue crack formation with the distance between consecutive striations [89]. In 1968, Elber brought up the idea of crack closure. This phenomenon causes the effective stress intensity extension acting on the crack to decrease, which lowers the fatigue crack growth rate [2].

Irwin (1957) proposed that linear elastic fracture mechanics may be used to characterise the magnitude of stress singularity ahead of a crack in terms of the stress intensity factor [89]. Scientist P. Paris used Paris's formula to demonstrate analytically, between 1961 and 1962, how the fatigue crack growth rate depends on the stress intensity component [2]. Elber observed in 1970 that fatigue cracks could stay closed even under cyclic tensile loads. Elber's research focused on the impact of plastic deformation on crack closure. Though the majority of studies on fatigue had been focused on metallic materials, from the 1980s, an interest in the fatigue behaviour on non-metallic materials and ceramics started [89].

2.5.2. The crack initiation, propagation and final fracture of fatigue

Fatigue, according to the ASTM International standards, is described as the gradual, localised, permanent structural change that happens to materials when they are subjected to varying loads and strains, which, after a sufficient number of variations, may cause cracks or fracture [91,

92]. Fatigue follows the progression of crack initiation, crack growth, and quick fracture. Once the growth of cracks initiates, they keep getting bigger under varying loads until they reach a certain critical length [5, 92] beyond which the material experiences sudden catastrophic failure. The rate of growth of cracks is primarily driven by the stress range of cyclic loading, although additional factors such as mean stress, temperature, loading frequency, stress concentration, surface flaws, and corrosion can also affect the rate of growth [6]. The continued growth of cracks slowly subtracts the area from the rest of the section carrying the applied load. Fast crack growth happens when the remaining part can no longer support the load, causing the components to separate into two or more pieces [5, 92]. Figure 2.10 is a typical micrograph illustrating the various zones of a fatigue fracture surface.

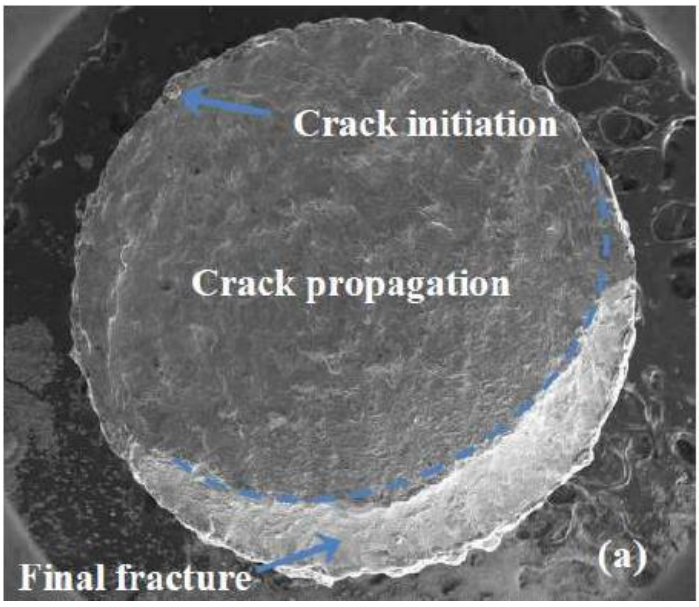

Figure 2.10: Zones of fatigue crack initiation, propagation and final fracture [93]

a) Crack initiation

The process by which cracks in the material are created is known as crack initiation. Fatigue is the main effect of the formation of cracks on the surface of the material. The primary cause of early fracture formations is typically a pile-up of dislocations or pre-existing flaws such as internal voids and surface scratches [92]. The material's microstructure, the kind of applied load, and the material's micro-geometry all influence the formation of fatigue cracks. In the case of contact mechanical elements, cracks are initiated at the sites of the largest equivalent stress on contact surfaces [94]. A significant amount of the total number of cycles during

fatigue testing is devoted to crack initiation, which typically accounts for 90% of a component's life [91, 95].

b) Crack growth

In the first stage of fatigue crack propagation, the crack propagates along planes of high-shear stress. The crack spreads until it is slowed down by a microstructural barrier, such as inclusions or a grain boundary, that is unable to accommodate the original direction of the crack's growth. The refinement of grains can increase the fatigue strength of the material due to the creation of many barriers to the propagation of cracks [96]. When the applied load is sufficiently strong, and the propagation of a crack proceeds with an increase in stress intensity factor, slips begin to form in various planes around the crack tip, signalling the commencement of the second stage of crack propagation. Using a scanning electron microscope, striations can be seen on the fracture surface at this point. While many ductile alloys and pure metals exhibit striations, not all engineering materials do [96]. The final phase of crack propagation is unstable crack growth. This occurs when the stress intensity factor at the material's crack tip equals or surpasses the toughness of the loaded material under the given temperature, loading rate, and environmental circumstances [95].

c) Final fracture

When the crack reaches its maximum size, and the remaining portion is unable to support the imposed load any longer, the component separates into two or more pieces, resulting in a final fracture [92].

2.5.3. Types of fatigue loading

Fatigue loading may be applied in the various regimes of tension-tension, tension-compression, compression-compression [3], [97] and complete reversal. Figure 2.11 shows tension-tension, compression-compression, tension-compression, and complete reversal fatigue loading.

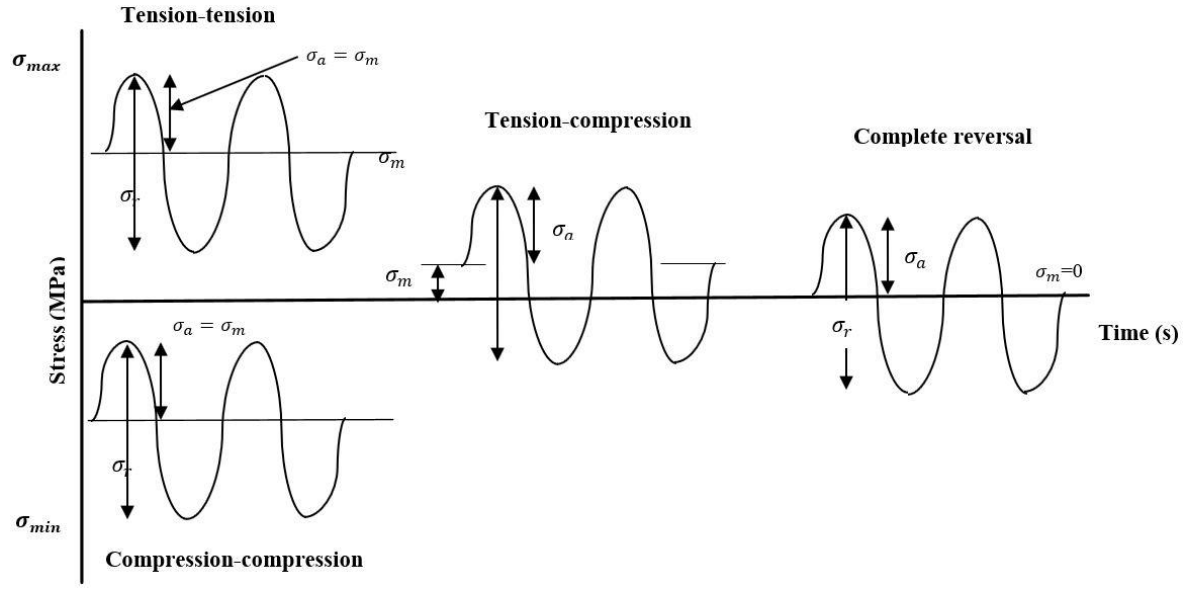

Figure 2.11: Tension-tension, compression-compression, tension-compression, and complete reversal fatigue loading

Tension-tension fatigue is a form of fatigue loading in which all the cyclic loading stress is in tension. In this type of loading, dislocations occur as a result of stress flow and are initially a consequence of the material's formation process, resulting in a uniform distribution of dislocations within the material [3, 98]. Failure is anticipated to occur anywhere along a test specimen's gauge length with this type of loading, as it guarantees the development of uniform stress through the specimen's cross-section along the gauge length. Thus, the microstructure of a material determines failure rather than the distribution of stress. [98]. Tension-tension fatigue can be found in sporting goods, cars, ships, aircraft, and structural applications [99]. Temperature, stress regime, surface and internal defects, and the frequency of loading all have a major impact on how damage develops under this kind of loading [100].

A form of fatigue loading known as compression-compression fatigue occurs when all the cyclic loading stress is in compression. Up to a certain length, cracks can start and spread; under compressive loading, residual stress is crucial to the development of cracks. Ships and offshore structures' tubular joints experience compression-compression fatigue loading [101]. Temperature, frequency, and the applied stress regime all influence failure under this kind of loading [3].

Compression-tension is a type of fatigue loading in which material is loaded in alternate tension and compression during a single cycle. Where the amplitude of the tension and compression

cycles are the same, then loading is called fully reversed loading [98]. In fully reversed loading, the stress alternates around zero-mean stress [5]. For service applications in vibrating structures like aeroplane wings, turbine blades, windmill blades, and other rotating structures, fully reversed tension-compression fatigue is a typical loading waveform [102, 103]. One of the loading conditions that aerospace components frequently encounter is fatigue. The temperature, stress regime, frequency of loading, and existence of defects all influence how failure develops under this kind of loading. Numerous studies have looked at the effects of fully reversed loading, in addition to pure tension-tension and compression-compression fatigue. It is generally concluded that the most severe type of fatigue among these types is tension-compression fatigue [3, 97, 98]. This is because of the Bauschinger effect, which causes materials' yield strengths to gradually decline with each half-cycle [104].

2.5.4. High- and low-cycle fatigue

There are two types of fatigue loading: low-cycle fatigue and high-cycle fatigue. The stress that causes plastic deformation determines when fatigue transitions from high- to low-cycle [105]. A form of fatigue known as high-cycle fatigue (HCF) is brought on by tiny elastic strains under a high number of load cycles prior to failure. HCF failure is defined as a stress-based parameter, such as mean stress, stress amplitude, shear stress, stress ratio, nominal stress, and maximum stress, and it happens between 10^4 to 10^8 cycles.

The frequencies of HCF range from 20 to 50 Hz. It happens at stresses lower than low-cycle fatigue (LCF), which is also lower than a material's yield strength. It mostly occurs when there is deformation in the elastic or slightly inelastic range. The three main factors influencing HCF are maximum stress, cyclic frequency, and temperature. Large or inelastic plastic strains under a low number of load cycles before failure result in low-cycle fatigue. This parameter, which is strain-based, is said to occur at roughly 10^4 to 10^5 cycles and lower, with strain cycles occurring at roughly 0.01–5 Hz [12, 106]. Material with higher values of strength typically have lower ductility, which means that if a component is subjected to LCF, its fatigue life may be shortened [106].

2.5.5. Fatigue fracture in metallics

A fracture occurs when a single, solid body splits into two or more pieces as a result of stress. Understanding the different types of fracture that a metal can have is crucial because the

fracture surface provides a wealth of information [76]. The study of fracture surfaces in materials, fractography, helps identify the underlying causes of failure. After experiencing some difficulties getting the microscope's lens close enough to the uneven fracture surface to see details of individual grains, Carl Zapffe coined the term "fractography" in 1944. The word fractography is similar to the origin word metallography, it is a combination of the words fracto- and -graphy. Fracto is from the Latin term fractus, meaning fracture, and graphy from the Greek term grapho, meaning descriptive treatment [78]. For the examination of fracture surfaces usually, scanning electron microscopes (SEMs) and transmission electron microscopes (TEMs) are used [78].

There are two types of fractures: brittle and ductile. When cracks propagate, ductile fracture is typified by noticeable plastic deformation. There is a considerable degree of gross deformation at the fracture surfaces in this case. The rapid rate of crack propagation in metals, without any significant deformation, is a characteristic of brittle fracture. As the temperature drops, brittle fracture increases. The consequences of a brittle fracture can be disastrous and happen with little to no warning [4]. Both SEM and TEM are used for the analysis of the cleavage patterns that occur on brittle fracture surfaces, the size and shape dimples in a ductile fracture, and the initiation of cracks, growth of cracks, and coalescence of micro-voids. [78].

2.5.6. Damage tolerance approach in fatigue

Engineers use fracture mechanics as a design tool to forecast structural fractures that have cracks and are exposed to specified loads and environmental factors. In essence, fracture mechanics is a scientific method of forecasting a structure's ability to support the load and resist cracking. Because a crack propagates to a fracture at a given stress level, the fracture mechanism allows researchers to determine whether or not a crack of a given length in a material of known fracture toughness is hazardous. The ability of a structure to withstand the growth of cracks is evaluated using two methods. Elastic-plastic fracture mechanics (EPFM) and linear elastic fracture mechanics (LEFM) [6, 76, 95]. Here, it is assumed that the component contains a crack or a flaw is a flat surface in a linear elastic field and that the energy released during rapid crack propagation is a basic material property that is not influenced by part size [76].

The theory behind the LEFM states that under specific temperatures, loading rates, and environmental conditions, unstable crack propagation takes place when the stress intensity

factor at the crack tip in the material equals or exceeds the material fracture toughness. The method is based on the elastic solution in a pure elastic material to the stress and strain field in the vicinity of the crack tip [95]. The amount of stress surrounding a flaw is described by the stress intensity factor [76]. In order to prevent unstable crack propagation, this method guarantees that the stress intensity factor caused by the applied load is less than the fracture toughness [95]. The technique is less useful for low-strength structural materials but performs well on high-strength materials with values of strength greater than 100 MPa. The application of LEFM helps engineers estimate a material's resistance to the propagation of cracks and provides for fracture safety application. The method is limited to materials that are exposed to load only within the linear elastic range of deformation [95]. While EPFM is used in metallics with lower strength and higher toughness, LEFM is frequently used for high-strength metallics, such as high-strength steels, titanium, and aluminium alloys [76]. This was developed in that way, as each theory models the behaviour of cracks in a different way. The choice between LEFM and EPFM depends on the specific material properties and the desired level of accuracy in the analysis. The LEFM is suited for high-strength metallics, and EPFM for low-strength metallics.

The stress intensity factor is a scaling factor that can be used to describe the stresses surrounding a crack. Figure 2.12(a) shows a two-dimensional crack, length 2a in the x- and y-directions, under a uniaxial tensile stress σ_0. An infinite solid under uniform remote tensile stress, σ_0, in the z-direction is shown with an internal crack on the x-y plane in Figure 2.12(b) [107].

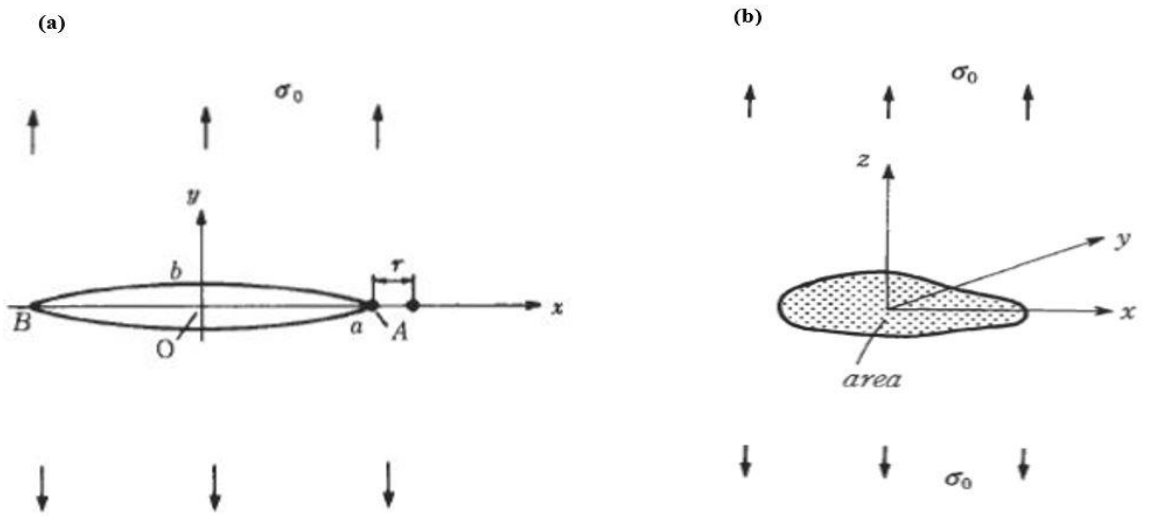

Figure 2.12: (a) 2D-crack length, 2a, and (b) an arbitrarily 3D-shaped internal pore [107]

Figure 2.12(a) describes the singular stress distribution in the vicinity of the crack tip. The stress intensity, represented by parameter K, is written as:

$$K = \sigma\sqrt{\pi a}$$

The normal stress σ_y , [107], [83], near the crack tip can be written as:

$$\sigma_y = \frac{K_I}{\sqrt{2\pi r}}$$

when there is an internal defect on the x-y plane of a solid which is under uniform tensile stress σ_0, in the z-direction, as shown in Figure 2.12(b) [107]. When the area of this defect is 'area', then the maximum value of the stress intensity factor, K_{Imax}, along the defect, is expressed as:

$$K = C\sigma\sqrt{\pi\sqrt{area}}$$

where the symbol C, is a dimensionless parameter taken as 0.5 for an internal defect and 0.65 for a defect on the surface, σ, is the maximum stress applied [41, 107]. The change in stress intensity factor is expressed:

$$\Delta K = C\Delta\sigma\sqrt{\pi\sqrt{area}}$$

when the stress applied σ, exceeds some critical stress value, σ_c, crack propagates, and failure occurs. This critical value of K, is called the fracture toughness K_c [26]. The fracture toughness K_c, measures the resistance of material to brittle fracture when a crack is present.

$$K_c = \sigma_c\sqrt{\pi r}$$

where Y is a dimensionless parameter, σ_c, the critical stress for crack propagation and a, crack length. The fracture toughness depends on the thickness of the specimen, for a thick specimen, the value of K_C is known as the plane strain fracture toughness K_{Ic},

$$K_{Ic} = \sigma_{Ic}\sqrt{\pi r}$$

Ductile materials exhibit high values of the plane strain fracture, and brittle materials have low values. The magnitude of the plane strain fracture toughness usually increases with a reduction

in the sizes of the grains. The K_{Ic} values decrease with the increasing strain rate and decreasing temperature [83]. Ductile materials will exhibit much higher values of K_{Ic}, than brittle materials because of plastically deformation and blunt cracks. Factors such as temperature, strain rate, material processing, and microstructures are very significant in the value of plain-strain fracture toughness K_{Ic}, where else the specimens' dimensions or type of loading have no effect [76].

A defect that results in a value of stress intensity factor that is greater than a change in stress intensity threshold ΔK_{th} will lead to the growth of cracks and, finally, fracture of the loaded object. It was reported [108] that the stress intensity threshold, ΔK_{th} of specimens built vertically and heat treated at 800 °C and 1050 °C and cooled in argon gas and a vacuum, respectively, is between 3.7 MPa.m$^{1/2}$ and 6.1 MPa.m$^{1/2}$. The stress intensity threshold is important in plant design because it is the value below which fatigue crack growth slows significantly.

2.5.7. High-temperature applications of metals and metal alloys

For many applications, maintenance of properties at high temperatures is essential. High-temperature applications in metals and metal alloys require customised blends of corrosion resistance, microstructural stability, and mechanical strength [7]. For increased efficiency in coal-fired power plants, advanced steels, stainless steels, and nickel superalloys that can withstand temperatures and pressures above 700 °C and 35 MPa, respectively, are suitable for use. Aeroplane engine turbine blades are subjected to high temperatures and pressures exceeding 1600 °C and 4 MPa, respectively [7]. High-temperature alloys are defined as those that remain functional at 500 °C and higher. A comparison of materials' specific tensile strengths at different temperatures is displayed in Figure 2.13.

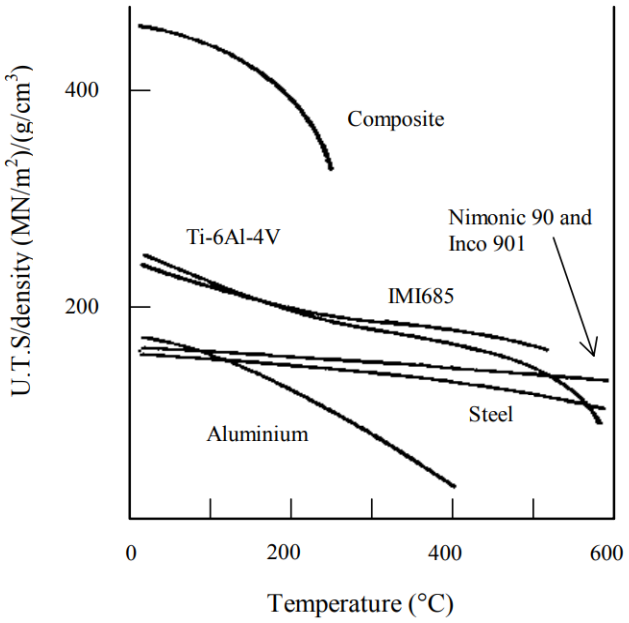

Figure 2.13: A comparison of specific tensile strength at changing temperatures for various materials [109]

It is evident from the curves in this figure that for all the materials, as the temperature is raised their strength drops. The figure shows much greater strength for composites than all other materials at room temperature. The drop in strength with temperature is greater though for composites. Due to their limited temperature capability, composites are not suited for application in aerospace components [109]. Aluminium is the cheapest choice, if the temperature does not exceed 300 ℃, noting it is resistant to oxidation. Plain carbon steel has good strength up to 400–500 ℃ but does not possess a high oxidation resistance. Most titanium alloys function for up to a maximum temperature of approximately 480 ℃. Most titanium alloys exhibit high strength and are lightweight, but they are generally not suitable for applications requiring high temperatures, like rocket and jet propulsion, where temperatures can reach over 1000 ℃. The materials utilized in these applications have undergone broad research and development that include material selection and design-creating an alloy-specific composition to enhance high-temperature properties and microstructural stability; manufacturing processes such as casting and forging; surface treatment, protective coating, and testing and characterisation [7, 109]. Elevated temperatures cause metallics to oxidise on their surfaces; for instance, carbon steel is known to oxidise above 540 ℃ (1000 ℉). Chromium and molybdenum are examples of alloying elements that are added to metallics to minimise oxidation. Protective coatings such as thermal barrier coating (TBC), epoxy coatings, corrosion-resistant barrier coatings, and nickel plating are other ways to control oxidation [76].

Fatigue properties are affected by temperature. An increase in operating temperature causes metallic materials to lose some of their fatigue resistance and strength, which ultimately results in a reduction in fatigue life. Certain metallic alloys experience a fatigue transition mechanism at elevated temperatures that changes from brittle cleavage fracture to ductile quasi-cleavage fracture [8]. Hence, a metal placed under a constant tensile load at elevated temperature will undergo creep to experience some time-dependent increase in length. Because of high temperatures, atoms move more easily, and creep takes place more easily. This leads to an increase in the mobility of dislocations and an increase of slip and deformation at grain boundaries, resulting in loss of strength and, ultimately, a decrease in fatigue life [76]. It is reported that as the temperature exceeds ⅓ to ½ of the metallics' melting temperature, creep becomes significant, and failure becomes more imminent [76, 110]. Generally, ferrous alloys exhibit an endurance limit at room temperature but show no fatigue limit above 425 °C. At elevated temperatures, an interaction of both creep and fatigue conditions can occur at the same time, leading to catastrophic fracture and brittle failure [76].

2.5.7.1. Thermal fatigue

When a component or structure develops stresses in thermal cycling with no external load, that phenomenon is classified as thermal fatigue or thermal stress fatigue [76]. These thermal stresses are produced by cyclic material expansion and contraction when the temperature changes. High temperatures cause compressive stresses, while tensile stresses are due when the component cools down [106]. Here, when the material surface is heated, the cooler part of the material beneath the surface constrains it, and the surface experiences compressive stresses. Upon cooling, the converse happens, and tensile stresses develop. These heating/cooling cycles result in surfaces undergoing thermal fatigue damage, which is often encountered in turbine blades. Thermal fatigue will lead to damage to the materials [76].

2.5.8. Fatigue S-N curves

Fatigue S-N curves, also known as Wöhler's curves, such as the one shown in Figure 2.14, are used to describe the fatigue life of materials [12]. The stress-based approach has been the accepted technique for fatigue analysis and design since the middle of the 1800s. This method is also referred to as the stress life or the S-N approach [5]. It is the basic method of presenting engineering fatigue data, which represents the life of the specimen in cycles to failure (N) against the applied stress [83]. Semi-log S-N curves are used in this method to display fatigue

data. The number of cycles is plotted in logarithm to base 10, whereas the stress values are plotted exactly as they are; thus, the term semi-log [111]. An S-N curve plot shows that the relationship between the magnitude of stress and the number of cycles to fatigue failure are inverse to one another. Put another way, the material's ability to withstand a given number of cycles before failing decreases with increasing stress levels [83].

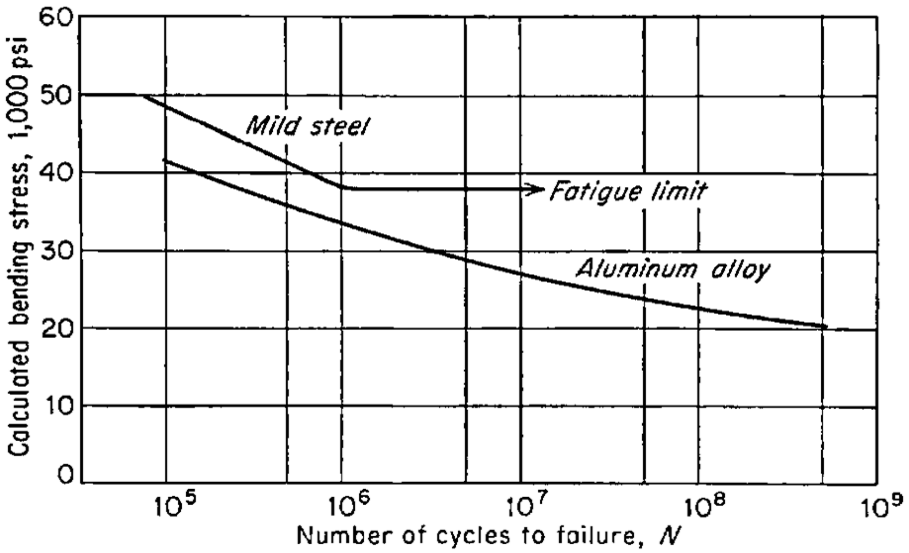

Figure 2.14: Typical fatigue S-N curve for ferrous and non-ferrous metal [6]

This total number of fatigue cycles is made up of the number of cycles to initiate a crack and the number of cycles to grow the crack completely through the specimen. Fatigue tests are normally carried out for nonferrous metals for 10^5, 10^7, and 10^8 cycles for medical, automotive, and aircraft industries, respectively. The fatigue limit also referred to as the endurance limit, is defined by the number of cycles at which the S-N curve becomes horizontal, the point with a sharp knee that is present in metals like steel and titanium that age under stress. These materials can withstand an infinite number of cycles without failing below this limiting stress line. The S-N curves of almost all nonferrous materials, including copper alloys, magnesium, and aluminium, gradually slope downward as the number of cycles increases. These materials never exhibit a horizontal S-N curve, indicating that they lack a true fatigue limit [6].

In mild steel, fatigue testing showed that the S-N curve flattened out, and the knee appeared at a higher number of cycles when the carbon and nitrogen contents were lowered compared to when they were higher [6]. Eight to twelve specimens are usually used to determine an S-N curve. This can provide a preliminary understanding of the material's fatigue behaviour.

However, a large number of specimens is required to arrive at the mean curve and obtain a statistically significant and reliable S-N curve. This ensures that the design decisions based on the curve are accurate and conservative [6]. The first specimen is typically tested under high stress, where failure is anticipated after a limited number of cycles until one or more specimens fail at a predetermined number of cycles, typically, at least 10^5, 10^7, and 10^8 cycles for the medical, automotive, and aircraft industries, respectively. The test stress is then reduced for each subsequent specimen. The fatigue strength is determined by taking the highest stress at which no failure occurs [6]. During fatigue testing, if a material does not fail before the set number of limiting cycles, the material is deemed to have an infinite life [6]. However, this infinite life does not truly exist for metals that do not depict an S-N curve with a knee, as they will reach their fatigue limit when sufficient fatigue cycles are imposed on them. For some studies, tests are usually cancelled for practical considerations where the design life of components is set for specific applications [6, 92].

2.6. Fatigue Behaviour of LPBF Ti6Al4V(ELI)

2.6.1. Factors that influence the fatigue behaviour of metallics, focusing on the LPBF Ti6Al4V(ELI) alloy

The factors that influence the fatigue behaviour of LPBF Ti6Al4V alloy include mean stress, stress concentration, stress ratio, type of fluctuating loading, presence of internal and surface flaws, frequency of loading, temperature, heat treatment, and microstructure, as well as AM build orientation [3, 4, 5, 6].

a) **Mean stress**

The mean stress (σ_m) is defined as ½ of the sum of the maximum and minimum stresses thus, $\sigma_m = (\sigma_{max} + \sigma_{min})/2$. Most of the time, fatigue testing is conducted using fully reversed loading, the term fully reversed indicating that the applied load alternates about zero-mean stress. Structural components are usually subjected to alternating loads with a non-zero mean stress [5]. The mean stress can have a substantial influence on fatigue behaviour. At intermediate or high-stress levels under load control test conditions, substantial cyclic creep, which increases the mean strain, can occur in the presence of tensile mean stresses. This cyclic creep adds to the detrimental effects of fatigue through the creation of additional undesirable deformation. A decrease in fatigue life will always result from an increase in mean stress [92].

In their work on the influence of mean stress on the fatigue behaviour of LPBF Ti6Al4V, Benedetti *et al*. [112] and Wycisk *et al*. [113], confirmed this to be so. Cutolo *et al*. [114], studied the effect of mean stress on the fatigue strength of the LPBF Ti6Al4V and reported that the specimens were very sensitive to the mean stress, with fatigue strength reducing with the increasing mean stress [114].

b) **Stress concentration**

In manufactured parts, geometric discontinuities like fillets, notches, and holes inevitably raise stress. The fatigue strength is decreased by these stressors [66]. Usually, fatigue cracks in structures start at such geometrical irregularities. Fatigue cracks in structures typically originate from these kinds of geometric irregularities. The stress concentration factor $k_t = \sigma_{max}/\sigma_{nom}$, is defined as the ratio of the maximum to the nominal stress. Stress concentration can also arise from surface roughness and metallurgical stress raisers, such as porosity and inclusions, and local overheating due to grinding and decarburization. The optimal way of minimizing fatigue failure in such cases is by the reduction of avoidable stress raisers through careful design and the prevention of accidental stress raisers by careful machining and fabrication. Specimens with notches on their surfaces generate triaxial states of stress around the notches and stress gradients descending from the roots of the notches towards the centres of the specimens [6]. Triaxial stress takes place when a notch disrupts uniform stress distribution in a material, leading to stress concentration at the root of the notch, this results in a higher stress level in the region. This localised high stress can cause the surrounding material to deform plastically. However, the material away from the notch, which is subjected to lower stress, restricts this plastic deformation. This constraint results in the development of triaxial stresses around the notch. The development of triaxial stresses promotes brittle fracture even in a ductile material and reduce the fatigue life of a material [6].

Baragetti [115] studied the effect of notches on the fatigue behaviour of Ti6Al4V by comparing notched and unnotched specimens. He reported that the fatigue limit of the notched specimens was attained after 200 000 load cycles [115]. Ziaja and Kawalec [116] stated that stress concentration leads to fast initiation of cracks, leading to short fatigue lives and quasi-cleavage facet fracture. Wycisk *et al*. [113] reported that large defects significantly lead to increased stress concentration and reduction in the lifetime to failure of LPBF Ti6Al4V samples. The work of Wycisk *et al*. [113] is consistent with the study of Jiao et al. [10].

c) **Frequency of loading**

Fatigue life is dependent on loading frequency. Variations in the frequency of the applied load during fatigue testing will result in variations in the number of cycles to failure. High-frequency testing can affect the mechanical properties of materials and thus improve the fatigue performance of materials [3, 6] as a result of the related high strain rate and strain hardening effect. Fatigue testing at high frequency will, on the other hand, generate cracks faster, as a large number of cycles are obtained in a short period of time as compared to low-frequency testing. For a project where 10^8 cycles are desired and assuming that there are no mechanical problems with the testing equipment, it could take years to obtain a single S-N curve under low frequencies. Therefore, there is a need for testing at high frequencies [3, 6]. Ritchie *et al*. [117] loaded in compact tension at 50 Hz and 200 Hz. When comparing the results, they observed a faster crack growth rate on samples loaded at 50 Hz [117]. This could be the effect of higher strain rates and related strain hardening at a lower frequency, 50 Hz, and thermal softening at a higher frequency, 200 Hz. Janeček *et al*. [118] studied the HCF behaviour of Ti6Al4V at a frequency of 30 Hz and 20 000 Hz. For both frequencies, they observed cleavage facets and similar fatigue crack initiation sites and crack growth mechanisms, implying that the frequency of cyclic straining had no effect on the fracture characteristics [118].

d) **Temperature**

The fatigue behaviour of metals and metal alloys is influenced by temperature. Metals lose fatigue strength as temperatures rise above room temperature [6]. Inter-crystalline fatigue failure gives way to trans-crystalline creep failure at temperatures higher than half of their melting temperature, where creep takes precedence over fatigue [6]. For low-temperature fatigue, fatigue life normally increases with decreasing temperatures. Walters *et al*. [45] reported that low temperatures cause a decrease in fatigue crack growth rates. An endurance limit is typically present for ferrous alloys at room temperature, but when the temperature rises above about 425 °C, the endurance limit disappears [26]. In general, the higher the creep strength of an alloy, the higher will be its high-temperature fatigue strength [6].

Figure 2.15 shows the S-N curves of Ti6Al4V samples tested at room temperature and elevated temperatures.

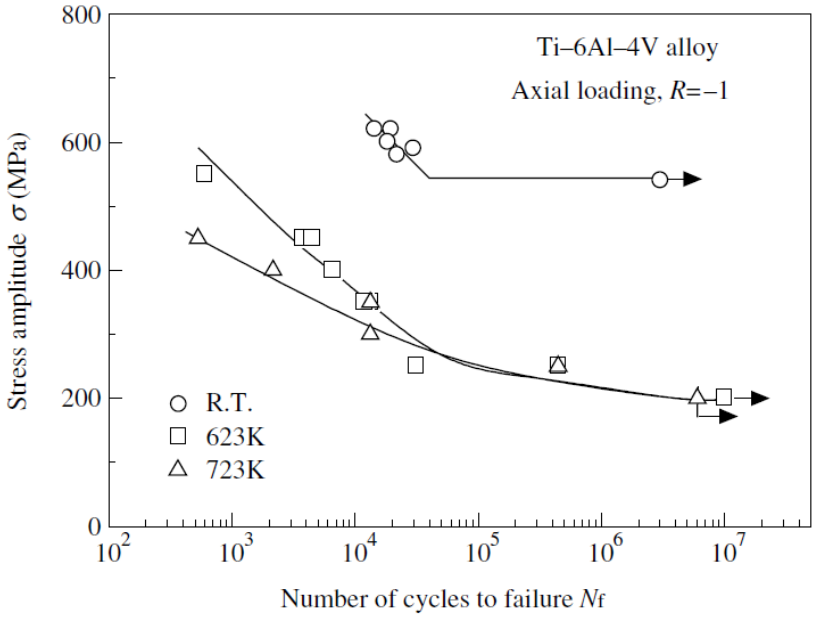

Figure 2.15: S-N curves of Ti6Al4V tested at room temperature and elevated temperatures [9]

Tokaji [9] studied the effect of elevated temperature on the fatigue behaviour of Ti6Al4V. He observed that at ambient temperature, the knee of the S-N curve appeared at a lower number of cycles, resulting in a definite fatigue limit of 540 MPa. The author reported that at elevated temperatures, the fatigue strength of the alloy decreased significantly compared to the value at ambient temperature. There was no difference in the fatigue strength at the two elevated temperatures of 623 K and 723 K above 30 000 cycles. Tokaji [9] compared the fracture surfaces of Ti6Al4V samples tested at room temperature and elevated temperatures and observed ductile fracture at room temperature and transgranular fracture at elevated temperatures. The author found that at a temperature of 623 K, small cracks grew faster than at room temperature, and at a temperature of 723 K, a similar trend was observed as well [9]. Jiao *et al*. [10] compared the fatigue crack resistance of SLM Ti6Al4V tested at room temperature and a temperature of 400 °C (673 K) and found that at a temperature of 673 K, the fatigue crack growth rate was higher than at room temperature [10]. Zhu *et al*. [8] studied the fracture surface of Ti6Al4V at room temperature and a temperature of 250 °C. They reported cleavage fracture at room temperature and quasi-cleavage fracture at a temperature of 250 °C. They further reported the presence of fatigue striations and ductile at both temperatures, which was noted to be a sign of the effects of load interaction. They noted that the variation of load within the real random spectrum load history was the source of this load-interaction effect. Real random spectrum load history is a time-varying load profile that fluctuates in an

unpredictable manner over time. It is often encountered in engineering applications such as mechanical machines, engine vibrations, and bridges due to wind loads [8]. Pantazopoulos [119] stated that the effect of load interaction and the development of a compressive stress field ahead of the crack tip can decrease the rate of crack propagation. Zhu *et al*. [8] reported that plastic fatigue striations appeared on both the low- and high-temperature fracture surfaces, which was indicative of the occurrence of local plastic deformation at the crack tip at room and high temperatures, reflecting the significant movement of the crack at each cycle of loading. They further reported that the higher temperature had an insignificant effect on the crack growth rate behaviour [8]. Arakere *et al*. [11] studied the effect of temperature on the fatigue behaviour of Ti-6Al-4V at room temperature and elevated temperatures of 175, 230, 290, and 345 °C. They reported no significant change in crack growth rates with the change in test temperature [11]. It has been reported that the Ti6Al4V alloy is stable at temperatures below 400 °C [68]. This observation is consistent with the work reported by Zhao *et al*. [68], which states that the alloy is suited for application below 400 °C.

Figure 2.16 shows the fractured surface of Ti6Al4V at room temperature and a temperature of 250 °C.

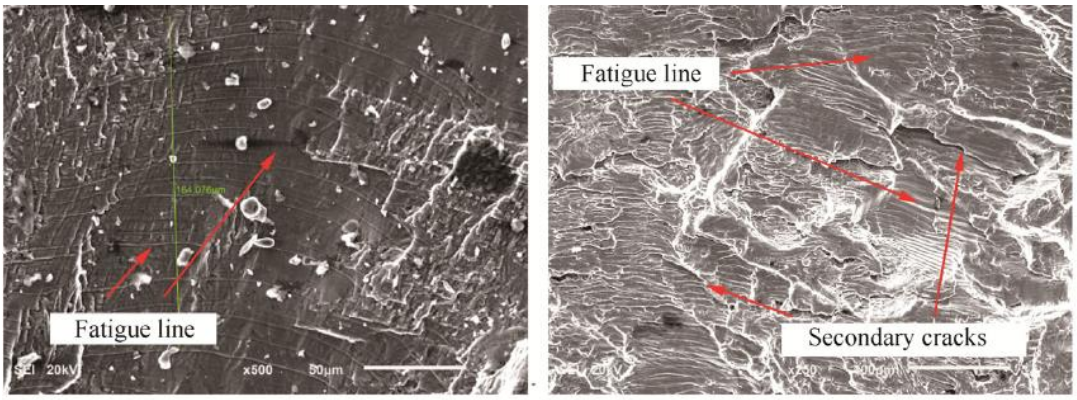

(a) *T*=25 ℃, Ti-6Al-4V/ELI (b) *T*=250 ℃, Ti-6Al-4V/ELI

Figure 2.16: Fractography of a Ti6Al4V fracture surface at 25 °C and 250 °C [8]

Figure 2.16 shows a brittle fracture at 25 ℃ and ductile fracture at 250 ℃. The fracture surface is rough in Figure 2.16(b); fatigue striations, tear ridges, and cracks are visible, while in Figure 2.16(a), the fracture surface is partly smooth.

From the above-mentioned studies, it can be stated that temperature does affect the fatigue behaviour of Ti6Al4V. Thus, as the test temperature is increased, the fatigue strength of the

Ti6Al4V alloy decreases, the mode of failure changes from ductile to transgranular fracture, and an increase in the rate of crack growth occurs for testing above a temperature of 345 ℃. Moreover, the mode of fracture changed from cleavage fracture at room temperature to mixed brittle cleavage and ductile quasi-cleavage fracture at 345 ℃. Work carried out by the authors elsewhere [21, 24] has demonstrated that the widths of α- and β-laths increase with increasing temperature and, with this, a decrease and increase of some quasi-static tensile mechanical properties of the alloy. An increase in temperature leads to a decrease in strength and an increase in ductility. The two properties affect the fatigue behaviour of Ti6Al4V, with a decrease in strength reducing the fatigue strength and an increase in ductility improving the fatigue strength. As reported [68] Ti6Al4V is stable at temperatures below 400 ℃, implying that tensile strength and ductility counteract each other, leading to an insignificant effect on the fatigue behaviour. It is expected that at temperatures above 400 ℃, tensile strength drops rapidly while ductility increases gradually, leading to a reduction in fatigue life.

e) **Heat treatment**

Metals and metal alloys can undergo heat treatment, which involves heating and cooling the material to change phases and their microstructures and, as a result, alter their properties [120]. The three variables that are most important during the heat treatment process are the heat treatment temperature, holding time, and rate of cooling [121]. There are many purposes for heat treatment, but controlling the microstructure and, consequently, the mechanical properties, particularly the hardness, ductility, strength, toughness, and internal stresses, is the most crucial [120]. To achieve the desired microstructure and improve a material's strength, ductility, hardness, and remove residual stresses, heat treatment is used [122, 123].

Any process involving temperature changes, such as machining, grinding, welding, or hardening, has the potential to introduce residual stresses on a part's surface [95]. Stress is relieved from titanium and titanium alloys produced additively without compromising their ductility or strength [124]. Stress relief heat treatment is typically used to eliminate residual stresses that result from machining or welding. This preserves the shape of components and does away with undesirable conditions like loss of yield strength [44, 125, 126]. Annealing of titanium and titanium alloys serves primarily to increase fracture toughness, ductility at room temperature, dimensional and thermal stability, and creep resistance [44]. Solution heat treatment is a process where the alloy is heated into its beta-phase region and quenched to cause precipitation hardening [95, 120]. Quenching is the rapid cooling of a workpiece to obtain

certain material properties. This process is normally used to harden and strengthen workpieces and leads to a reduction in the fatigue life of such workpieces. Chandramohan *et al*. [127] reported that β-annealing heat treatment for Ti6Al4V can increase ductility by more than 10% for medical applications. Hot isostatic pressing (HIP) is a heat treatment process that compresses materials at high temperatures and isostatic pressures of up to 2 000 °C and 200 MPa, respectively, at the same time. Argon gas is the most used pressure medium in this process [31]. HIP is employed to reduce porosity and microstructural inhomogeneities that affect the fatigue performance of materials [31, 128].

Frkan *et al*. [129] studied the effect of heat treatment on the fatigue life of LPBF Ti6Al4V samples. They observed longer fatigue life for samples that were soaked for four hours at 900 °C than for samples that were soaked for four hours at 740 °C [129]. This is because the samples that were soaked at 900 °C had coarser microstructures that led to higher ductility and lower tensile strength in them compared to samples that were soaked at 740 °C. Malefane *et al*. [85] reported that Ti6Al4V(ELI) specimens that were stress-relieved, followed by high-temperature annealing, had slightly higher fatigue strength at about 10 000 load cycles than as-built specimens. They further reported that the fatigue cracks, in both as-built and stress-relieved followed by high-temperature annealing LPBF Ti6Al4V(ELI) parts, initiated from surface roughness and LPBF process-related micro-pores near the surface [85]. Chastand *et al*. [54] studied the fatigue life of LPBF Ti6Al4V, for as-built, stress-relieved, and HIPed samples. They reported that as-built samples had the lowest fatigue life while the HIPed samples had the highest number of cycles to failure. They demonstrated further that the fatigue life of the HIPed samples was improved by almost 90% at 10^7 cycles [54]. Leuders *et al*. [108] studied the effect of heat treatment and HIP on the HCF behaviour of SLM Ti6Al4V. The average number of cycles to failure recorded were 27 000, 93 000, and 290 000 for as-built, annealed at 800 °C, and annealed at 1 050 °C, respectively. They reported that none of the HIPed samples failed before 2 000 000 cycles, which was taken to be their runout. They demonstrated that even if pores within the samples could be reduced in size by the HIP process, there were micropores that remained within the material which would then affect the fatigue behaviour of the material in the HCF regime [108] .

Hasib *et al*. [130] studied the role of heat treatment processes on the fatigue crack growth behaviour of PBF Ti6Al4V samples. They reported that the as-built samples had the lowest near-threshold fatigue crack growth rates (less than 10^9 m/cycle), followed by HIPed samples

at 850 ℃ and 950 ℃, while samples annealed at 1 020 ℃ showed the highest fatigue crack growth rate [130]. Dhansay *et al*. [131] studied the effect of heat treatment on the fatigue fracture behaviour of the LPBF Ti6Al4V alloy. They observed fracture surfaces dominated by transgranular and faceted quasi-cleavage for both the as-built and stress-relieved samples. Dimples were observed for the samples double annealed at 940 ℃ for two hours, furnace cooled to 910 ℃ and held there for eight hours, followed by water quenching, then aged for two hours at 750 ℃ and thereafter, furnace cooled [131]. They further reported that the double-annealed samples had more than a 50% increase in near-threshold stress intensity compared to the as-built and stress-relieved samples [131].

The foregoing studies have shown that as-built Ti6Al4V parts have the lowest fatigue life and that post-heat treatment plays an important role in improving the fatigue life of Ti6Al4V parts. The HIP-treated specimens exhibited the longest fatigue life except in the study by Hasib *et al*. [130], where β-annealing led to the longest fatigue life, which is unusual and can be due to a much higher annealing temperature above the β-transus temperature. At high temperatures, the thermal energy of atoms increases and causes the atoms to migrate more easily, thus allowing a rearrangement of the microstructure [76], and growth of grains, leading to an increase in ductility.

f) **Microstructure**

The microstructure of a material is described by the size, shape, and arrangement of grains. The mechanical properties and the service life of a material are determined by its microstructure [132]. Titanium alloys heated above the β-transus temperature have a bcc crystal structure instead of an hcp structure [24]. The cooling rates imposed thereafter, act as the deciding factors for the parameters of the resulting microstructures [69]. Grain size is also known to affect the fatigue behaviour of Ti6Al4V alloy, such that when the grains become larger fatigue strength decreases while small grains result in higher fatigue strength [133]. The rate at which fatigue cracks propagate slows down at low temperatures and speeds up at high ones [134]. In contrast to brittle materials, ductile materials have lower values of stress intensity factor. The stress required to produce a brittle fracture will, therefore, be less than the stress required to produce a ductile fracture. As a result, fractures in brittle materials will propagate cracks more quickly than in ductile materials [135]. Therefore, the propagation of fatigue cracks is a complex combination of the different converse trends noted here and in the last paragraph of the previous section. The Ti6Al4V alloy occurs in various forms, as shown in Figure 2.17.

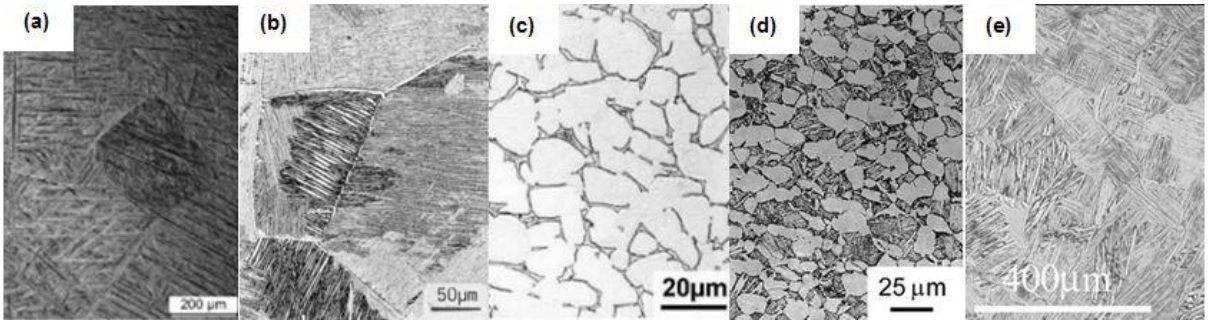

Figure 2.17: Microstructures of Ti6Al4V (a) martensitic, (b) lamellar, (c) equiaxed, (d) bimodal, and (e) Widmanstätten [30, 136]

The martensitic microstructure is characterised by needle-like α'-lath structures, as shown in Figure 2.17(a), which are formed as a result of high cooling rates greater than 410 °C/s of the alloy from the β-region and have high hardness, strength, and stiffness, and low ductility [71, 72]. The main disadvantage of this microstructure is its high brittleness. The lamellae microstructure shown in Figure 2.17(b) consists of alternating layers of α and β and is formed by slow cooling of the alloy from the β-region. The microstructure is characterised by lower strength, high ductility, and better fatigue properties than equiaxed microstructures, with good resistance to the growth of fatigue cracks. The equiaxed microstructure shown in Figure 2.17(c) is formed from the recrystallization of the alloy from the β-region followed by globulisation that leads to the formation of α-grains with β-grains deposited at their grain boundaries. The microstructure has good resistance to the initiation of fatigue cracks but poor resistance to the propagation of fatigue cracks [71, 72]. The bimodal microstructure, shown in Figure 2.17(d), is formed from recrystallization in the α+β phase field, consists of primary α-grains and leads to a combination of lamellae and equiaxed microstructures. It has better fatigue properties arising from a combination of good resistance to the initiation of fatigue cracks of the equiaxed microstructure with high resistance to the propagation of fatigue cracks of the lamellae microstructure. The microstructure also has the highest ductility among the five microstructures of Ti6Al4V alloy shown in this figure [37, 75, 137]. The Widmanstätten microstructure shown in Figure 2.17(e), is achieved when the alloy is gradually cooled by air from the β-phase region. When the temperature of the alloy starts to drop below the β-transus temperature, the hcp α-phase starts to appear in the form of plates from the β-grain boundaries [65]. This microstructure is known to have low strength and low ductility, as well as the poorest fatigue resistance among the different microstructures of Ti6Al4V [138, 139].

Studies have shown that the LPBF Ti6Al4V as-built samples exhibit the acicular α' martensite within prior β-grains [140, 141, 142]. Lekoadi *et al*. [121] observed large columnar prior β-grains oriented along the build direction for SLM Ti6Al4V as-built samples. These grains grow epitaxially perpendicular to the direction of travel of the laser beam and in the direction of the build. This is mainly due to the temperature gradient of the molten pool being essentially perpendicular to the scanning direction during LPBF processing [121]. Cao *et al*. [143] stated that for cracks that are perpendicular to the build direction, the prior β-grains act as crack deflectors. This means that the columnar prior β-grain boundaries interrupt the cracks, resulting in their slow rate of propagation. However, for the cracks that propagate parallel to the build direction, the authors observed that they propagate along the boundaries of the prior β-grains without much resistance. They demonstrated that the faster crack growth occurred in a direction parallel to the build direction and would lead to lower fracture toughness due to the easier propagation of cracks along the weaker prior β-grain boundaries [143]. This is consistent with the work of Malefane *et al*. [85]. Cerri *et al*. [144] observed few microstructural changes when heat-treating as-built parts at 740 °C (which is below the β-transus) for 130 minutes and noted that the α' martensite did not completely transform to α+β-grains in addition to which, the columnar prior β-grains remained visible [144]. Neikter *et al*. [145] reported that the α-grain boundary was dependent on the cooling rate, where a high cooling rate rendered thin and discontinuous α-grain boundary, while slow cooling led to thick and continuous α-grain boundaries [145]. Jaber *et al*. [45] observed differences arising from furnace and water cooling and stated that the volume fraction of the α-grains was higher after furnace cooling than after water cooling.

Hasib *et al*. [130] studied the role of microstructures on the fatigue behaviour of LPBF Ti6Al4V alloy. They found the thickness of the α'- or α-laths to be the main factor contributing to the fatigue crack growth rate resistance. They reported that larger thickness of the α-laths gave rise to higher fatigue thresholds and better fatigue crack growth resistance at growth rates less than 10^7 cycles. They demonstrated that above 10^7 cycles, fatigue crack growth resistance was insensitive to the thickness of the α-laths for samples that were heat-treated [130]. Kunz *et al*. [146] found the α' martensitic microstructure to have the lowest resistivity to the propagation of fatigue cracks for the as-built LPBF Ti6Al4V alloy [146]. Agius *et al*. [140] stated that the effect of α' martensitic microstructure was significant during the crack initiation stage because of a lower number of long slip bands or less irreversible slip, which led to the presence of fewer initiation sites of cracks [140]. Hosseini [66] stated that the development of

equiaxed or lamellar microstructure will lead to shorter fatigue life while the formation of bimodal microstructure is desirable as it resists fatigue crack initiation and propagation [66]. Yuri *et al*. [147] studied the effect of microstructure on the HCF properties of Ti6Al4V alloy for samples that were furnace-cooled, air-cooled, and water-quenched separately. They found the width of α-lamellar to be 4 to 12 μm for furnace-cooled samples, 2 to 3 μm for air-cooled samples, and finer α-lamellar for water-quenched samples. They reported that at 10^7 cycles, the fatigue strength increased from samples that were water-quenched, air-cooled, and furnace-cooled, in this order [147]. On the other hand, Ziaja and Kawalec [116] annealed Ti6Al4V samples at 850 °C and 910 °C and observed average grain diameters of 8.8 μm and 8.2 μm, respectively. They reported that lower volume fractions of the α-laths led to a longer fatigue life. This is likely because the alpha phase is stronger than the beta phase, and its reduction in volume fraction will, therefore, lead to an increase in ductility and an attendant increase in fatigue life.

g) **Surface roughness**

Roughly 90% of all in-service fatigue failures initiate from the component's surface [6]. Since the surface experiences the greatest stress under many loading scenarios (bending and torsional loading), failure is anticipated to begin there. According to Chern *et al*. [50] the most detrimental factor affecting the fatigue performance of AM parts is surface roughness. Fatigue life rises with decreasing surface roughness because lower surface roughness reduces local stress raisers [6]. Consequently, preparation of the surfaces of fatigue test specimens needs to be done with extra care. It is required that the surfaces be smooth and free of scratches and machining grooves [91]. Carrion *et al*. [148] in their study of fully reversed loading of Ti6Al4V ELI samples with a fully equiaxed microstructure, they reported that cracks were initiated at sites of inclusions near their surfaces. They observed shorter fatigue life for specimens with large sizes of inclusions [148]. Vayssette *et al*. [149] carried out an HCF test on SLM Ti6Al4V samples and observed an increase in fatigue strength from as-built samples to machined samples. Edwards and Ramulu [4] and Wycisk *et al*. [150] observed longer fatigue life on machined SLM Ti6Al4V specimens compared to as-build specimens. It was observed that the roughness on the surfaces of machining samples was removed, thus reducing the effects of stress concentration, and ultimately resulting in longer fatigue lives of AM parts [53]. Wycisk *et al*. [151] studied the HCF performance of SLM Ti6Al4V as-built and polished, as well as shot-peened samples. They observed a much lower fatigue limit of 210 MPa for the as-built

samples compared to that of 510 MPa for the polished samples. For the shot-peened samples, they recorded a 15% reduction of the fatigue limit in comparison with the polished samples. This was an unexpected trend, suggesting that crack initiation in this case was due to internal pores [151]. Alternatively, it is possible that the short peening did not raise high enough compressive stresses on the surfaces of the specimens to counter the effect of surface-defects, while polishing minimised their effect.

h) **Residual stresses and porosity in LPBF**

In the LPBF process, the laser beam energy is set so that the layer of metallic powder is completely liquefied by heat throughout its thickness at the point of application of the laser beam. The scanning speed, hatch distance, and power of the laser beam are set so that each run partially overlaps the preceding run and penetrates beyond the layer of powder. This ensures the formation of good metallic bonds between the adjacent tracks and layers to produce homogeneous solids. Once a layer has been printed, the build table drops down by one layer thickness, and a new layer of powder is deposited on the build platform. The top surface of this layer is then levelled out using a re-coater, and the process of printing starts all over again. This cycle continues until the part being built is complete. The building platform delivers heat away from built parts as well, and this way increases the rate of solidification of the parts. For most materials, the working chamber is filled with an environment of inert gas to protect parts from oxidation. The thickness of the one powder layer is typically 20 to 100 µm. The as-built parts may contain some structural defects due to the tendency of the process to build an unbalanced stress profile into parts between layers during printing [47]. Parts built through EBM are less liable to develop residual stresses than the LPBF parts since their built environment is maintained at temperatures ranging from 600–700 ℃. Titanium alloy parts exposed to these temperatures for long periods during fabrication develop minimal residual stresses in the final fabricated parts [49].

Residual stresses can be defined as self-equilibrium stresses of deformed materials that remain within the structure even after the load that deformed it is removed. Residual stresses are formed when the printed layers restrain the contraction of the current layer. They can cause initiation of cracks and delamination and can reduce the fatigue life of a part [47]. Using optimum process parameters or post-heat treatment processes can reduce residual stresses [49]. Stress-relieving heat treatment is applied to decrease unwanted residual stresses that occur within metallic parts without affecting the mechanical properties of the parts. This process

ensures maintenance of the shape of built parts [44, 125, 126]. Other mechanical treatments, such as shot-peening or surface rolling are used to reduce residual stress [49]. Common defects in additive manufacturing include gas pores and lack of fusion pores [50]. Gas pores are formed because of gas that is trapped in the molten metal as it solidifies rapidly [51]. It was observed that samples that fail due to this type of defect have longer fatigue life as compared to the case of other AM defects [54]. Lack of fusion defects are usually oriented perpendicular to the build direction and are located at the interface between layers [50]. They are formed because of powder that is not fully melted [51]. They are more detrimental to fatigue life than gas pores [55]. Porosity contributes to shorter fatigue life in LPBF samples, especially in the case of internal defects that are located near the surface. A micro-CT scanner is usually used to examine porosity. Due to variations of contrast between scans, the type of metal and the size of the pores relative to the scanning resolution, and due to limited time for the analysis of scans, some pores can be missed [55]. The problem of porosity and large microstructural defects can degrade the tensile properties of built parts, and this problem can be solved by optimizing the LPBF process parameters [56]. To have the best mechanical properties, maximum density should be achieved. The scanning speed, layer thickness, scanning strategy, and other process parameters must be optimal to produce non-porous LPBF parts [52]. However, the effect of residual stress/porosity on the fatigue properties of the material is not as severe as that of the microstructure [62]. Figure 2.18 shows various forms of defects on fatigue failure surfaces of the LPBF Ti6Al4V alloy.

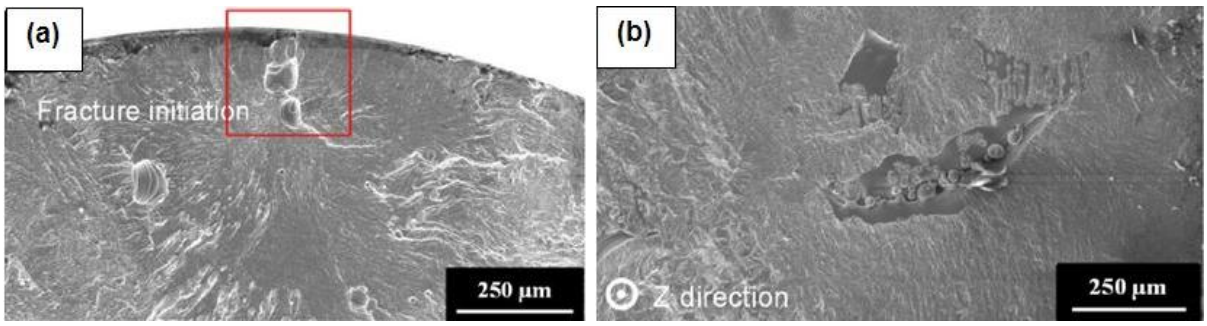

Figure 2.18: Micrographs showing different types of defects (a) porosities and (b) unmelted zones on Ti6Al4V parts [62]

Benedetti *et al*. [112] studied the fatigue behaviour of LPBF Ti6Al4V(ELI) specimens and found that crack initiation sites were due to larger internal defects located near the surfaces. Fotovvati *et al*. [53] claimed that the effect of internal pores on fatigue behaviour was less significant compared to surface defects. Edwards and Ramulu [4] reported that because of

porosity and residual stresses, the fatigue performance of SLM Ti6Al4V was lower than that of wrought Ti6Al4V. Gong *et al*. [93] found defects to be very detrimental to the performance of LPBF Ti6Al4V fatigue specimens, as cracks initiated there. Le *et al*. [152] studied the role of defects on the fatigue behaviour of Ti6Al4V alloy for as-built and machined samples. They reported that for the machined samples, cracks were initiated due to a lack of fusion and gas pores, both near the surfaces and within the samples. For as-built samples, cracks were initiated due to a lack of fusion on the surfaces and due to surface roughness. They demonstrated that lack-of-fusion pores would likely cause the initiation of cracks in additively manufactured samples [152]. Wycisk *et al*. [151] investigated the cause of failure in as-built and polished samples of LPBF Ti6Al4V. They reported that for the polished samples, cracks that resulted in fractures were initiated due to internal pores, while for the as-built samples, cracks were initiated due to rough surfaces. It was also reported that as-built samples exhibited shorter fatigue life, while polished samples had longer fatigue life [151]. Methods such as the Archimedes principle, gas pycnometry, and X-ray computed tomography are first applied to detect defects [53]. Thereafter, the HIP process can be used to reduce defects such as gas pores and lack of fusion of AM parts to improve their fatigue life. However, if these pores are formed at the surface, in which case they are referred to as open pores, they pose a problem with their removal using post-processing operations [31]. The only available method to reduce these pores is to make sure that the optimum process parameters are used in printing [52].

i) **Process parameter of the LPBF**

Parts made by AM are produced within predetermined process parameters. The most important ones, as well as the ones that AM machine operators can easily adjust, are layer thickness, hatch spacing or distance, laser power, laser scanning speed, and laser diameter [92]. Moletsane [52] stated that to produce non-porous LPBF parts, the scanning speed, layer thickness, laser power, and other process parameters must be optimal. According to Wang *et al*. [153], a higher laser power will increase the fluidity of the melt pool and consequently cause spattering, whereas a lower laser power will probably result in parts with less fusion of powder. They stated that lower scanning speeds can lead to the injection of large amounts of laser energy into the particles of powder and, therefore, the formation of unstable molten pool flow, while high scanning speeds result in poor multi-track overlap and large gaps between the layers [153], due to the formation of tracks with irregular cross-sections. If the laser scanning speed is too high, the powder material will not melt completely due to limited dwell time. If the laser scanning

speed is too low, the powder material may be exposed to the laser beam for too long, thus leading to the creation of voids and the formation of wider and shallower tracks. Fotovvati *et al*. [53] reported that porosity is increased by increasing scanning speed because of insufficient melting of the powder. They also demonstrated that high laser power or low scanning speed are detrimental because they lead to the production of parts with porosity [53]. Clearly, optimal process parameters are essential. It was reported that by optimizing process parameters, residual stresses are lowered [140]. Studies [140, 141, 142], have proven that utilizing a scanning strategy that uses the residual heating of new layers on the previous layer and a very tight hatch distance in as-built SLM Ti6Al4V contains the formation of martensitic α' microstructure and will result in the formation of a microstructure with α' and ($\alpha + \beta$) grains [140].

j) **Build-direction**

The AM build platform is set with the x-, y- and z-directions as reference axes, as shown in Figure 2.19. The length of the built parts is normally placed parallel and perpendicular to the direction of movement of the re-coater, which is either the x- or y-direction. The build direction is normally defined as the z-direction, but the other two axis directions can also serve as built directions as well [15].

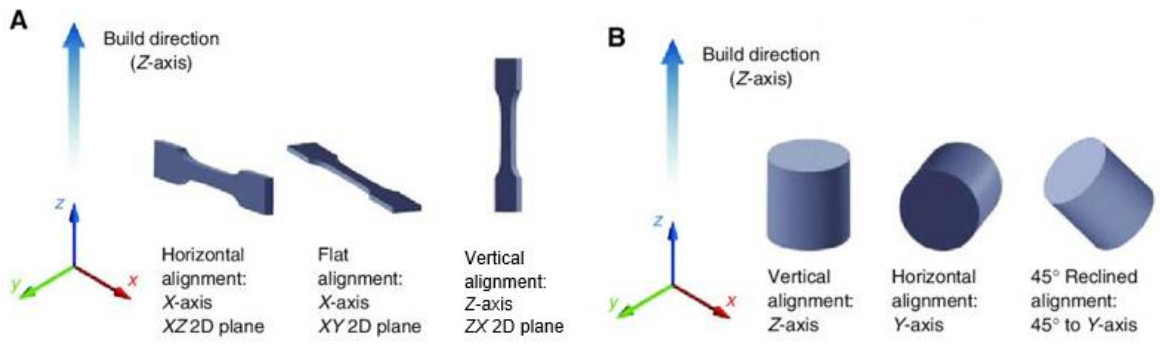

Figure 2.19: Build directions in AM [154].

The build direction influences the mechanical properties of the material. Several studies have revealed that parts build horizontally often had a higher mechanical strength compared to those built vertically [50, 127, 155]. Chandramohan *et al*. [127] observed fine martensite on the metallography of both horizontally and vertically build parts. Knowles *et al*. [156] stated that residual stresses that remain within the as-built parts will affect the yield strength of built parts in either the horizontal or vertical directions. Due to the different principles of the various AM

technologies in existent and due to the build directions used, differences in structure, mechanical, or fatigue properties will exist [56]. This is consistent with the work of Malefane [157].

Malefane [157] studied the effect of build direction on the S-N curve for the LPBF Ti6Al4V(ELI) specimens annealed at a temperature of 950 °C. They reported that the endurance limit and number of cycles to failure for specimens built in the x- and y-directions were 450 MPa for a run-out of 5 000 000 cycles, and for the z-direction 486 MPa for 1 183 000 cycles [157]. Figure 2.20 shows SEM fractographs of a specimen built in the x-direction that was cycled at a maximum stress of 675 MPa and which fractured at 896 033 cycles in the work of Malefane [157].

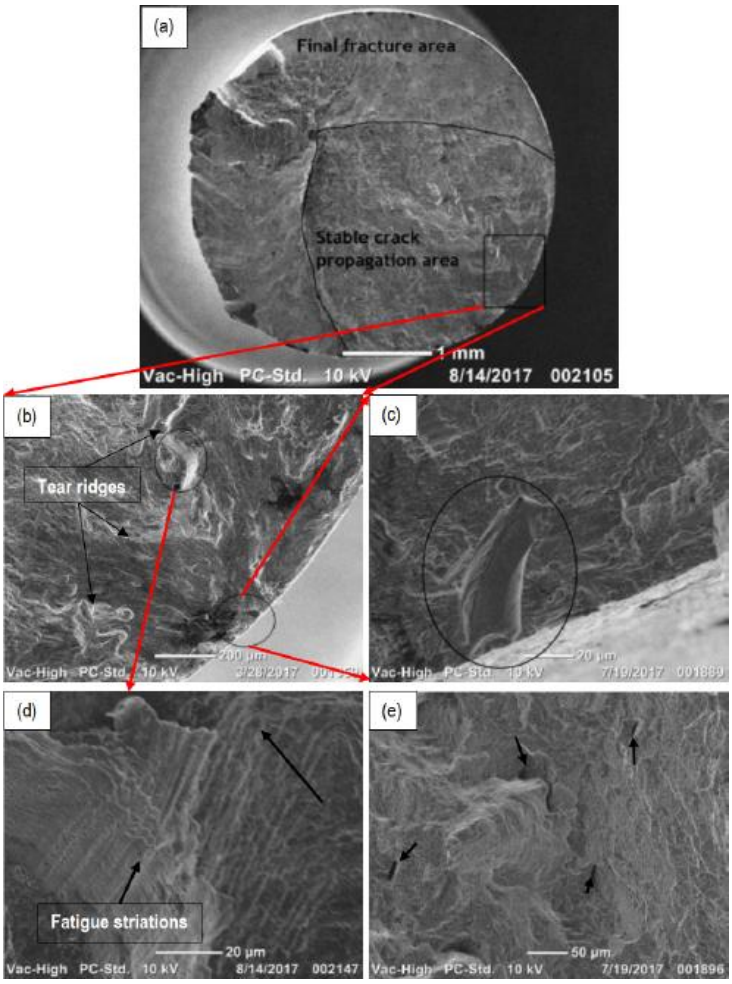

Figure 2.20: Fractograph of a LPBF Ti6Al4V (ELI) fractured sample (a) overall fracture, (b) magnified micrograph of the transverse crack propagation area, (c) further magnification, (d) high magnification and (e) high magnification of the shear lip area [157]

The overall fractograph in Figure 2.20(a) shows tear ridges, which are characteristics of stable crack propagation through the entire crack propagation area. The fatigue striations were magnified from the face of one of the tear ridges that slipped from the crack initiation site encircled, as shown in Figure 2.20(b). Figure 2.20(d) shows fine fatigue striations, indicative of a high number of cycles to failure and a bow-out from the crack initiation pore in the direction indicated by the arrow in the micrograph. The tear ridges, which are characteristic of stable crack propagation, run through the entire crack propagation area up until the area of final fracture, as is evident from the overall fractograph. Internal micropores were identified in this region and were all found to be elongated in the direction of the tear ridges, as indicated by arrows in Figure 2.20(e). Malefane [157] reported that for specimens built in the y- and z-direction, crack initiation was due to AM surface pores and shallow dimples were observed, as well as shear regions.

Edwards and Ramulu [4] reported a higher fatigue limit on specimens built in the x-direction and a lower fatigue limit on specimens built in the z-direction. They assumed that for the specimens built in the z-direction, which was also the longitudinal direction of the columnar β-grains, the reason for the lower fatigue limit could be due to long oriented slip planes parallel to the columnar grains. They further reported that specimens built in the z-direction had the roughest fracture surfaces after fatigue testing with loading along this direction [4]. Liu et al. [158] studied the fatigue behaviour of SLM Ti6Al4V specimens built vertically and horizontally. They also reported that cracks were initiated due to a lack of fusion for the two build directions. They observed that the horizontally built specimens had a higher number of cycles to fatigue failure than the vertically built specimens [158]. Leuders *et al*. [108] recorded higher fatigue resistance on SLM Ti6Al4V specimens built in the zx-direction as compared to the specimens built in the xz-direction [108]. Chan *et al*. [159] demonstrated that the fatigue strength in the x- and y-build directions was higher compared to the fatigue strength in the z-build direction. They reported that this was because of lack-of-fusion pores, which were located in between layers and were aligned perpendicular to the loading direction or the z-build direction specimens [159]. Dhansay [131] observed larger transgranular cleavage facets in the zx-build direction than in the xz- and xy-build directions for the samples that were double annealed. The author reported that this was likely due to the zx-direction's crack plane and direction of orientation of grains, which was more favourable for faceted fracture than for the xz- and xy-build directions [131]. Dhansay [131] also reported the highest residual stresses in the samples built in the zx build direction as compared to the samples built in the xz- and

xy-directions. The author further reported that the samples built in the xy-direction had the lowest residual stresses [131]. Ter Haar and Becker [160] studied the martensitic microstructure of SLM Ti6Al4V. They reported that the α′ laths had different aspect ratios when observed in the zx- or xz- and xy-build directions [160]. In contrast, Cain *et al*. [161] studied the effect of build direction on crack propagation and fracture toughness of SLM Ti6Al4V samples built in the xy- and xz-directions. They reported that the xy- and xz-build directions had less influence on fatigue crack growth rate and fracture toughness [161]. Hasib *et al*. [130] found the build direction to have little influence on the near-threshold fatigue crack growth rate. On the other hand, Xu *et al*. [162] reported that samples built at 0° and 45° had higher fracture toughness compared to the samples built at 90°.

2.7. The Effect of Heat Treatment on the Microstructure and Mechanical Properties of Ti6Al4V(ELI)

Heating, soaking, and cooling metal to change its properties without changing its physical form is known as heat treatment [163]. The processes involved in heat treatment include quenching, normalising, tempering, hardening, and annealing. Using a furnace, air, water, oil, brine, or molten salts, metals and metal alloys can be heated above or below their critical temperatures, held there for a period of time, and then cooled to room temperature [120]. Its primary goal is to control mechanical properties, particularly strength, ductility, and hardness [95]. This section presents a review of the effects of annealing, normalising and high-temperature annealing heat treatments on the microstructures and mechanical properties of Ti6Al4V(ELI).

2.7.1. Heat treating titanium and its alloys

Titanium and its alloys can undergo various types of heat treatment processes which include annealing, solution, and aging treatment, as well as hot-isostatic-pressing (HIP). Application of these processes is done to achieve selected mechanical properties [44, 120, 121]. Heat treatment of the alloy above 410 ℃ should be carried in under vacuum or in an environment of argon gas because, above 410 ℃, oxygen enters the solid solution of the alloy and causes embrittlement, which leads to a reduction of its service life [164].

a) Stress Relieving

The printed layers in LPBF undergo repeated melting and solidification during the building process. The solidified layers are remelted to enable bonding with the current layer to produce a solid part in AM. Residual stresses are generated when the solidified layers prevent the current layer from contracting during cooling. Residual stresses have the potential to shorten the fatigue life of parts through delamination and initiation of cracks [47]. Applying stress-relief heat treatment to metallic parts reduces undesired residual stresses without necessarily changing the parts' microstructure and, thus, mechanical characteristics. This procedure guarantees that the shapes of fabricated components are maintained [44, 125, 126].

b) Annealing

Annealing is a process involving heating and cooling, often applied to soften and alter mechanical properties by producing a desired microstructure [165]. The alloy is heated near the β-transus temperature in the $\alpha+\beta$ phase field, held at that temperature for 30 or more minutes, depending on the desired properties, and then cooled in a furnace. Annealing of titanium and titanium alloys serves primarily to increase fracture toughness, ductility at room temperature, dimensional and thermal stability, and creep resistance [44].

c) Normalising

When the alloy is heated to a pre-determined elevated temperature, held at that temperature for a set period and then allowed to cool freely in the air back to room temperature, it is said to have undergone normalising heat treatment. After this heat treatment process, the alloy will either exhibit its initial ductility or be slightly reduced, and its strength will have increased. This heat treatment process is employed to reduce thermal stresses, improve machinability, and normalize microstructures.

d) Solution treating and hardening

Solution heat treatment of titanium alloys involves heating to temperatures either slightly above or below the β-transus temperature and cooling at a fast rate to cause precipitation hardening. Elevated temperatures may cause excessive grain growth due to the recrystallization of grains. Too low temperatures may result in an incomplete process. Titanium alloys are usually solution heat treated below the β-transus to obtain high strength and an increase in hardness [95, 120].

e) Hot Isostatic Pressing

HIP is a heat treatment process that compresses materials at high temperatures and isostatic pressure up to 2 000 °C and 200 MPa, respectively, at the same time. Argon gas is the most used pressure medium to avoid oxidation of the alloy. The method is employed to decrease porosity while improving the density of materials [31, 166]. The process can be used to remove residual stresses from the as-built parts and improve the microstructure to a more fatigue-resistant microstructure [167]. HIP can be used to heal defects such as internal pores and microcracks of AM parts to improve the fatigue life of AM parts. However, the process may not be effective on pores that are formed at the surface, called open pores. Open pores are a problem in post-processing operations [31]. This method is reported to improve ductility [166].

2.7.2. The effect of heat treatment on the microstructures of Ti6Al4V(ELI)

2.7.2.1. Annealing Ti6Al4V(ELI)

Annealing is a process involving heating and cooling, often applied to soften and alter mechanical properties by producing a desired microstructure [165]. The alloy is heated near the β-transus temperature in the $\alpha+\beta$ phase field (between ~750 ℃ and ~950 ℃), held at that temperature for 30 or more minutes depending on the desired properties, and then cooled gradually in a furnace. Annealing of titanium and titanium alloys serves primarily to increase fracture toughness, ductility at room temperature, dimensional and thermal stability, and creep resistance [44]. Atoms have low mobility at ambient temperatures. However, when their temperature is raised to a sufficient degree during annealing, the atoms' thermal energy rises, causing them to move around and overcome the grain boundaries' surface energy. This results in the growth of grains and the movement of grain boundaries. The consequence is the coarsening of the α-laths [21, 26, 76, 77]. As the soaking time increases, so do the sizes of the α-laths. A slow cooling rate results in further growth of grains [168]. Rapid cooling prevents the movement and rearrangement of atoms into a more stable state, which results in a high number of defects in the crystal lattice and increases the hardness and strength of the material. These defects increase the likelihood of the material cracking [76].

Vrancken *et al*. [169] annealed an SLM Ti6Al4V sample at 850 °C for two hours, followed by furnace cooling, to produce a basket-weave microstructure composed of α-laths with a width of 1.27±0.13 µm, shown in Figure 2.21 [169]. Jovanović *et al*. [22] annealed Ti6Al4V parts at

950 and 800 ℃ for two hours, followed by furnace cooling to produce a microstructure consisting of α-laths with a thickness of 7 µm and 6 µm [22]. Formanoir *et al*. [170] reported that annealing heat treatment at 950 ℃ followed by slow cooling induced coarse α-lamellae with an average width of 2.9±0.2 µm that took up globular shapes [170]. Fan *et al*. [171] observed an equiaxed microstructure after annealing at a temperature of 750 ℃, while Becker *et al*. [17] observed an equiaxed microstructure with plate-like α-β-grains after annealing at 950 ℃ followed by furnace cooling. Malefane *et al*. [85] when studying the microstructures on LPBF Ti6Al4V samples annealed at 950 °C, observed equiaxed and basket-weave microstructures, as shown in Figure 2.22. It was further reported in their research that the average width of the α-laths was 6.7 µm [85].

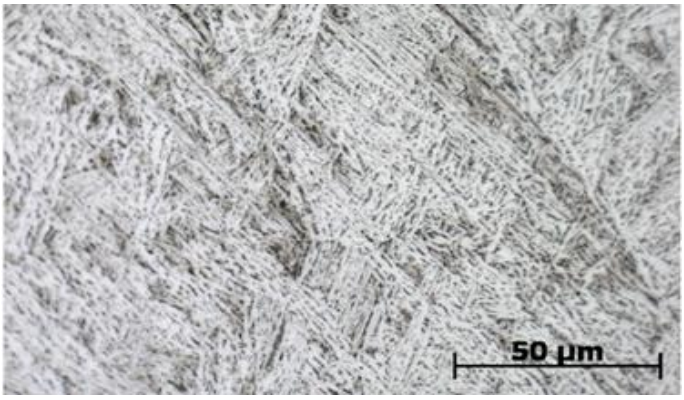

Figure 2.21: Microstructure of LPBF Ti6Al4V sample annealed at 850 ℃ for two hours followed by furnace cooling [169]

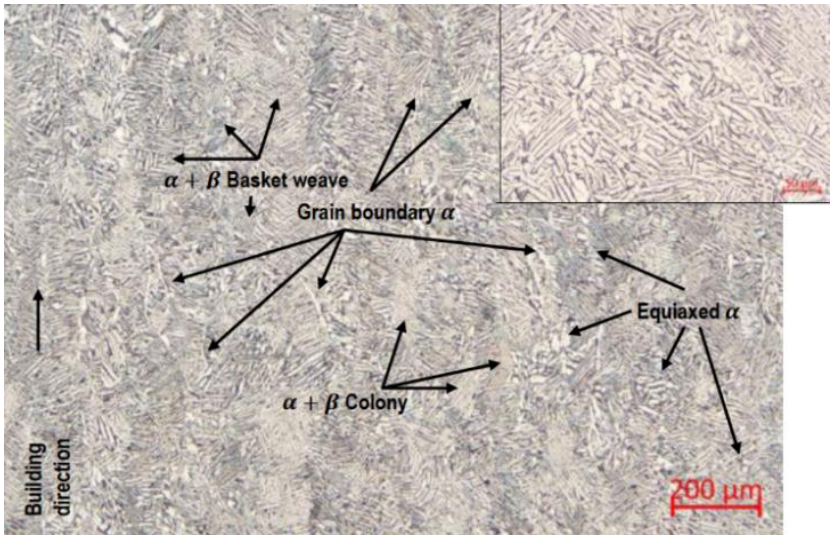

Figure 2.22: Microstructure of Ti6Al4V (ELI) annealed at 950 ℃ for two hours followed by furnace cooling [85]

It is noted from the foregoing discussion that there is a difference in the width of the α-laths in all the highlighted cases, which is likely due to differences in soaking temperature and time, as well as cooling rates. Zöllner [21] stated that higher temperatures lead to even coarser α-laths, as is evident in the study by Jovanović et al. [22]. Higher initial soaking temperature and slower eventual cooling rate are likely causes of the formation of course α-laths. The different widths of α-laths in the works of Malefane *et al*. [85], Jovanović et al. [22], and Formanoir *et al*. [170], annealed Ti6Al4V samples at 950 ℃ of 6.7, 7, and 2.9 µm, respectively, are likely because of the difference in cooling rates in the three studies. Similar microstructures were obtained for annealing at different temperatures, while different microstructures were obtained for annealing at the same temperatures, as noted in the works of Becker *et al*. [17], and Malefane *et al*. [85], who obtained equiaxed microstructure after annealing at 950 °C, while Fan et al. [171] obtained equiaxed microstructure after annealing at 750 °C. Annealing at 950 °C by Formanoir *et al*. [170] resulted in coarse globular α-lamellar.

2.7.2.2. Normalising Ti6Al4V(ELI)

When the alloy is heated to a pre-determined elevated temperature, held at that temperature for a set period, and then allowed to cool freely in the air back to room temperature, it is said that the alloy has undergone normalising heat treatment. After this heat treatment process, the alloy will either exhibit its initial ductility or ductility will be slightly reduced, and strength will be increased. This heat treatment process is employed to reduce thermal stresses, improve machinability, and normalize the microstructures. Figure 2.23 shows the microstructure of Ti6Al4V heated at 1 050 ℃ and then allowed to cool in the air. Shaikh *et al*. [24] observed lamellar microstructure consisting of α and transformed β with grain boundary α on the prior β-grains obtained after air cooling.

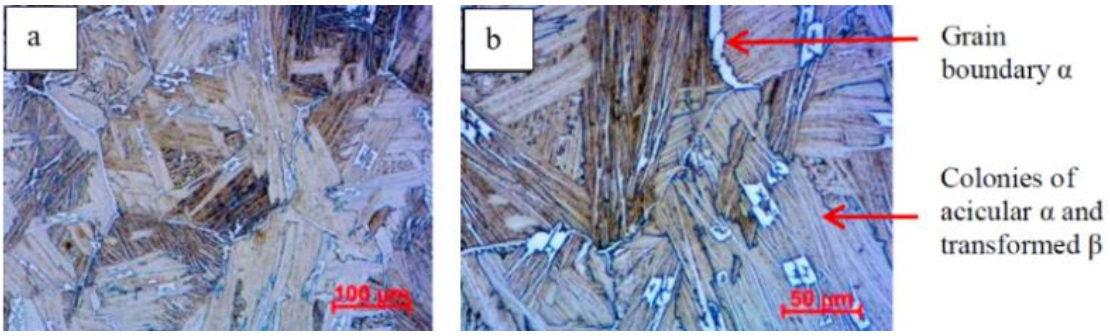

Figure 2.23: Microstructure of Ti6Al4V heated at 1 050 ℃ and then allowed to cool in the air [24]

2.7.2.3. High-temperature annealing Ti6Al4V(ELI)

High-temperature annealing involves heating the alloy above the beta transition temperature, holding it at that temperature for some time, and finally cooling it gradually in a furnace. Due to heating at elevated temperatures, recrystallization occurs, where new sets of grains nucleate and grow inside the old-deformed grains and at the grain boundaries. The holding time must be controlled because holding the material at temperatures for too long leads to excessive growth of grains. Large grains are undesirable because they reduce toughness and ultimately lead to a shorter lifetime of components. High-temperature annealing leads to a well-balanced combination of strength and ductility [120].

Jovanović *et al*. [22] annealed Ti6Al4V parts at 1100 ℃ for two hours, followed by furnace cooling to produce a microstructure consisting of α-laths with a thickness of 9 µm. They further reported that a higher annealing temperature than this results in coarser α-lath [52]. Shaikh *et al*. [24], after heat treating Ti6Al4V samples at 1 050 ℃ and furnace cooling, observed a coarse microstructure consisting of α- and β-grains, as shown in Figure 2.24. On the other hand, Ding *et al*. [172] observed equiaxed microstructure after heat treating a Ti6Al4V bar at 1 150 ℃ for two hours and cooling in a furnace. Formanoir *et al*. [170] pointed out that annealing heat treatment at about 1 040 ℃, above the β-transus temperature, followed by slow cooling, induced the growth of large α-lamellae and β-grains with diameters of up to 1 mm and resulted in the formation of an equiaxed microstructure. Eshawish *et al*. [173] and Lekoadi *et al*. [121] observed a coarse lamellar microstructure of α+β, after annealing heat treatment for 15 minutes at 1 015 ℃ and for two hours at 1 000 ℃, respectively, followed by furnace cooling. Fan *et al*. [171] observed a typical α equiaxed and basket-weave, Widmanstätten microstructure, with α-grain boundaries in the prior β-grains on samples annealed at 1 050 ℃. Moloi *et al*. [23] observed α- and β-laths with the widths of 10.1±0.9 µm and 3.4±0.3 µm, respectively, forming lamellar, Widmanstätten, and bimodal microstructures after annealing LPBF Ti6Al4V(ELI) at 980 ℃.

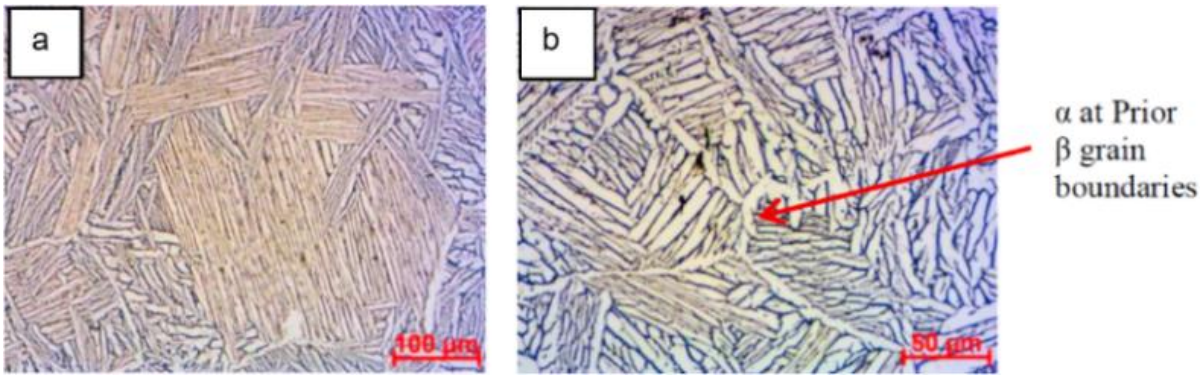

Figure 2.24: Microstructure of Ti6Al4V heated at 1 050 ℃ and then furnace cooled [24]

It is noted that there are slight differences in the width of the α-laths in the foregoing results, which, as observed previously in this section, is likely due to differences in soaking time and cooling rates. Some of the researchers [22, 23, 170, 172] observed globular α-phases or the equiaxed microstructure, while other researchers [24, 173] observed globular α-lamellar. Thus, heat treatment above the β-transus temperature, followed by slow cooling led to coarsening of the α-phase. Jovanović *et al*. [22] recorded a 9 µm thickness of the α-laths for annealing at 1 100 ℃ and two hours, while Moloi *et al*. [23] recorded an average width of 10.1±0.9 µm for annealing at 980 ℃ and one hour. The former works would be expected to record larger widths of α-laths than the latter, as the annealing temperature was higher and the soaking time was longer. This is likely due to differences in the initial microstructures and errors in the measured thickness or width of the α-laths.

2.7.3. Effect of heat treatment on the mechanical properties of Ti6Al4V(ELI)

The mechanical properties of materials define their behaviour under the action of load. They are measures of strength, stiffness, and ductility and are very significant in the design of tools, machines, and structures. The most common mechanical properties considered are strength, hardness, ductility, brittleness, toughness, stiffness, and impact resistance.

Table 2.6 compares the data obtained by different researchers on the effect of different heat treatment processes on the mechanical properties of Ti6Al4V(ELI).

Table 2.6: Mechanical properties of Ti6Al4V exposed to different heat treatment processes

Heat treatment processes	Heat treatment temperature (℃) and period (hours)	Young's modulus (GPa)	Ultimate tensile strength (MPa)	Yield strength (MPa)	Percentage elongation (%)	Vickers hardness HV	Reference
SLM as-built	-	109.2±3.1	1267±5	1110±9	7.28±1.12	-	[169]
Annealing	@850 for 2h	114.7±3.6	1004±6	955±6	12.84±1.36	-	
Normalising	@1015 for 0.5h	112.8±2.9	902±19	822±25	12.74±0.56	-	
High-temperature annealing	@1020 for 2h	114.7±9	840±20	760±19	14.06±2.53	-	
SLM as-built	-	-	1180	1060	8	-	[45]
Annealing	@850 for 2h	-	986	932	13	-	
High-temperature annealing	@1020 for 1h	-	833	748	14.5	-	
AM as-built	-	122.1±1	1135±4	1038±7	7.3±1.9	372±4	[174]
Annealing	@780 for 2h	120.7±1	1133	1042	8.9	372±3	
High-temperature annealing	@1000 for 2h	118±1	1063±8	927±7	13.7±1	338±4	
Annealing	@800 for 1h	-	1130	-	2.5	363	[22]
High-temperature annealing	@1050 for 1h	-	1260	-	1.7	400	
High-temperature annealing	@980 for 1h	99.5 ±17	953.7±59	888.4±33.9	13±2.1	318.4±13.6	[23]
As-received	-	111.0±3.1	1054±4.3	978.2±15.2	13.6±1.7	362.5±5.3	[175]
Annealing	@850 for 1h	-	-	987±15.5	13.5±1	365.2±2.3	
High-temperature annealing	@1050 for 1h	-	-	1041±32	10.3±0.6	389.4±5.9	
EBM as-built	-	-	1073	1001	11	366	[176]
Normalising	@1100 for 0.5h	-	998±52	847±90	13±7	365±31	
High-temperature annealing	@1100 for 0.5h	-	913±38	774±112	13±2	378±44	
SLM as-built	-	112	1130	1010	9.3	-	[86]
Annealing	@850 for 2.5h	117	1150	1020	13.5	-	
High-temperature annealing	@1050 for 2.5h	110	1000	850	15.5	-	
SLM as-built	-	-	1152±11.3	1065±6.8	6.1±0.8	-	[87]
Annealing	@850 for 2h	-	989±6.1	943±5.2	10.2±0.1	-	
High-temperature annealing	@1020 for 2h	-	839±6.2	742±13.5	15.3±0.3	-	

From Table 2.6, it is clear that normalising gave rise to the highest value for ultimate tensile strength and yield strength. Annealing at high temperatures resulted in an increased percentage

elongation, except for the studies done by Jovanović *et al*. [22] and Fan *et al*. [175], which showed annealing to lead to higher values instead. This is because the two studies [22] and [175] annealed at 1 050 ℃ for a shorter period of one hour. Ganor *et al*. [174] reported the highest value of modulus of elasticity after annealing heat treatment, while Moloi *et al*. [23] recorded the lowest value of modulus of elasticity after annealing. Reference [174] annealed the alloy at a temperature of 1 000 ℃ for two hours, while reference [23] annealed the alloy at a temperature of 980 ℃ for one hour. This is likely due to differences in the initial microstructure, as the former reported a very fine 1 µm thickness *α'* for the as-built samples, and the latter measured an average width of 2.4±0.4 µm for the as-built samples. Vrancken *et al*. [169] recorded a lower value of ultimate tensile strength after normalising heat treatment than Galarraga *et al*. [176]. This difference is because lower normalising temperature and longer duration time in the study of Vrancken *et al*. [169], as Vrancken et al. [169] heat-treated to a temperature of 1 020 ℃ for two hours, while Galarraga *et al*. [176] heat-treated to a temperature of 1 100 ℃ for half an hour. Jin *et al*. [86] recorded the highest percentage of elongation after annealing at high temperatures. This is because of the longer soaking time than in the other studies. It can be deduced from the data in this table, in studies of [86, 87, 169, 174, 176] that elevated-temperature annealing leads to well-balanced mechanical properties of the alloy, with good values of strength and ductility. It is evident in the table that an increase in strength is accompanied by a loss of ductility. Therefore, though the main objective of heat treatment is to improve the mechanical properties of metallics, an improvement in one or more properties is often gained at the expense of a reduction in the values of some other properties.

2.8. Scope and Opportunity for Future Work

2.8.1. On fatigue of LPBF Ti6Al4V(ELI)

Fatigue testing at temperatures below 350 ℃ has been reported [11] to have an insignificant effect on the fatigue behaviour of Ti6Al4V samples. This can be because the opposing effects of temperature on the two mechanical properties of ductility and tensile strength tend to cancel out in this range of temperatures. It has been reported [10, 25, 26] that an increase in temperature causes a reduction in tensile strength and an increase in ductility. An increase in ductility improves fatigue strength, while a decrease in strength reduces fatigue strength. The relationships between the increase in test temperature and these two mechanical properties are of great importance, and the temperature at which the significance of these two trend changes needs to be clearly identified. This is particularly important given the results of some studies

in which it has been reported that at high temperatures, the fatigue strength of alloys is weakened. It is essential to identify the temperatures at which the fatigue strengths of metallics start weakening. Moreover, fatigue trends with further increase of test temperature for different metallics beyond this changeover point should be investigated.

It is reported [6] that testing at high frequency will lead to faster generation of cracks, which will result in a decrease in the fatigue life of test samples. On the other hand, high-frequency testing can improve the fatigue performance of the materials because of the high strain rate, strain hardening effect because of mechanical deformation [3, 6]. The two phenomena and their interplay should be investigated further for different metal alloys.

It was reported [85] that the LPBF samples built in the x- and y-directions have similar microstructures, and therefore, the expectation is that the samples will have similar fatigue behaviour, as this is dependent on their microstructures. However, the fatigue performance of the samples built in the y- and x-directions has been reported to have significant differences. The cause of these differences should be investigated further.

LPBF-manufactured parts are considered less reliable for certain applications because of their poor surface finish. Because of this, LPBF parts require some post-processing, such as machining, to improve their surface finish. Studies in references [4, 149, 150] reported that the fatigue strength of machined LPBF Ti6Al4V samples was higher compared to those of as-built samples that have rough surfaces. Therefore, there is a need to produce LPBF parts with better surface finish to improve their fatigue performance, and ways of improving the LPBF process should be investigated.

LPBF parts have inherent shortcomings, such as residual stresses and internal flaws. These play a huge role in the fatigue life of Ti6Al4V alloy, as many studies have reported that fatigue initiates from such defects. The use of optimum process parameters has been proven to minimise these shortcomings, and therefore, there is a need to ensure that optimal process parameters are used for the manufacturing of LPBF parts. The use of HIP is reported to reduce the number of these defects and, in this way, lead to an improvement of fatigue life by up to 90%. Investigations on how to further reduce these internal defects are essential.

It is noted that most studies, as is the case here, are conducted at different stress ratio values. This makes it difficult to compare the results from such different studies as different stress

ratios lead to different maximum stresses and, therefore, different extents of plastic deformation. Another issue that makes it difficult to compare the studies is the different geometries of specimens and the different standards used, and a study to harmonise them is necessary.

2.8.2. On heat-treatment processes and their effects on microstructure and mechanical properties of Ti6Al4V(ELI)

The microstructures of additively manufactured Ti6Al4V(ELI) components that undergo similar build processes and heat treatment show similar morphologies on examination under microscopes. Studies discussed here have shown that the effect of heat treatment is significant on the distribution and size of grains. Moreover, it has been noted here that the type and size of grains affect the mechanical properties of the alloy and, therefore, its service life. The challenge of fully relating the various heat-treatment processes, the resulting arrangement and sizes of grains and the arising mechanical properties of different metallics is significant and current.

During heat treatment, the effect of soaking time and cooling rate has been reported here from the literature to be very significant in the microstructure and mechanical properties of metal alloys. Less attention has been given to the effect of heating rate and the different percentages of alloying elements. Studies have shown that the effect of wt% of the alloying elements is significant in the microstructure and, therefore, mechanical properties of metallics. Future investigations of these factors should be pursued.

The mechanical properties of metallics are not solely dependent on the heat-treatment processes and composition but also on the testing regime. Thus, for instance, different strain rates applied to a metallic exposed to an annealing heat-treatment process will give different tensile mechanical properties. This can be due to the strain-hardening of thermal softening effects. These are yet other factors to be considered that affect the mechanical properties of metallics.

During the application of heat-treatment processes, big components have been a problem in the past since they cannot fit in the furnace. However, engineers have now developed huge furnaces for larger components. The price of these large furnaces is high, which reduces their number across the world, leading to limited access to them. Because of the high cost and limited

number of these large furnaces, it is normal to use scaled-down specimens to predict the behaviour of full-scale specimens. This calls for a good understanding of dimensional analysis and the processes taking place during heat treatment.

The use of HIP has increased in the past years because the method leads to a reduction in the size and number of defects found in metallic parts. It is also used to close microcracks and pores in parts, and this way leads to an improvement in the strength and ductility of metallics. Notwithstanding its benefits, its extended treatment duration and high cost are some of its drawbacks [177]. Therefore, there is a need to investigate possible improvements to this process to reduce the long treatment times.

2.9. Conclusions

2.9.1. On fatigue of LPBF Ti6Al4V(ELI)

This review provides background information on titanium and Ti6Al4V. It gives insight into the influence of mean stress, stress concentration, loading frequency, temperature, heat treatment, microstructure, surface roughness, residual stress and porosity, as well as the build direction of the LPBF Ti6Al4V alloy. The following can be deduced from the information presented in the chapter regarding fatigue:

- An increase in the mean stress leads to a reduction in the fatigue life of Ti6Al4V.
- Loading at different frequencies leads to different numbers of cycles to failure.
- At elevated temperatures, cracks grow faster compared to the case at lower temperatures.
- The fatigue strength of Ti6Al4V decreases with increasing temperature.
- Post-heat-treatment processes are applied to alter the mechanical properties of Ti6Al4V by altering its microstructures to the desirable ones.
- The α' martensitic microstructure of LPBF as-built parts causes them to exhibit low fatigue lives.
- Thicker α-laths that are the result of high-temperature annealing of Ti6Al4V have a higher resistance to the growth of fatigue cracks than thinner α-laths.
- Amongst the microstructures of Ti6Al4V, the bimodal microstructure is the most desirable as it has a combination of good resistance to both the initiation and

propagation of fatigue cracks. The microstructure also has the highest ductility of all the microstructures of the alloy.

- The SLM as-built samples with rough surfaces have lower fatigue lives compared to samples that are machined or polished. However, and contrary to expectations, shot peening leads to a reduction of fatigue life.
- Porosity is detrimental to the fatigue life of LPBF Ti6Al4V samples and can be reduced by optimizing process parameters.
- HIP is employed to reduce porosity and residual stresses and leads to an improvement of fatigue performance by up to 90%.
- The samples built horizontally have longer fatigue lives compared to the samples built vertically.

2.9.2. On heat treatment processes and their effects on microstructure and mechanical properties of Ti6Al4V(ELI)

The aim of this review section was to investigate the effects of heat treatment processes on the microstructure and mechanical properties of Ti6Al4V(ELI). The following conclusions arise from the discussions presented here:

- Annealing coarsens microstructural features, reduces hardness and strength, and increases ductility and machinability of parts.
- Normalising refines microstructures and improves strength while ductility is reduced.
- High-temperature annealing leads to coarser microstructural features than annealing and improves ductility more than annealing.

Clearly, heat treatment plays an important role in determining the microstructure and mechanical properties of parts. Therefore, structural parts with well-balanced mechanical properties needed in various industries can be achieved through the applications of various heat treatment processes.

CHAPTER 3: RESEARCH METHODOLOGY

3.1. Introduction

This chapter contains details on the procedure adopted to carry out research in this work. The present study commenced with a literature review on titanium, Ti6Al4V and AM of metals, particularly Ti6Al4V. This was followed by material on fatigue in general and with a focus on additively manufactured titanium Ti6Al4V(ELI) alloy, and finally on the effect of temperature on the fatigue behaviour of the alloy. Uniaxial tensile test and fatigue test specimens were manufactured as rods using a DMLS EOSINT M290 and then machined to size to comply with the ASTM standards E8 and E466, respectively. The machine was set to the optimal process parameters. All 48 test specimens printed were exposed to stress-relief heat treatment, and then 39 (18 fatigue and 21 tensile) test specimens were further exposed to high-temperature annealing. The two heat treatment processes were performed; the first one to remove residual stresses, and the second one to reduce hardness and increase ductility.

Uniaxial tensile tests were performed on an Instron 1342 and 8801 Servo-hydraulic Fatigue Testing System. A total of 30 specimens (9 stress-relieved and 21 stress-relieved followed by high-temperature annealing) were loaded in uniaxial tension at various temperatures (20 ℃, 175 ℃, 325 ℃, and 475 ℃). Fatigue tension-tension testing was performed on the same Instron 8801 machine. Eighteen fatigue test specimens that were stress-relieved followed by high-temperature annealing were tested in tension-tension fatigue at a frequency of 25 Hz and at test temperatures of 20 ℃, 175 ℃, and 325 ℃, thus six specimens tested at each temperature. After both uniaxial tensile testing and fatigue testing, scanning electron microscopy was used to study the characteristics of failure on the fracture surfaces and investigate the causes of failure. This was carried out on mounted, polished, and etched specimens. An optical microscope was used to establish the changes from the edge-of-fracture surfaces away along the gauge length. Vickers microhardness tests were performed using a Future Tech FM 7E microhardness testing machine to measure the hardness of the alloy.

From the foregoing analysis and results of failure for both the tensile and fatigue testing, the effect of temperature changes and elevated temperatures on the tensile and fatigue behaviour of additively manufactured Ti6Al4V(ELI) were determined. The foregoing process is summarized in the flow diagram shown in Figure 3.1.

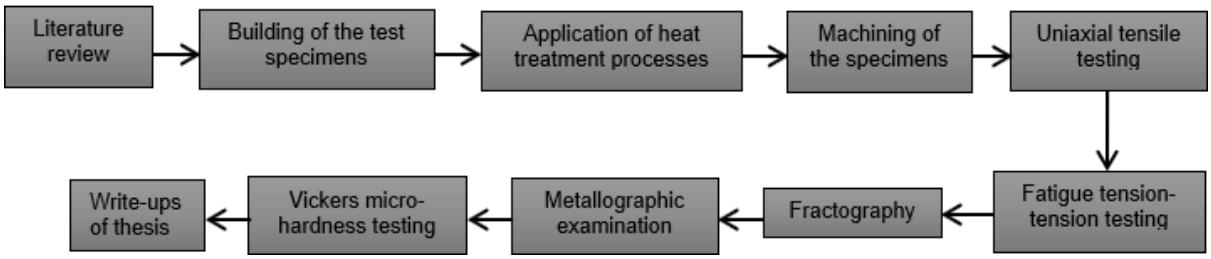

Figure 3.1: Flow diagram of the adopted research methodology

3.2. Building of the Test Specimens

Uniaxial tensile test and fatigue test specimens were manufactured using the DMLS EOSINT M290 shown in Figure 3.2. A large variety of materials can be processed with the EOS M290, including superalloys, stainless steel, and light metals. The machine has a build volume of 250 x 250 x 325 mm, a 400 W Yb-fibre laser, and a scanning speed of up to 7 m/s [178].

Figure 3.2: Image of a DMLS EOSINT M290 machine

The machine was set to the optimal process parameters, as shown in Table 6.1, that were established by the manufacturer of the machine for Ti6Al4V(ELI) powder.

Table 3.1: Process parameters for Ti6Al4V(ELI) manufactured by a DMLS EOSINT M290 machine

Parameters	Laser power (W)	Laser diameter (μm)	Scanning speed (mm/s)	Hatch spacing (μm)	Layer thickness (μm)
Ti6Al4V(ELI)	280	80-100	1300	120	40

3.3. Heat Treatment Processes

The stress-relieving and high-temperature annealing heat treatments were applied using the Super Series X Vacuum Furnace manufactured by TM-Vacuum Products Inc., shown in Figure 3.3. This is a high-vacuum, high-temperature (2 000 °C) furnace able to accommodate up to 200 pounds (71 kg) of material for a variety of custom vacuum processes, including bonding, annealing, brazing, sintering, hardening, and stress-relieving [179].

Figure 3.3: Image of a TM Vacuum furnace

All 48 specimens were stress-relieved and 39 were further exposed to high-temperature annealing. The stress relief and high-temperature annealing heat treatment regimes used in this work are shown in Figure 3.4 and Figure 3.5, respectively, and were all undertaken in the furnace shown in Figure 3.3.

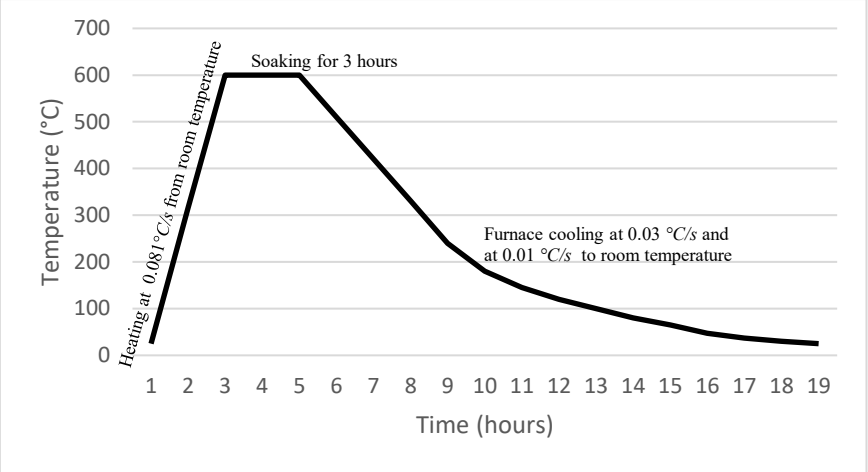

Figure 3.4: Curve for stress-relief heat treatment

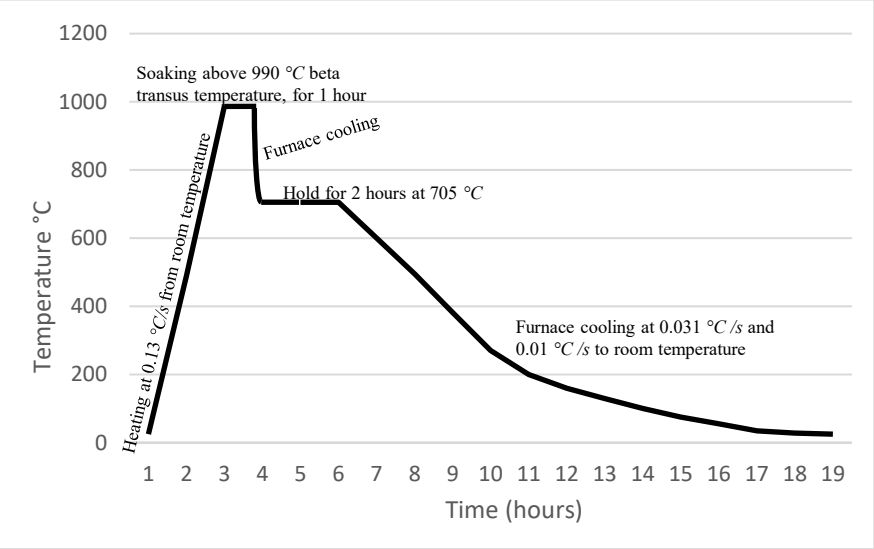

Figure 3.5: Curve for high-temperature annealing heat treatment.

The stress-relief heat treatment regime, shown in Figure 3.4, was applied while the specimens were still attached to the building substrate to avoid distortion upon removal of the specimens prior to this due to the residual stresses inherent in them. In this process, the specimens were heated to a temperature of 600 °C at the rate of 0.08 °C/s, held at this temperature for three hours, and then furnace-cooled in a vacuum to room temperature at the rate of 0.06 °C/s initially and then at 0.01 °C/s. This stress-relieving heat treatment was done to remove residual stresses developed during printing [180]. Research conducted over the years has led to the adoption of this stress-relieving heat treatment regime, which has been shown to effectively relieve residual stress without compromising the microstructure of the as-built part.

Thereafter, nine of the uniaxial test specimens were cut off from the building substrate, and the remaining 39 specimens were exposed to high-temperature annealing (18 fatigue tension-tension test specimens and 21 uniaxial tensile test specimens). In this process, the specimens were heated at the rate of 0.13 ℃/s to a temperature of 980 ℃, just below the β-transus temperature, and held at this temperature for one hour. This was followed by furnace cooling to 705 ℃, then holding at this temperature for two hours; and thereafter, vacuum cooling at a rate of 0.031 ℃/s first, then at 0.01 ℃/s to ambient temperature. The vacuum pressure used was $5.9X10^{-6}$ Torr. The temperature of 980 ℃ was selected to ensure significant transformation of α-grains to β-grains, and the ensuing soaking was carried out at this temperature to ensure homogenisation of the resulting $\alpha+\beta$ microstructure. Furnace cooling to a temperature of 705 ℃ was carried out to ensure the transformation of β-grains to α-grains, and soaking at the same temperature was done to ensure their growth in size to enhance the ductility of the alloy.

3.4. Machining of Specimens

Uniaxial tensile and fatigue tension-tension test specimens that were manufactured as rods were further machined to comply with relevant ASTM standards. Figures 6.6(a) and 6.6(b) show the tensile and fatigue test specimens that comply with the ASTM standards E8 and E466, respectively.

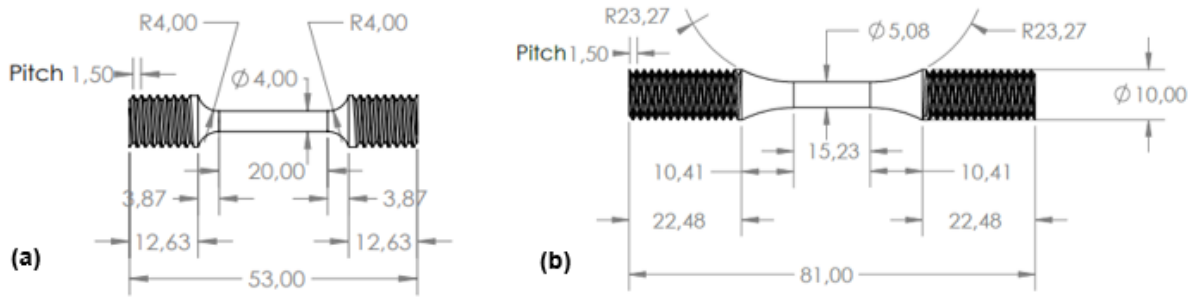

Figure 3.6: Test specimens for (a) uniaxial tension and (b) fatigue tension-tension

3.5. Tensile Testing

The tensile testing was initially conducted on the Instron 1342 Servo Hydraulics Testing Frame, H7051, in the laboratory of Metallurgy at Mintek, in Randburg, shown in Figure 3.7(b). The testing machine is designed for both dynamic and static testing, with an adjustable upper

crosshead with hydraulic lifts and locks. Eighteen specimens (nine stress-relieved and nine stress-relieved followed by high-temperature annealing) were tested on this machine. Testing at Mintek broke down, and testing was further conducted on the Instron 8801 Servo-hydraulic Fatigue Testing Frame in the laboratories of the Department of Mechanical Engineering at the University of South Africa (UNISA), shown in Figure 3.7(a). The testing frame is double-acting with a maximum force capacity of ±100 kN, designed for both dynamic and static testing. It has extra height for testing with longer load strings, high stiffness with twin support columns and an actuator in its lower base. It also comes with a 150 mm stroke, adjustable upper crosshead with hydraulic lifts and locks and is designed to be used with the 3520 series of hydraulic power units [181]. The furnace or heating chamber on it can go up to a temperature of 600 ℃. Twelve specimens that were stress-relieved, followed by high-temperature annealing, were tested for tension on this machine.

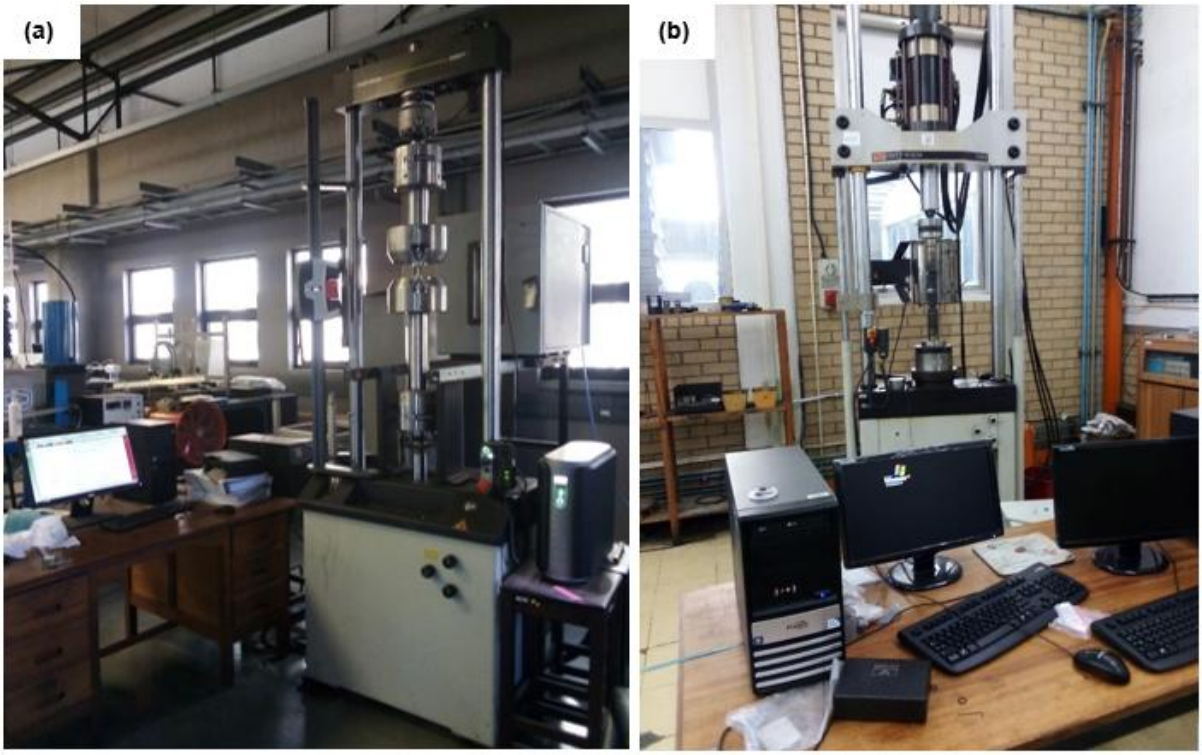

Figure 3.7: Image of an Instron (a) 8801 and (b) 1342 Servo-hydraulic Fatigue Testing machines

Two sets of specimens (stress-relieved and stress-relieved followed by high-temperature annealing) were tested at temperatures of 20 ℃, 175 ℃, 325 ℃, and 475 ℃. Three specimens for each set were tested at each temperature. During testing, each specimen was mounted on the testing frame, heated up to the intended test temperature, and kept at this temperature for

30 minutes to ensure thermal equilibrium. Following this, a tensile load was applied on each specimen at a displacement rate of 2 mm/min until failure and complete separation. A total of 30 specimens were tested. The tensile properties investigated here were yield strength, ultimate tensile strength, percentage elongation, and modulus of elasticity. The average yield stress obtained at each test temperature was used as a reference to conduct fatigue tests later. Table 3.2 gives a summary of some of the preceding information.

Table 3.2: Summary of the heat treatment regimes, number of specimens and changes in temperature for tensile test

Material	Heat treatment regimes	Specimens at each temperature change	Test temperature changes	Total number of specimens
Ti6Al4V(ELI)	2	3	4	30

3.6. Fatigue Testing

Fatigue tension-tension tests were performed on the Instron 8801 Servo-hydraulic Fatigue Testing Frame shown in Figure 3.7(a). The testing frame is double-acting with a maximum force capacity of ±100 kN, designed for both dynamic and static testing. It has extra height for testing with longer load strings, high stiffness with twin support columns, and an actuator in its lower base. It also comes with a 150 mm stroke, adjustable upper crosshead with hydraulic lifts and locks and is designed to be used with the 3520 series of hydraulic power units [181]. The furnace or heating chamber on it can go up to a temperature of 600 ℃. Eighteen specimens that were stress-relieved followed by high-temperature annealing were tested at various temperatures (20 ℃, 175 ℃, and 325 ℃). Each specimen was mounted on the testing frame, heated up to the intended test temperature, and then loaded in tension-tension fatigue at a test frequency of 25 Hz and stress ratio, R, of 0.1. Six specimens were tested at each test temperature. Runout was set at 5 000 000 cycles. Maximum test stresses of 80, 70, 60, 50, 40, and 30% of the average yield strength at each temperature, obtained from uniaxial tensile tests carried out here, were used in this round of testing. To minimise costs, one specimen each was used from testing at each of the foregoing maximum test stresses at each temperature. All the fatigue tension-tension test specimens were stress-relieved and annealed at a high temperature prior to testing. Table 3.3 gives a summary of some of the preceding information.

Table 3.3: Summary of the heat treatment regimes, number of specimens and changes of temperature for fatigue tension-tension testing

Material	Heat treatment regimes	Test stress levels	Test temperature changes	Total number of specimens
Ti6Al4V(ELI)	1	6	3	18

3.7. Fractographic Analysis of Test Samples

The JOEL JSM-6610 Series Scanning Electron Microscope, shown in Figure 3.8, was used to analyse the characteristics of failure on the fracture surfaces of the tested specimens to determine the causes of failure. The machine is in the Geology building at the University of the Free State (UFS) in Bloemfontein.

Figure 3.8: Image of a JOEL JSM-6610 SEM

3.8. Metallographic Examination of Test Specimens

Metallographic examination was done on test specimens closer to the fracture surfaces and at distances of 15 mm and 25 mm away from the fracture surface for tensile and fatigue specimens, respectively. An electrical discharge machine (EDM) wire cutter was used to cut one of each set of three specimens loaded with the uniaxial tension at each temperature, and each specimen loaded in fatigue tension-tension along the longitudinal z-build direction. The specimens were then cut in a transverse direction at 15 mm and 25 mm away from the fracture

surface for tensile and fatigue specimens, respectively. Thereafter, the cut samples were mounted in cylinders in Multifast resin using the Struers Mounting Press machine, Citopress-1, type 05776127, shown in Figure 3.9(a). The cut surfaces were ground using a 320-grit size silicon carbide (SiC) grinding paper with water as a lubricant using a Struers tegramin machine, tegramin-20, type 06026127, shown in Figure 3.9(b). This was followed by polishing at three stages to obtain a mirror finish surface. Polishing was carried out on the Struers tegramin machine, using a Largo Diapro cloth with a 9 µm diamond suspension for five minutes, followed by the use of a Mol Diapro cloth for two minutes, and then finally using an MD-Chem cloth with a 4 µm suspension of diamonds for 110 seconds. Kroll's reagent (water 92.82 %, nitric acid 6.11%, and hydrofluoric acid 1.07%) was used to etch the samples to reveal their microstructures. Thereafter, the Carl Zeiss Microscopy GmbH, Axio A1 optical microscope, 3326001120, shown in Figure 3.9(c), was used to examine the microstructures of the etched samples. This equipment is housed in the Materials Laboratory of the Ya Rona building at Central University of Technology, Free State.

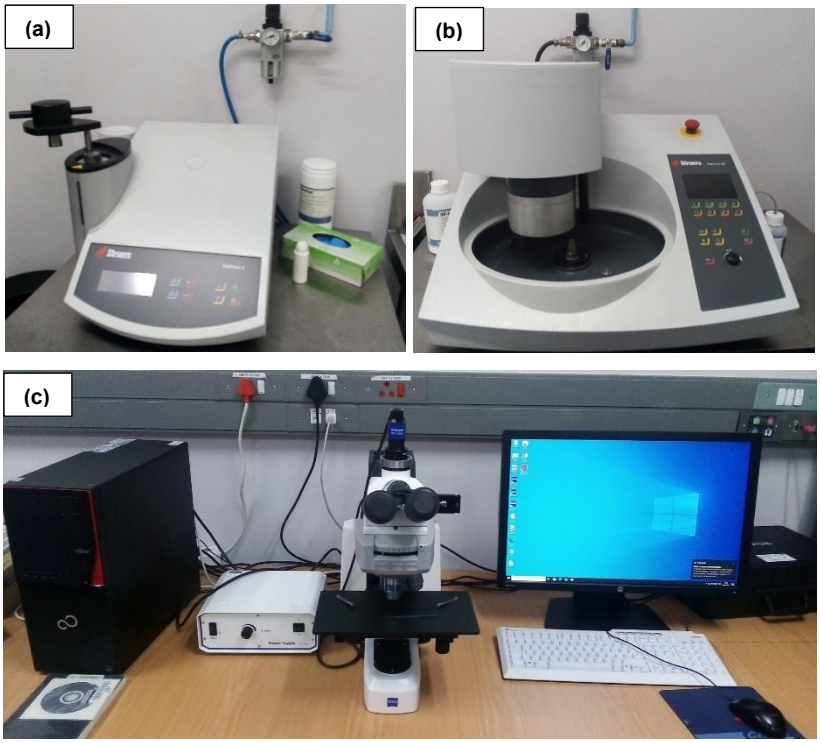

Figure 3.9: Images of (a) a Citopress mounting machine, (b) a Struers tegramin polishing machine, and (c) a Carl Zeiss Axio A1 optical microscope

3.9. Vickers Microhardness Tests

Vickers microhardness tests were performed on a Future Tech FM 7E, FM7639 microhardness testing machine manufactured by Advanced Laboratory Solutions and located in the Materials Laboratory of the Ya Rona building at Central University of Technology, Free State, shown in Figure 3.10. The machine is used to determine the Vickers, Knoop, and Brinell hardness of specimens. The machine uses diamond indenters and a measuring microscope with X400 (lens 40 x ocular 10) magnification. The machine uses standard loads with values of hardness between 98.07–9807 mN, calculated according to SEA (J-417b), ASTM E-140, and JIS, with accuracies according to JIS B-7734 and ASTM E-384 [182].

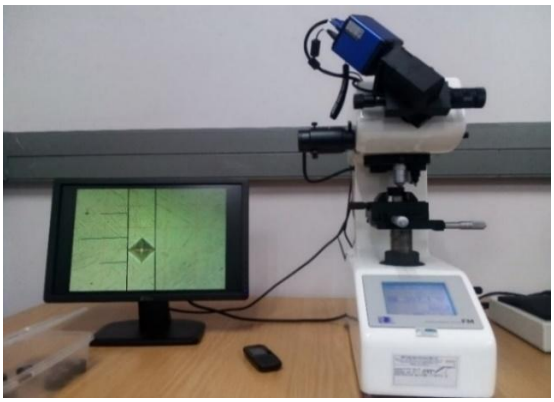

Figure 3.10: Image of a Future Tech FM 7E microhardness testing machine.

The hardness tests were carried out under normal room temperature on the polished and etched surfaces of the selected samples. Ten indentations were made on each sample under the same conditions with a test load of 2942 mN and a dwell time of ten seconds.

3.10. Analysis of Data

The raw data from the tensile tests was converted into a Microsoft Excel file, and the software was used to plot curves and graphs. The values of the tensile strengths, strain, and stiffness that were given by the machine were captured and compared to the values on the plots. Fatigue test data were captured and recorded in a Microsoft Word document. The images captured from the SEM machine were put on Microsoft Word, and the software was used for demonstrations of micrographs.

CHAPTER 4: THE EFFECTS OF TEMPERATURE ON THE MICROSTRUCTURES OF ADDITIVELY MANUFACTURED Ti6Al4V(ELI)

The material contained in this chapter was published in a peer-reviewed journal, as detailed below:

T. D. Moloi, T. C. Dzogbewu, M. Maringa, and A. M. Muiruri, "*The Effect of Temperature on the Microstructures of Additively Manufactured Ti6Al4V(ELI)", Iranian Journal of Materials Science and Engineering*, vol. 21(3), Sept. 2024, http://dx.doi.org/10.22068/ijmse.3589

4.1. Introduction

The stability of microstructure at high temperatures is necessary for many applications. In this chapter, investigations on the effects of changes in temperature on the microstructures of additively manufactured Ti6Al4V(ELI), as a prelude to high-temperature fatigue testing of the material, are presented. The results of these investigations showed that changes in temperature do affect the microstructure of the Ti6Al4V(ELI) alloy. The conclusion was arrived at that changes in temperature will affect the fatigue properties of the alloy.

4.2. Metallographic Examination of Samples Soaked at Different Temperatures

4.2.1. The microstructures of an as-built sample

The optical micrographs of an as-built Ti6Al4V(ELI) sample made by LPBF are displayed in Figure 4.1 in both the top and side views. It should be noted that the build direction is parallel to the side view and orthonormal to the top view, respectively.

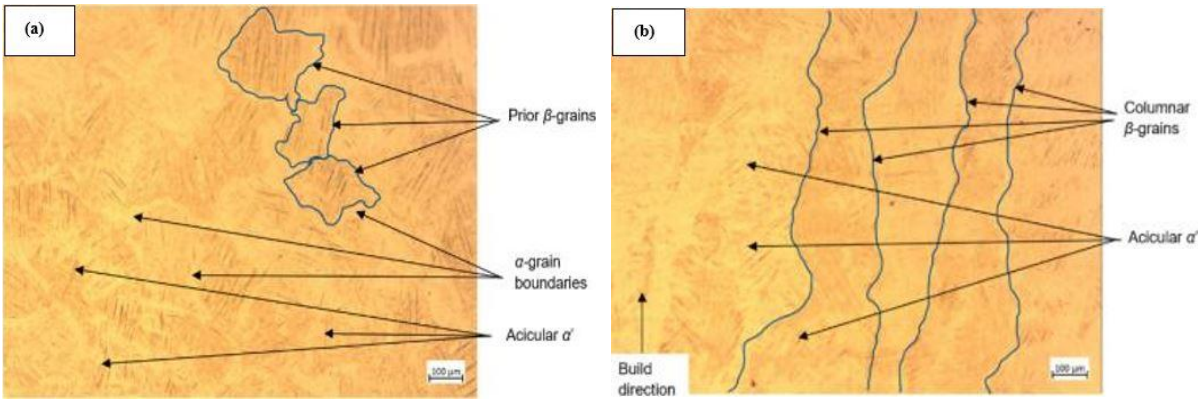

Figure 4.1: Optical micrograph of the (a) top and (b) side view of an as-built LPBF Ti6Al4V(ELI) sample

The two micrographs in this figure display distinct prior β-grain morphologies that are separate from one another. The as-built sample's top view, depicted in Figure 4.1(a), displays needle-like α'-laths with a lighter shade that is known as the α' martensite microstructure. The figure additionally displays epitaxial (columnar) prior β-grains, defined by α-grain boundaries and whose outlines are indicated by blue colour lines superimposed on the micrograph. The sample's side view is displayed in Figure 4.1(b). It is made up of columnar β-grains, the outlines of which are represented by continuous blue colour lines superimposed on the micrograph. These grains developed epitaxially in the build direction and perpendicular to the laser beam's path of travel. [121]. This is mostly because, during the LPBF process, the molten pool's temperature gradient is practically perpendicular to the scanning direction. With a coefficient of variance (CoV) of 11.8%, the columnar β-grains' average width was determined to be 136±16 µm. This moderate CoV suggests moderate dispersion of the data from the mean value. Within these columnar β-grains, α' martensitic laths with a CoV of 16.7% and an average width of 2.4±0.4 µm were observed. A wide dispersion of the data is implied by this high CoV. During the LPBF process, the alloy cools quickly (at rates between 10^4-10^6 *K/s* [183]) from the high-melt temperature of 1660 °C in the β-field, to an acicular α' martensitic microstructure [183]. Agius *et al*. [140] reported that the width of the α'-laths varies from 1–3 µm, whereas Madikizela *et al*. [184] found α'-laths with a width of 0.3–2.4 µm for SLM as-built Ti6Al4V samples. In SLM as-built Ti6Al4V samples, Phutela *et al*. [185] reported an average columnar β-grain width of 90 µm, while Li *et al*. [186] reported an average grain diameter of prior β-grains of 135.5 µm on as-fabricated Ti6Al4V samples. The variations in these values of width probably stem from distinct process parameters employed in the AM procedure of the corresponding specimens.

4.2.2. The microstructures of stress-relieved samples

4.2.2.1. At room temperature, 25 ℃

The optical micrographs of the top and side views of a stress-relieved Ti6Al4V(ELI) sample are displayed in Figure 4.2.

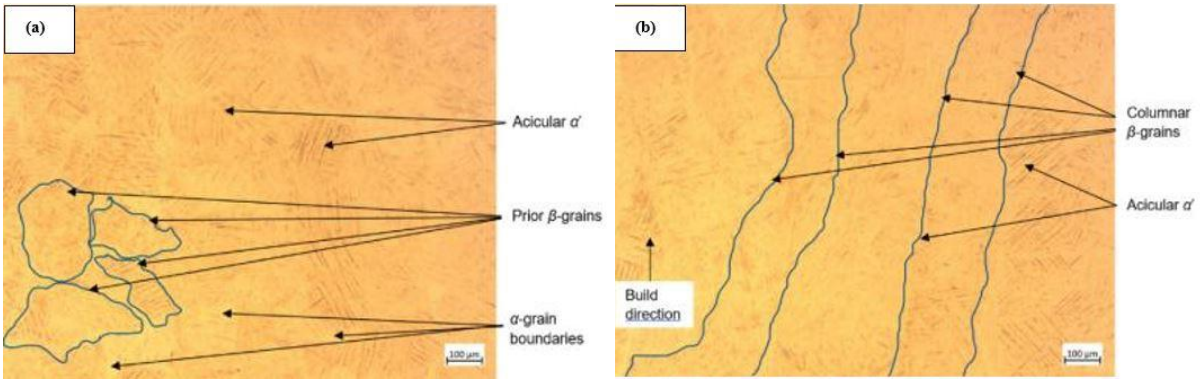

Figure 4.2: Optical micrograph of the (a) top view (perpendicular to the build direction) and (b) side view (parallel to the build direction) of a stress-relieved LPBF Ti6Al4V(ELI) sample

Figure 4.2(a) and Figure 4.2(b) show microstructures similar to those of the as-built samples presented in Figure 4.1(a) and Figure 4.1(b), respectively. The acicular α' laths, which have an average width of roughly 2.6±0.47 µm, are still apparent in Figure 4.2(a). These statistical measures have a CoV of 18.1%, indicating a wide scatter of data. The mean and standard deviations have increased by 8 and 17%, respectively, from the as-built samples shown in Figure 4.2(a). Figure 4.2(b) shows columnar β-grains, which were also evident in the side view of the as-built samples. Acicular α' laths were found within these columnar β-grains, suggesting that no noticeable microstructure transformation took place during stress-relieving heat treatment, as observed under an optical microscope. The average width of the columnar β-grains in Figure 4.2(b) was measured to be 142±17 µm, giving rise to a CoV of 11.9%. Jazdzewska *et al*. [187] reported that stress-relieving only lessens residual stresses; it has no effect on the mechanical characteristics of titanium alloys, such as strength or ductility. This aligns with the finding here that stress-relieving heat treatment did not cause any microstructure variation.

4.2.2.2. *Soaked at a temperature of 133 ℃*

The optical micrographs of the top and side views of stress-relieved Ti6Al4V(ELI) samples, which were soaked for three hours at 133 ℃ and then allowed to cool gradually in the air, are displayed in Figure 4.3.

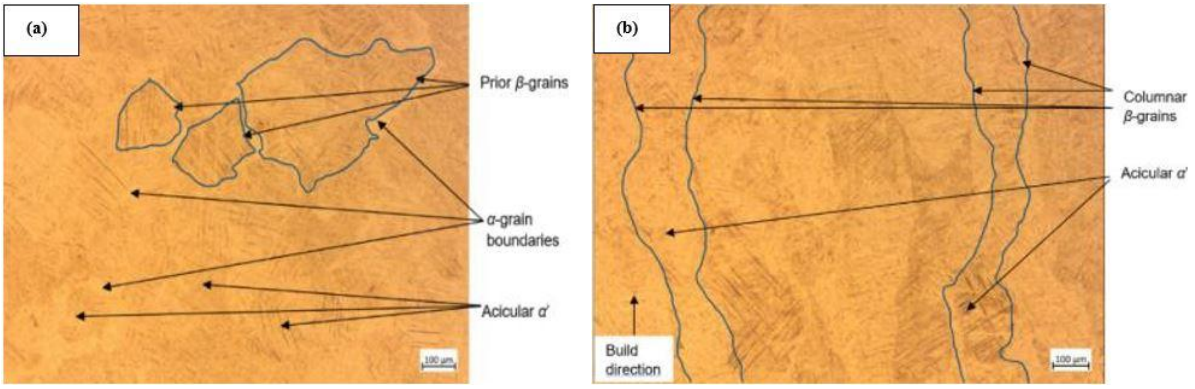

Figure 4.3: Optical micrograph of the (a) top view (perpendicular to the build direction) and (b) side view (parallel to the build direction) of a LPBF Ti6Al4V(ELI) sample stress-relieved and then soaked at 133 ℃ for three hours.

Figure 4.3(a) shows a microstructural morphology that is comparable to Figures 4.1(a) and 4.2(a). The needle-like α' martensite laths in Figure 4.3(a) have an average width of 2.64±0.55 µm and a CoV of 20.8%. This high CoV suggests a broad distribution of data. The as-built samples shown in Figure 4.1(a) have mean and standard deviations that are 0.24 and 0.15 higher than those of Figure 4.2(a), respectively, an increase of 10% and 38%. This suggests that between this case and the one for Figure 4.2(a), there has been a slight increase in the size of α-laths and a notable increase in the size of the grains and scatter of the data. The prior β-grains are displayed in Figure 4.3(a), whose outlines are shown in blue colour lines and are separated by α-grain boundaries. The columnar β-grains in this figure contain α' martensitic laths, just like in Figure 4.2(b). In this instance, the average width of the columnar β-grains' is approximately 144±16 µm, resulting in a CoV of 11.1%. This represents an additional rise over the values of 142±17 µm and 136±16 µm noted for the stress-relieved and as-built specimens, respectively. The increase in the average width of the epitaxial grains here from the case for stress-relieved specimens is slightly (1%) over stress-relieved, noting the large increase from the as-built to stress-relieved samples of 4%. The former increase is attributed to soaking at 133 ℃ after stress-relieving. It is right to conclude that this soaking temperature is too low to

have a significant effect on the microstructure of the alloy, as was observed in the separate studies done by Zhao *et al*. [68] and Song *et al*. [188].

4.2.2.3. Soaked at a temperature of 241 °C

The optical micrographs of the top and side views of stress-relieved LPBF Ti6Al4V(ELI) samples that were soaked at 241 °C for three hours and then allowed to cool gradually in the air are displayed in Figure 4.4.

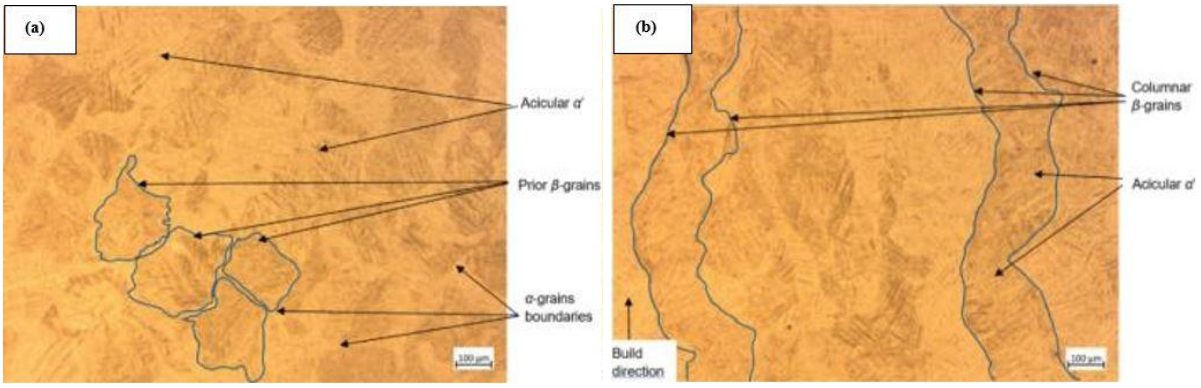

Figure 4.4: Optical micrograph of the (a) top view (perpendicular to the build direction) and (b) side view (parallel to the build direction) of a LPBF Ti6Al4V(ELI) stress-relieved sample, soaked at a temperature of 241 °C for three hours

The micrograph in Figure 4.4(a) clearly displays prior β-grains, which are separated by α-grain boundaries and displayed as blue colour lines. These grains contain the acicular α' martensitic microstructure. The average width of the α' laths is 2.9±0.6 µm, which has a CoV of 20.7%. This high percentage implies a high dispersion away from the mean value. When compared to the value derived from Figure 4.3(a), it is observed that the average width of the α' laths has increased from 2.64 to 2.9 µm. This is a slight rise of roughly 1%, which is insignificant because it is contained within the standard deviations of the two mean values. The columnar β-grains depicted in Figure 4.4(b) are outlined by continuous blue lines that contain α' martensite grains. The columnar prior β-grains have an average thickness of approximately 147±26 µm, resulting in a CoV of 17.7%. This high value suggests that the data was widely dispersed. Compared to Figure 4.3(a), the morphology in the above figure demonstrates a predominance of grains that are slightly darker. This is probably because of the higher soaking temperature, which led to a rise in the β-lath content and is consistent with the work of Shaikh *et al*. [24] who found that when the soaking temperature rose, the content of β-laths increased.

4.2.2.4. *Soaked at a temperature of 349 °C*

The optical micrographs of the top and side views of stress-relieved Ti6Al4V(ELI) samples, which were soaked for three hours at 349 °C and then cooled gradually in the air, are displayed in Figure 4.5.

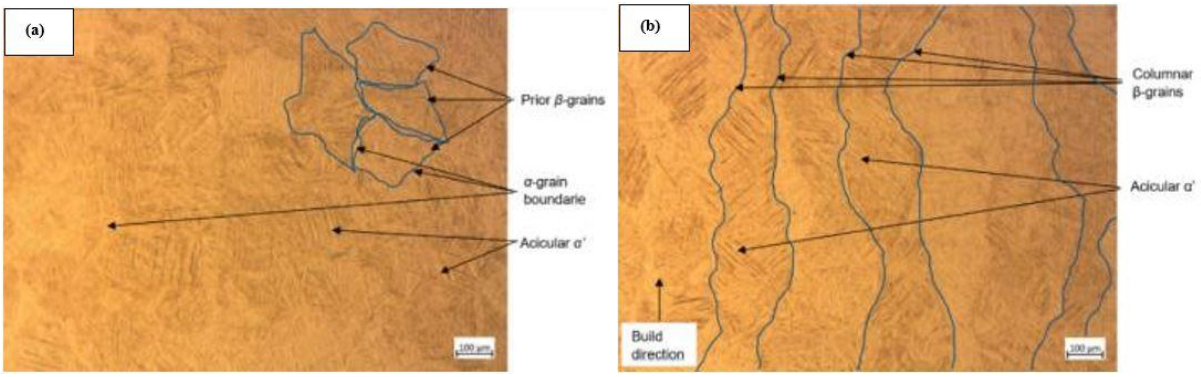

Figure 4.5: Optical micrograph of the (a) top view (perpendicular to the build direction) and (b) side view (parallel to the build direction) of a stress-relieved LPBF Ti6Al4V(ELI) sample soaked at a temperature of 349 °C for three hours.

Figure 4.5 depicts microstructure morphologies that are comparable to those seen in Figure 4.4. Prior β-grains with α' martensite laths inside are depicted in Figure 4.5(a). The prior β-grains in this figure have martensitic α' laths that measure 3.1±1.2 µm in width. This results in a very high CoV of 38.7%. The width of the α' laths has increased by 0.2 µm, or 7%, from the value of 2.9 µm recorded in Figure 4.4(a). According to Agius *et al.* [140], as-built samples have acicular α′ laths that range in width from 1 to 3 µm. These results show slightly higher values for the width of the α' martensitic laths, which can be attributed to the higher soaking temperature. The width of the columnar prior *β*-grains measured in Figure 4.5(b) is about 137±25 µm, with a CoV of 18.2%. Such a high percentage suggests a high dispersal of data.

4.2.3. The microstructures of stress-relieved followed by high-temperature annealing samples

4.2.3.1. *At room temperature, 25 °C*

The optical micrographs of stress-relieved followed by high-temperature-annealed Ti6Al4V(ELI) samples are displayed in Figure 4.6 in both top and side views.

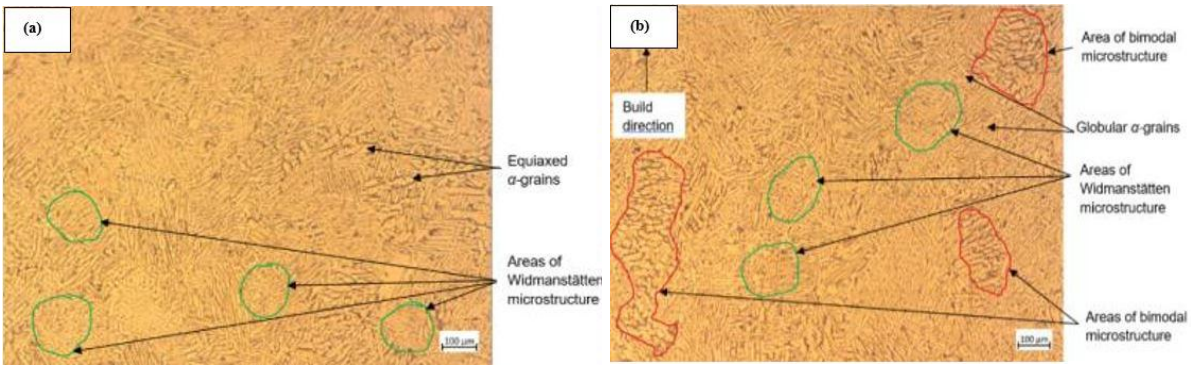

Figure 4.6: Optical micrograph of the (a) top view (perpendicular to the build direction) and (b) side view (parallel to the build direction) of a sample stress-relieved and then high-temperature annealed LPBF Ti6Al4V(ELI)

The microstructural morphologies depicted in Figure 4.6 are entirely different from those in Figures 4.1 to 4.5. The high-temperature annealing added to the heat treatment process imposed on the specimens is thought to be the cause of this difference in microstructure. The acicular α' martensitic needles are not present in Figure 4.6(a), and in their place are longer and wider globular α-laths. When the temperature rises to a certain point, the thermal energy of atoms increases, causing them to move around and overcome the grain boundaries' surface energy, the result of the growth of grains and concurrent movement of grain boundaries. Applying higher temperatures to Ti6Al4V(ELI) causes the grains to move more freely, which coarsens the α-laths [21], [76]. A combination of equiaxed and lamellar α-laths is shown in Figure 4.6(a). Both the micrographs in Figure 4.6 feature the Widmanstätten microstructure, that is shown inside the boundaries of green coloured circles on the micrographs. Globular α-laths are also evident in the micrograph. A portion of the micrographs in Figure 4.6(b) display bimodal microstructures, some of which are depicted inside red contour lines. An average width of 8.2±1.2 µm is recorded in this micrograph for the α-laths, with a CoV of 14.6%. The average width of the β-laths is measured at 1.2±0.25 µm, with a CoV of 20.8%. Such high CoVs imply a large scatter of data. Malefane *et al.* [31] observed equiaxed and basket-weave microstructures on LPBF Ti6Al4V samples annealed at high temperature. It was further reported in their research that the average width of the α-laths built in the y-direction was 6.7 µm. The discrepancy in the findings between this investigation and that of Malefane *et al.* [157] is probably the result of differences in the annealing processes used. In the present study, annealing was done at 980 °C, with soaking for one hour, followed by very rapid cooling to a temperature of 705 °C, and then soaking there for two hours, followed by cooling at 0.03 °C/s

to room temperature. In their [157] study, the annealing was done at a temperature of 950 °C, followed by soaking at this temperature for two hours and subsequent cooling at 0.13 °C/s to room temperature. The higher initial soaking temperature and slower eventual cooling rate are likely causes of the coarser α-laths obtained in the present study. Zöllner [21] stated that higher temperatures lead to even coarser α-laths. Jovanovic *et al*. [32] reported that the thickness of α-laths increases as the annealing temperature increases. They found the average thickness of α-laths to be 9 µm, 7 µm and 6 µm at soaking temperatures of 1 100 °C, 950 °C, and 800 °C, respectively.

4.2.3.2. Soaked at a temperature of 133 °C

The top and side view optical micrographs of LPBF Ti6Al4V(ELI) samples that were stress relieved and then high-temperature annealed, followed by soaking at a temperature of 133 °C for three hours and finally, gradual cooling in air, are displayed in Figure 4.7.

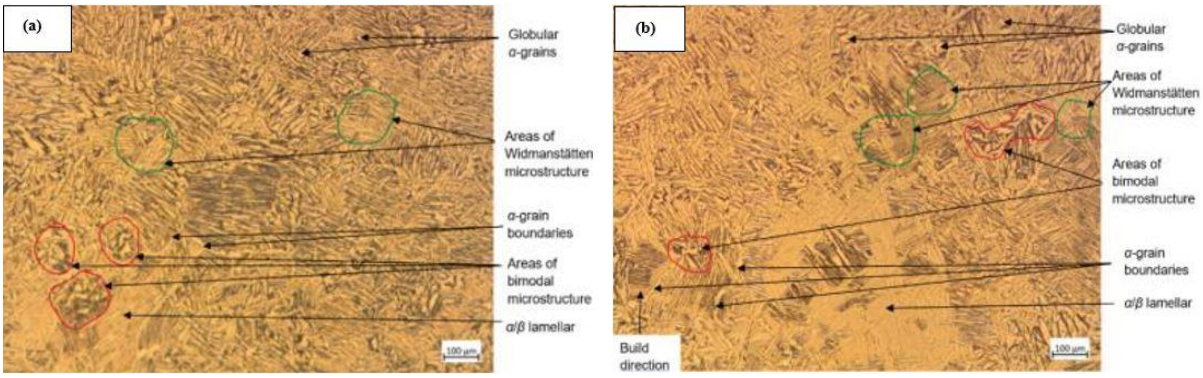

Figure 4.7: Optical micrograph of the top view (perpendicular to the build direction) of a stress-relieved, high-temperature annealed and then soaked at 133 °C LPBF Ti6Al4V(ELI) sample

The α- and β-phases can be clearly seen in Figure 4.7, in which the arrows point to the brighter α-laths and the darker β-laths. These two figures show globular α-laths, lamellar, bimodal, and Widmanstätten microstructures. The micrographs display green and red coloured lines surrounding the Widmanstätten and bimodal microstructures, respectively. It is observed that a Widmanstätten microstructure dominates the micrograph in Figure 4.7(b). Among the various Ti6Al4V microstructures, this one is recognised to have the lowest strength [139]. The average width of α-laths in these two micrographs is 8.3±1.4 µm, with a CoV of 16.9%. When comparing the average width of α-laths for the case of stress-relieving followed by high-

temperature annealing at the two soaking temperatures of 25 ℃ and 133 ℃ in Figures 4.6(a) and 4.6(b), respectively, the average values in the latter figure show an increase to 8.3 µm from 8.2 µm in the former figure. There is a negligible 1% increase, suggesting that the soaking temperature of 133 ℃ did not affect the width of α-laths significantly. Additionally, the two means are within each other's standard deviation. The average width of β-laths at a soaking temperature of 133 ℃ was determined to be 1.8±0.45 µm, with a CoV of 25%. This high percentage implies a wide distribution of data from the mean value. It is observed that, in comparison to the equivalent value derived from Figure 4.6(b), the mean width for β-laths has increased from 1.2 µm in this figure to 1.8 µm in Figure 4.7(b). This indicates a significant impact of soaking at 133 °C on the growth of β-laths, which is 50% greater than the increase that was observed for the α-laths. This increase in the width of β-laths is thought to be because of an increase in the mobility of atoms due to the higher soaking temperature and is anticipated to give rise to improved ductility of the alloy [189].

4.2.3.3. Soaked at a temperature of 241 ℃

The optical micrographs of the top and side views of the stress-relieved, followed by high-temperature-annealed Ti6Al4V(ELI) samples are displayed in Figure 4.8. The samples underwent three hours of soaking at 241 °C before being cooled gradually in the air.

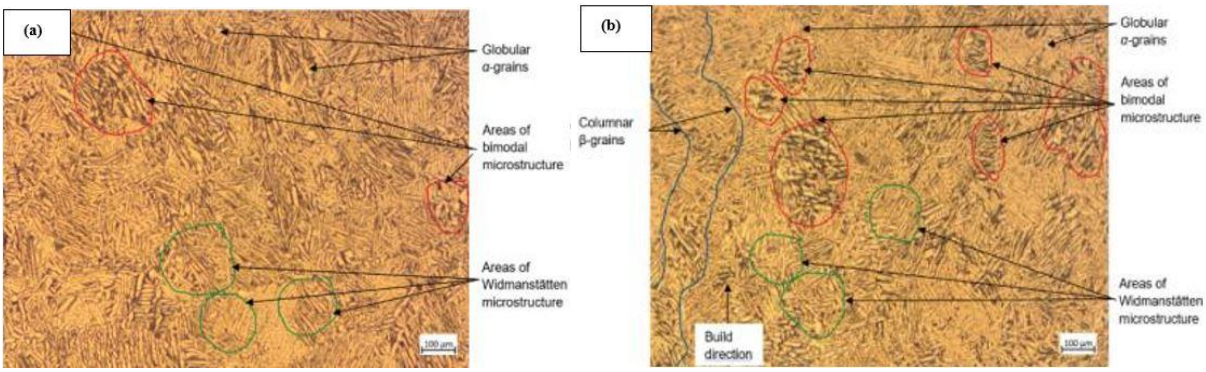

Figure 4.8: Optical micrograph of the (a) top view (perpendicular to the build direction) and (b) side view (parallel to the build direction) of a sample soaked at 241 ℃ for three hours after stress-relieving followed by high-temperature annealing

The α-laths are brighter, and the β-laths are darker in Figure 4.8. The two figures display globular α-laths, as well as areas of Widmanstätten and bimodal microstructures. Green and red coloured lines have been used in the figure to encircle the Widmanstätten and bimodal

microstructures, respectively. Figure 4.8(b) illustrates a columnar β-grain with colonies of α-and β-laths within, identified by blue lines. The bimodal microstructure in Ti6Al4V is known to have greater ductility than the other microstructure of the alloy [37, 75]. The average width of the β-laths measured 1.9±0.7 µm, while the measured average width of the α-laths was determined as 8.3±2.3 µm. The CoVs for the width of the β-laths and α-laths were calculated as 36.8% and 27.7%, respectively. Such high percentages imply a high dispersal of data. It is noted that the width of β-laths had increased by 0.1 µm from the value of 1.8 µm measured in Figure 7.7(b) for the lower soaking temperature of 133 °C, an increase of 6%.

4.2.3.4. Soaked at a temperature of 349 °C

The optical micrographs of the top and side views of the stress-relieved and then high-temperature annealed Ti6Al4V(ELI) samples are displayed in Figure 4.9. The samples were soaked for three hours at a temperature of 349 °C before being cooled in the air.

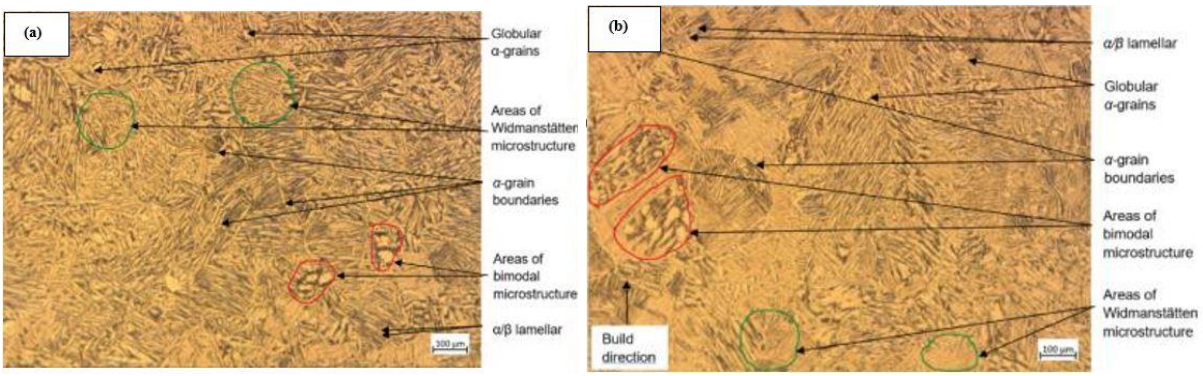

Figure 4.9: Optical micrograph of the (a) top view (perpendicular to the build direction) and (b) side view (parallel to the build direction) of LPBF Ti6Al4V(ELI) samples that were stress-relieved and then annealed at high temperature followed by soaking at 349 °C for three hours

The micrographs in Figure 4.9 demonstrate an additional increase in darker areas in comparison to Figure 4.8 following a three-hour soaking at 349 °C. The alloy's transformation phase diagram suggests a higher content of β-laths, which could be the cause of this rise in the darker areas. Areas of the α- and β-phases are stacked parallel to one another in the micrographs, forming a lamellar microstructure. The green coloured circles in the figure indicate the outlines of the Widmanstätten microstructure. Areas with globular α-grain have been identified with arrows. Bimodal microstructure is visible in both micrographs and their outlines have been

identified by red circles. It is well known that the bimodal microstructure demonstrates balanced strength and ductility [190]. The α-lath's average width was determined to be 8.9±1.9 µm, with a CoV of 21.3%. For the β-laths, an average width of 2.4±0.3 µm was determined, with a CoV of 12.5%. High percentages like the first one imply that the data was dispersed away from the mean. It is observed that there was a 28% increase in the mean width of the β-lath, from 1.9 µm in Figure 4.8(a) to 0.5 µm in Figure 4.9(a). Shaikh *et al*. [24] observed a similar trend, as the soaking temperature increased. According to Xing *et al*. [191], the width of the β-lath increases with an increase in the temperature of the powder bed.

A summary of the observations made in Figure 4.1 to Figure 4.9 is depicted in Figure 4.10. The symbol SR and HTA denote stress-relieved and high-temperature annealed, respectively.

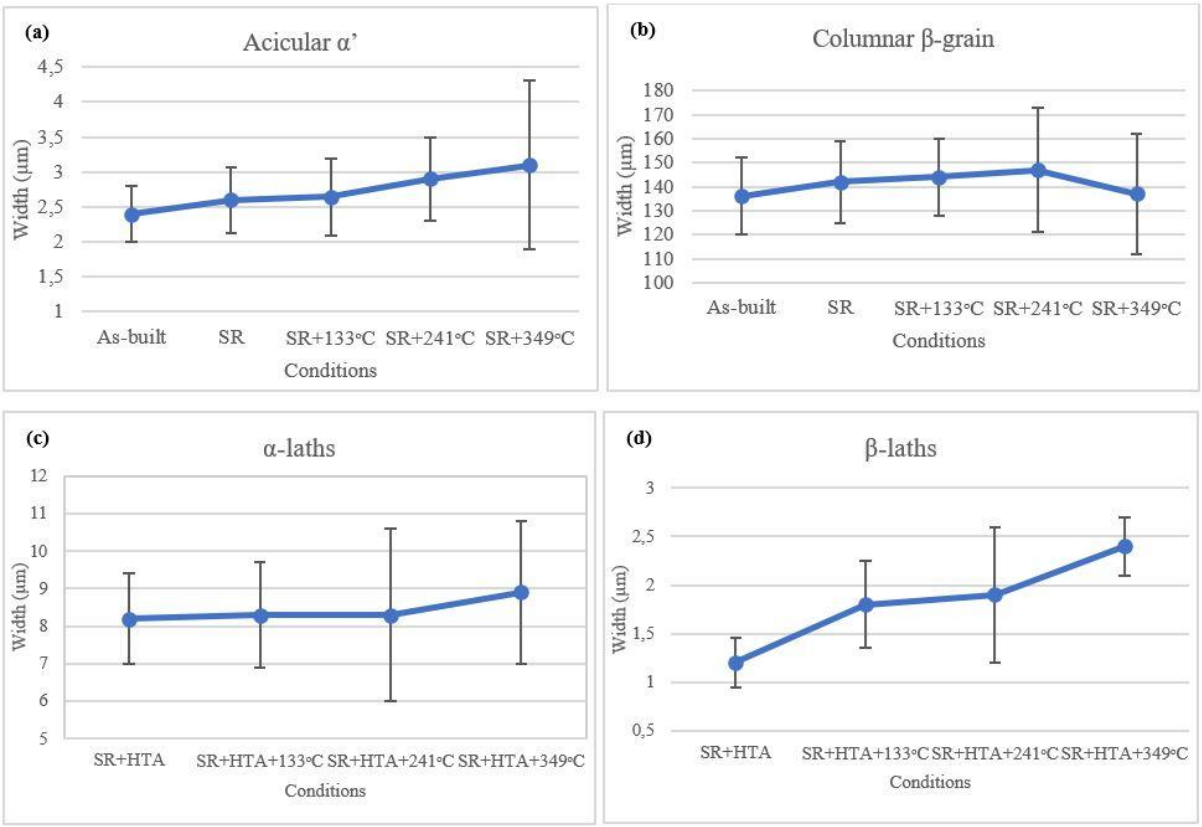

Figure 4.10: The average width of the (a) acicular α' laths, (b) columnar β-grains, (c) α-laths and (d) β-laths

Figure 4.10(a) illustrates how the widths of α' laths increased continuously in tandem with the soaking temperature, rising from room temperature to 349 °C. The width of the columnar prior β-grains increased continuously with the soaking temperature from room temperature to 241 °C, as seen in Figure 4.10(b). However, there was a subsequent decrease in the width as

the temperature increased further to 349 °C. The width of the α- and β-laths increased continuously with an increase in soaking temperature, as demonstrated by Figures 4.10(c) and 4.10(d). This corresponds partly with the study done by Zöllner [21], who reported that higher temperatures result in coarser α-laths. The measured mean values in the aforementioned figures, however, fall within the error bars in all but a few cases, suggesting that the differences seen in the graphs are not statistically significant. So, it is right to conclude that soaking temperatures below 350 ℃ have little to no effect on the microstructures of the Ti6Al4V(ELI) alloy.

4.3. Conclusions

This chapter aimed to investigate the effect of temperature on the microstructure of the Ti6Al4V(ELI) alloy. The following conclusions were derived from the study.

- Stress-relieving heat treatment did not change the original microstructure of acicular α' laths existing within columnar β-grain.
- High-temperature annealing heat treatment significantly influenced the microstructure of Ti6Al4V(ELI), as the α' laths were replaced by α- and β-laths.
- As the soaking temperature was increased from 20 ℃ up to 349 ℃, the width of the α' laths, α-laths, and β-laths were observed to increase slightly. However, the increases were small and fell within the error bars of the plotted graphs.

CHAPTER 5: QUASI-STATIC TENSILE PROPERTIES OF DMLS TI6AL4V(ELI) SPECIMENS EXPOSED TO DIFFERENT HEAT TREATMENT PROCESSES AND TESTED AT DIFFERENT ELEVATED TEMPERATURES

The material contained in this chapter was published in a peer-reviewed journal as detailed below:

T. Moloi, T.C. Dzogbewu, M. Maringa, and A. Muiruri, "*Quasi-static tensile properties of DMLS TI6AL4V(ELI) specimens exposed to two different heat treatment processes and tested at different elevated temperatures*", Results in Engineering, vol. 22, p. 102290, Jun. 2024, https://doi.org/10.1016/j.rineng.2024.102290

5.1. Introduction

The aerospace industry has, in recent years, seen a continued increase in the use of Ti6Al4V components [192]. When in use, Ti6Al4V jet engine components, such as compressor blades, exhaust ducts, and hydraulic systems, as well as landing gear and numerous airframe parts, are subjected to a variety of temperatures, which may have an impact on their mechanical characteristics. Thus, figuring out how stable they are at various temperatures is crucial. Uniaxial tensile tests were conducted at various test temperatures up to fracture. The properties of the fracture surfaces were then investigated using fractography. The findings of this work demonstrated that the microstructure and mechanical characteristics of the alloy are significantly impacted by temperatures ranging from 175 to 325 °C. Here, the specimens that were only stress-relieved are taken as "specimen group A", and specimens that underwent both stress-relief followed by high-temperature annealing are taken as "specimen group B".

5.2. Tensile Properties

5.2.1. Tensile properties of specimen in group A

Tensile test results for stress-relieved LPBF Ti6Al4V(ELI) specimens that were tested at various temperatures are presented in Table 5.1.

Table 5.1: Tensile Properties of Specimens in Group A

Temperature °C	Specimen number	Ultimate tensile strength (MPa)	Yield strength (0.2 % offset) (MPa)	Modulus of elasticity (GPa)	Percentage elongation (%)
20	SR1	1271.2	1218.7	124.1	6.0
	SR2	1317.0	1280.6	127.4	4.7
	SR3	1344.8	1300.7	120.0	7.0
	Average	**1311**	**1266.7**	**123.8**	**5.9**
	Standard deviation	52	5.2	60.4	1.6
	Coefficient of variations (%)	4.0	4.2	4.8	27.1
175	SR4	1097.2	1042.4	116.7	7.7
	SR5	1103.0	1044.7	117.6	8.1
	SR6	1019.4	938.8	116.3	7.5
	Average	**1073.2**	**1008.6**	**116.9**	**7.8**
	Standard deviation	66	85.5	0.9	0.4
	Coefficient of variations (%)	6.1	8.4	0.8	5.1
325	SR7	988.9	898.9	103.5	8.7
	SR8	997.6	928.7	108.3	12.8
	SR9	-	-	-	-
	Average	**993.3**	**913.8**	**105.9**	**10.8**
	Standard deviation	6.2	21.1	3.4	2.9
	Coefficient of variations (%)	0.6	2.3	3.2	26.9

It is clear from Table 5.1 that while ductility increases with temperature, the ultimate tensile strength, yield strength, and modulus of elasticity decrease. Similar findings were observed in the independent investigations reported in references [10, 25, 26]. In these works, the authors discovered that the tensile strength of the Ti6Al4V(ELI) tensile test specimens decreased while their ductility increased as the test temperature rose. From 20 ℃ to 325 ℃, the average values of yield strength, tensile strength, and modulus of elasticity in the present work reduced by 27.9%, 24.2%, and 14.5%, respectively, while ductility increased by 83.1%. In work carried out elsewhere at 20 ℃, values of yield strength, tensile strength, and percentage elongation of 1 110 MPa, 1 267 MPa, and 7.28%, respectively, for stress-relieved LPBF Ti6Al4V specimens were recorded [169], and separately values of ultimate tensile strength and percentage elongation of 1 155 MPa and 4.1%, respectively, for the stress relieved LPBF Ti6Al4V specimens [35]. This compares with the average values obtained in the present work at 20 ℃ of 1 267 MPa, 1 311 MPa and 5.9%. In the present study. the specimens were loaded at a rate of 2 mm/min, while in references [35] and [169] the specimens were loaded at a rate of 1 mm/min. The difference between the two sets of results is likely due to the higher loading rate

used in the present work, as higher rates of loading lead to strain hardening with the attendant increase in yield strength, ultimate tensile strength and reduction of the percentage elongation. The low values of CoV for the ultimate tensile strength, yield strength and stiffness point to a clustering of data around the respective mean values in each case, while the large CoV of 27.1% for the percentage elongation denotes a large dispersal from the mean. This latter value reduces the statistical value of the calculated mean for percentage elongation.

Figure 5.1 shows a bar diagram of the tensile mechanical properties of stress-relieved specimens tested at various test temperatures.

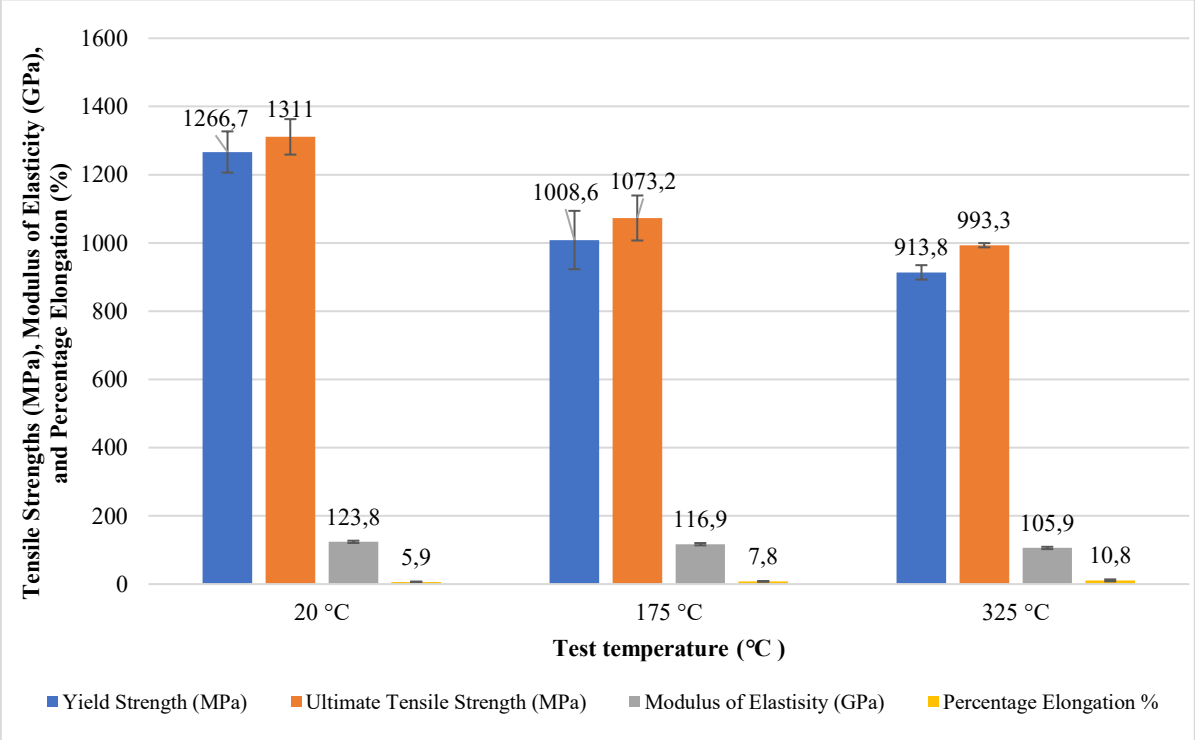

Figure 5.1: Tensile mechanical properties of specimens in group A tested at different test temperatures

As the test temperature was increased, Figure 5.1 illustrates how the average values of ultimate tensile strength, yield strength, and modulus of elasticity decreased while the average values of ductility increased.

The stress-strain curves of the stress-relieved specimens tested at different test temperatures are shown in Figure 5.2.

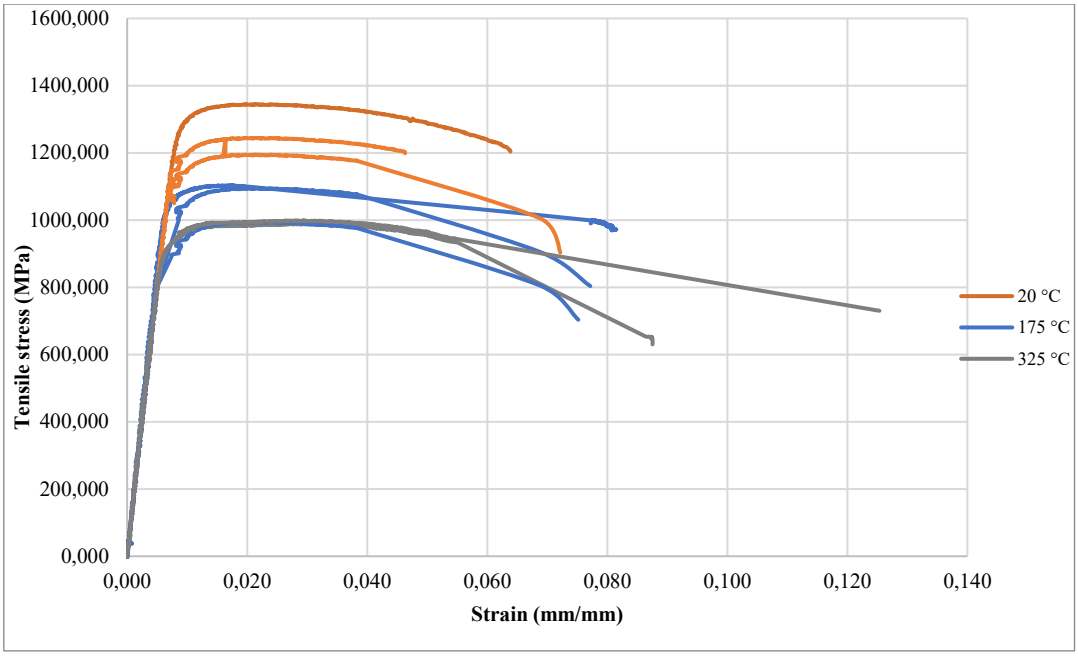

Figure 5.2: Stress-strain curves for specimens in group A that were tested at different temperatures

It is clear from the curves in Figure 5.2 that the specimens tested at a temperature of 20 °C had the highest values of yield stress and ultimate tensile stress but had smaller strains of failure than those tested at temperatures of 175 °C and 325 °C. The curves in the figure clearly show that yield strength and ultimate tensile decreased and elongation to failure increased as the test temperature increased. It was reported in reference [193], for the Ti6Al4V samples, the values of ultimate tensile stress for specimens tested at temperatures of 25 °C and 600 °C were 1 842 MPa and 808 MPa, respectively, both of which are seen to be higher than the values shown in Table 5.1. Since the test was not done at 600 °C in the present work, the estimated value of ultimate tensile strength at 600 °C is 538 MPa. This difference is because of the high strain rate of 12 000 s^{-1} used in the work in reference [193].

5.2.2. Tensile properties of specimen in group B

The results of the tensile testing of LPBF Ti6Al4V(ELI) specimens that were first stress-relieved and then high-temperature annealed at various temperatures are presented in Table 5.2.

Table 5.2: Tensile Properties of Specimen in Group B

Temperature °C	Specimen number	Yield strength (0.2 % offset) (MPa)	Ultimate tensile strength (MPa)	Modulus of elasticity (GPa)	Percentage elongation (%)
20	SR+HTA1	847.5	911.5	112.8	14.3
	SR+HTA2	930.5	994.9	96.3	14.9
	SR+HTA3	887.2	954.8	89.4	12.1
	Average	**888.4**	**953.7**	**99.5**	**13.8**
	Standard deviation	33.9	59	17	2.1
	Coefficient of variations (%)	3.8	6.2	17.1	15.2
175	SR+HTA4	669.5	697.7	102.4	15.1
	SR+HTA5	643.0	718.6	84.2	13.0
	SR+HTA6	479.0	608.1	88.5	13.5
	Average	**597.2**	**674.8**	**91.7**	**13.9**
	Standard deviation	84.3	83	13.5	1.6
	Coefficient of variations (%)	14.1	12.3	14.7	11.5
325	SR+HTA7	520.7	650.1	84.1	14.0
	SR+HTA8	567.9	659.6	82.5	20.6
	SR+HTA9	-	-	-	-
	Average	**544.3**	**654.9**	**83.3**	**17.3**
	Standard deviation	33.4	6.7	1.1	4.6
	Coefficient of variations (%)	6.1	10.2	13.2	26.6

The data in Table 5.2 shows that increasing the testing temperature from 20 ℃ to 175 ℃ and 325 ℃ led to a reduction of yield strength, ultimate tensile strength, modulus of elasticity, and an increase of ductility. The reductions at test temperatures of 175 ℃ and 325 ℃ were 32.8% and 38.7% in yield strength, 29.2% and 31.3% in ultimate tensile strength, and 7.8% and 16.3 % in modulus of elasticity, respectively. The increase in ductility at test temperatures of 175 ℃ and 325 ℃ were 0.7% and 25.4%, respectively. Zöllner [21] observed that as temperatures rose, α-laths became coarser, and their tensile strength decreased. This is because grains get bigger at higher temperatures, which implies a decrease in material strength according to the Hall-Petch relationship. This is accompanied by an increase in ductility [194, 195]. The reliability of the mean values that were calculated in this table is hampered by the predominantly high values of CoV, which indicates that the associated data points were widely scattered away from the calculated values of the mean.

A bar diagram of the tensile mechanical properties of the specimens in group B at different test

temperatures is presented in Figure 5.3.

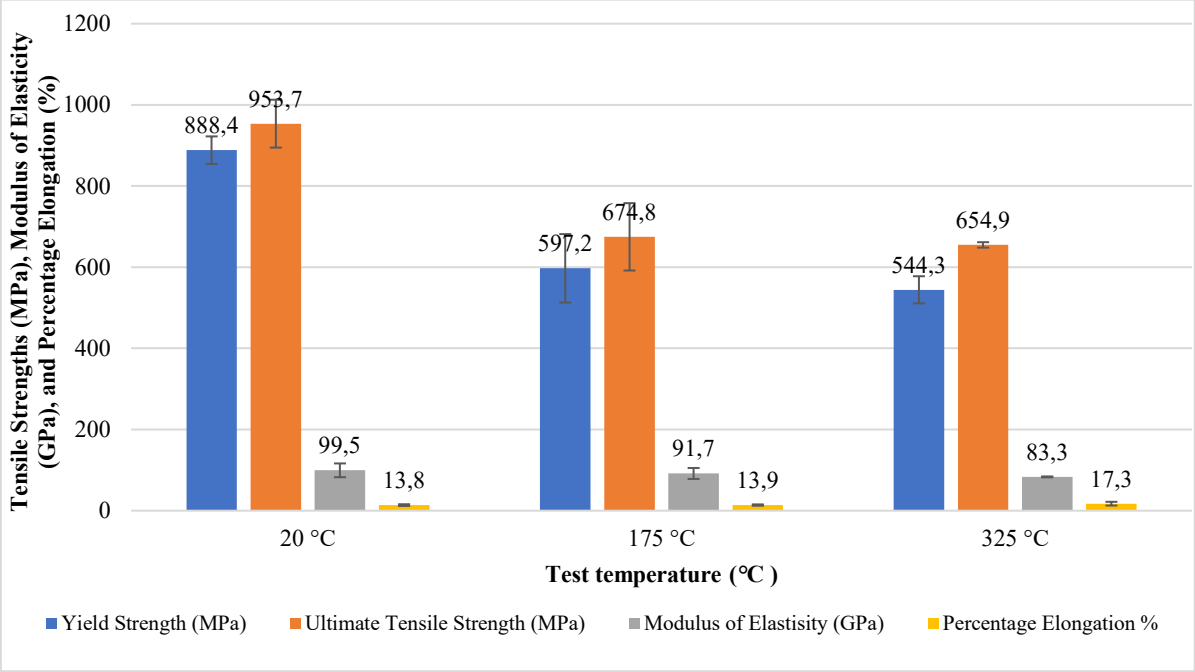

Figure 5.3: Tensile mechanical properties of the specimens in group B at different test temperatures

The bar charts in Figure 5.3 indicate a decrease in the average values of ultimate tensile strength, yield strength, and modulus of elasticity and an increase in the average values of ductility with increasing test temperatures.

Figure 5.4 displays the stress-strain curves of specimens in group B that were tested at various temperatures.

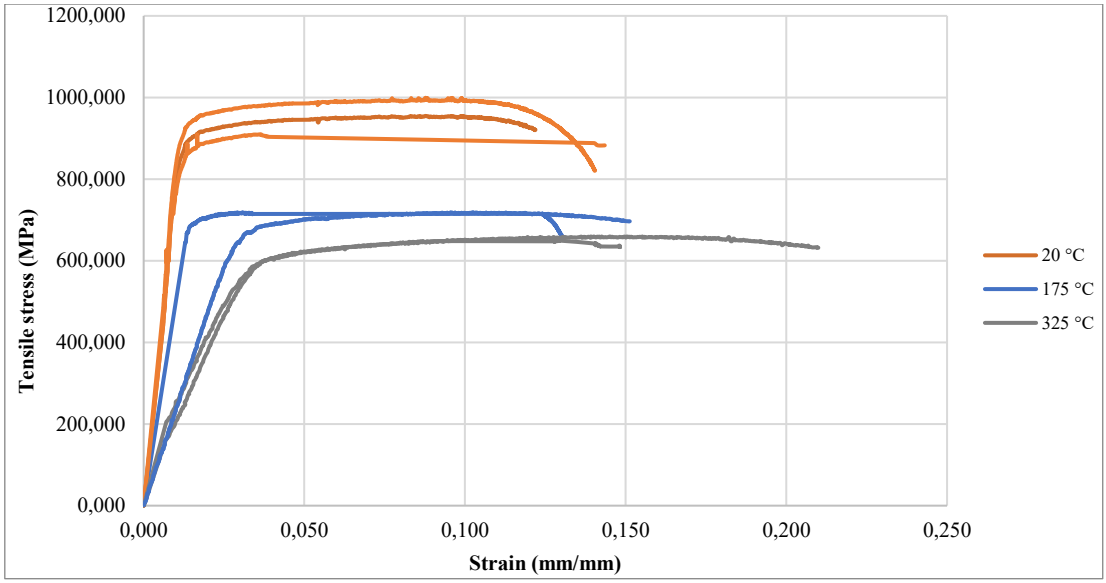

Figure 5.4: Stress-strain curves of specimens in group B that were tested at different temperatures

The curve in Figure 5.4 demonstrates the decrease of yield strength, ultimate tensile strength and stiffness and the attendant increase of percentage elongation with increasing test temperature. High-temperature annealing heat treatment has a major impact on the curves because all the stress-relieved specimen curves shown in Figure 5.2 fall at or below 1 000 MPa, a value that was reached and, in some cases, exceeds the yield stress prior to the onset of non-uniform deformation.

5.2.3. Comparison of the tensile properties of specimens in group A to those in group B

Figure 5.5 displays the average curves of each of the mechanical properties for the specimens in groups A and B that were tested at various temperatures.

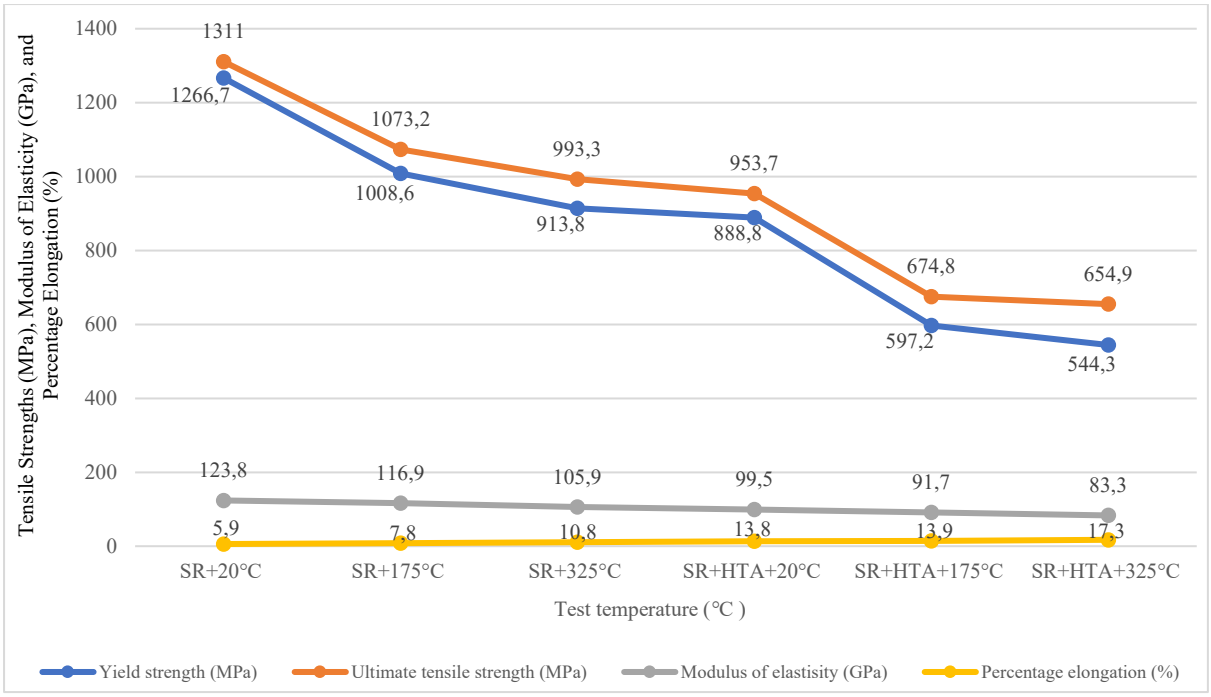

Figure 5.5: Average curves of each of the mechanical properties for the specimens in groups A and B that were tested at different temperatures

Figure 5.5 shows that when the test temperature was raised from 20 °C to 325 °C, both specimen groups, A and B, demonstrated increased ductility and decreased yield strength, tensile strength, and modulus of elasticity. For specimens in groups A and B, at these two temperatures, the values of yield strength decreased by 27.9% and 38.7%, ultimate tensile strength decreased by 24.2% and 31.3%, and modulus of elasticity decreased by 14.5% and 16.2%. In contrast, ductility increased by 83.1% and 25.4%, respectively. Thus, except for ductility, where a greater increment was measured in specimens from group A, the test temperature had a greater impact on specimens from group B than from group A. This may be because of an error in the results for ductility.

Figure 5.6 displays the stress-strain curves of three specimens from groups A and B, each of which underwent testing at a temperature of 20 °C.

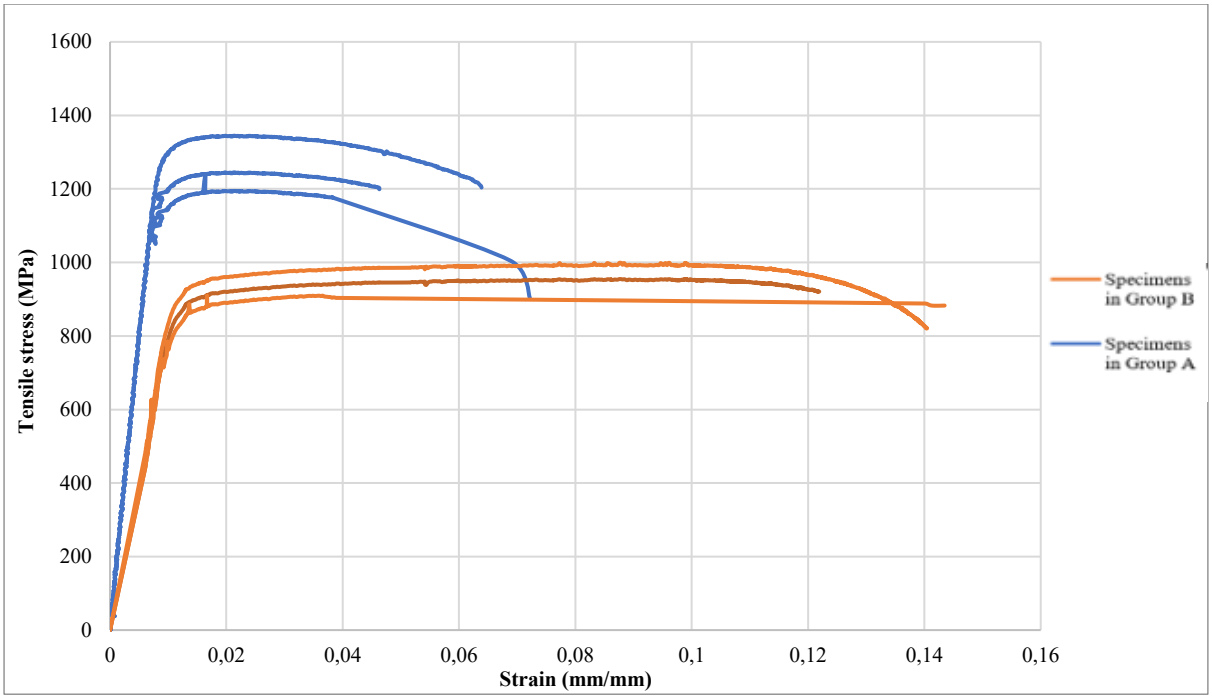

Figure 5.6: Stress-strain curves of specimens in groups A and B that were tested at a temperature of 20 ℃

Figure 5.6 makes it clear that, in comparison to the specimens in group B, the specimens in group A had smaller strains to failure but higher yield stresses and ultimate tensile stresses. It is evident that the tensile characteristics of the LPBF TI6Al4V(ELI) specimens were significantly impacted by high-temperature annealing heat treatment. At 20 ℃, it was observed that the yield, tensile strength, and modulus of elasticity decreased by 29.9%, 27.3%, and 19.6 %, respectively, while the ductility increased by up to 43% from the values for specimens that were stress-relieved to those that were stress-relieved followed by high-temperature annealing. The primary reason for this is the changes in microstructure that took place during high-temperature annealing, where the original acicular α' martensitic microstructures were replaced by the ($\alpha + \beta$) dual phase, with its known lower strength and higher ductility [169].

5.3. Metallographic Examination

5.3.1. Typical microstructures of specimens in group A

Optical micrographs of Ti6Al4V(ELI) specimens that were stress-relieved and then tested at temperatures of 20 ℃ and 175 ℃ are depicted in Figure 5.7.

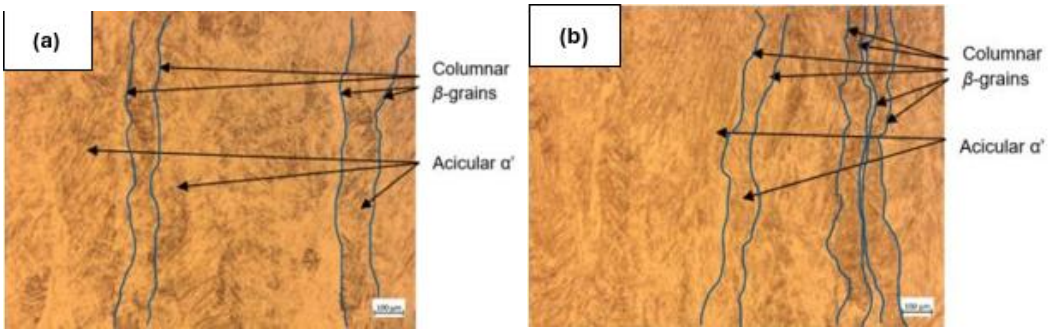

Figure 5.7: Optical micrographs of LPBF Ti6Al4V(ELI) specimens in group A that were tested at temperatures of (a) 20 ℃ and (b) 175 ℃.

The two figures show needle-like α' laths (dark lines), known as martensite microstructure inside columnar β-grains. The average widths of the columnar β-grains in Figure 5.7(a) and Figure 5.7(b) are 135±14 µm and 146±13 µm, respectively, with CoVs of 10.4% and 8.9%, respectively. The average widths of α' martensitic laths in Figure 5.7(a) and Figure 5.7(b) are 3.8±0.3 µm and 3.8±0.4 µm, respectively, with CoVs of 7.9% and 10.5%, respectively. It is noted that the CoVs are moderate, which implies that the data was moderately spread out away from the calculated values of the mean. Though different, the average values of the widths of the columnar β-grains in this figure for the two test temperatures fall within the respective standard deviations on each other. This implies that their differences are not significant.

5.3.2. Typical microstructures of specimens in group B

The optical micrographs displayed in Figure 5.8 are those of Ti6Al4V(ELI) specimens that were stress-relieved, followed by high-temperature annealing, and then tested at temperatures of 20 ℃ and 175 ℃.

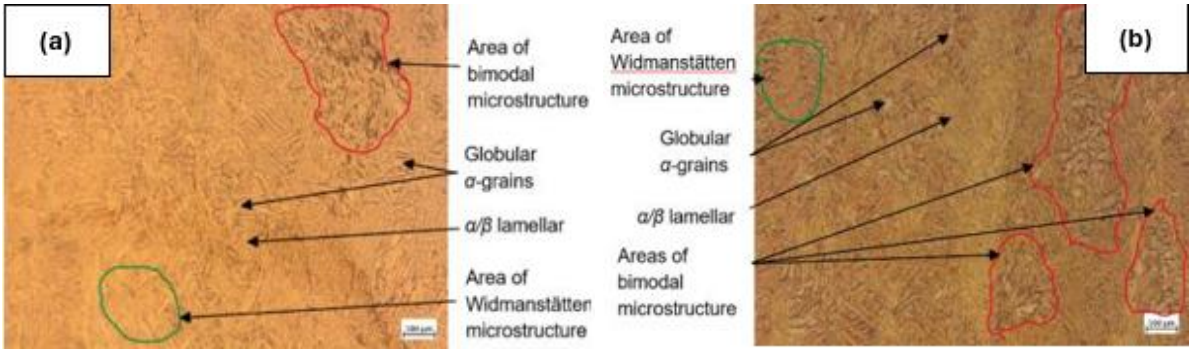

Figure 5.8: Optical micrograph of LPBF Ti6Al4V(ELI) specimens in group B that were tested at temperatures of (a) 20 ℃ and (b) 175 ℃

The two foregoing micrographs are similar. Both have areas with α- and β-phases that are packed parallel to each other, forming lamellar microstructures. There are also areas in both with Widmanstätten and bimodal microstructures. In Figure 5.8(a), the average widths of the α-laths and β-laths were measured at 10.1±0.9 µm and 3.4±0.3 µm, respectively, with CoVs of 8.9% and 8.8%, respectively. In Figure 5.8(b), the average widths of the α-lath and β-lath were measured at 13.1±1.2 µm and 4.0±0.4 µm, respectively, with CoVs of 9.2% and 10%, respectively. It is noted that the average width of α-laths and β-laths are higher for the specimen that was tested at 175 ℃ than for the specimen tested at 20 ℃. This is thought to be because of the higher testing temperature. Zöllner [21] reported that increasing temperatures led to the formation of coarser α-laths and a reduction in tensile strength. This is consistent with the findings in the present work from tensile testing, which showed that as the test temperature was raised, there was a drop in values of yield and ultimate strength as well as modulus of elasticity. In Figure 5.8(b), the darker area has increased. The darker area presents the content of the β-phase. This is consistent with the study by Shaikh *et al*. [24]. It has been reported that the β-phase is responsible for the ductility of the alloy [22, 196]. This agrees with the findings from tensile tests, resulting in the present work that showed that as the test temperature was raised, the ductility increased.

5.3.3. Comparing the microstructure of specimens in group A to those in group B

The microstructure in Figure 5.7 is completely different from the one in Figure 5.8. This difference in microstructure is due to the additional effect of high-temperature annealing heat treatment leading to the microstructure in the latter figure. In Figure 5.6, acicular α' needle-like microstructures are replaced by larger globular α-laths and β-laths that are longer and wider. This occurs when the temperature is high enough, and so also the thermal energy of atoms, which causes the atoms to migrate and overcome the surface energy of the grain boundaries. This results in the movement of grain boundaries and the growth of grains and, thus a coarsening of α-laths [21, 76] and formation of coarse β-grains.

5.4. Fractography

5.4.1. Analysis of fracture surface of specimens in group A

Typical secondary electron images (SEIs) of a fracture surface for a stress-relieved LPBF

TI6Al4V(ELI) specimen tested at 20 ℃ are shown in Figure 5.9.

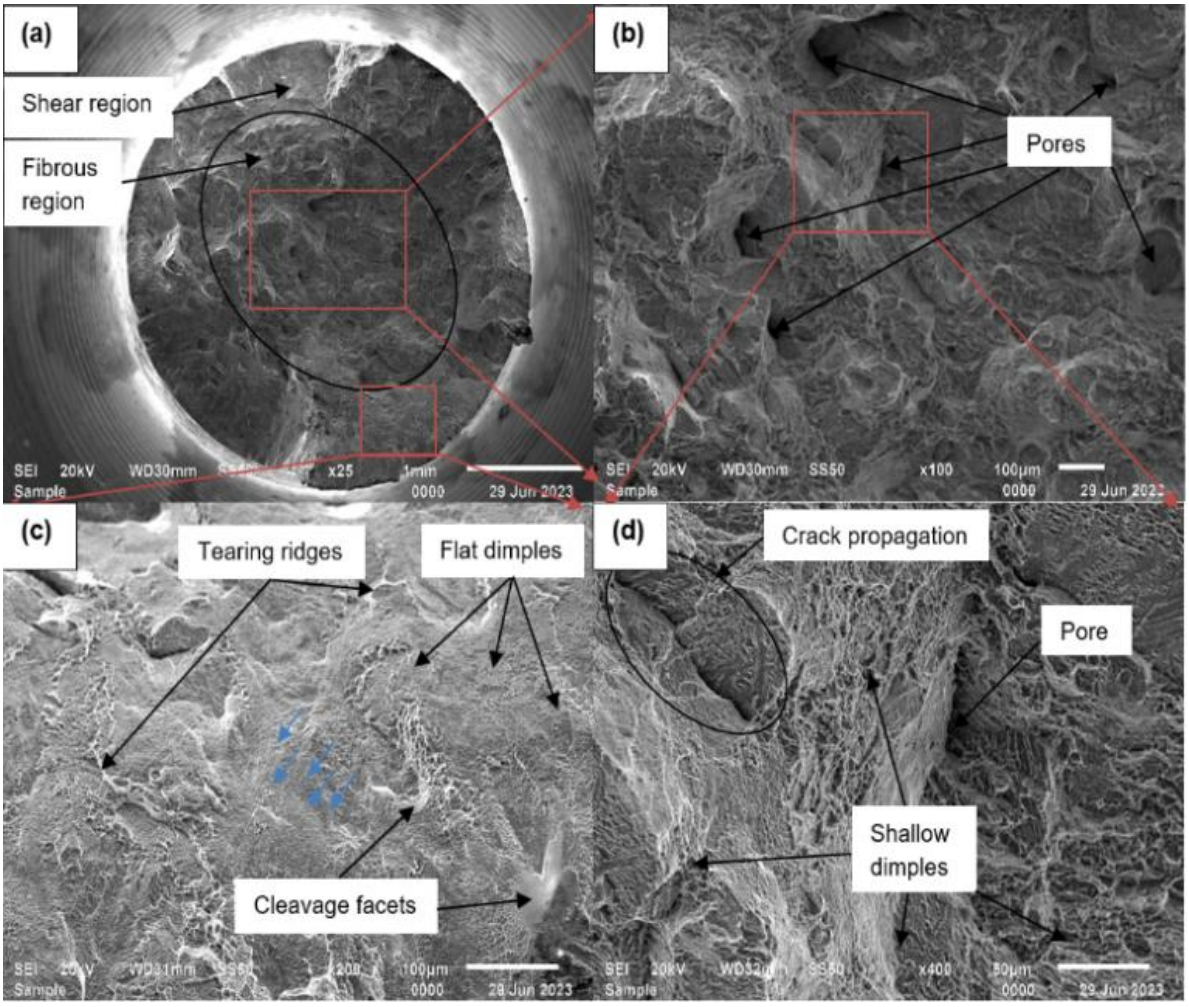

Figure 5.9: Typical SEIs of the fracture surface of a specimen in group A tested at a temperature of 20 ℃ (a) overall morphology, (b) fibrous region, (c) shear region, and (d) higher magnification of the fibrous region

The morphology of the entire fracture surface is depicted in Figure 5.9(a). The central section of this surface, which is named the fibrous fracture region and is marked by ridges, indicates the location of propagation of cracks. Shear, the specimen's ultimate failure mode, occurs in the outer region, which is smoother than the central region [84]. There are gas pores visible on the central fracture surface magnified in Figure 5.9(b), which is where cracks are thought to have started. Several dimples are present in Figure 5.9(c), and they are elongated in the direction of shear, as indicated by blue arrows. Some cases of quasi-cleavage fracture and a substantial number of tear ridges are depicted in the figure. This is consistent with the work of Dieter [6], who stated that dimples and tear ridges are characteristics of quasi-cleavage fracture,

which is typically seen at room temperature. One-half of the usual cup-and-cone fracture, a cone fracture feature seen in uniaxial tensile loading to failure, is evident in Figure 5.9(a). When examining the tensile fracture behaviour of Ti6Al4V samples independently, several authors [84, 85, 86, 87, 197] noted the cup-and-cone fracture feature, where the fracture surfaces' edges showed ductile failure-indicating dimples. The fibrous region, where shallow dimples are visible on the fracture surface, is magnified more in Figure 5.9(d).

A typical fracture surface of a specimen in group A, tested at a temperature of 175 ℃, is depicted by the SEI micrographs shown in Figure 5.10.

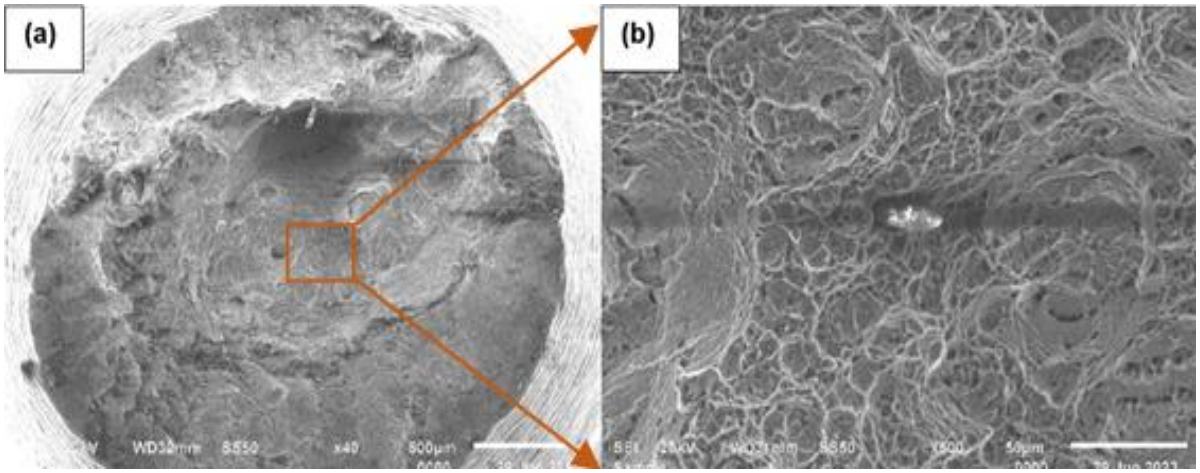

Figure 5.10: Typical SEIs of the fracture surface of a specimen in group A tested at a temperature of 175 ℃

The features of the fracture surface shown in this figure for loading at 175 °C are similar to those seen in Figure 5.9 for loading at 20 ℃. The cup feature on the fracture surface is clearly visible in Figure 5.10(a). It is seen in Figure 5.10(b) to be fibrous and exhibits pores and ridges. The smoother shear region surrounding this central region is seen in Figure 5.10(a) to be characterised by dimples, which suggest ductile fracture. After testing at a temperature of 175 ℃, the diameter of the specimen was reduced from 4 mm to 3.3 mm at the section of fracture. This was thought to be caused by deformation during necking. The size of the dimples on this fracture surface is seen to have increased from 3.4 µm for testing at 20 ℃ to 3.7 µm measured at 175 ℃.

Standard SEI micrographs of a group A specimen's fracture surface tested at 325 ℃ are displayed in Figure 5.11.

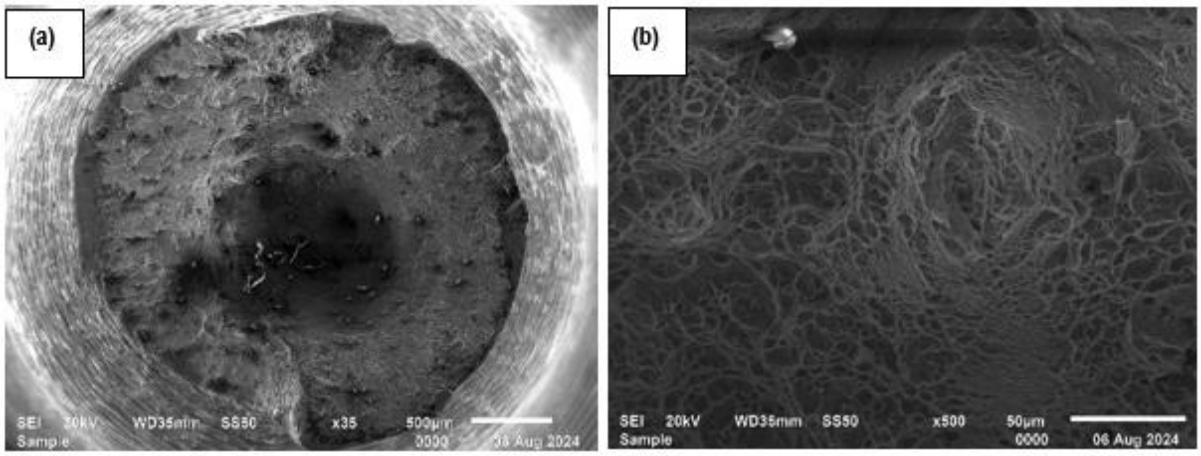

Figure 5.11: Typical SEIs of the fracture surface of a specimen in group A tested at a temperature of 325 ℃

After testing at a temperature of 325 ℃, the diameter of the specimen was reduced from 4 mm to 2.9 mm at the section of fracture because of necking. In Figure 5.11(a), the size of the shear region has reduced, and pores and fracture-related particles are visible. The size of the dimples on this fracture surface is seen to have increased from 3.4 µm for testing at 20 ℃ to 4.0 µm measured at 325 ℃.

Figure 5.12 shows typical SEI micrographs of the fracture surface of specimens in group A tested at temperatures of 20 ℃, 175 ℃, and 325 ℃.

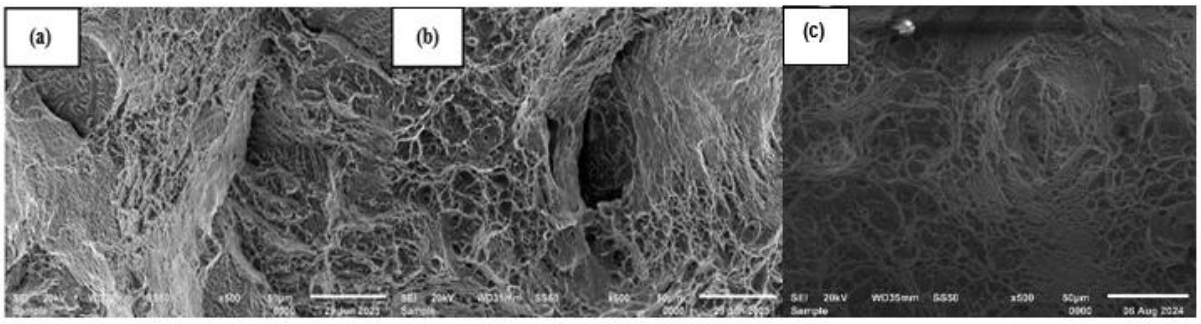

Figure 5.12: Typical SEIs of the fracture surfaces of specimens in group A tested at a temperature of (a) 20 ℃, (b) 175 ℃, and (c) 325 ℃

It is noted from these micrographs that as the testing temperature was raised, the size of the dimples increased. The sizes of dimples increased by 8.8% from 20 ℃ to 175 ℃ and by 17.6% from 20 ℃ to 325 ℃. This is consistent with the separate works reported in the references [25, 26].

5.4.2. Analysis of fracture surfaces of specimens in group B

Figure 5.13 shows typical SEIs of the fracture surface of specimens in group B tested at a temperature of 20 ℃.

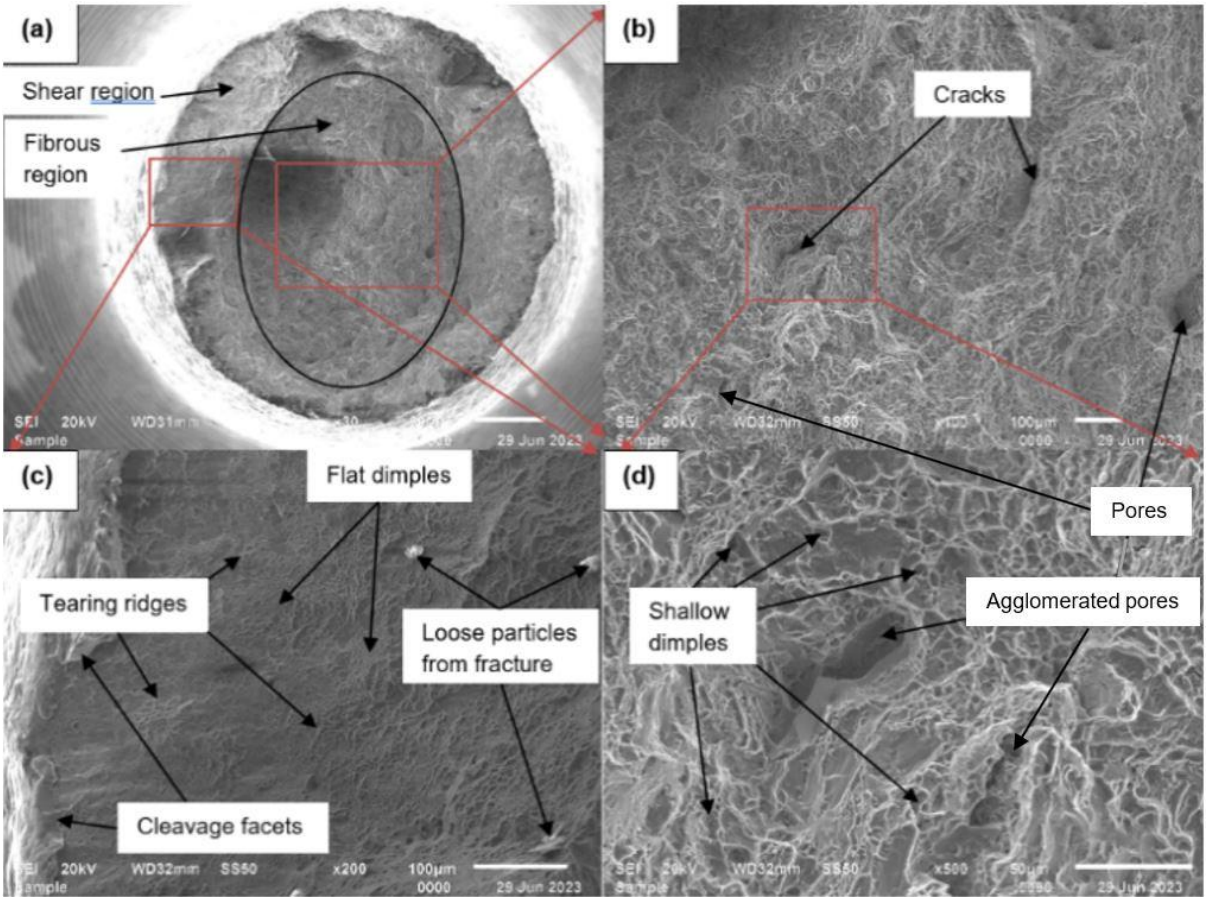

Figure 5.13: Typical SEIs of the fracture surface of a specimen in group B tested at a temperature of 20 °, (a) overall morphology, (b) fibrous region, (c) shear region, and (d) higher magnification in the fibrous region

It is clear from the micrographs in Figure 5.13 that the specimen fractured in a ductile manner due to the presence of cup features and dimples. The cup-shaped feature depicted in Figure 5.13(a) is part of a typical cup-and-cone fracture in ductile failure, suggesting that the specimen underwent necking prior to fracture. The area of slow crack growth corresponds with the central fibrous region. This central fibrous zone is surrounded by a shear region, which is where fast crack propagation and eventual fracture occur [26]. The fibrous region is magnified in Figure 5.13(b) to show the shallow dimples that are linked to voids that nucleate, grow, and coalesce as loading progresses. A higher magnification of the fibrous region is shown in

Figure 5.13(d), where shallow dimples and deep pores are visible. Such pores are associated with AM processing and are the result of partially melted powder and gas trapped in the molten metal during its quick solidification [198]. The cleavage facets and flat dimples seen in the shear fracture region depicted in Figure 5.13(c) are indicative of a faster mode of fracture. The cup and cone characteristics seen in this work are consistent with the observations made in references [85], wherein the Ti6Al4V(ELI) samples were tested in tension at room temperature after 2 hours of annealing at 950 ℃ to produce cup-and-cone fracture.

Typical SEIs of a group B specimen's fracture surface, tested at 175 ℃, are displayed in Figure 5.14.

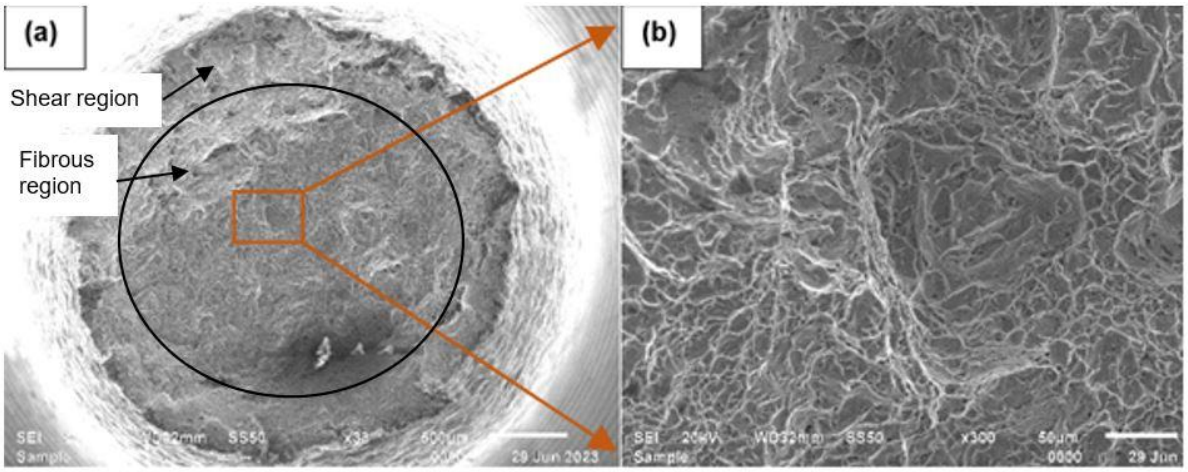

Figure 5.14: Typical SEIs of a fracture surface of a specimen in group B tested at a temperature of 175 ℃

The fracture surface displayed in Figure 5.14 shows that the specimen fractured in a ductile manner, as is evidenced by the presence of cup features and dimples. In comparison to the size displayed in Figure 5.13(d), the dimple sizes in Figure 5.14(b) appear larger. The size of the dimples has increased from 4.5 µm for testing at 20 ℃ to 4.8 µm at 175 ℃. This is in line with research reported in reference [26], on the mechanical characteristics of direct laser deposition (DLD) Ti6Al4V specimens, where it was found that as the testing temperature was raised, the size of the dimples increased. The diameter of the specimen at the section of fracture was reduced from 3.4 mm for the specimen that was tested at room temperature to 2.8 mm at 175 ℃. This is thought to be due to the severity of deformation taking place during necking at a test temperature of 175 ℃.

Figure 5.15 shows typical SEIs of the fracture surface of a specimen in group B that was tested at a temperature of 325 ℃.

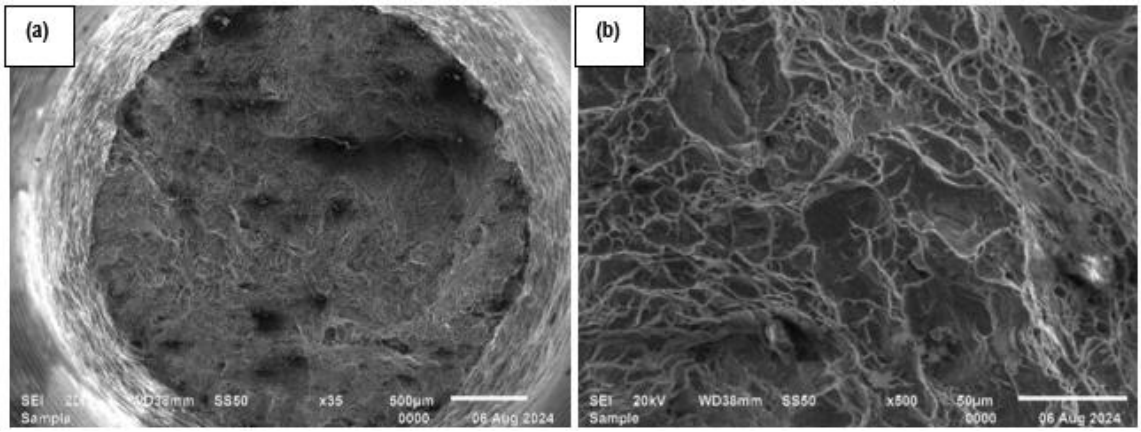

Figure 5.15: Typical SEIs of a fracture surface of a specimen in group B tested at a temperature of 325 ℃

Figure 5.15 shows a similar fracture surface to the one in Figure 5.12. A mixture of small and large dimples can be observed in Figure 5.15(b). The average dimple size on this fracture surface is seen to have increased from 4.8 µm for testing at 20 ℃ to 5.2 µm at 325 ℃.

5.4.3. Comparison of the fracture surface of specimens in group A to those in group B

Figure 5.16 shows typical SEIs of the fracture surfaces of specimens in groups A and B that were tested at temperatures of 20 ℃.

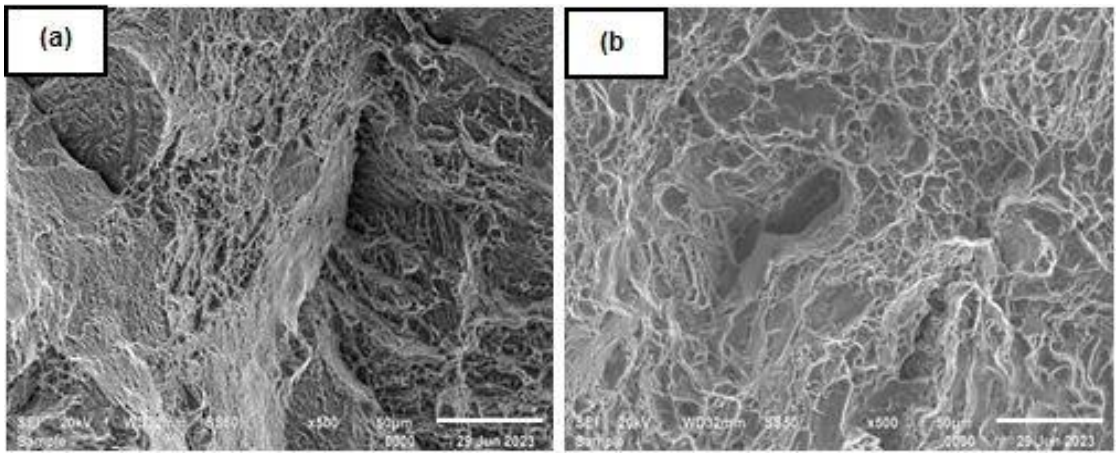

Figure 5.16: SEIs of the fracture surfaces of specimens in groups (a) A and (b) B, that was tested at a temperature of 20 ℃

The two SEIs in Figures 5.16(a) and 5.16(b) demonstrate that the specimens in group B generally had larger dimples. This is due to the high-temperature annealing of the specimens in group B. After testing at 20 ℃, the measured average dimple sizes were 3.4 µm and 4.5 µm for specimens in groups A and B, respectively.

Figure 5.17 shows typical SEIs of the fracture surfaces of specimens in groups A and B that were tested at temperatures of 175 ℃.

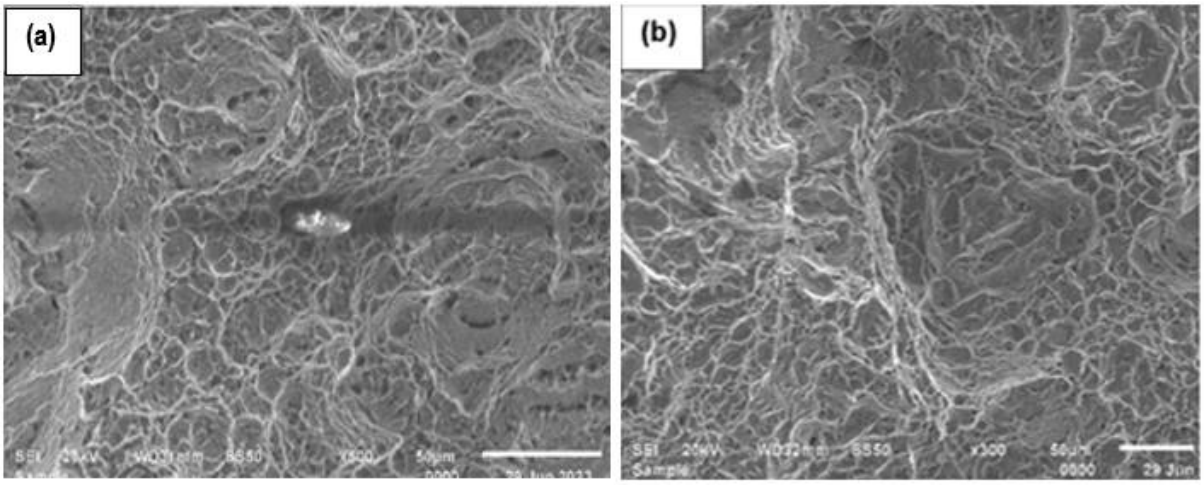

Figure 5.17: SEIs of the fracture surfaces of specimens in groups (a) A and (b) B, that was tested at a temperature of 175 ℃

The two micrographs in Figure 5.17 show similar morphology. After testing at 175 ℃, the measured average dimple sizes were 3.7 µm and 4.8 µm for specimens in groups A and B, respectively.

Figure 5.18 shows typical SEIs of the fracture surfaces of specimens in groups A and B that were tested at temperatures of 325 ℃.

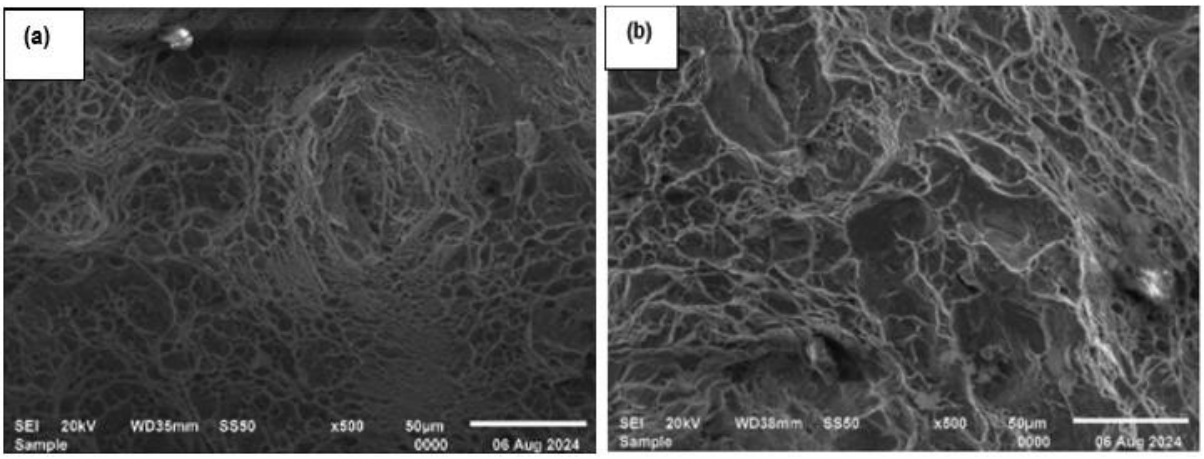

Figure 5.18: SEIs of the fracture surfaces of specimens in groups (a) A and (b) B, that was tested at a temperature of 325 ℃

It is evident in Figure 5.18 that the dimples for a specimen in group B are larger than those of a specimen in group A. The measured average dimple sizes were 4.0 µm and 5.2 µm for specimens in groups A and B, respectively.

5.4.4. Effect of temperature on the size of dimples

Table 5.3 presents the dimples of Ti6Al4V(ELI) samples that underwent heat-treatment processes and were then exposed to different test temperatures.

Table 5.3: Dimple sizes of Ti6Al4V(ELI) samples that underwent heat-treatment processes and were then exposed to different test temperatures

Heat-treatment process	Temperature ℃	Average dimple sizes (µm)	Standard deviation	Coefficient of variance (%)
Specimen Group A	20	**3.4**	0.26	7.2
	175	**3.7**	0.36	13.1
	325	**4.0**	0.22	5.3
Specimen Group B	20	**4.5**	0.53	28.2
	175	**4.8**	0.41	16.5
	325	**5.2**	0.50	24.9

It is evident from Table 5.3 that high-temperature annealing has a significant effect on the dimple's sizes. The size of dimples increased by 24.4 % after annealing-heat treatment. Table 5.3 shows that as the test temperature was raised, there was a further increment in the sizes of dimples too. The average dimple sizes of the stress-relieved samples increased by 8.1%

and 15% when the test temperature was increased to 175 ℃ and 325 ℃, respectively. The average dimple sizes of the annealed samples increased by 6.3% and 13.5% when the test temperature was increased to 175 ℃ and 325 ℃, respectively. It is noted that the CoVs for the annealed samples are high, implying that the data was scattered. This is evident in Figures 5.11, 5.12, and 5.13, where a mixture of large and small dimples was observed.

5.5. Vickers Microhardness Test Results

5.5.1. Values of Vickers microhardness for specimens in group A

A Vickers Future Tech FM 7E microhardness tester, set at a test load of 2 942 mN and a dwell time of 10 seconds, with the distribution of indentations shown in Figure 5.19, was used to undertake hardness tests in the present work. The figure shows six of the ten rows made away from the fracture surface, with distances of 20 µm in between them. This was done to determine the effect of distance away from the fracture surface on the hardness of the alloy.

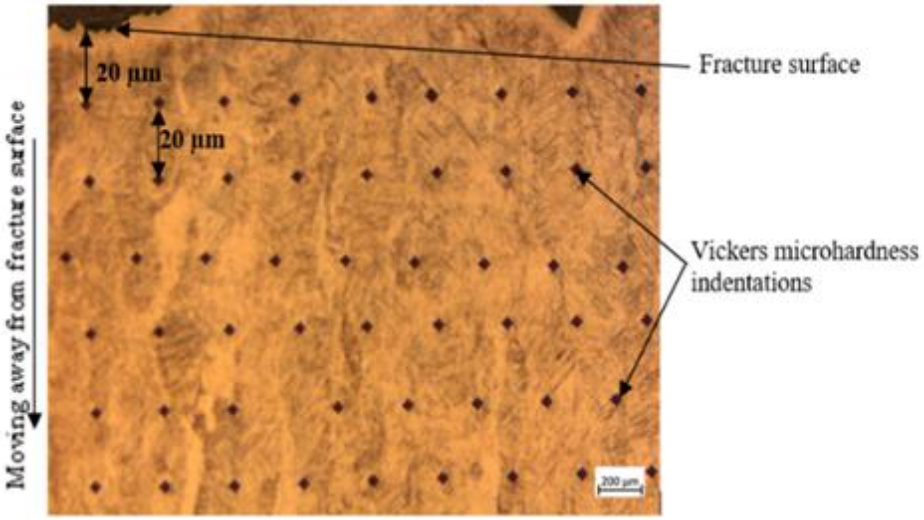

Figure 5.19: Vickers microhardness diamond indentations on a Ti6Al4V(ELI) sample

The Vickers microhardness average values, standard deviations, and CoV for a stress-relieved specimen in Group A that was tested at 20 ℃ are shown in Table 5.4.

Table 5.4: Average Values of Vickers Hardness of a Specimen in Group A that was Tested at a Temperature of 20 ℃

Distance from the fracture surface (µm)	Average microhardness (HV)	Standard deviation	Coefficient of variance (%)	Total change in hardness from far distance hardness (%)
20	348.6	12.7	3.6	3.6
40	349.4	14.0	4.0	3.3
60	353.7	10.9	3.1	2.2
80	357.1	15.6	4.4	1.2
100	357.6	13.4	3.7	1.1
120	358.8	16.3	4.5	0.8
140	361.4	17.3	4.8	0.1
160	360.3	9.4	2.6	0.4
180	361.2	13.9	3.8	0.1
5 000	361.6	13.6	3.8	0

The data in Table 5.4 makes it clear that the mean values of hardness decrease with proximity to the fracture surface. The lowest value of hardness was at 20 µm from the fracture surface. Vickers microhardness values increased with increasing distance from the fracture surface up to 180 µm, after which they essentially remained constant. These results show that the hardness of the Ti6Al4V(ELI) specimens under test depends on the severity of deformation taking place during necking at a test temperature of 20 °C. The highest CoV in the table was 4.8%. This low value implies that the collected data was highly reliable, as its values were close to the mean and with each other.

The mean values of Vickers microhardness for the specimen in group A, whose values were reported in Table 8.4, are displayed in Figure 5.20.

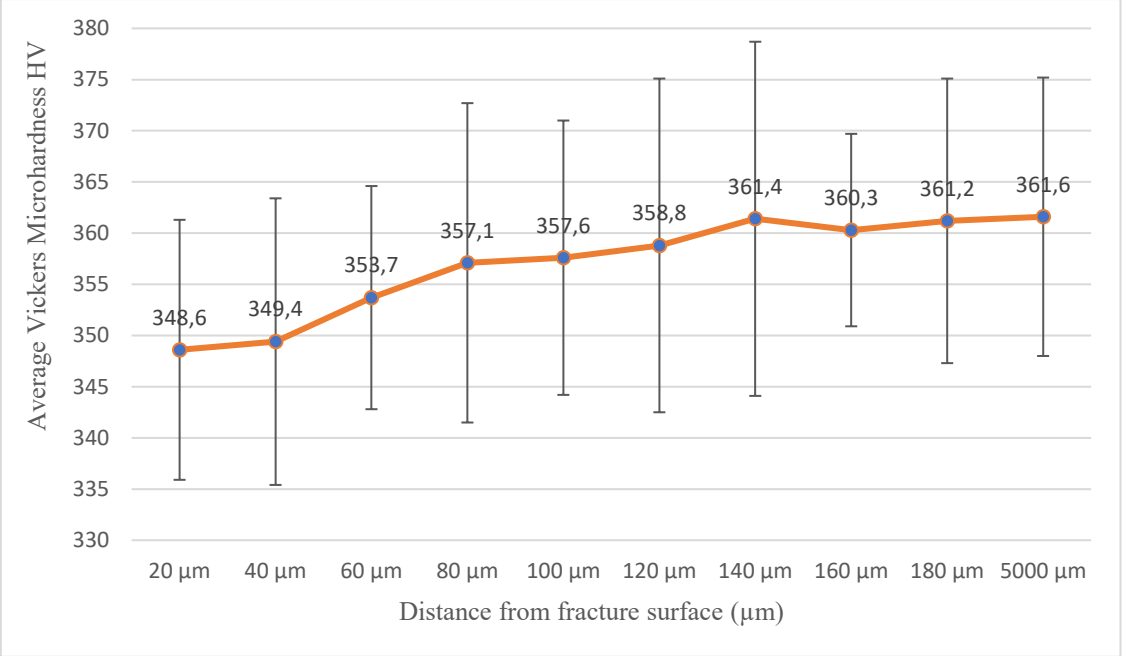

Figure 5.20: Average values of Vickers microhardness of a specimen in group A that was tested at a temperature of 20 ℃

The relationship between the mean values of hardness and the distance from the fracture surface is depicted in Figure 5.20. The curve supports the observations based on the values in Table 5.4, which show that the hardness of the specimen increased with increasing distance from the fracture surface until no further increase was observed. The plot depicts a four-stage curve with an initial low change in hardness, three stages of successive reduction in the rate of change in hardness, and an eventual levelling out of the curve, and thus provides more information than the related table. The observed trend of the curve in Figure 5.20 suggests that the strain-hardening effect that characterises uniform plastic deformation of ductile materials is not prevalent in the region of non-uniform plastic deformation. Instead, the material undergoes a softening that intensifies with more necking during this final stage of deformation. It should be acknowledged, however, that the data plotted in this figure all fall within the error bars, which reduces the significance of any trend inferred from its curve. This calls for more data to be collected.

Table 5.5 displays the average, standard deviation, and CoV values of microhardness for a specimen in group A that was tested at 175 ℃.

Table 5.5: Average Values of Vickers Hardness of a Specimen in Group A, Tested at a Temperature of 175 ℃

Distance from the fracture surface (µm)	Average microhardness (HV)	Standard deviation	Coefficient of variance (%)	Total change in hardness from far distance hardness (%)
20	327.3	12.5	3.8	9.3
40	333.1	9.0	2.7	7.8
60	336.2	16.6	4.9	6.9
80	351.1	13.7	3.9	2.8
100	351.6	12.8	3.6	2.7
120	353.2	12.5	3.5	2.2
140	361.5	12.6	3.5	0.1
160	361.0	9.2	2.5	0.1
180	361.1	6.1	1.7	0.03
5 000	361.2	11.4	3.2	0

Similar to the case in Table 5.4, the values in Table 5.5 demonstrate that the average values of Vickers microhardness rise with increasing distance from the fracture surface until no further increase occurs. The table indicates that testing at 175 ℃ caused the average hardness values to decrease from 361.2 HV a far distance from the fracture surface to 327.3 HV, at a distance of 20 µm from the fracture surface. The low value of the highest CoV in this table of 4.9% denotes clustering of the collected data around the mean values and to one another, which raises the dependability of the determined mean values.

The mean values of Vickers microhardness shown in Table 5.5 are plotted in Figure 5.21.

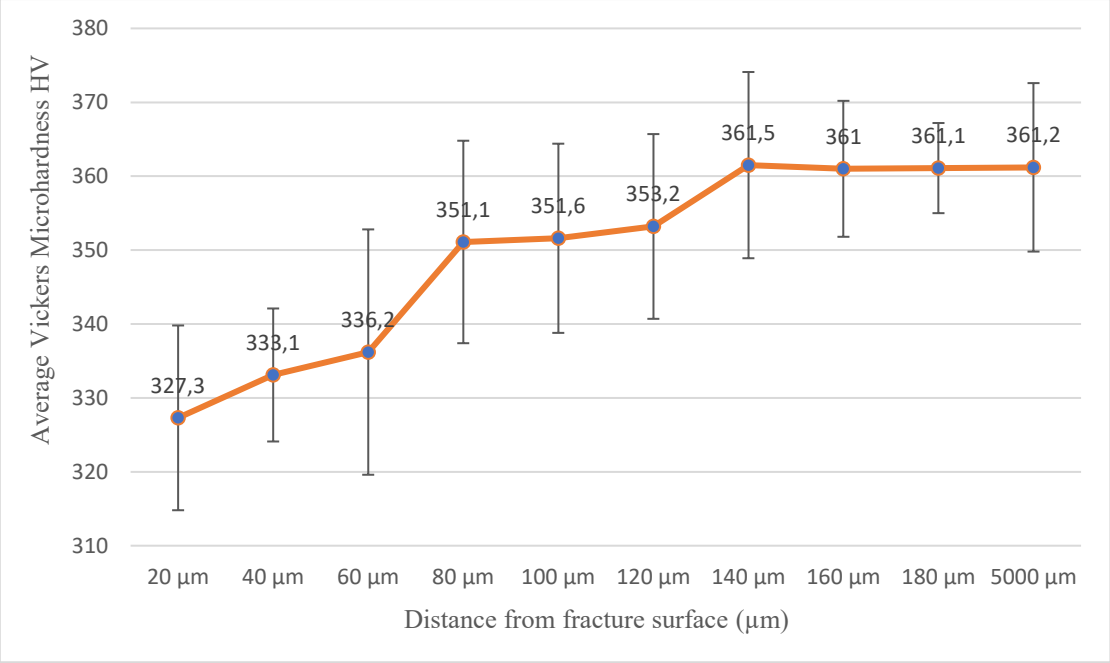

Figure 5.21: Average values of Vickers microhardness of a specimen in group A tested at a temperature of 175 ℃

The curve depicted in Figure 5.21 bears a resemblance to that in Figure 5.20 in that it displays four distinct stages and a continuous increase in the mean values of Vickers microhardness with increasing distance from the fracture surface until no further increase occurs. As was observed for the specimens that were tested at 20 ℃, necking-induced material softening appears to have led to the observed decrease of hardness with proximity to the fracture surface. It is noted that not all mean values of hardness in this figure fall within the error bars. Therefore, inferences of a trend concerning the data in this case are more significant than in the previous case.

Plotting the values of mean hardness in Tables 5.4 and 5.5 in the same graph gives rise to the curves shown in Figure 5.22.

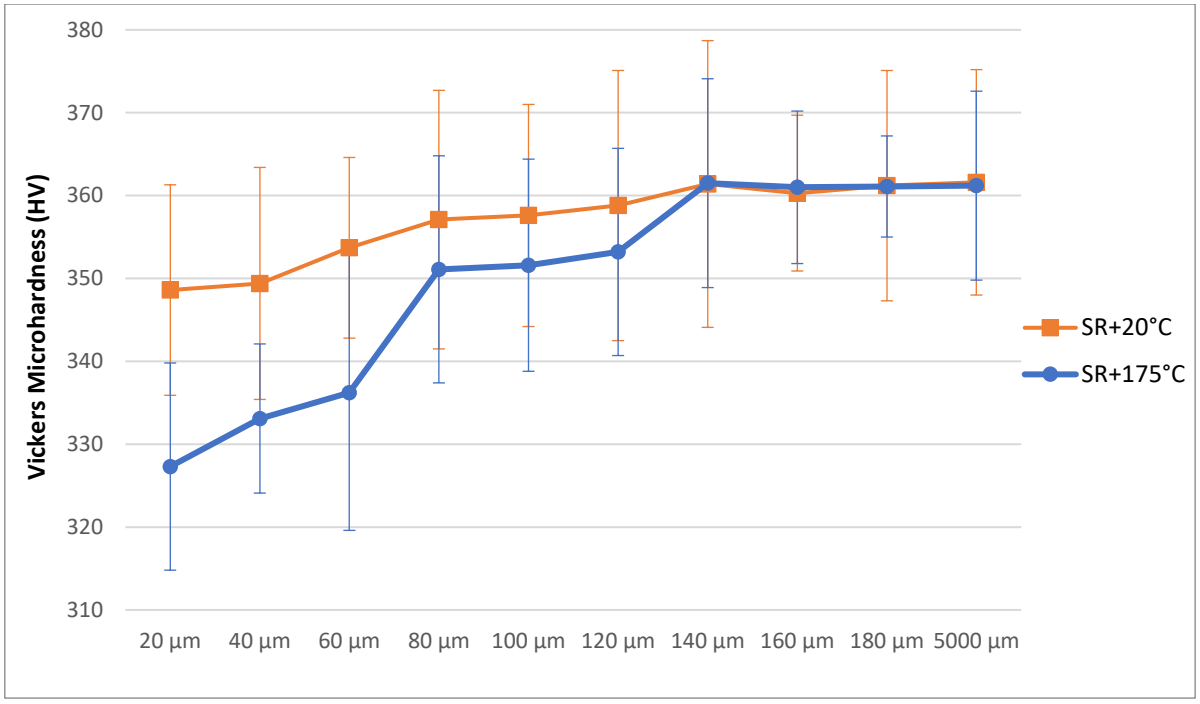

Figure 5.22: Average values of Vickers microhardness of specimens in group A tested at temperatures of 20 ℃ and 175 ℃

Comparing the curves in this figure leads to the conclusion that increasing the testing temperatures causes the hardness of the Ti6Al4V(ELI) alloy to decrease at all distances from the fracture surface until the point where the hardness levels out. Based on Figure 5.22, the average hardness values for a specimen tested at 20 ℃ and 175 ℃ are 348.6 HV and 327.3 HV, respectively, at a distance of approximately 20 µm from the fracture surface. It is observed that testing at 175 ℃ yields a lower hardness value than testing at 20 ℃. This is consistent with the observation in [26] and is believed to be the result of the testing temperature being raised, as was mentioned in [174].

5.5.2. Vickers microhardness values for specimens in group B

Table 5.6 presents the obtained average values, standard deviations and CoV of microhardness for a specimen in group B tested at 20 ℃.

Table 5.6: Average Values of Vickers Hardness of a Specimen in Group B, Tested at a Temperature of 20 ℃

Distance from the fracture surface (µm)	Average microhardness (HV)	Standard deviation	Coefficient of variance (%)	Total change in hardness from far distance hardness (%)
20	312.5	25.3	8.1	1.8
40	314.8	17.3	5.5	1.1
60	314.1	14.2	4.5	1.3
80	316.0	19.8	6.3	0.8
100	316.9	21.0	6.6	0.5
120	317.7	16.3	5.1	0.2
140	319.1	22.3	7.0	0.2
160	319.2	23.2	7.3	0.3
180	318.9	27.3	8.6	0.2
5 000	318.4	13.6	4.3	0

Table 5.6 demonstrates that annealing heat treatment decreased the hardness of the Ti6Al4V(ELI) alloy by 11.9%, a far-distance from the edge of the fracture surface. This is consistent with a study published in reference [196], which found that metallics are frequently softened by annealing-heat treatment. The stress-relieved and then high-temperature annealed samples have a CoV that is largely above 5%, which indicates that the data points were slightly more dispersed away from the mean and from each other for this set of specimens than for the previous ones. This minimally decreases the dependability of the mean values that were calculated in this case. As with the specimens in group A, it is observed that the mean values of hardness increased continuously with increasing distance from the fracture surface, except for the distances between 40 µm and 60 µm and 160 µm and 180 µm.

The mean values of microhardness for the specimen in group B, as depicted in Table 5.6, are displayed in Figure 5.23.

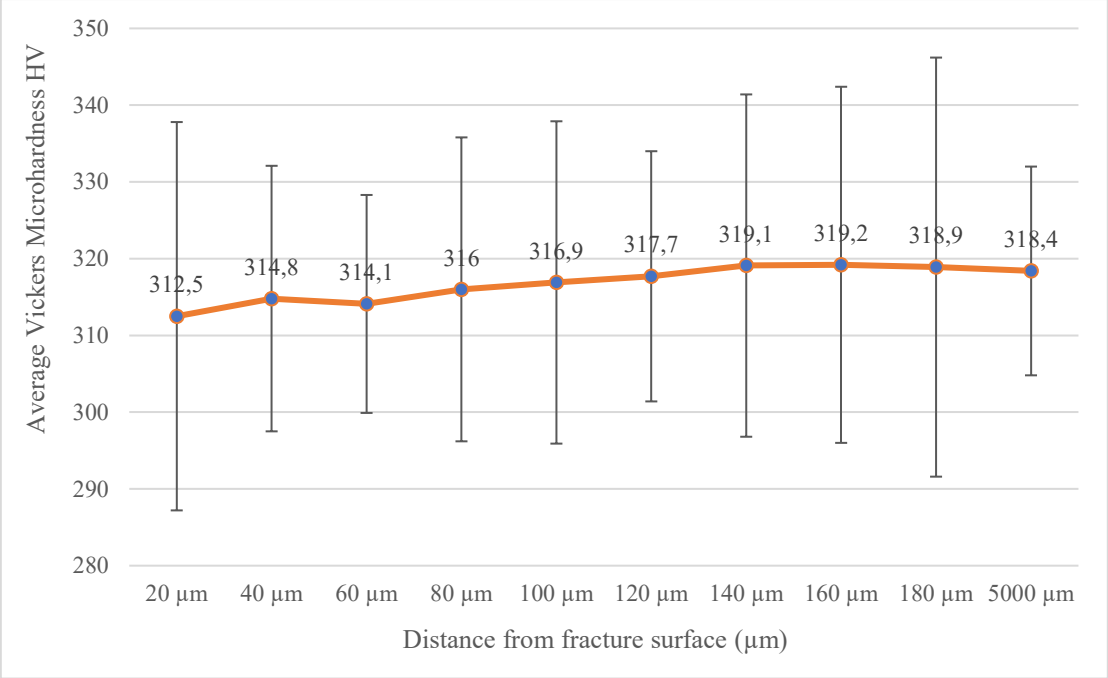

Figure 5.23: Average values of Vickers microhardness of a specimen in group B tested at a temperature of 20 ℃

With the exception of values at points 40 µm, 160 µm, and 180 µm from the fracture surface, Figure 5.23 illustrates the continuously decreasing value of mean hardness with increasing proximity to the fracture surface. Nonetheless, the values of mean hardness displayed in Figure 5.22 are all observed to fall within the error bars, thereby reducing the significance of their disparity and any associated trends.

The microhardness average values, standard deviations, and CoV for a specimen in group B that was tested at 175 ℃ are shown in Table 5.7.

Table 5.7: Average Values of Vickers Hardness of a Specimen in Group B Tested at a Temperature of 175 ℃

Distance from the fracture surface (µm)	**Average microhardness (HV)**	**Standard deviation**	**Coefficient of variance (%)**	**Total change in hardness from far distance hardness (%)**
20	310.4	33.9	10.9	2.4
40	312.1	40.3	12.9	1.8
60	312.6	26.3	8.4	1.7
80	312.2	21.8	7.0	1.8
100	314.0	32.1	10.2	1.2

120	314.2	29.3	9.2	1.2
140	316.9	29.8	9.4	0.3
160	318.2	18.4	5.8	0.1
180	317.8	25.6	8.1	0.1
5 000	318.0	21.4	6.7	0

The data in Table 5.7 indicates that the mean values of hardness increased with increasing distance from the fracture surface. The data in the table further indicate that the data points were dispersed farther from the mean and from one another than in previous cases, with even higher values of CoV than those that were noted for the earlier mean values in this section.

The average values of microhardness for the specimen in group A, listed in Table 5.7, are displayed in Figure 5.24.

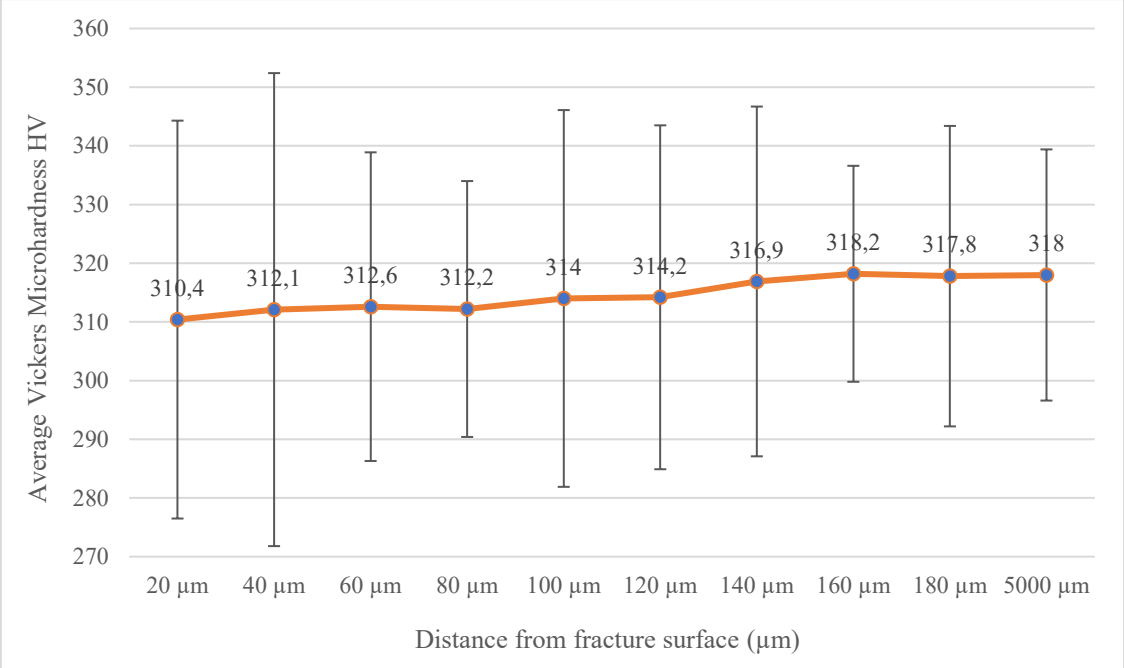

Figure 5.24: Average values of Vickers microhardness of a specimen in group B tested at a temperature of 175 °C

The curve in this figure shows that the mean Vickers values of hardness generally decrease continuously with proximity to the fracture surface. The exception to this trend occurs at distances between 60 µm and 80 µm and 160 µm and 180 µm from the fracture surface, where the values of hardness decreased. That the mean values of hardness were all within the error bars, as was observed in the earlier cases, reduces the significance of any conclusions or trends drawn from the table and accompanying figure.

Plotting the data in Tables 5.6 and 5.7 in the same graph gives rise to the curves shown in Figure 5.25.

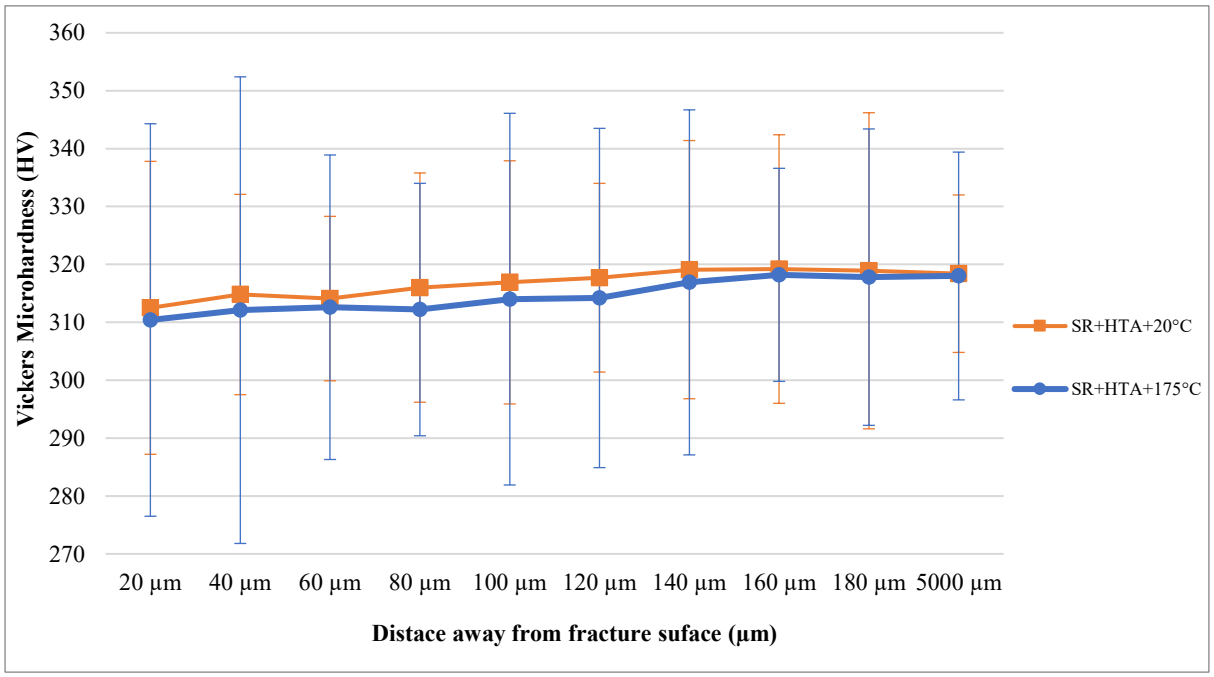

Figure 5.25: Average values of Vickers microhardness of specimens in group B tested at temperatures of 20 ℃ and 175 ℃

It is evident from Figure 5.25 that the value of hardness for specimens tested at 175 ℃ is lower than that of specimens tested at 20 ℃. Testing at 175 ℃ resulted in a 0.7% decrease in the alloy's hardness when compared to testing at 20 ℃. This is in line with what was noted in [22]. It is noted that at each selected distance away from the fracture surface, the value hardness for the specimens tested at 20 ℃ is higher than those tested at 175 ℃. However, all the values fall within each other's error bars.

5.6. Summary

The values of yield strength, ultimate tensile strength, and modulus of elasticity decreased, and the values of ductility increased with increased test temperature. The values of yield strength, ultimate tensile strength, and modulus of elasticity decreased, and the values of ductility increased with high-temperature annealing heat treatment.

The widths of the α- and β-laths increased as the test temperature increased. The specimens failed by ductile fracture at all test temperatures, with side shear regions showing flat dimples and central fibrous regions with shallow dimples.

Hardness was reduced by high-temperature annealing over the values for stress-relieved specimens. The mean values of Vickers microhardness decreased as the test temperature increased. At all test temperatures, the severity of necking caused was consistent with the degree of reduction of hardness.

5.7. Conclusions

The results obtained showed that test temperature impacted the mechanical properties and microstructure of Ti6Al4V(ELI) specimens. Moreover, the hardness of the specimens varied with the distance away from the fracture surface.

CHAPTER 6: FATIGUE BEHAVIOUR OF TI6AL4V(ELI)

6.1. Introduction

This chapter presents the experimental results of fatigue testing, along with their analysis and discussion. It includes a microstructural analysis of the fatigue fracture surface and the results of Vickers microhardness tests on the fractured specimens, along with their analysis. The testing frame at Mintek, from which the tensile test results presented in Chapter Five were obtained, eventually broke down, and a different testing frame was accessed at UNISA for fatigue testing. Therefore, it was deemed necessary to conduct preliminary uniaxial tensile tests on the latter frame to provide a reference for fatigue testing. The results of these tensile tests are presented and analysed in this chapter.

6.2. Tensile Properties

Table 6.1 presents the tensile properties of the specimens that were stress-relieved, followed by high-temperature annealing and then tested in tension at different temperatures.

Table 6.1: Tensile properties of specimens that were stress-relieved followed by high-temperature annealing and tested in tension at 20 ℃, 175 ℃, 325 ℃, and 475 ℃

Temperature (°C)	Specimen number	Yield strength (MPa)	Ultimate tensile strength (MPa)	Modulus of elasticity (GPa)	Percentage elongation (%)
20	**1**	788.5	859.9	97.23	15.7
	2	882.4	931.5	99.9	20.1
	3	828.7	940.3	111.4	19.6
	Average	833.2	910.6	102.8	18.5
	Standard deviation	47.1	44.1	7.5	2.4
	Coefficient of variance (%)	5.7	4.8	7.3	12.9
175	**4**	732.3	835.2	89.8	20.3
	5	715.6	820.2	87.8	20.5
	6	714.7	817.8	87.9	21.5
	Average	721.9	824.4	88.5	20.8
	Standard deviation	11.6	9.4	1.1	0.7

	Coefficient of variance (%)	1.6	1.1	1.9	3.2
325	**7**	593.3	717.5	86.8	19.8
	8	574.2	707.8	87.9	20.1
	9	571.5	705.9	85.3	20.9
	Average	579.7	710.4	86.7	20.3
	Standard deviation	11.9	6.2	1.3	0.6
	Coefficient of variance (%)	2.1	0.9	2.3	2.78
475	**10**	433.9	587.2	80.4	19.4
	11	396.4	579.7	81.4	18.2
	Average	415.2	583.4	80.9	18.8
	Standard deviation	26.5	5.3	0.5	0.8
	Coefficient of variance (%)	6.4	0.9	0.7	4.3

The average values of yield strength, ultimate tensile strength, modulus of elasticity, and percentage elongation are presented in Table 6.1. The results show that as the test temperature was increased from 20 ℃ to 175 ℃, 325 ℃, and 475 ℃, there was a reduction in yield strength, ultimate tensile strength, and modulus of elasticity. This observation is consistent with the works of [10, 25, 26]. It was observed that the reduction in the values of yield strength, ultimate tensile strength, and modulus of elasticity from 20 ℃ to 175 ℃ were 13.4%, 9.5%, and 13.9%, from 20 ℃ to 325 ℃ 19.7%, 22.0%, and 15.7%, and from 20 ℃ to 475 ℃ 54.8%, 35.9%, and 21.3%, respectively. It is noted that the test temperature of 475 ℃ remarkably reduced the strength of the alloy. Table 6.1 shows that testing at elevated temperatures increased the percentage elongation. The percentage elongation increased by 12.4% from 20 ℃ to 175 ℃, 9.7% from 20 ℃ to 325 ℃, and 1.6% from 20 ℃ to 475 ℃. It is noted that testing at 475 ℃ slightly increased the percentage elongation. It has been reported in literature [68] that the Ti6Al4V alloy is suited for applications at temperatures below 400 ℃, as temperatures above 400 ℃ do affect its properties. This was observed to be the case here, as testing at 475 ℃ significantly reduced the tensile strength of the alloy, though with a slight increase of the percentage elongation. A reduction in tensile strength will decrease the fatigue strength, while an increase in ductility will improve the fatigue strength. It was reported in ref. [6] that testing at higher temperatures, reduces the fatigue strength of the metals. Noting that the fatigue life of Ti6Al4V(ELI) alloy is dependent on both the tensile strength and ductility of the alloy, it is expected that fatigue testing at 475 ℃ will reduce the fatigue life of Ti6Al4V(ELI) alloy given the remarkable reduction of strength and low increase of ductility observed in the present work. It is noted in Table 6.1 that the coefficients of variance are generally relatively low. This increases the reliability of the measured values of mean.

Table 6.2 compares the tensile properties of testing on different testing machines. These are for specimens that were stress-relieved, followed by high-temperature annealing and then testing at different temperatures. The Instron 8801 and Instron 1342 are test machines at UNISA and Mintek, respectively. The data for Instron 8801 and Instron 1342 are adopted from Tables 6.1 and 5.2, respectively.

Table 6.2: Tensile properties of the Ti6Al4V(ELI) specimens tested at different testing equipment and different temperatures

	Temperature (℃)	Instron 8801	Instron 1342
Yield strength (MPa)	20	833.2±41.7	888.4±33.9
	175	721.9±11.6	597.2±84.3
	325	579.7±11.9	544.3±33.4
Ultimate tensile strength (MPa)	20	910.6±44.1	953.7±59
	175	824.4±9.4	674.8±83
	325	710.4±6.2	654.9±6.7
Modulus of elasticity (GPa)	20	102.8±7.5	99.5±17
	175	88.5±1.1	91.7±13.5
	325	86.7±1.3	83.3±1.1
Percentage elongation (%)	20	18.5±2.4	13.2±2.1
	175	20.8±0.7	13.9±1.6
	325	20.3±0.6	17.3±4.6

The average values of yield strength, ultimate tensile strength, modulus of elasticity, and percentage elongation presented in Table 6.2 differ by 0.6%, 4.7%, 3.2%, and 28.6% at a test temperature of 20 ℃; 17%, 18.1%, 3.6%, and 33.2% at a test temperature of 175 ℃; 6.1%, 7.8 %, 3.9%, and 14.7% at 325 ℃, all respectively.

The tensile properties of the specimens obtained from the two testing frames differ, as shown in Table 6.2. There is a difference in yield strength of 0.6% at 20 ℃, 17% at 175 ℃, and 6.1% at 325 ℃. The percentage differences at 20 ℃ and 325 ℃ are quite low and are within their respective standard deviations. This increases the reliability of the measured results. However, at a temperature of 175 ℃, this percentage is high. A difference in ultimate tensile strength of 4.7% at 20 ℃, 18.1% at 175 ℃, and 7.8% at 325 ℃. It is noted that there is a higher difference at a temperature of 175 ℃; again, the standard deviation is high for the Intron 1342. There is a difference in modulus of elasticity of 3.2% at 20 ℃, 3.6% at 175 ℃, and 3.9% at 325 ℃. The difference in the modulus of elasticity is relatively low, which shows an increase in the

reliability of the results measured. This is a good statement of replicability of data for the same type of specimens, same alloy, additively built on the same equipment and tested on different tensile testing frames in two different laboratories in two different locations. There is a difference in percentage elongation of 28.6% at 20 ℃, 33.2% at 175 ℃, and 14.7% at 325 ℃. The differences in percentage elongation are high, however, these measured values are within the values recorded in the literature. These differences in the measured values are likely due to machine calibration. It is likely that one of the machines was not calibrated properly which led to inaccurate measurements, or it could be test specimens that were not aligned properly in the grips that induced stress that affected the results.

Figure 6.1 presents the stress-strain curves of the specimens that were tested in tension at different temperatures.

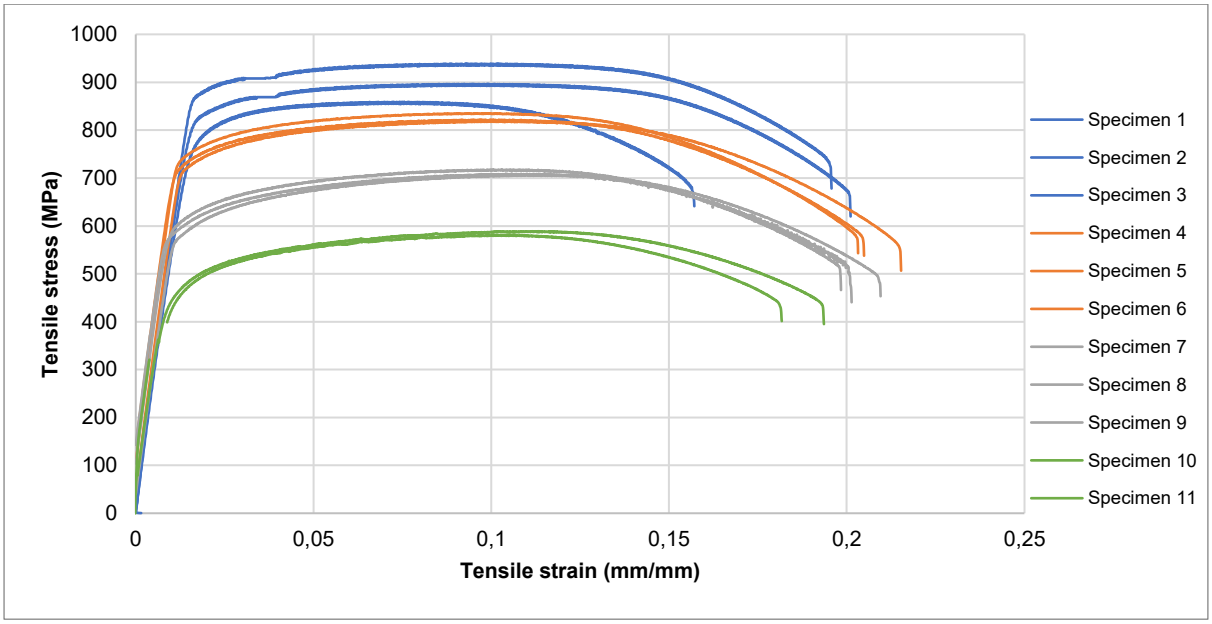

Figure 6.1: Stress-strain curves of the specimens that were stress-relieved followed by high-temperature annealing and then tested in tension at different temperatures

Figure 6.1 shows the stress-strain curves of stress-relieved and high-temperature annealed specimens, all with values of tensile strength below 950 MPa. It is evident that the specimens that were tested at a temperature of 20 ℃, shown in blue colour, have the highest tensile stresses. As the test temperature was raised, the tensile stress decreased. Specimens that were tested at a temperature of 475 ℃, in green colour, had the lowest tensile stresses. The average strain of the specimens tested at a temperature of 20 ℃ is smaller. There is not much difference

among the specimens tested at the same temperature, except those tested at a temperature of 20 ℃. This could have been caused by changes in testing parameters due to different testing works carried out on the machine, as the specimens tested at a temperature of 20 ℃ were tested first.

Figure 6.2 shows the SEIs of specimen 2 that was stress-relieved followed by high-temperature annealing and then tested in uniaxial tension at room temperature, 20 ℃.

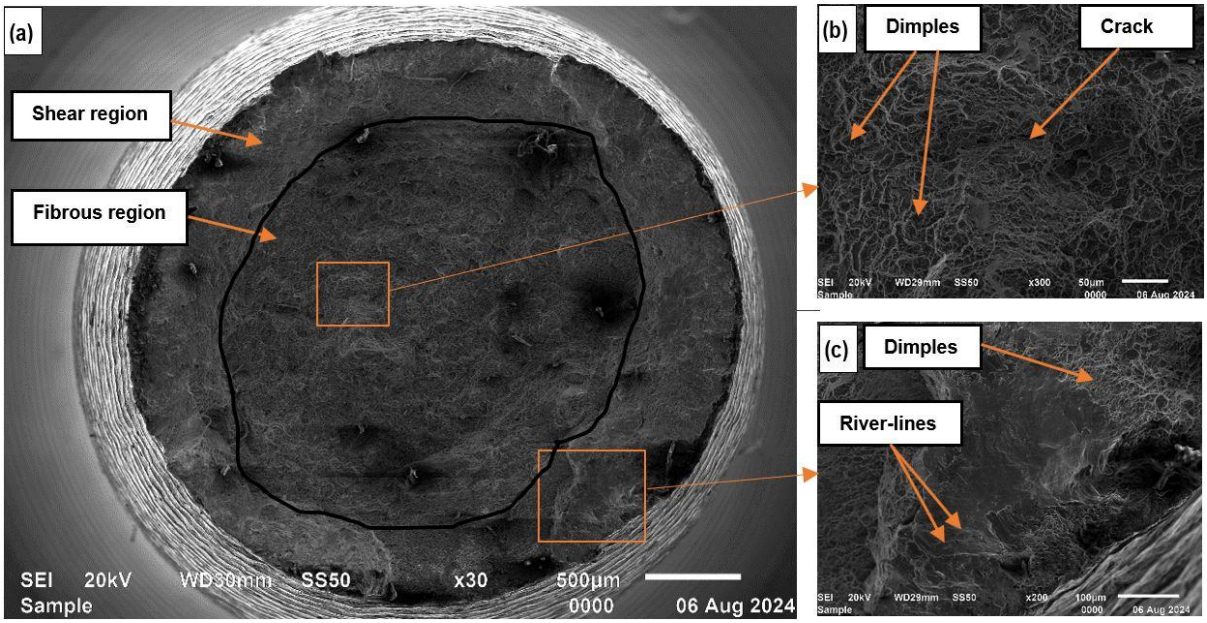

Figure 6.2: SEIs micrographs of the fracture surface of tensile specimen 2

One-half of a cup-and-cone fracture feature can be seen in Figure 6.2(a). The figure shows the fibrous region in the centre and the shear region on the periphery of the fracture surface. A higher magnification of the fibrous region is shown in Figure 6.2(b), which shows shallow dimples and tear ridges, as well as cracks. In Figure 6.2(c), a higher magnification of the shear region is shown and exhibits a blend of cleavage and ductile fracture. Dimples elongated in the direction of fracture and river-line patterns are also evident in this figure. The diameter of the specimen at the fracture section was measured at 3.4 mm and that of the fibrous region was measured at 2.2 mm.

Figure 6.3 shows the tensile fracture surfaces of specimens 5, 8, and 10 tested at temperatures of 175 ℃, 325 ℃, and 475 ℃, respectively.

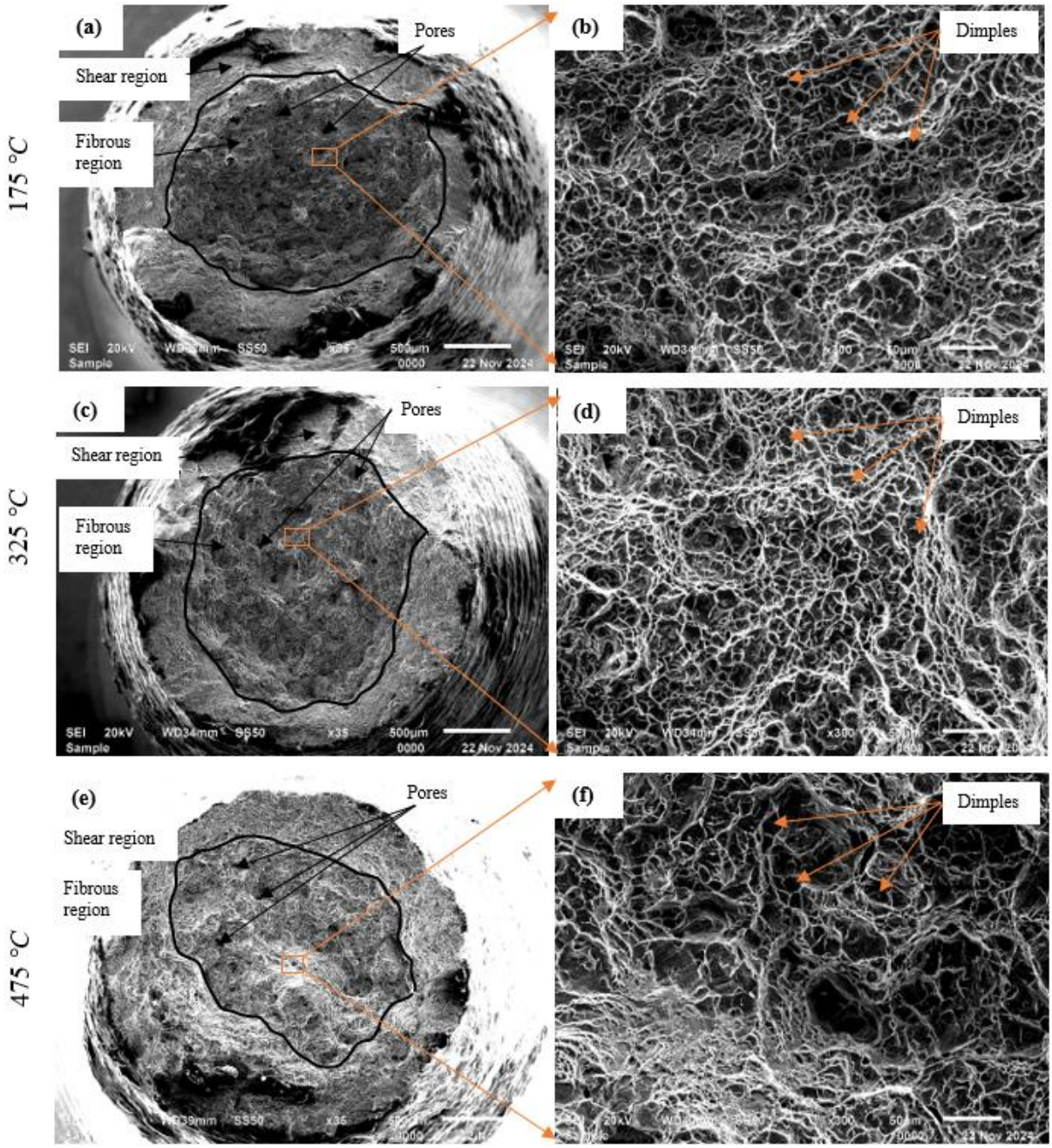

Figure 6.3: SEIs micrograph of the fracture surface of specimens (a, b) 5, (c, d) 8, and (e, f) 11, which were tested at 175 ℃, 325 ℃, and 475 ℃, respectively

It is evident in Figure 6.3 that the three specimens fractured in a ductile manner. Figures 6.3(a), (c), and (e) show a black circular line that separates the regions of shear and fibrous. The diameter of the specimen at the section of fracture was measured at 2.8 mm, 2.6 mm, and 2.5 mm for the specimens that were tested at test temperatures of 175 ℃, 325 ℃, and 475 ℃, respectively. It is noted that as the test temperature was increased, the diameter of the specimens was reduced by 17.6% at 175 ℃, 23.5% at 325 ℃, and 26.5% at 475 ℃. This

reduction in the diameter of the specimens is thought to be due to the severity of deformation taking place during necking. The diameter of the specimen at the fibrous region was measured at 2.0 mm, 1.9 mm, and 1.7 mm. It was observed that as the testing temperature was raised, the size of the dimples increased. The dimples increased from 5 µm measured at room temperature to 5.8 µm at 175 ℃, 6.3 µm at 325 ℃, and 7.1 µm at 475 ℃. This is consistent with the separate works reported in references [25, 26] dimples.

6.3. Fatigue Properties

Six specimens that underwent stress-relieving followed by high-temperature annealing were tested at a temperature of 20 °C, 175 °C, and 325 °C and at varying maximum test stresses of 80, 70, 60, 50, 40, and 30% of the specific average yield stress for each test temperature shown in Table 6.1. One specimen was tested at each of these maximum stresses.

6.3.1. At a temperature of 20 ℃

Table 6.3 shows the number of cycles endured by the specimens at different maximum test stresses at a test temperature of 20 ℃.

Table 6.3: Fatigue life of Ti6Al4V(ELI) specimens at a test temperature of 20 °

Specimen number	Maximum test stress (MPa)	Number of cycles to failure or runout	Change in stress intensity factor (MPa.m$^{0.5}$)
1	666.6	373,193	9.54
2	583.2	Runout	-
3	499.9	Runout	-
4	416.6	Runout	-
5	333.3	Runout	-
6	249.9	Runout	-

It is evident from Table 6.3 that specimen 1, loaded at the highest value of maximum stress, endured 373 193 cycles before failure, while specimens 2-6 attained runout, which was set at 5 000 000 cycles. It is surprising that only specimen 1 underwent fracture and specimens 2-6 did not, as the expectation was that specimens 5 and 6 tested at 40% and 30% of the yield strength could be the only specimens that did not fracture, as normally happens in fatigue testing. The results in Table 6.3 suggest an endurance limit of 583.2 MPa; as below this value, no failure was encountered. Malefane *et al*. [85] studied the high-cycle fatigue life of LPBF

Ti6Al4V(ELI) specimens built in the z-direction at room temperature and obtained at 483 MPa. Similar to the present study, Malefane *et al*. [85] specimens were machined and polished after being additively manufactured. The difference is thought to be due to the longer soaking time at the annealing temperature in the work of Malefane *et al*. [85]. The differences in values of maximum stresses and other factors, such as porosity sizes, may have contributed to this.

The change in stress intensity factor is calculated using the expression, as shown in section 2.5.6 [107] in this document:

$$\Delta K = C\Delta\sigma\sqrt{\pi\sqrt{area}}$$

Specimen 1, which endured maximum stress of 666.6 MPa for 373 193 cycles, had two large defects on the fracture surface, one which was an internal defect of 0.027 mm^2 and the other one which was a surface defect of 0.036 mm^2. It is noted that the area of the surface defect was greater than that of the internal defect. The areas of the two defects were used to determine respective stress intensity factors to determine which one of the two was more critical.

For a surface defect with an area of 0.027 mm^2, a change in stress of 599.94 MPa, with a dimensionless parameter C of 0.5 [41] for this case, since it is an internal defect, the stress intensity factor was calculated as:

$$\Delta K = 0.5 \times 599{,}940{,}000 \times \sqrt{\pi\sqrt{0.00000000271125}}$$

$$\Delta K = 6.82\ MPa.m^{0.5}$$

For a surface defect with an area of 0.036 mm^2, a change in stress of 599.94 MPa, and a dimensionless parameter C of 0.65 [41] for this case, since it is a surface defect, the stress intensity factor, ΔK is equal to:

$$\Delta K = 0.65 \times 599{,}940{,}000 \times \sqrt{\pi\sqrt{0.00000000362748}}$$

$$\Delta K = 9.54\ MPa.m^{0.5}$$

It is evident from the above-calculated values of ΔK that the internal defect is lower than that of the surface defect. This implies that surface defect is more critical.

The change in stress intensity threshold, $\Delta K_{th,}$ was adopted from the reference [108], of vertically built specimens and annealed at temperatures of 800 ℃ and 1 050 ℃ and cooled in argon gas and in a vacuum, to be 3.7 MPa.m$^{1/2}$ and 6.1 MPa.m$^{1/2,}$ respectively. It reported that defects can tolerate an infinite number of load cycles if their stress intensity factor is below the threshold. Above this point, cracks will propagate, and the specimens will have limited lifespans. The calculated values of ΔK, for surface defect and internal defect are greater than that of the adopted values of ΔK_{th}, implying the two defects are capable of propagating a crack and that failure is imminent.

The average value of fracture toughness, K_{IC}, was adopted from the reference [199], for SLM Ti6Al4V specimens that were machined and annealed at a temperature of 780 ℃ for four hours and cooled in a vacuum, to be 148.3 MPa.m$^{1/2}$. If stress intensity is greater than the fracture toughness the material will fail instantaneously, but if the stress intensity factor is lower than the fracture toughness, the material will not experience catastrophic failure. In this scenario, the crack will either remain stable or grow slowly in a stable manner [200], [201]. From section 2.5.6, the fracture toughness K_{IC} [26] is calculated using the expression:

$$K_{IC} = C\sigma_c\sqrt{\pi\sqrt{area}}$$

The calculated value of K_{IC}, for internal defects is 7.58 MPa.m$^{1/2}$, and for surface defects is 10.60 MPa.m$^{1/2}$. The calculated values of K_{IC}, for the internal and surface defects are lower than that of the adopted value of fracture toughness. This implies that the specimen did not experience catastrophic failure but failed slowly in a stable manner.

Figure 6.4 shows the fatigue life of stress-relieved followed by high-temperature annealed Ti6Al4V(ELI) specimens presented in an S-N curve from the data in Table 6.3.

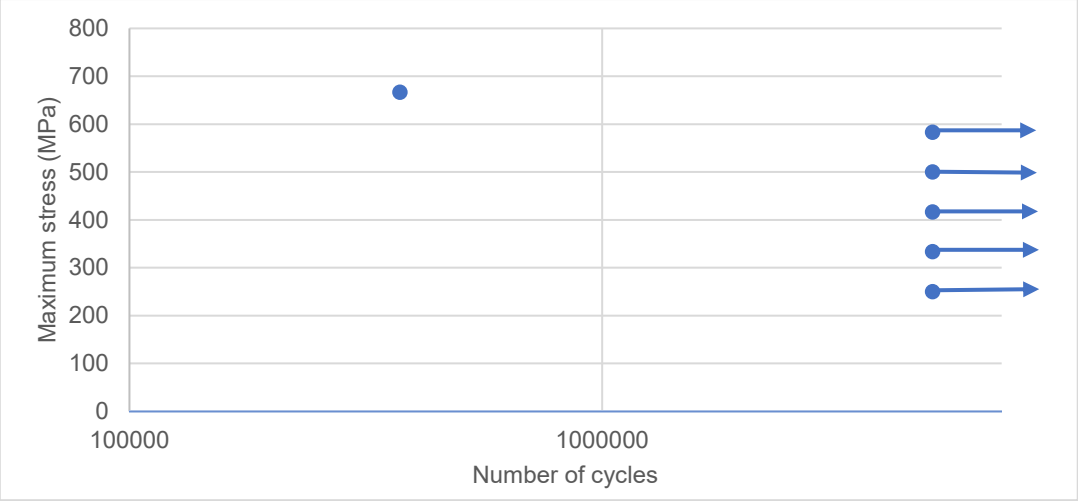

Figure 6.4: S-N curve for LPBF Ti6Al4V(ELI) specimens tested at room temperature

The horizontal arrows in Figure 6.4 imply the presence of a knee at 5 000 000 cycles, and a fatigue endurance limit of 583.2 MPa. This implies that failure is not expected to occur below a maximum stress of 583.2 MPa for a set runout of 5 000 000.

After tension-tension fatigue testing, the fracture surface of the test specimens was analysed using a scanning electron microscope. Figure 6.5 shows the SEI fracture surface of specimen 1 that tested at a temperature of 20 ℃, stressed at a maximum stress of 666.6 MPa, and fractured after 373 193 cycles.

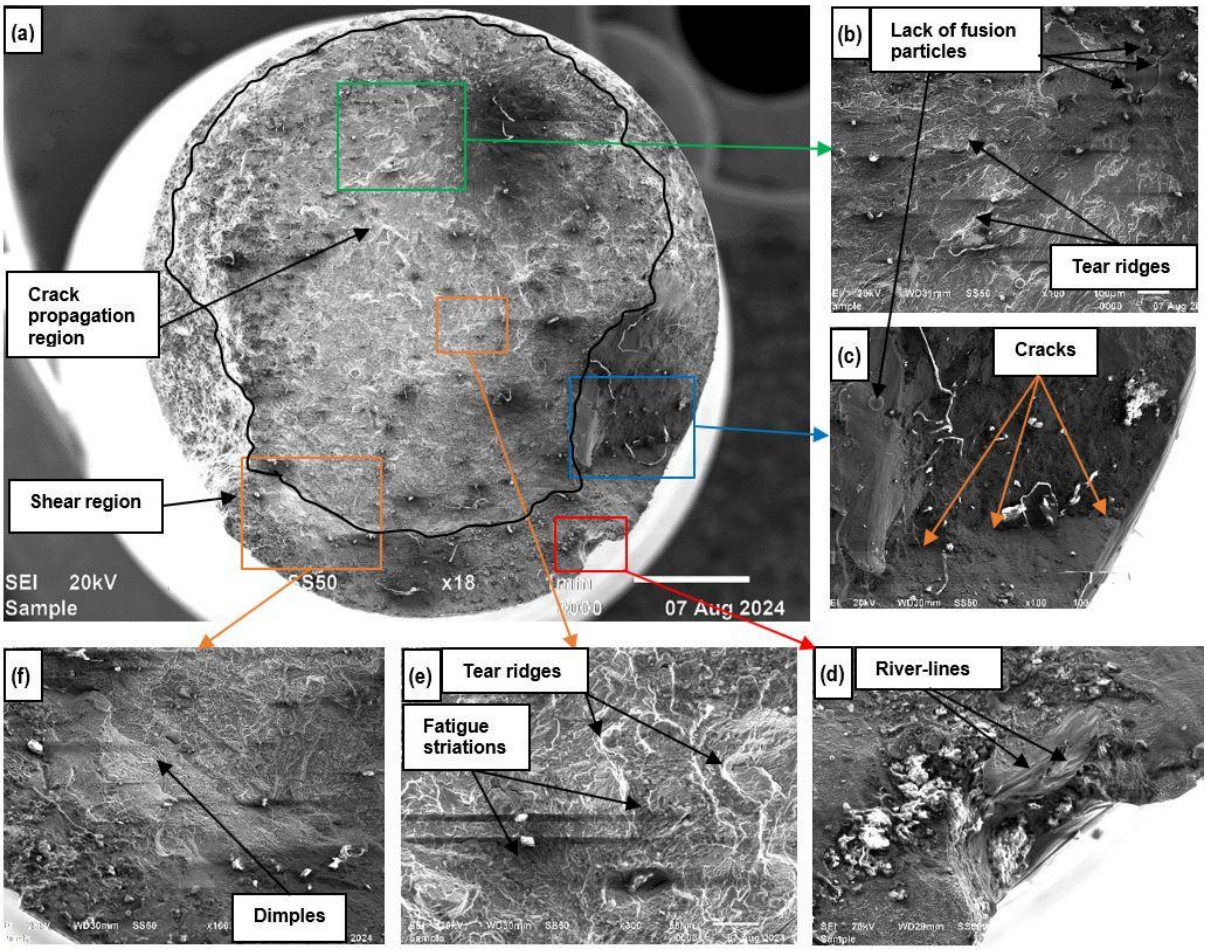

Figure 6.5: Second electron images of the fracture surface of a specimen that was tested at 20 ℃

Figure 6.5(a) shows the overall micrograph of the one-half of a cup-and-cone fracture. The micrograph shows three visible areas of porosity. The first area contains a lack-of-fusion defect, with an area of 0.027 mm^2 shown inside a green outline on the micrograph. Lack-of-fusion pores are formed because of powder that is not fully melted [51]. The second area shows lack of fusion pores with cracks located close to the surface, as shown by a blue outline. These pores have a greater negative impact on fatigue life than gas pores. The third area exhibits an open pore or surface defect located on the surface of the specimen, as outlined in red, with an area of 0.036 mm^2 on the micrograph. This pore can be very detrimental to fatigue performance. Figure 6.5(b) is a higher magnification of a selected area in Figure 6.5(a) that shows unmelted particles of powder with spherical shapes. The figure also contains tear ridges. These tear ridges are visible throughout the crack propagation area shown in Figure 6.5(a). Cracks are indicated in Figure 6.5(c) which also exhibits unmelted particles of powder. A cleavage fracture feature with river-line patterns is visible in the figure too. Higher magnification of an area in Figure

6.5(a) with open-pore defect is shown in Figure 6.5(d). The figure shows river-line patterns as well as fracture-related features. Figure 6.5(e) shows a higher magnification of the crack propagation area, with tear ridges, fatigue cracks, and fatigue striations. These fatigue striations highlight the propagation of a fatigue crack. A higher magnification of the shear region is shown in Figure 6.5(a) is shown in Figure 6.5(f), where quasi-cleavage fracture dimples are present. It can be concluded from the foregoing observations that failure in specimen 1 was significantly influenced by the high incidence of porosity, which explains why this specimen alone failed while other specimens tested at room temperature did not.

6.3.2. At a temperature of 175 °C

Table 6.4 shows the number of cycles endured by the specimens at different maximum test stresses. Testing here was carried out at average yield strength (721.9 MPa as shown in Table 6.1).

Table 6.4: Fatigue life of Ti6Al4V(ELI) specimens at a temperature of 175 °C

Specimen number	**Maximum test stress (MPa)**	**Number of cycles to failure or runout**	**Change in stress intensity factor ($MPa.m^{0.5}$)**
7	577.5	Runout	-
8	505.3	Runout	-
9	433.1	-	-
10	361.0	-	-
11	288.8	-	-
12	216.6	-	-

The limited data in Table 6.4 showing runout at the two highest maximum stresses indicates that specimens tested at a temperature of 175 °C would not fail at and below runout of 5 000 000 cycles. The specimens were tested at lower maximum stresses compared to those tested at room temperature, as a function of the reduced yield stress at the test temperature.

6.3.3. At a temperature of 325 °C

Table 6.5 shows the number of cycles endured by the specimens at different maximum test stresses. Testing here was carried out at an average yield strength (579.7 MPa, as shown in Table 6.1).

Table 6.5: Fatigue life of Ti6Al4V(ELI) specimens at a temperature of 325 °C

Specimen number	Maximum test stress (MPa)	Number of cycles to failure or runout	Change in stress intensity factor (MPa.m$^{0.5}$)
13	463.9	Runout	-
14	405.9	-	-
15	347.9	-	-
16	290.0	-	-
17	214.0	-	-
18	174.0	-	-

Table 6.5 shows that specimen 13 which was tested at the highest maximum stress did not fail till the attainment of 5 000 000 cycles, which was a set runout.

6.4. Microstructures

Figure 6.6 displays microstructures of a LPBF Ti6Al4V(ELI) sample that was tested at room temperature, maximum stress of 666.6 MPa and which endured fatigue 373 931 cycles before fracture. Micrographs were obtained from this specimen near the fatigue fracture surface and a distance of 25 mm away from the fracture surface.

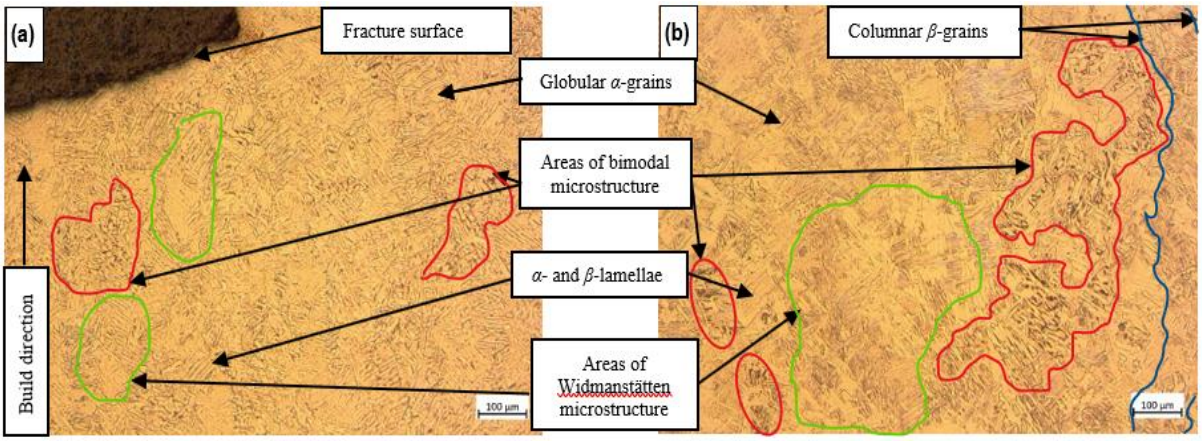

Figure 6.6: Optical micrograph of LPBF Ti6Al4V(ELI) samples (a) near the fatigue fracture area and (b) 25 mm away from the fracture area

The fracture surface of specimen is depicted in Figure 6.6(a). The top left edge of this micrograph shows the microstructure near and on the edge of the specimen. The figure shows the presence of α- and β-laths forming lamellae. The Widmanstätten microstructure is visible

in the micrograph and is shown encircled within green coloured contours on the micrograph. Areas of bimodal microstructure are evident on the micrograph, shown inside red coloured boundaries on the micrograph. Globular α-grains are visible as well on the micrograph. The average widths of the α- and β-laths in this micrograph were measured at 7.4±0.4 µm and 1.2±0.2 µm, respectively. The microstructure of the fatigue sample on the grip section at a distance of 25 mm away from the fracture surface is shown in Figure 6.6(b). Both α- and β-lath lamellae and Widmanstätten microstructure are observed in this micrograph. The bimodal microstructure is also evident and is shown encircled inside red colour boundaries on the micrograph. The figure illustrates a columnar β-grain that is identified by a blue line, which has colonies of α- and β-laths within it,. The average widths of the α- and β-laths in this micrograph were measured at 6.7±0.3 µm and 1.1±0.3 µm, respectively. The difference in the average widths of the α- and β-laths in these two figures, is thought to be the result of deformation effects which produced heat during fatigue fracture that could have contributed to the enlarged widths of the α- and β-laths in Figure 6.6(b).

Comparing the α- and β-laths in Figure 6.6(b) with those in Figure 4.6(b) in section 4.2.3, the average widths of α- and β-laths were measured at 8.2±1.2 µm and 1.2±0.25 µm, respectively. It is noted that there are differences in the average widths; for the β-laths, the difference is 9%, though the difference falls within their respective standard deviation, which renders them insignificant; for the α-laths, the difference is high at 18%. This reduces the reliability of the measured values' widths.

Comparing the α- and β-laths in Figure 6.6(a) with those in Figure 4.6(b) in section 4.2.3, shows there to be no difference in the measured average values of β-laths, as both were at 1.2 µm. The difference in the widths of the α-laths in both cases was 9%, and fell within their respective standard deviations, thus implying that it was insignificant.

6.5. Vickers Microhardness

Table 6.6 presents the average values of Vickers hardness of the fatigue.

Table 6.6: Statistical values of Vickers hardness at different distances from the fracture surface

Distance from the fracture surface (µm)	Average hardness (HV)	Standard deviation	Coefficient of variance (%)	Total change in hardness from far distance hardness (%)
20	300.1	22.1	7.4	5.8
120	299.7	29.1	9.7	5.9
220	307.9	19.3	6.2	3.4
320	314.1	14.3	4.5	1.4
420	318.7	13.2	4.1	0.0
25000	318.6	11.9	3.7	0

The average value of hardness for as-built Ti6Al4V alloy is about 362 HV [168]. It is evident from Tabe 6.6 that high-temperature annealing heat treatment significantly reduced the hardness of the alloy to 318 HV. It is evident from Table 6.6 that the average values of Vickers microhardness rounded off to the nearest whole number remained constant initially and then recorded a continuous increase with distance away from the fracture surface, and then remained constant (at ~318 HV) beyond a distance of 420 µm. This trend indicates a dependence of the hardness of the tested Ti6Al4V(ELI) specimens on the severity of deformation during fracture. The highest CoV for the values presented in this table was determined to be 9.7%. This moderate CoV implies that the obtained data were moderately dispersed away from the mean and each other.

The average values of Vickers microhardness listed in Table 6.6 are plotted in Figure 6.7.

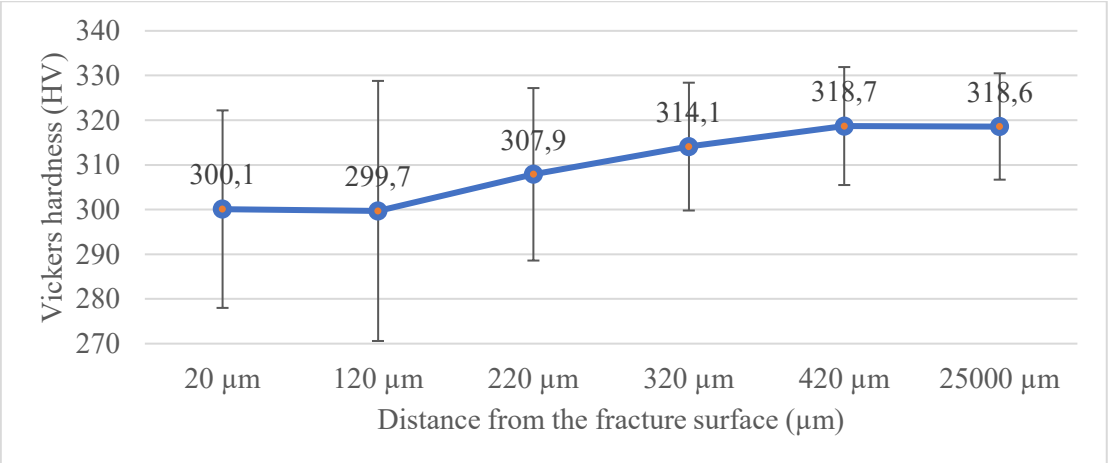

Figure 6.7: Average values of Vickers hardness of specimen 1 that was tested in tension-tension fatigue at a temperature of 20 ℃

Figure 6.7 shows a direct relationship between the mean values of hardness and distance away from the fracture surface, with the exception of points between distances of 20 µm and 120 µm, as well as 420 µm and 25 000 µm, away. The curve confirms the observations made on the values presented in Table 6.6 that, as the distance away from the fracture surface increased, the values of hardness were initially constant and then increased at a more or less constant rate up to a point and then remained constant beyond there. The results show that fracture due to fatigue did influence the hardness of the alloy, though the significance of this influence is in doubt as the calculated average values were all within the error bars of one another.

6.6. Conclusions

This chapter aimed to determine the effect of temperature on the fatigue behaviour of Ti6Al4V(ELI). The results showed that:

- Failure did not occur for maximum stresses below 583.2 MPa.
- Fracture occurred slowly in a stable manner for the sole fractured specimen, as the calculated values of the stress intensity factor were higher than the stress intensity threshold adopted from literature but were lower than the value of fracture toughness adopted from literature.
- Testing at a temperature of 475 ℃ significantly affected the mechanical properties of the alloy, as tensile strength decreased significantly with a slight increase in ductility.
- The severity of fracture marginally increased the average widths of α- and β-laths, as the widths were marginally wider near the fatigue fracture surface.
- The severity of fracture slightly reduced the average values of Vickers microhardness, as average values of hardness were lowest closer to the fracture.

The obtained results showed that the additively manufactured Ti6Al4(ELI) that was used in the present study had high fatigue strength. Reference [52] reported that the micro-CT scans of LPBF samples revealed a low degree of porosity, and the material's density was greater than 99.9%.

CHAPTER 7: CONCLUSIONS AND RECOMMENDATIONS

7.1. Introduction

This chapter contains conclusions based on the results obtained and the recommendations for future work on studies similar to this one.

7.2. Conclusions

This study aimed to determine the effect of changes in temperature above room temperature and the effect of elevated temperatures on the quasi-static behaviour of the additively manufactured Ti6Al4V(ELI) alloy, as a prelude to high temperature fatigue testing of the material. The following conclusions were be drawn from the obtained results.

- High-temperature annealing heat treatment caused a reduction of the values of yield strength, ultimate tensile strength, modulus of elasticity and an increase in ductility.
- An increase in test temperature led to a reduction in yield strength, ultimate tensile strength, and modulus of elasticity, as well as an increase in ductility.
- The test temperature of 475 ℃ significantly affected the mechanical properties of the alloy, as tensile strength dropped significantly, though with a slight increase of ductility.
- The tensile specimens failed in a ductile manner, with the fracture surfaces showing regions of fibrous and shear failure and exhibited dimples.
- An increase in test temperature caused an increase in the sizes of dimples.
- Stress-relieving did not influence the original microstructure, but high-temperature annealing replaced the α’ laths with α- and β-laths.
- An increase in soaking temperature led to an increase in the widths of α-laths and β-laths.
- High-temperature annealing led to a reduction of the hardness of the alloy.
- An increase in test temperature caused a reduction of the mean values of Vickers microhardness.
- The severity of necking led to an increased reduction in the hardness of the tested specimens at all test temperatures.

- Failure due to fatigue did not occur for maximum stresses below 583.2 MPa.

The obtained results showed that the application of the Ti6Al4V(ELI) alloy at a temperature of 475 °C will significantly affect their mechanical properties.

7.3. Recommendations for Future Work

The following recommendations should be considered for future work:

- Tensile testing at a temperature of 475 °C significantly affected the mechanical properties, as ductility was increased slightly and tensile strength dropped significantly. Because of this, it is expected that the fatigue testing at 475 °C will influence the fatigue behaviour of the alloy. Therefore, it is recommended that future work be done at this temperature and possibly even higher temperatures to obtain confirmation of the effect of higher temperatures on the fatigue behaviour of the alloy.
- Since it is known that a decrease in tensile strength lowers the fatigue strength of the alloy, and an increase in ductility increases its fatigue strength, it is crucial to investigate the relationships between these two mechanical characteristics and as the test temperature rises. Moreover, the temperatures at which each one of these two trends becomes insignificant should be identified. Further, the temperature at which the fatigue strength of the alloy starts to decrease must be determined, as must the trend of the fatigue strength with further increase of test temperature.
- The Ti6Al4V(ELI) components in aircraft experience both temperatures above and below room temperature while in service. As the present study only focused on temperatures above room temperature, future fatigue studies should be conducted at temperatures below room temperature to determine the effect of low temperatures on the fatigue behaviour of the alloy.
- It is recommended that future works use micro-CT to identify micro-cracks and pores on test specimens prior to testing in order to predict the fatigue life of specimens prior to fatigue testing and provide comparison of such results with those from actual fatigue testing.

REFERENCES

[1] Madyira D.M., "The Effect of High Speed Machining on the Fatigue Performance of Ti6Al4V," Doctor of Engineering Dissertation, University of Johannesburg, Johannesburg, 2016, https://hdl.handle.net/10210/225157

[2] Milella P.P., *Fatigue and Corrosion in Metals*. Milano: Springer Milan, 2013. http://dx.doi.org/10.1007/978-88-470-2336-9

[3] Belinky A.J., "High cycle compressive fatigue of unidirectional glass/polyester performed at high frequency," Master of Science Dissertation, Montana State University, Montana, 1994, https://www.montana.edu/composites/documents/Andrew%20Belinky%20thesis.PDF

[4] Edwards P., and Ramulu M., "Fatigue performance evaluation of selective laser melted Ti–6Al–4V," *Materials Science and Engineering: A*, vol. 598, pp. 327–337, Mar. 2014, http://dx.doi.org/10.1016/J.MSEA.2014.01.041

[5] Lee Y., Pan J., Hathway R., and Barkey M., *Fatigue Testing and Analysis (Theory and Practice)*. Burlington: Elsevier Butterworth Heinemann, 2005.

[6] Dieter G.E., *Metallurgy and Metallurgical Engineering*. New York: McGRAW-HILL BOOK COMPANY, 1961.

[7] Basuki E.A., Prajitno D.H., and Muhammad F., "Alloys developed for high temperature applications," in *AIP Conference Proceedings*, American Institute of Physics Inc., Jan. 2017. http://dx.doi.org/10.1063/1.4974409

[8] Zhu Y., Xiong Z., LV J., and Zhao Y, "Testing and evaluation for fatigue crack propagation of Ti-6Al-4V/ELI and 7050-T7452 alloys at high temperatures," *Chinese Journal of Aeronautics*, vol. 31, no. 6, pp. 1388–1398, Jun. 2018, http://dx.doi.org/10.1016/j.cja.2017.06.013

[9] Tokaji K., "High cycle fatigue behaviour of Ti–6Al–4V alloy at elevated temperatures," *Scripta Matererialia*, vol. 54, no. 12, pp. 2143–2148, Jun. 2006, http://dx.doi.org/10.1016/J.SCRIPTAMAT.2006.02.043

[10] Jiao Z.H., Xu R.D., Yu H.C., and Wu X.R., "Evaluation on Tensile and Fatigue Crack Growth Performances of Ti6Al4V Alloy Produced by Selective Laser Melting," in *Procedia Structural Integrity*, Elsevier B.V., 2017, pp. 124–132, http://dx.doi.org/10.1016/j.prostr.2017.11.069

[11] Arakere N.K., Goswami T., Krohn J., and Ramachandran N., "High Temperature Fatigue Crack Growth Behavior of Ti-6A1-4V," *High Temperature Materials and Processes*, vol. 21, no. 4, 2011, http://dx.doi.org/10.1515/HTMP.2002.21.4.229

[12] Sterling A., Shamsaei N., Torries B., and Thompson S.M., "Fatigue Behaviour of Additively Manufactured Ti-6Al-4 v," in *Procedia Engineering*, Elsevier Ltd, 2015, pp. 576–589, http://dx.doi.org/10.1016/j.proeng.2015.12.632

[13] Rabalo M.A., Rubio E.M., Agustina B., and Camacho A.M., "Hybrid additive and subtractive manufacturing: Evolution of the concept and last trends in research and industry," in *Procedia CIRP*, Elsevier B.V., 2023, pp. 741–746, http://dx.doi.org/10.1016/j.procir.2023.06.127

[14] Bourell D., Kruth J.P., Leu M., Levy G., Rosen D., Beese A.M., Clare A., "Materials for additive manufacturing," *CIRP Annals Manufacturing Technology*, vol. 66, no. 2, pp. 659–681, 2017, http://dx.doi.org/10.1016/j.cirp.2017.05.009

[15] ASTM International, "Standard Terminology for Additive Manufacturing—Coordinate Systems and Test Methodologies," Ohio, 2013.

[16] Wohlers T., and Gornet T., "History of Additive Manufacturing," 2015, https://wohlersassociates.com/wp-content/uploads/2022/08/history2015.pdf

[17] Becker T.H., Beck M., and Scheffer C., "14 th International RAPDASA conference held at the Central University of Technology in South Africa in 2013," 2013, http://www.scielo.org.za/scielo.php?script=sci_arttext&pid=S2224-78902015000100002

[18] Atatreh S., Alyammahi M.S., Vasilyan H., Alkindi T., and Susantyoko R.A., "Evaluation of the infill design on the tensile properties of metal parts produced by fused filament fabrication," *Results in Engineering*, vol. 17, Mar. 2023, http://dx.doi.org/10.1016/j.rineng.2023.100954

[19] Patterson A., Messimer S.L., and Farrington P.A., "Overhanging Features and the SLM/DMLS Residual Stresses Problem: Review and Future Research Need", http://dx.doi.org/10.20944/preprints201703.0202.v2

[20] Ribeiro A.S., Correia J.A., Silva A.L., and de Jesus A.M., "Evolution nof Fatigue History," 2010. [Online]. Available: https://www.researchgate.net/publication/299397997

[21] Zöllner D., "Impact of a strong temperature gradient on grain growth in films," *Model Simul Mat Sci Eng*, vol. 30, no. 2, Mar. 2022, http://dx.doi.org/10.1088/1361-651X/ac44a8

[22] Jovanović M.T., Tadić S., Zec S., Mišković Z., and Bobić I., "The effect of annealing temperatures and cooling rates on microstructure and mechanical properties of investment cast Ti-6Al-4V alloy," *Materials & Design*, vol. 27, no. 3, pp. 192–199, 2006, doi: http://dx.doi.org/10.1016/j.matdes.2004.10.017

[23] Moloi T., Dzogbewu T.C., Maringa M., and Muiruri A., "Quasi-static tensile properties of DMLS TI6AL4V(ELI) specimens exposed to two different heat treatment processes and tested at different elevated temperatures," *Results in Engineering*, vol. 22, p. 102290, Jun. 2024, http://dx.doi.org/10.1016/j.rineng.2024.102290

[24] Shaikh A., Kumar S., Dawari A., Kirwai S., Patil A., and Singh R., "Effect of temperature and cooling rates on the α+β morphology of Ti-6Al-4V alloy," in *Procedia Structural Integrity*, Elsevier B.V., 2019, pp. 782–789, http://dx.doi.org/10.1016/j.prostr.2019.07.056

[25] Kumar S., Chattopadhyay K., and Singh V., "Tensile Behavior of Ti-6Al-4V alloy at Elevated Temperatures," 2014. [Online]. Available: https://www.researchgate.net/publication/308787239

[26] Ivanov S., Gushchina M., Artinov A., Khomutov M., and Zemlyakov E., "Effect of Elevated Temperatures on the Mechanical Properties of a Direct Laser Deposited Ti-6Al-4V," *Materials*, vol. 14, no. 21, 2021, http://dx.doi.org/10.3390/ma

[27] Singh A., and Singh H., "Metal Additive Manufacturing: From History to Applications," 2022, pp. 3–32. http://dx.doi.org/10.1007/978-3-030-89401-6_1

[28] Shellabear M., and Nyrhilä O., “DMLS-DEVELOPMENT HISTORY AND STATE OF THE ART,” Erlangen, Sep. 2004. Accessed: Nov. 13, 2024. [Online]. Available: https://laseroflove.wordpress.com/wp-content/uploads/2009/10/dmls_history.pdf

[29] Bourell D.L., Beaman Jr. J.J., Leu M.C., and Rosen D.W., “A Brief History of Additive Manufacturing and the 2009 Roadmap for AM,” Austin, Sep. 2009. Accessed: Nov. 13, 2024. [Online]. Available: https://www.turkcadcam.net/haber/2009/rapidtech-workshop/presentations/Presentation02.pdf

[30] Sharma A., Liu Y., Nian Q., and Jiao Y., “Data-driven Approach to Predict the Static and Fatigue Properties of Additively Manufactured Ti-6Al-4V,” Arizona State University, Tempe, 2020, https://keep.lib.asu.edu/items/158581

[31] Carlos J., and Santos C., “A Qualification Methodology for Additively Manufactured Parts,” Repositorio Aberto da Universidade do Porto, Porto, 2016, https://repositorio-aberto.up.pt/bitstream/10216/88491/2/145662.pdf

[32] ISO/ASTM 52900, “Additive manufacturing-General principles-Fundamentals and vocabulary,” 2021, https://www.iso.org/obp/ui/#iso:std:iso-astm:52900:ed-2:v1:en

[33] Calderaro D.R., Lacerda D.P., and Veit D.R., “Selection of additive manufacturing technologies in productive systems: a decision support model,” *Gestão & Produção*, vol. 27, no. 3, 2020, http://dx.doi.org/10.1590/0104-530x5363-20

[34] Mwema F.M., and Akinlabi E.T., “Basics of Fused Deposition Modelling (FDM),” 2020, pp. 1–15. http://dx.doi.org/10.1007/978-3-030-48259-6_1

[35] Dehghanghadikolaei A., and Fotovvati B., “Additive Manufacturing Methods A Brief Overview,” 2018. [Online]. Available: https://www.researchgate.net/publication/327701079

[36] Tofail S.A.M., Koumoulos E.P., Bandyopadhyay A., Bose S., O’Donoghue L., and Charitidis C., “Additive manufacturing: scientific and technological challenges, market uptake and opportunities,” *Materials Today*, vol. 21, no. 1, pp. 22–37, Jan. 2018, http://dx.doi.org/10.1016/j.mattod.2017.07.001

[37] Nalla R.K., Boyce B.L., Campbell J.P., Peters J.O., and Ritchie R.O., "Influence of microstructure on high-cycle fatigue of Ti-6Al-4V: Bimodal vs. lamellar structures," in *Metallurgical and Materials Transactions A: Physical Metallurgy and Materials Science*, Minerals, Metals and Materials Society, 2002, pp. 899–918. http://dx.doi.org/10.1007/s11661-002-0160-z

[38] Zenou M., and Grainger L., "Additive manufacturing of metallic materials," in *Additive Manufacturing*, Elsevier, 2018, pp. 53–103. http://dx.doi.org/10.1016/B978-0-12-812155-9.00003-7

[39] Azarniya A., Colera X.G., Mirzaali M.J., Sovizi S., Brtolomeu F., St. Weglowski M., Wits W.W., Yap C.Y., Ahn J., Miranda G., Silva F.S., Madaah H., Hamid R., Ramakrishna S., Zadpoor A.A., "Additive manufacturing of Ti–6Al–4V parts through laser metal deposition (LMD): Process, microstructure, and mechanical properties," *Journal of Alloys and Compounds*, vol. 804, pp. 163–191, Oct. 2019, http://dx.doi.org/10.1016/j.jallcom.2019.04.255

[40] Gibson I., Rosen D., and Stucker B., "Directed Energy Deposition Processes," in *Additive Manufacturing Technologies*, New York, NY: Springer New York, 2015, pp. 245–268. http://dx.doi.org/10.1007/978-1-4939-2113-3_10

[41] Günther J., Krewerth D., Lippmann T., Leuders S., Troster T., Weidner A., Biermann H., Niendorf T., "Fatigue life of additively manufactured Ti–6Al–4V in the very high cycle fatigue regime," *International Journal of Fatigue*, vol. 94, pp. 236–245, Jan. 2017, https://doi.org/10.1016/j.ijfatigue.2016.05.018

[42] Singh R., Singh S., and Hashmi M.S.J., "Implant Materials and Their Processing Technologies," in *Reference Module in Materials Science and Materials Engineering*, Elsevier, 2016. http://dx.doi.org/10.1016/B978-0-12-803581-8.04156-4

[43] Unionfab, "3D Printing Tolerance: What It Is and How to Improve (2024)," Unionfab. Accessed: Nov. 25, 2024. [Online]. Available: https://www.unionfab.com/blog/2024/09/3d-printing-tolerance

[44] Boyer R.R., "Titanium and Its Alloys: Metallurgy, Heat Treatment and Alloy Characteristics," in *Encyclopedia of Aerospace Engineering*, Wiley, 2010. https://doi.org/10.1002/9780470686652.eae198

[45] Jaber H., Kónya J., Kulcsár K., and Kovács T., "Effects of Annealing and Solution Treatments on the Microstructure and Mechanical Properties of Ti6Al4V Manufactured by Selective Laser Melting," *Materials*, vol. 15, no. 5, Mar. 2022, https://doi.org/10.3390/ma15051978

[46] IN3DTEC, "Metal 3D Printing Technologies: SLM vs. DMLS." Accessed: Nov. 19, 2024. [Online]. Available: https://www.in3dtec.com/metal-3d-printing-technologies-slm-vs-dmls/

[47] Patterson A.E., Messimer S.L., and Farrington P.A., "Overhanging Features and the SLM/DMLS Residual Stresses Problem: Review and Future Research Need," *Technologies (Basel)*, vol. 5, no. 4, p. 15, Apr. 2017, https://doi.org/10.3390/technologies5020015

[48] Brennan M.C., Keist J.S., and Palmer T.A., "Defects in Metal Additive Manufacturing Processes," *Journal of Materials Engineering and Performance*, vol. 30, no. 7, pp. 4808–4818, Jul. 2021, https://ui.adsabs.harvard.edu/link_gateway/2021JMEP...30.4808B/doi:10.1007/s11665-021-05919-6

[49] Shamsaei N., and Simsiriwong J., "Fatigue behaviour of additively-manufactured metallic parts," in *Procedia Structural Integrity*, Elsevier B.V., 2017, pp. 3–10. https://doi.org/10.1016/j.prostr.2017.11.053

[50] Chern A.H., Nandwana P., Yuan T., Kirka M.M., Dehoff R.R., Liaw P.K., Duty C.E., "A review on the fatigue behavior of Ti-6Al-4V fabricated by electron beam melting additive manufacturing," *International Journal of Fatigue*, vol. 119, pp. 173–184, Feb. 2019, https://doi.org/10.1016/j.ijfatigue.2018.09.022

[51] Kan W.H., Chiu L.N.S., Lim C.V.S., Zhu Y., Tian Y., Jiang D., Huang A, "A critical review on the effects of process-induced porosity on the mechanical properties of alloys

fabricated by laser powder bed fusion," Jun. 01, 2022, *Springer*. https://doi.org/10.1007/s10853-022-06990-7

[52] Moletsane M.G., "Microstructure and mechanical properties of Ti6Al4V (ELI) parts produced by DMLS," Master Dissertation, Central University of Technology, Free State, Bloemfontein, 2016.

[53] Fotovvati B., Namdari N., and Dehghanghadikolaei A., "Fatigue performance of selective laser melted Ti6Al4V components: State of the art," *Material Research Express*, vol. 6, no. 1, Jan. 2019, http://dx.doi.org/10.1088/2053-1591/aae10e

[54] Chastand V., Tezenas A., Cadoret Y., Quaegebeur P., Maia W., and Charkaluk E., "Fatigue characterization of Titanium Ti-6Al-4V samples produced by Additive Manufacturing," in *Procedia Structural Integrity*, Elsevier B.V., 2016, pp. 3168–3176, https://doi.org/10.1016/j.prostr.2016.06.395

[55] Moletsane M.G., Krakhmalev P., Kazantseva N., du Plessis A., Yadroitsava I., and Yadroitsev I., "Tensile properties and microstructure of direct metal laser-sintered Ti6Al4V (ELI) alloy," *South African Journal of Industrial Engineering*, vol. 27, no. 3SpecialIssue, pp. 110–121, 2016, http://dx.doi.org/10.7166/27-3-1667

[56] Guzanová A., Ižaríková G., Brezinová J., Živčák J., Draganovská D., and Hudák R., "Influence of build orientation, heat treatment, and laser power on the hardness of Ti6Al4V manufactured using the DMLS process," *Metals (Basel)*, vol. 7, no. 8, Aug. 2017, https://doi.org/10.3390/met7080318

[57] Vranić A., Bogojević N., Ćirić-Kostić S., Croccolo D., and Olmi G., "Advantages and drawbacks of additive manufacturing," *IMK-14 - Istrazivanje i razvoj*, vol. 23, no. 3, pp. 57–62, 2017, http://dx.doi.org/10.5937/IMK1702057V

[58] Khidhir B.A., Ahmed Y.M., Sahari K., Ishak M., Salleh K., Sahari M., Khidhir A., "Titanium and its Alloy," 2014. [Online]. Available: https://www.researchgate.net/publication/267034976

[59] Leyens. C and Peters M., *Titanium and Titanium Alloys : Fundamentals and Applications*. Wiley, 2006, http://dx.doi.org/10.1002/3527602119

[60] Inc. C. RMI Titanium International Metals, "TITANIUM ALLOY GUIDE," Niles, Jan. 2000. [Online]. Available: www.RMITitanium.com

[61] Dickins A., "Fabrication of Micro-scale Features on Titanium Alloys Through Micromilling," 2017, https://doi.org/10.13140/RG.2.2.21835.23840

[62] Sun H., Yu L.M., Liu Y.C., Zhang L.Y., Liu C.X., Li H.J., Wu J.F., "Effect of heat treatment processing on microstructure and tensile properties of Ti-6Al-4V-10Nb alloy," *Transactions of Nonferrous Metals Society of China (English Edition)*, vol. 29, no. 1, pp. 59–66, Jan. 2019, https://doi.org/10.1016/S1003-6326(18)64915-5

[63] Veiga C., Davim J.P., and Loureiro A.J.R., "Properties and applications of titanium alloys: A brief review," *Rev. Advance Material Science*, no. 32, pp. 14–34, 2012, [Online]. Available: https://www.researchgate.net/publication/283863116

[64] Ran C., Sheng Z., Chen P., Zhang W., and Chen Q., "Effect of microstructure on the mechanical properties of Ti–5Al–5Mo–5V–1Cr–1Fe alloy," *Materials Science and Engineering: A*, vol. 773, Jan. 2020, https://doi.org/10.1016/j.msea.2019.138728

[65] Gospodinov D., Ferdinandov N., and Dimitrov S., "Classification, properties and application of titanium and its alloys," 2016. [Online]. Available: https://www.researchgate.net/publication/324152759

[66] Hosseini S., "Fatigue of Ti-6Al-4V," in *Biomedical Engineering - Technical Applications in Medicine*, InTech, 2012. https://doi.org/10.5772/45753

[67] Liu S., and Shin Y.C., "Additive manufacturing of Ti6Al4V alloy: A review," *Material Design*, vol. 164, p. 107552, Feb. 2019, https://doi.org/10.1016/J.MATDES.2018.107552

[68] Zhao J.R., Hung F.Y., Lui T.S., and Wu Y.L., "The relationship of fracture mechanism between high temperature tensile mechanical properties and particle erosion resistance of selective laser melting Ti-6al-4v alloy," *Metals (Basel)*, vol. 9, no. 5, May 2019, https://doi.org/10.3390/met9050501

[69] Yan M., and Yu P., "An Overview of Densification, Microstructure and Mechanical Property of Additively Manufactured Ti-6Al-4V — Comparison among Selective Laser

Melting, Electron Beam Melting, Laser Metal Deposition and Selective Laser Sintering, and with Conventional Powder," in *Sintering Techniques of Materials*, InTech, 2015, https://doi.org/10.5772/59275

[70] Ahmed T., and Rack H.J., "Phase transformations during cooling in α+β titanium alloys," *Materials Science and Engineering: A*, vol. 243, no. 1–2, pp. 206–211, Mar. 1998, https://doi.org/10.1016/S0921-5093(97)00802-2

[71] Sieniawski J., Ziaja W., Kubiak K., and Motyk M., "Microstructure and Mechanical Properties of High Strength Two-Phase Titanium Alloys," in *Titanium Alloys - Advances in Properties Control*, InTech, 2013, https://doi.org/10.5772/56197

[72] Belan J., Uhricik M., Hanusova P., and Vasko A., "The Ti6Al4V Alloy Microstructure Modification Via Various Cooling Rates, its Influence on Hardness and Microhardness," *Manufacturing Technology*, vol. 20, no. 5, pp. 560–565, 2020, https://doi.org/10.21062/mft.2020.095

[73] Dai N., Zhang L., Zhang J., Zhang X., Ni Q., Chen Y., Wu M., Yang C. "Distinction in corrosion resistance of selective laser melted Ti-6Al-4V alloy on different planes," *Corrosion Science*, vol. 111, pp. 703–710, Oct. 2016, https://doi.org/10.1016/j.corsci.2016.06.009

[74] Murgau C.C., "Microstructure Model for Ti-6Al-4V used in Simulation of Additive Manufacturing Material Mechanics," Lulea University of Technology, Lulea, 2016.

[75] Benedetti M., and Fontanari V., "The effect of bi-modal and lamellar microstructures of Ti-6Al-4V on the behaviour of fatigue cracks emanating from edge-notches," *Fatigue & Fracture of Engineering Material & Structure*, vol. 27, no. 11, pp. 1073–1089, Nov. 2004, https://doi.org/10.1111/j.1460-2695.2004.00825.x

[76] Campbell F.C., *Fatigue and Fracture*. Ohio: ASM International, 2012.

[77] Mysen B., and Richet P., "Glasses Versus Melts," in *Silicate Glasses and Melts*, Amsterdam: Elsevier B.V, 2005, pp. 35–68.

[78] Nunes R., "Fractogarphy Volume 12: ASM Handbook," Ohio, 1987.

[79] Walker P., and Tarn W.H., *CRC handbook of metal etchants*. CRC Press, 1991.

[80] Nikon SLM Solutions, "Ti-Alloy Ti6Al4V ELI (Grade 23) / 3.7165 / B348 / F136," Lubeck. Accessed: Nov. 20, 2024. [Online]. Available: https://www.slm-solutions.com/fileadmin/Content/Powder/MDS/MDS_TiAlloy_Ti6Al4V__ELI_0719_EN.pdf

[81] Davim J.P., Veiga C., Davim J.P., and Loureiro A.J.R., "Properties and applications of titanium alloys: A brief review," *Reviews on Advanced Materials Science*, pp. 14–34, 2012, [Online]. Available: https://www.researchgate.net/publication/283863116

[82] Lim S. J., and Huh H., "Ductile fracture behavior of BCC and FCC metals at a wide range of strain rates," *International Journal of Impact Engineering*, vol. 159, Jan. 2022, https://doi.org/10.1016/j.ijimpeng.2021.104050

[83] Callister Jr. W.D. and Rethwisch D., *Material Science and Engineering - An introduction*, 10th ed. John Wiley & Sons, Inc, 2018.

[84] Krakhmalev P., Fredriksson G., Yadroitsava I., Kazantseva N., Du Plessis A., and Yadroitsev I., "Deformation behavior and microstructure of Ti6Al4V manufactured by SLM," in *Physics Procedia*, Elsevier B.V., 2016, pp. 778–788. https://doi.org/10.1016/j.phpro.2016.08.080

[85] Malefane L.B., du Preez W.B., Maringa M., and du Plessis A., "Tensile and high cycle fatigue properties of annealed TI6AL4V (ELI) specimens produced by direct metal laser sintering," *South African Journal of Industrial Engineering*, vol. 29, no. 3 Special Edition, pp. 299–311, 2018, https://doi.org/10.7166/29-3-2077

[86] Jin N., Yan Z., Wang Y., Cheng H., and Zhang H., "Effects of heat treatment on microstructure and mechanical properties of selective laser melted Ti-6Al-4V lattice materials," *Internation Journal of Mechanical Sciences*, vol. 190, Jan. 2021, https://doi.org/10.1016/j.ijmecsci.2020.106042

[87] Bai H., Deng H., Chen L., Liu X., Qin X., Zhang D., Liu T., Cui X., "Effect of heat treatment on the microstructure and mechanical properties of selective laser-melted Ti64

and Ti-5Al-5Mo-5v-1Cr-1Fe," *Metals (Basel)*, vol. 11, no. 4, Apr. 2021, https://doi.org/10.3390/met11040534

[88] Topper T. H., Wetzel R. M., and Morrow J., "Neuber's Rule Applied to Fatigue of Notched Specimens," 1967.

[89] Suresh S.S., *Fatigue of materials*. Cambridge University Press, 1998.

[90] Sharma A., Oh M.C., and Ahn B., "Recent advances in very high cycle fatigue behavior of metals and alloys—a review," Sep. 01, 2020, *MDPI AG*. https://doi.org/10.3390/met10091200

[91] Boyer H.E., *Atlas of Fatigue Curves*. Ohio: ASM lnternatlonal, 1986. [Online]. Available: www.asminternational.org

[92] Campbell F.C., *Elements of Metallurgy and Engineering Alloys*. ASM International, 2008.

[93] Gong H., Rafi H.K., Rafi K., Starr T., and Stucker B., "Effect of defects on fatigue tests of as-built TI-6AL-4V parts fabricated by selective laser melting," 2012. [Online]. Available: https://www.researchgate.net/publication/279687860

[94] Glodez S., Flasker J., and Ren Z., "Crack initiation and crack propagation in the contact area of two cylinders," 1996. [Online]. Available: www.witpress.com

[95] Blake A., *Handbook of Mechanics, Material and Structures*. Arizona: A Wiley-Interscience Publication, 1985.

[96] Totten G., "Fatigue Crack Propagation," *Advanced Materials & Processes*, 2008, [Online]. Available: www.asminternational.org

[97] Lietaert K., Cutolo A., Boey D., and Van Hooreweder B., "Fatigue life of additively manufactured Ti6Al4V scaffolds under tension-tension, tension-compression and compression-compression fatigue load," *Sci Rep*, vol. 8, no. 1, Dec. 2018, https://doi.org/10.1038/s41598-018-23414-2

[98] Mouritz A., *Introduction to Aerospace Material*. Woodhead Pub, 2012.

[99] Surowska B., Bieniaś J., and Dębski H., "Fatigue of Unidirectional Carbon Fiber Reinforced Epoxy Composites," in *ECCM15 - 15th European Conference on Composite Materials*, Venice, 2012.

[100] Padmaraj N.H., Vijaya K.M., and Dayananda P., "Experimental study on the tension-tension fatigue behaviour of glass/epoxy quasi-isotropic composites," *Journal of King Saud University - Engineering Sciences*, vol. 32, no. 6, pp. 396–401, Sep. 2020, https://doi.org/10.1016/j.jksues.2019.04.007

[101] Cui W., Wang F., and Huang X., "A unified fatigue life prediction method for marine structures," *Marine Structures*, vol. 24, no. 2, pp. 153–181, Jun. 2011, https://doi.org/10.1016/j.marstruc.2011.02.007

[102] Kumara M.C.M, and Nandish R.V., "Fatigue Failure Analysis of Rotating Turbine Blade with Damage at the Leading Edge," Bangalore, 2014. https://doi.org/10.13140/RG.2.1.3949.3207

[103] Gamstedt E.K., and Sjoègren B.A., "Micromechanisms in tension-compression fatigue of composite laminates containing transverse plies," *Compos Sci Technol*, vol. 59, pp. 167–178, 1999.

[104] Moss D.R., and Basic M., *Pressure vessel design manual, Fourth edition: Chapter 8 on high pressure vessel*. 2010.

[105] Kim Y., and Hwang W., "High-cycle, low-cycle, extremely low-cycle fatigue and monotonic fracture behaviors of low-carbon steel and itswelded joint," *Materials*, vol. 12, no. 24, p. 4111, Dec. 2019, https://doi.org/10.3390/MA12244111

[106] Xin Q., "Durability and reliability in diesel engine system design," in *Diesel Engine System Design*, Elsevier, 2013, pp. 113–202. https://doi.org/10.1533/9780857090836.1.113

[107] Yukitaka Murakami, *Metal Fatigue: Effects of Small Defects and Nonmetallic Inclusions*. Elsevier, 2002.

[108] Leuders S., Thöne M., Riemer A., Niendorf T., Troster T., Richard H.A., Maier H.J., "On the mechanical behaviour of titanium alloy TiAl6V4 manufactured by selective laser melting: Fatigue resistance and crack growth performance," *Int J Fatigue*, vol. 48, pp. 300–307, Mar. 2013, https://doi.org/10.1016/j.ijfatigue.2012.11.011

[109] Pederson R., "Microstructure and Phase Transformation of Ti-6Al-4V," Lulea, 2002. Accessed: Mar. 16, 2024. [Online]. Available: https://www.diva-portal.org/smash/get/diva2:991369/FULLTEXT01.pdf

[110] Moore P., and Booth G., "Mechanical testing of welds," in *The Welding Engineers Guide to Fracture and Fatigue*, Elsevier, 2015, pp. 113–141. https://doi.org/10.1533/9781782423911.2.113

[111] Pedersen M., "Introduction to Metal Fatigue-Concepts and Engineering Approaches," 2018, https://doi.org/10.13140/RG.2.2.25216.28163

[112] Benedetti M., Fontanari V., Bandini M., Zanini F., and Carmignato S., "Low- and high-cycle fatigue resistance of Ti-6Al-4V ELI additively manufactured via selective laser melting: Mean stress and defect sensitivity," *International Journal of Fatigue*, vol. 107, pp. 96–109, Feb. 2018, https://doi.org/10.1016/j.ijfatigue.2017.10.021

[113] Wycisk E., Siddique S., Herzog D., Walther F., and Emmelmann C., "Fatigue performance of laser additive manufactured Ti–6Al–4V in very high cycle fatigue regime up to 109 cycles," *Frontiers in Materials*, vol. 2, Dec. 2015, https://doi.org/10.3389/fmats.2015.00072

[114] Cutolo A., Elangeswaran C., and Van Hooreweder B., "On the Effect of the Stress Ratio on Fatigue Properties of Ti-6Al-4V Produced by Laser Powder Bed Fusion," *Material Design & Processing Communications*, vol. 2022, pp. 1–7, Feb. 2022, https://doi.org/10.1155/2022/3530603

[115] Baragetti S., "Notch corrosion fatigue behavior of Ti-6Al-4V," *Materials*, vol. 7, no. 6, pp. 4349–4366, 2014, https://doi.org/10.3390/ma7064349

[116] Ziaja W., and Kawalec A., "Dwell Fatigue Behavior of Two-Phase Ti-6Al-4V Alloy at Moderate Temperature," *Journal of The Minerals, Metals & Materials Society*, vol. 74, no. 10, pp. 3745–3751, Oct. 2022, https://doi.org/10.1007/s11837-022-05461-3

[117] Ritchie R.O., Davidson D.L., Boyce B.L., Campbell J.P., and Order O., "High-cycle fatigue of Ti-6Al-4V," *Fatigue Fracture Engineering Material Structure*, vol. 22, pp. 621–631, 1999, https://www2.lbl.gov/ritchie/Library/PDF/ROR-HCF_99.pdf

[118] Janeček M., Novy F., Harcuba P., Strasky J., Trsko L., Mhaede M., Wagner L., "The very high cycle fatigue behaviour of Ti-6Al-4V alloy," in *Acta Physica Polonica A*, Polish Academy of Sciences, Oct. 2015, pp. 497–502, https://doi.org/10.12693/APhysPolA.128.497

[119] Pantazopoulos G., "A Short Review on Fracture Mechanisms of Mechanical Components Operated under Industrial Process Conditions: Fractographic Analysis and Selected Prevention Strategies," *Metals (Basel)*, vol. 9, no. 2, p. 148, Jan. 2019, https://doi.org/10.3390/met9020148

[120] ASM International, "Heat treating," Ohio, 2015. Accessed: Mar. 15, 2024. [Online]. Available: https://www.amgindustries.com/ASM%20Subject%20Guide_HeatTreating.pdf

[121] Lekoadi P., Tlotleng M., Maledi N., and Masina B.N., "Effect of heat treatment on microstructure, hardness and tensile properties of high-speed selective laser melted Ti6Al4V," in *2022 RAPDASA-RobMech-PRASA-CoSAAMI Conference*, Pretoria: CSIR, 2022, https://doi.org/10.1051/matecconf/202237011003

[122] Fuad Z.B., "Effect of Heat Treatment on Fatigue Life," Universiti of Malaysia Pahang, Malaysia, 2012, http://umpir.ump.edu.my/id/eprint/6504/1/Effect%20of%20heat%20treatment%20on%20fatigue%20life.pdf

[123] Fragoudakis R., Karditsas S., Savaidis G., and Michailidis N., "The effect of heat and surface treatment on the fatigue behaviour of 56SiCr7 spring steel," in *Procedia Engineering*, Elsevier Ltd, 2014, pp. 309–312. https://doi.org/10.1016/j.proeng.2014.06.268

[124] Rajagopal K.P.A., Jose A.M., Soman A., Dcruz C.J., and Sankar N.N., "Investigation of Physical and Mechanical Properties of Ti Alloy (Ti-6Al-4V) Under Precisely Controlled Heat Treatment Processes," 2015. [Online]. Available: www.jifactor.com

[125] Teixeira Ó., Silva F.J.G., Ferreira L.P., and Atzeni E., "A review of heat treatments on improving the quality and residual stresses of the Ti–6Al–4V parts produced by additive manufacturing," Aug. 01, 2020, *MDPI AG*, https://doi.org/10.3390/met10081006

[126] Mueller F.H., *Heat Treatment and Properties of Iron and Steel*. National Bureau of Standards Library, 1960.

[127] Chandramohan P., Bhero S., Obadele A., Olubambi P.A., and Ravisankar B., "Effect of built orientation on direct metal laser sintering of Ti-6Al-4V," *Indian Journal of Engineering & Materials Sciences*, vol. 25, pp. 69–77, 2018.

[128] Greitemeier D., Palm F., Syassen F., and Melz T., "Fatigue performance of additive manufactured TiAl6V4 using electron and laser beam melting," *International Journal of Fatigue*, vol. 94, pp. 211–217, Jan. 2017, https://doi.org/10.1016/j.ijfatigue.2016.05.001

[129] Frkan M., Konecna R., Nicoletto G., and Kunz L., "Microstructure and fatigue performance of SLM-fabricated Ti6Al4V alloy after different stress-relief heat treatments," in *Transportation Research Procedia*, Elsevier B.V., 2019, pp. 24–29. https://doi.org/10.1016/j.trpro.2019.07.005

[130] Hasib M.T., Ostergaard H.E., Li X., and Kruzic J.J., "Fatigue crack growth behavior of laser powder bed fusion additive manufactured Ti-6Al-4V: Roles of post heat treatment and build orientation," *International Journal of Fatigue*, vol. 142, Jan. 2021, https://doi.org/10.1016/j.ijfatigue.2020.105955

[131] Dhansay N.M., Becker T.H., and Vanmeensel K., "Fatigue crack growth rate threshold of laser powder bed fusion Ti-6Al-4V," 2021. [Online]. Available: https://scholar.sun.ac.za

[132] Clemens H., Mayer S., and Scheu C., "Microstructure and Properties of Engineering Materials," in *Neutrons and Synchrotron Radiation in Engineering Materials Science: From Fundamentals to Applications: Second Edition*, wiley, 2017, pp. 3–20, https://doi.org/10.1002/9783527684489.ch1

[133] Naab B., and Celikin M., "The role of microstructural evolution on the fatigue behavior of additively manufactured Ti–6Al–4V alloy," *Materials Science and Engineering: A*, vol. 859, Nov. 2022, https://doi.org/10.1016/j.msea.2022.144232

[134] Walters C.L., "The Effect of Low Temperatures on the Fatigue of High-strength Structural Grade Steels," *Procedia Materials Science*, vol. 3, pp. 209–214, 2014, https://doi.org/10.1016/j.mspro.2014.06.037

[135] Ritchie R.O., "Mechanisms of fatigue-crack propagation in ductile and brittle solids," *Internationa Journal of Fracture*, vol. 100, pp. 55–83, 1999, https://www2.lbl.gov/ritchie/Library/PDF/ROR_IJFract99.pdf

[136] Motyka M., "Martensite formation and decomposition during traditional and am processing of two-phase titanium alloys—an overview," Mar. 01, 2021, *MDPI AG*, https://doi.org/10.3390/met11030481

[137] Pilchak A.L., Bhattacharjee A., Williams R.E.A., and Williams J.C., "The Effect of Microstructure on Fatigue Crack Initiation in Ti-6Al-4V," The Ohio State University, Columbus, 2009, https://www.gruppofrattura.it/ocs/index.php/ICF/ICF12/paper/download/1623/9093

[138] Bao X., Cheng L., Ding J., Chen X., Lu K., and Cui W., "The effect of microstructure and axial tension on three-point bending fatigue behavior of TC4 in high cycle and very high cycle regimes," *Materials*, vol. 13, no. 1, Jan. 2020, https://doi.org/10.3390/ma13010068

[139] Zhao J., Wang Z., Tian L., Wan J., Zong X., Zhang S., Zhao H., "Study on mechanical properties of Ti-6Al-4 V titanium alloy with different microstructures under combined tension-bending load," *Journal of Alloys and Compound*, vol. 936, Mar. 2023, https://doi.org/10.1016/j.jallcom.2022.168201

[140] Agius D., Kourousis K.I., and Wallbrink C., "A review of the as-built SLM Ti-6Al-4V mechanical properties towards achieving fatigue resistant designs," Jan. 19, 2018, *MDPI AG*, https://doi.org/10.3390/met8010075

[141] Simonelli M., Tse Y.Y., and Tuck C., "Microstructure of Ti-6Al-4V produced by selective laser melting," in *Journal of Physics: Conference Series*, Institute of Physics Publishing, 2012. https://doi.org/10.1088/1742-6596/371/1/012084

[142] Zhang P., He A.N., Liu F., Zhang K., Jiang J., and Zhang D.Z., "Evaluation of low cycle fatigue performance of selective laser melted titanium alloy Ti-6Al-4V," *Metals (Basel)*, vol. 9, no. 10, Oct. 2019, https://doi.org/10.3390/met9101041

[143] Cao F., Zhang T., Ryder M.A., and Lados D.A., "A Review of the Fatigue Properties of Additively Manufactured Ti-6Al-4V," *Journal of The Minerals, Metals & Materials* , vol. 70, no. 3, pp. 349–357, Mar. 2018, https://doi.org/10.1007/s11837-017-2728-5

[144] Cerri E., Ghio E., and Bolelli G., "Effect of surface roughness and industrial heat treatments on the microstructure and mechanical properties of Ti6Al4V alloy manufactured by laser powder bed fusion in different built orientations," *Materials Science and Engineering: A*, vol. 851, Aug. 2022, https://doi.org/10.1016/j.msea.2022.143635

[145] Neikter M., "Microstructure and texture of additive manufactured Ti-6Al-4V," Luleå University of Technology, Luleå, 2017.

[146] Kunz L., Pokorný P., Konečná R., and Nicoletto G., "Propagation of long fatigue cracks in Ti6Al4V alloy produced by direct metal laser sintering," in *Procedia Structural Integrity*, Elsevier B.V., 2019, pp. 222–229. https://doi.org/10.1016/j.prostr.2019.08.030

[147] Yuri T., Ono Y., Ogata T., and Sunakawa H., "Effect of microstructure on high-cycle fatigue properties of Ti-6Al-4V alloy forging at cryogenic temperatures," in *AIP Conference Proceedings*, American Institute of Physics Inc., 2014, pp. 27–33, https://doi.org/10.1063/1.4860600

[148] Carrion P.E., Shamsaei N., Daniewicz S. R., and Moser R. D., "Fatigue behavior of Ti-6Al-4V ELI including mean stress effects," *International Journal of Fatigue*, vol. 99, pp. 87–100, Jun. 2017, https://doi.org/10.1016/j.ijfatigue.2017.02.013

[149] Vayssette B., Saintier N., Brugger C., Elmay M., and Pessard E., "Surface roughness of Ti-6Al-4V parts obtained by SLM and EBM: Effect on the High Cycle Fatigue life," in

Procedia Engineering, Elsevier Ltd, 2018, pp. 89–97. https://doi.org/10.1016/j.proeng.2018.02.010

[150] Wycisk E., Solbach A., Siddique S., Herzog D., Walther F., and Emmelmann C., "Effects of defects in laser additive manufactured Ti-6Al-4V on fatigue properties," in *Physics Procedia*, Elsevier B.V., 2014, pp. 371–378. https://doi.org/10.1016/j.phpro.2014.08.120

[151] Eric W., Claus E., Shafaqat S., and Frank W., "High cycle fatigue (HCF) performance of Ti-6Al-4V alloy processed by selective laser melting," in *Advanced Materials Research*, 2013, pp. 134–139. https://doi.org/10.4028/www.scientific.net/AMR.816-817.134

[152] Le V.D., Pessard E., Morel F., and Prigent S., "Fatigue behaviour of additively manufactured Ti-6Al-4V alloy: The role of defects on scatter and statistical size effect," *International Journal of Fatigue*, vol. 140, Nov. 2020, https://doi.org/10.1016/j.ijfatigue.2020.105811

[153] Wang D., Wang H., Chen X., Liu Y., Lu D., Liu X., Han C., "Densification, Tailored Microstructure, and Mechanical Properties of Selective Laser Melted Ti–6Al–4V Alloy via Annealing Heat Treatment," *Micromachines (Basel)*, vol. 13, no. 2, Feb. 2022, https://doi.org/10.3390/mi13020331

[154] Rybachuk M, Mauger C.A, Fiedler T, and Öchsner A, "Anisotropic mechanical properties of fused deposition modeled parts fabricated by using acrylonitrile butadiene styrene polymer," *Journal of Polymer Engineering*, vol. 37, no. 7, pp. 699–706, Sep. 2017, https://doi.org/10.1515/polyeng-2016-0263

[155] Bača A., Konečná R., Nicoletto G., and Kunz L., "Influence of Build Direction on the Fatigue Behaviour of Ti6Al4V Alloy Produced by Direct Metal Laser Sintering," in *Materials Today: Proceedings*, Elsevier Ltd, 2016, pp. 921–924, https://doi.org/10.1016/j.matpr.2016.03.021

[156] Knowles C.R., Becker T.H., and Tait R.B., "Residual Stress Measurements and Structural Integrity Implications for Selective Laser Melted TI-6AL-4V #," *South African Journal of Industrial Engineering*, vol. 23, no. 3, 2012, https://doi.org/10.7166/23-3-515

[157] Malefane L.B., "Determination of the Fatigue Properties of Ti6Al4V (ELI) Parts built by a Direct Metal Laser Sintering System with Standard Process Parameters Followed by Post-Processing Treatments," Master of Engineering, Central University of Technology, Free State, Bloemfontein, 2019.

[158] Liu Q.C., Elambasseril J., Sun S.J., Leary M., Brandt M., and Sharp P.K., "The effect of manufacturing defects on the fatigue behaviour of Ti-6Al-4V specimens fabricated using selective laser melting," in *Advanced Materials Research*, Trans Tech Publications, 2014, pp. 1519–1524. https://doi.org/10.4028/www.scientific.net/AMR.891-892.1519

[159] Chan K.S., Koike M., Mason R.L., and Okabe T., "Fatigue life of titanium alloys fabricated by additive layer manufacturing techniques for dental implants," *Metall Mater Trans A Phys Metall Mater Sci*, vol. 44, no. 2, pp. 1010–1022, Feb. 2013, https://doi.org/10.1007/s11661-012-1470-4

[160] Ter Haar G.M., and Becker T.H., "Low temperature stress relief and martensitic decomposition in selective laser melting produced Ti6Al4V," *Material Design and Processing Communications*, vol. 3, no. 1, Feb. 2021, https://doi.org/10.1002/mdp2.138

[161] Cain V, Thijs L, Van Humbeeck J, Van Hooreweder B, and Knutsen R, "Crack propagation and fracture toughness of Ti6Al4V alloy produced by selective laser melting," *Additive Manufacturing*, vol. 5, pp. 68–76, Jan. 2015, https://doi.org/10.1016/j.addma.2014.12.006

[162] Xu Z.W., Liu A., and Wang X.S., "The influence of building direction on the fatigue crack propagation behavior of Ti6Al4V alloy produced by selective laser melting," *Materials Science and Engineering: A*, vol. 767, Nov. 2019, https://doi.org/10.1016/j.msea.2019.138409

[163] Yahaya S.N.M., Azmi I.I., Ng C.H., Lai C.F., Hashim M.Y., Adam A., Baehr R., Grote K.H., "An overview on forming process and heat treatments for heat treatable aluminium alloy," *Journal of Advanced Research in Fluid Mechanics and Thermal Sciences*, vol. 70, no. 1, pp. 112–124, 2020, https://doi.org/10.37934/ARFMTS.70.1.112124

[164] SIMUWU Vacuum Furnace "Heat Treatment of Titanium And Titanium Alloys." Accessed: Nov. 16, 2024. [Online]. Available: https://www.vacfurnace.com/vacuum-

furnace-news/heat-treatment-of-titanium-and-titanium-alloys/#:~:text=Therefore%2C%20vacuum%20furnace%20or%20argon,in%20an%20oxidizing%20atmosphere%2C%20strict

[165] Digges T.G., Rosenberg S.J., and Geil G.W., *Heat treatment and Properties of Iron and Steel*. Washington DC: National Bereauu of Standards, 1960.

[166] Xu Q., Li W., Yin Y., Zhou J., and Nan H., "Effect of hot isostatic pressing on the cast Ti6Al4V alloy with shrinkage cavities inside: Healing behavior, microstructure evolution and tensile property," *Materials Science and Engineering: A*, vol. 832, p. 142496, Jan. 2022, https://doi.org/10.1016/j.msea.2021.142496

[167] Jamshidi P., Aristizabal M., Kong W., Villapun V., Cox S.C., Grover L.M., Attallah M.M., "Selective laser melting of ti-6al-4v: The impact of post-processing on the tensile, fatigue and biological properties for medical implant applications," *Materials*, vol. 13, no. 12, pp. 1–16, Jun. 2020, https://doi.org/10.3390/ma13122813

[168] Moloi T.D., Dzogbewu T.C., Maringa M., and Muiruri A.M., "The Effect of Temperature on the Microstructures of Additively Manufactured Ti6Al4V(Eli)," *Iranian Journal of Materials Science and Engineering*, vol. 21, no. 3, Sep. 2024, https://doi.org/10.22068/ijmse.3589

[169] Vrancken B., Thijs L., Kruth J.P., and Van Humbeeck J., "Heat treatment of Ti6Al4V produced by Selective Laser Melting: Microstructure and mechanical properties," *J Alloys Compd*, vol. 541, pp. 177–185, Nov. 2012, https://doi.org/10.1016/j.jallcom.2012.07.022

[170] De Formanoir C., Michotte S., Rigo O., Germain L., and Godet S., "Electron beam melted Ti–6Al–4V: Microstructure, texture and mechanical behavior of the as-built and heat-treated material," *Materials Science and Engineering: A*, vol. 652, pp. 105–119, Jan. 2016, https://doi.org/10.1016/J.MSEA.2015.11.052

[171] Fan Y., Tian W., Guo Y., Sun Z., and Xu J., "Relationships among the Microstructure, Mechanical Properties, and Fatigue Behavior in Thin Ti6Al4V," *Advances in Materials Science and Engineering*, vol. 2016, 2016, https://doi.org/10.1155/2016/7278267

[172] Ding X., Sun L., Huang X., and Zhao Z., "Research on Three-Roll Screw Rolling Process for Ti6Al4V Titanium Alloy Bar," *High Temperature Materials and Processes*, vol. 38, no. 2019, pp. 178–182, Jan. 2019, https://doi.org/10.1515/htmp-2016-0215

[173] Eshawish N., Malinov S., Sha W., and Walls P., "Microstructure and Mechanical Properties of Ti-6Al-4V Manufactured by Selective Laser Melting after Stress Relieving, Hot Isostatic Pressing Treatment, and Post-Heat Treatment," *Journal of Materials Engineering and Performance*, vol. 30, no. 7, pp. 5290–5296, Jul. 2021, https://doi.org/10.1007/s11665-021-05753-w

[174] Ganor Y.I., Tiferet E., Vogel S.C., Brown D.W., Chonin M., Pesach A., Hajaj A., Garkun A., Samuha S., Yeheskei O., "Tailoring microstructure and mechanical properties of additively-manufactured ti6al4v using post processing," *Materials*, vol. 14, no. 3, pp. 1–17, Feb. 2021, https://doi.org/10.3390/ma14030658

[175] Fan Y., Shipway P.H., Tansley G.D., and Xu J., "The Effect of Heat Treatment on Mechanical Properties of Pulsed Nd:YAG Welded Thin Ti6Al4V," *Advanced Material Research*, vol. 189–193, pp. 3672–3677, Feb. 2011, https://doi.org/10.4028/www.scientific.net/AMR.189-193.3672

[176] Galarraga H., Warren R.J., Lados D.A., Dehoff R.R., Kirka M.M., and Nandwana P., "Effects of heat treatments on microstructure and properties of Ti-6Al-4V ELI alloy fabricated by electron beam melting (EBM)," *Materials Science and Engineering: A*, vol. 685, pp. 417–428, Feb. 2017, https://doi.org/10.1016/J.MSEA.2017.01.019

[177] Kewate O.J., and Punniyakoti S., "Ti3AlC2 MAX phase and Ti3C2TX MXene-based composites towards supercapacitor applications: A comprehensive review of synthesis, recent progress, and challenges," *Journal of Energy Storage*, vol. 72, p. 108501, Nov. 2023, https://doi.org/10.1016/j.est.2023.108501

[178] Metal Solutions EOS M 290 The Additive Manufacturing System for the Production of Serial Components, Spare Parts and Functional Prototypes Directly in Metal. Accessed: May 02, 2024. [Online]. Available: https://engineering.cmu.edu/mfi/_files/documents/equipment/eos-m-290-description.pdf

[179] T-M Vacuum Products, "Super Series ™ Vacuum Furnace System It's super-precise and super-fast." [Online]. Available: www.tmvacuum.com

[180] Madeja M., Karoluk M., and Smolina I., "Welding of Ti-5Al-5Mo-5 V-1Cr-1Fe parts manufactured in the Electron Beam Melting," *Material Design*, vol. 195, p. 108969, Oct. 2020, https://doi.org/10.1016/J.MATDES.2020.108969

[181] Instron, "Servohydraulic | Fatigue Testing Systems," 2023, https://www.instron.com/en-in/resources/literature

[182] Riley Industries Ltd, "Future Tech Group FM7 Micro, The Marketplace for Surface Technology. New and Used Process Equipment & Machinery," https://www.rileysurfaceworld.co.uk/live/machines2/27767.pdf?srsltid=AfmBOopaXiUH1X5_TL7hrTpSCBjrlVo-zPU7jnC1fJcuNySeMN1hD--C

[183] Muiruri A.M., "Investigation of the High Strain Rate Behaviour and Impact Toughness of Ti6Al4V (ELI) Parts Built by the EOS M280 DMLS System with Standard Process Parameters; As-Built and Stress Relieved," Central University of Technology, Free State, Bloemfontein, 2018.

[184] Madikizela C., Cornish L.A., Chown L.H., and Möller H., "Microstructure and mechanical properties of selective laser melted Ti-3Al-8V-6Cr-4Zr-4Mo compared to Ti-6Al-4V," *Materials Science and Engineering: A*, vol. 747, pp. 225–231, Feb. 2019, https://doi.org/10.1016/j.msea.2018.12.100

[185] Phutela C., Aboulkhair N.T., Tuck C.J., and Ashcroft I., "The effects of feature sizes in selectively laser melted Ti-6Al-4V parts on the validity of optimised process parameters," *Materials*, vol. 13, no. 1, p. 117, Jan. 2020, https://doi.org/10.3390/ma13010117

[186] Li Y., Song L., Xie P., Cheng M., and Xiao H., "Enhancing Hardness and Wear Performance of Laser Additive Manufactured Ti6Al4V Alloy Through Achieving Ultrafine Microstructure," *Materials*, vol. 13, no. 5, p. 1210, Mar. 2020, https://doi.org/10.3390/ma13051210

[187] Jażdżewska M., Kwidzińska D.B., Seyda W., Fydrych D., and Zieliński A., "Mechanical properties and residual stress measurements of grade IV titanium and Ti-6Al-4V and Ti-

13Nb-13Zr titanium alloys after laser treatment," *Materials*, vol. 14, no. 21, Nov. 2021, https://doi.org/10.3390/ma14216316

[188] Song J., Han Y., Fang M., Hu F., Ke L., Li Y., Lei L., Lu W., "Temperature sensitivity of mechanical properties and microstructure during moderate temperature deformation of selective laser melted Ti-6Al-4V alloy," *Materials Characterization*, vol. 165, Jul. 2020, https://doi.org/10.1016/j.matchar.2020.110342

[189] Zhang H., Wang C., Zhou G., Zhang S., and Chen L., "Dependence of strength and ductility on secondary α phase in a novel metastable-β titanium alloy," *Journal of Materials Research and Technology*, vol. 18, pp. 5257–5266, May 2022, https://doi.org/10.1016/j.jmrt.2022.05.019

[190] Zha M., Zhang H., Yu Z., Zhang X., Meng X., Wan H., Jiang Q., "Bimodal microstructure - A feasible strategy for high-strength and ductility materials," *Journal of Materials Science & Technology*, vol. 34, no. 2, pp. 257–264, 2018, https://doi.org/10.1016/j.jmst.2017.11.018

[191] Xing L.L., Zhang W.J., Zhao C.C., Gao W.Q., Shen Z.J., and Liu W., "Influence of Powder Bed Temperature on the Microstructure and Mechanical Properties of Ti-6Al-4V Alloy Fabricated via Laser Powder Bed Fusion," *Materials*, vol. 14, no. 9, p. 2278, Apr. 2021, https://doi.org/10.3390/ma14092278

[192] Srivastava M., Jayakumar V., Udayan Y., Sathishkumar M., Muthu S.M., Gautam P., Nag A., "Additive manufacturing of Titanium alloy for aerospace applications: Insights into the process, microstructure, and mechanical properties," *Applied Materials Today*, vol. 41, p. 102481, Dec. 2024, https://doi.org/10.1016/j.apmt.2024.102481

[193] Hou X., Liu Z., Wang B., Lv W., Liang X., and Hua Y., "Stress-strain curves and modified material constitutive model for Ti-6Al-4V over thewide ranges of strain rate and temperature," *Materials*, vol. 11, no. 6, Jun. 2018, https://doi.org/10.3390/ma11060938

[194] Obayi C.S., Tolouei R., Mostavan A., Paternoster C., Turgeon S., Okorie B.A., Obikwelu D.O., Montovani D., "Effect of grain sizes on mechanical properties and biodegradation behavior of pure iron for cardiovascular stent application," *Biomatter*, vol. 6, no. 1, p. e959874, Jan. 2016, https://doi.org/10.4161/21592527.2014.959874

[195] Anwar M.S., Widjaya R.R., Prasetya L.B.A., Arfi A.A., Mabruri E., and Siradj E.S., "Effect of Grain Size on Mechanical and Creep Rupture Properties of 253 MA Austenitic Stainless Steel," *Metals (Basel)*, vol. 12, no. 5, p. 820, May 2022, https://doi.org/10.3390/met12050820

[196] Zhao J.R., Hung F.Y., Lui T.S., and Wu Y.L., "The relationship of fracture mechanism between high temperature tensile mechanical properties and particle erosion resistance of selective laser melting Ti-6al-4v alloy," *Metals (Basel)*, vol. 9, no. 5, May 2019, https://doi.org/10.3390/met9050501

[197] Moletsane M.G., Krakhmalev P., Kazantseva N., du Plessis A., Yadroitsava I., and Yadroitsev I., "Tensile properties and microstructure of direct metal laser-sintered Ti6Al4V (ELI) alloy," *South African Journal of Industrial Engineering*, vol. 27, no. 3SpecialIssue, pp. 110–121, 2016, https://doi.org/10.7166/27-3-1667

[198] Kan W.H., Chiu L.N.S., Lim C.V.S., Zhu Y., Tian Y., Jiang D., Huang A., "A critical review on the effects of process-induced porosity on the mechanical properties of alloys fabricated by laser powder bed fusion," Jun. 01, 2022, *Springer*. https://doi.org/10.1007/s10853-022-06990-7

[199] Zhang H., Dong D., Su S., and Chen A., "Experimental study of effect of post processing on fracture toughness and fatigue crack growth performance of selective laser melting Ti-6Al-4V," *Chinese Journal of Aeronautics*, vol. 32, no. 10, pp. 2383–2393, Oct. 2019, https://doi.org/10.1016/j.cja.2018.12.007

[200] Fracture Mecahnics, Accessed: Nov. 28, 2024. [Online]. Available: https://mechanicalc.com/reference/fracture-mechanics#:~:text=In%20fracture%20mechanics%2C%20a%20stress,material%20increases%2C%20fracture%20toughness%20decreases

[201] IOWA State University, "Physics of Nondestructive Evaluation." Accessed: Nov. 28, 2024. [Online]. Available: https://www.nde-ed.org/Physics/Materials/Mechanical/FractureToughness.xhtml

APPENDIXES

Appendix A-Tensile Fracture Surfaces

Figure A shows the fracture surfaces of specimens that were stress-relieved, followed by high-temperature annealing and tested in tension at different temperatures.

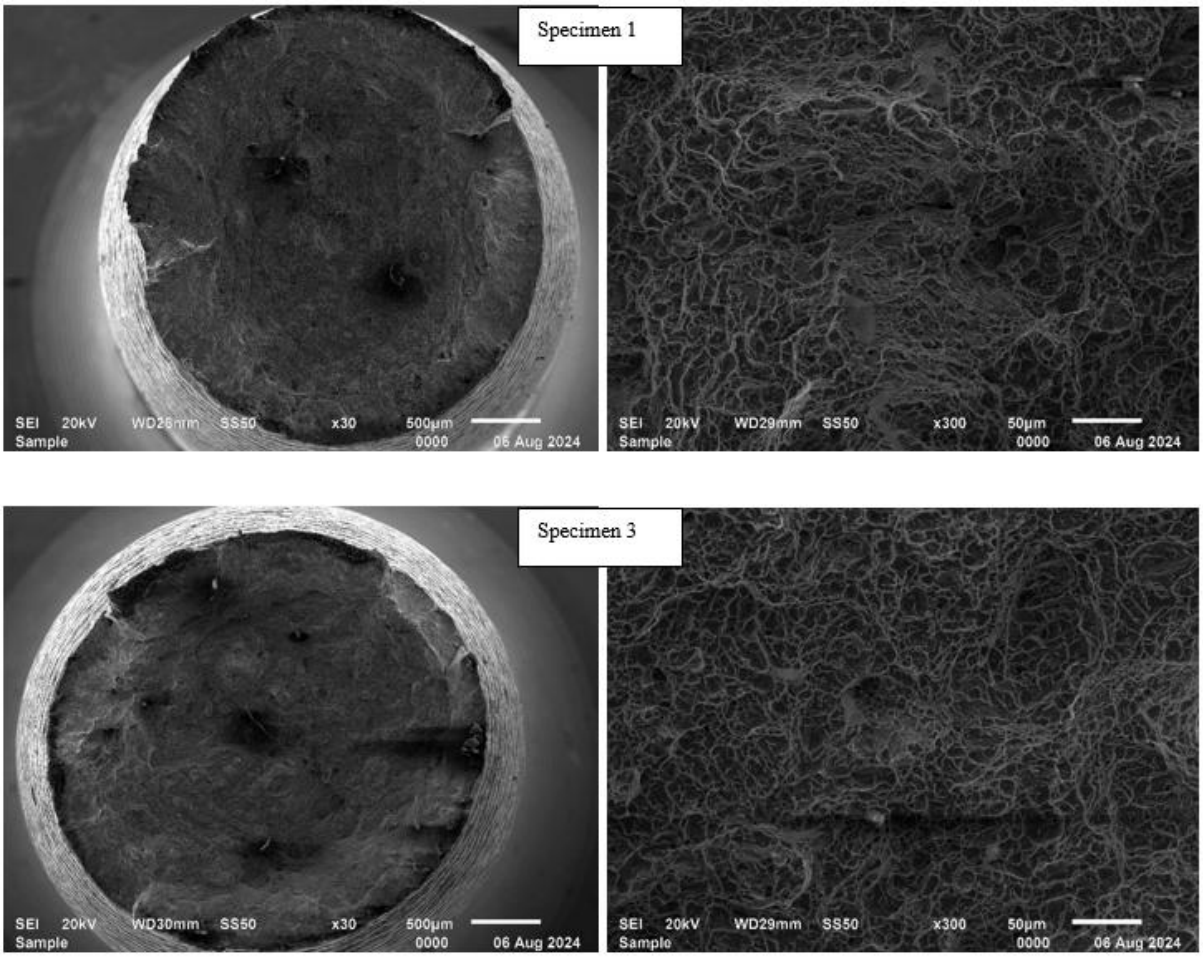

Figure A1: SEIs micrographs of the fracture surfaces of specimens that were stress-relieved followed by high-temperature annealing and tested in tension at 20 ℃

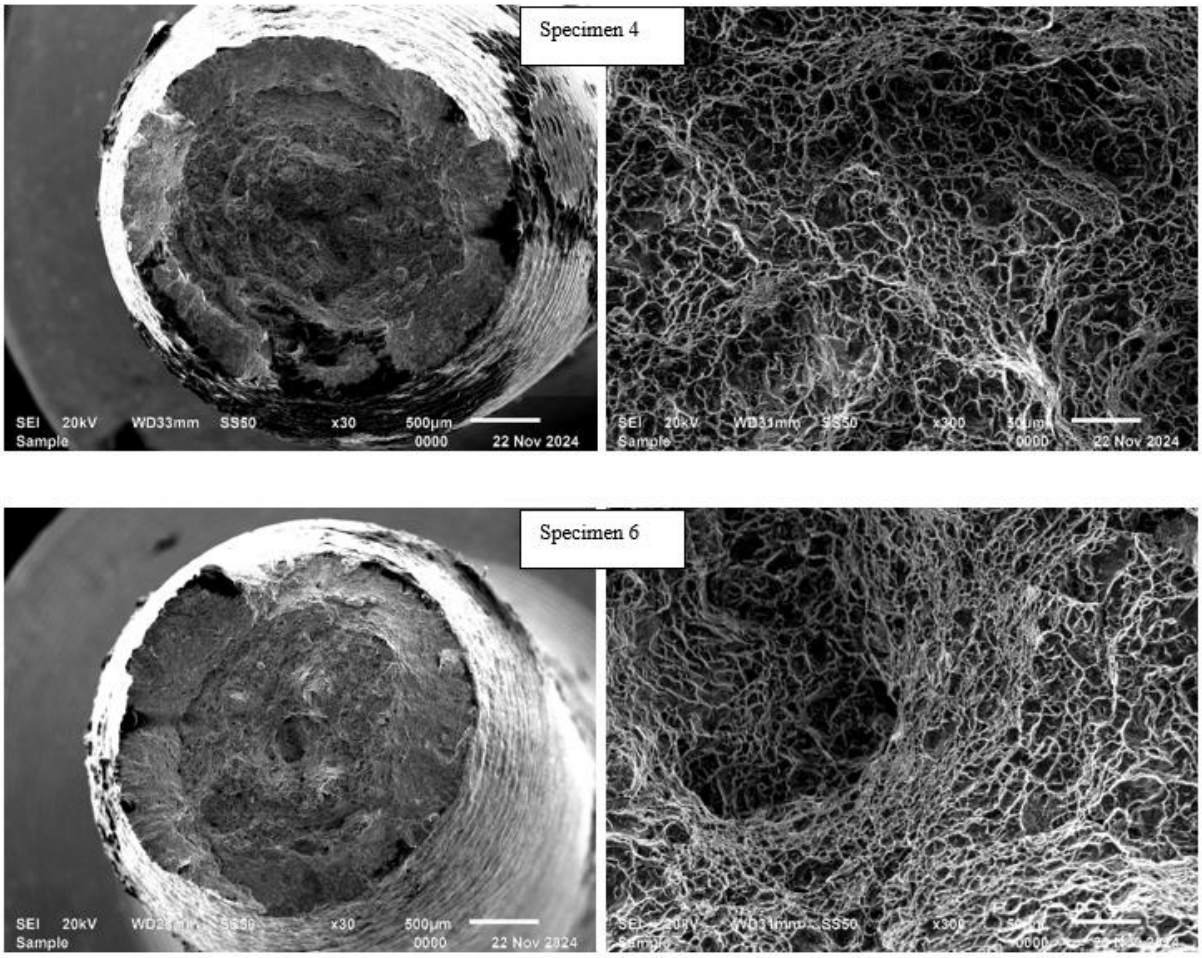

Figure A2: SEIs micrographs of the fracture surfaces of specimens that were stress-relieved followed by high-temperature annealing and tested in tension at 175 ℃

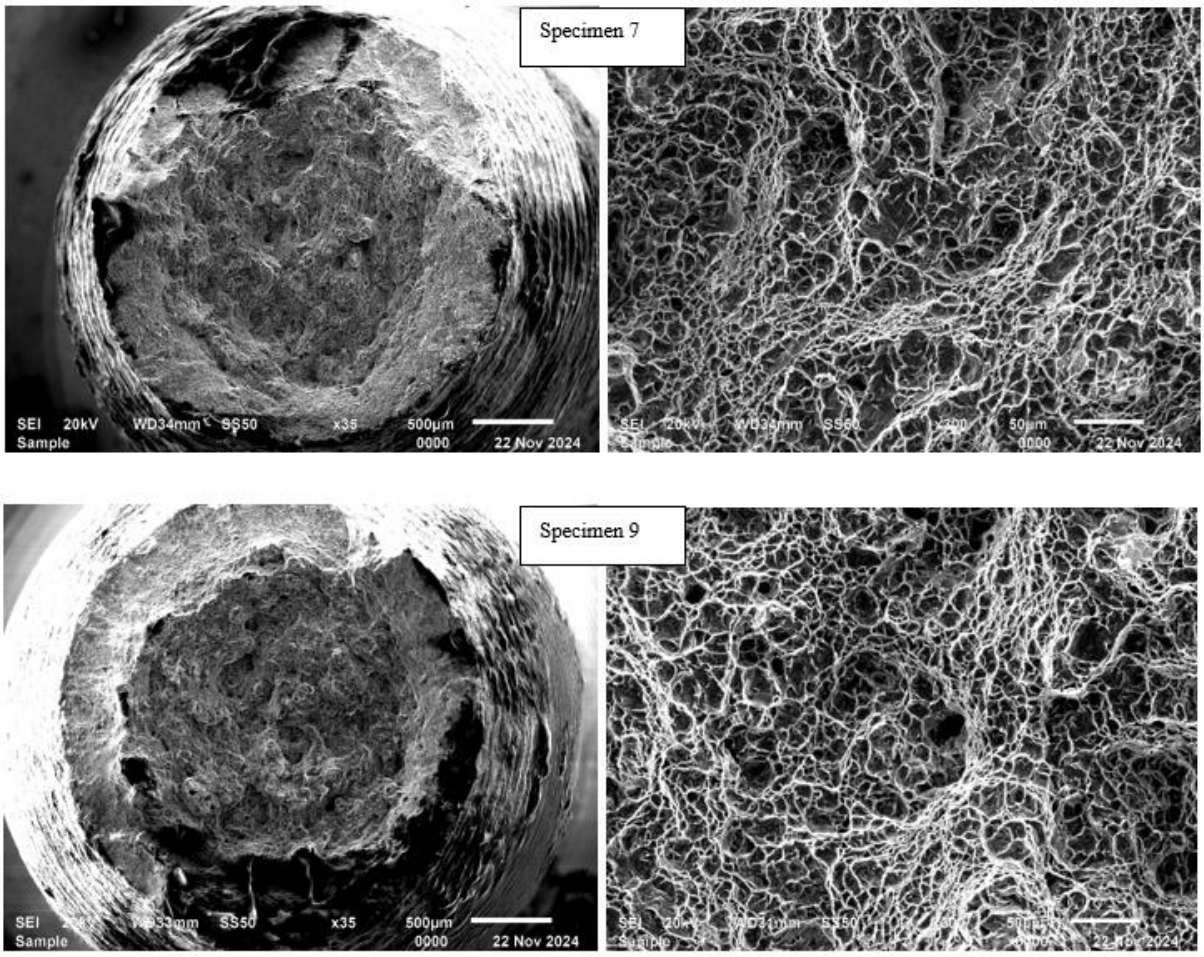

Figure A3: SEIs micrographs of the fracture surfaces of specimens that were stress-relieved followed by high-temperature annealing and tested in tension at 325 ℃

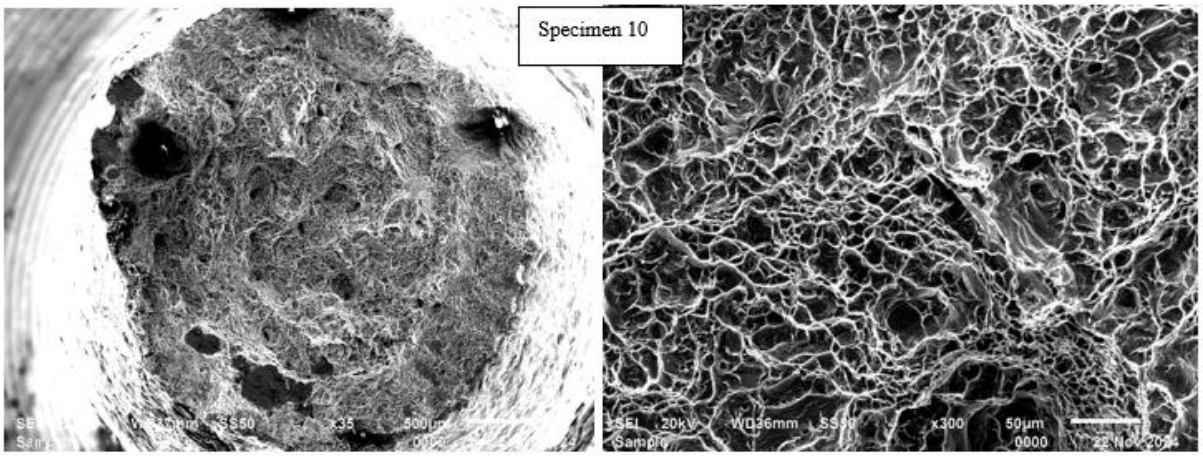

Figure A4: SEIs micrographs of the fracture surfaces of a specimen that were stress-relieved followed by high-temperature annealing and tested in tension at 475 ℃